Covalent Approach toward Optimum Bulk Hetero-junction Morphology in Organic Solar Cells

A dissertation

Submitted to Graduate School of Materials Science,

Nara Institute of Science and Technology

in partial fulfillment of the requirements

for the degree of

Doctor of Philosophy

in the subject of

Engineering

Yuto Tamura

March 2018

Table of Contents

Abbreviations

a.u.: Arbitrary unit

AFM: Atomic force microscopy

BP: Tetrabenzoporphyrin

BCOD: Bicyclo[2.2.2]octadieno

BHJ: Bulk-heterojunction

BIPVs: Building-Integrated Photovoltaics

CP: 1,4:8,11:15,18:22,25-Tetraethano-29*H*,31*H*-tetrabenzo[*b*,*g*,*l*,*q*]porphyin

D–A: Donor–acceptor

DCTB: *Trans*-2-[3-(4-*tert*-Butylphenyl)-2-methyl-2-propenylidene]malononitrile

DFT: Density functional theory

DDQ: 2,3-Dichloro-5,6-dicyano-1,4-benzoquinone

DPP: Diketopyrrolopyrrole

EDX: Energy dispersive X-ray

EQE: External quantum efficiency

ESI: Electrospray ionization

Fc/Fc$^+$: ferrocene/ferrocenium

FF: Fill factor

FWHM: Full-width at half-maximum

GIWAXD: Grazing-incident wide-angle X-ray diffractometry

GPC: Gel permeation chromatography

HOMO: Highest occupied molecular orbital

HR-MS: High-resolution mass spectrometry

Int.: Intensity

ITO: Indium-tin oxide

$\boldsymbol{J}_{\mathbf{SC}}$: Short-circuit current density

$\mathbf{L}_{\mathbf{D}}$: Exciton diffusion length

LUMO: Lowest unoccupied molecular orbital

$\boldsymbol{\mu}_{\mathbf{h}}$: Hole mobility

$\boldsymbol{\mu}_{\mathbf{e}}$: Electron mobility

MALDI: Matrix-assisted laser desorption/ionization

NBS: *N*-Bromosuccinimide

NMR: Nuclear magnetic resonance

ODCB: *o*-Dichlorobenzene

OFETs: Organic field-effect transistors

OSCs: Organic solar cells

P3HT: Poly(3-hexylthiophene-2,5-diyl)

$\mathbf{PC_{61}BM}$: [6,6]-Phenyl-C_{61}-butyric acid methyl ester

PCE: Power conversion efficiency

PEDOT:PSS: Poly(3,4-ethlenedioxythi-ophene):poly(4-styrenesulfonate)

PEG: Polyethylene glycol

r-DA: retro-Deals–Alder

RMS: Root-mean square

$\boldsymbol{R}_{\mathbf{s}}$: Serial resistance

R_{sh}: Shunt resistance

SCLC: Space charge limited current

SEM: Scanning electron microscope

SIMEF: Bis(dimethylphenylsilylmethyl) [60]fullerene

STEM: Scanning transmission electron microscope

$TBAPF_6$: Tetrabutylammonium hexafluorophosphate

TFA: Trifluoroacetic acid

TGA: Thermogravimetric analysis

THF: Tetrahydrofuran

TIPS: Triisopropylsilyl

TLC: Thin-layer chromatography

TMS: Trimethylsilyl

UV−vis: Ultraviolet–visible

V_{OC}: Open-circuit voltage

XRD: X-ray diffraction

Chapter 1.

General Introduction

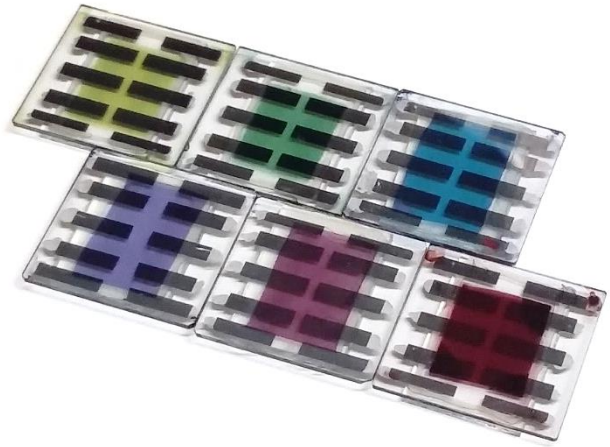

In this chapter, research background and aim of this study are described.

1-1. Solution-Processed Organic Solar Cells (OSCs)

1-1-1. Research Significance

A photovoltaic generation is one of valuable technologies because of the human- and environmental-friendliness. Silicon solar cells have already been in common use and are placed on roofs of buildings all over the world. Although the roof is the favorable places for solar cells, the space is limited because living facilities such as water storage tank, TV antenna, and outdoor machine of air conditioner must be in there. Toward the next generation of photovoltaic systems, Building-Integrated Photovoltaics (BIPVs) have been widely required. Solution-processed organic solar cells (OSCs) are one of the promising photovoltaic devices for BIPVs owing to the unique combination of their low environmental impact, low-weight, flexibility, and permeability[1–7] with large area device fabrication. As the active layer is composed chiefly of organic semiconducting materials, effective printing technic such as the roll-to-roll processing[8–11] can be applied for OSC fabrications to achieve the low-cost production. In addition, OSCs are interesting candidates to approach the interpretation and understanding for interfacial- and orientational-behavior of organic semiconducting materials with their developments.

Therefore, the author believes that the comprehensive study for OSCs is challenging work which can provide scientific- and social-contributions.

1-1-2. Working Mechanism

Figure 1 illustrates the fundamental steps of the photon-to-electron conversion mechanism for OSCs. They are classified into four general steps as follows. Here each step is explained in the case where electron donor material is the main photo-absorber.

First, an electron in the donor material undergoes photo-induced excitation resulting in a formation of excitons (electron (e^-) and hole (h^+) bound with Coulomb attraction) (Process 1 in Figure 1). The absorption range and the light harvesting ability of donor materials basically depend on their molecular structure and electron conjugate system. Toward the effective use of light energy from sunlight, donor materials should exhibit wide absorption range at 300–900 nm with high absorbance coefficient. The recent developments of conjugate systems for donor materials called push-pull,[12–19]

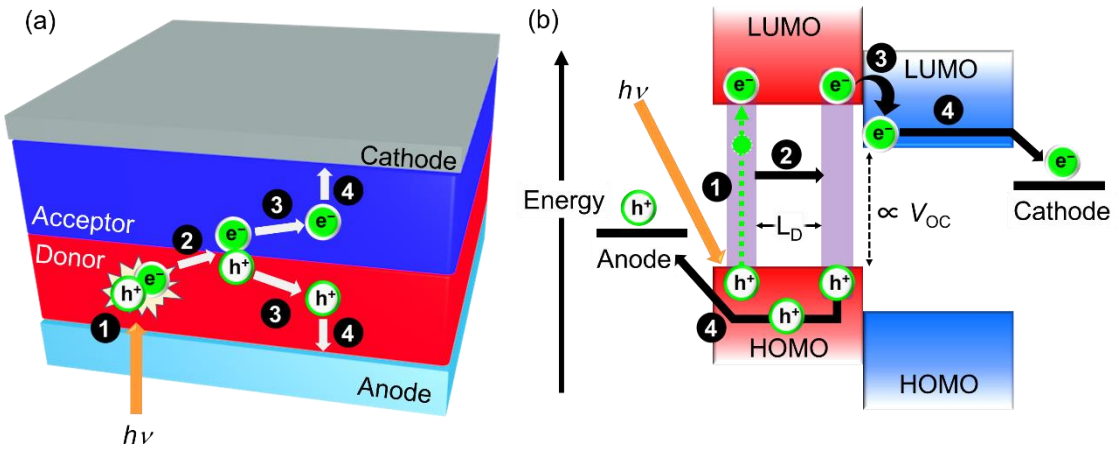

Figure 1. (a) Schematic working principle of OSCs. (b) Functional mechanism of OSCs. Each number (1−4) is equivalent processes between figure (a) and (b).

donor–acceptor–donor (D–A–D),[20–24] and acceptor–donor–acceptor (A–D–A)[25–30] conjugates have successfully achieved the small optical band gap resulting in the wide range absorption.

Second, generated excitons must migrate toward the donor–acceptor interface within the diffusion length (L_D) (Process 2 in Figure 1). Since the typical values of L_D in organic materials are a few to tens of nanometers,[31] the ideal donor and acceptor domain sizes are less than the twice of L_D. OSC materials generally have low dielectric permittivity (around 3–4.5),[32–42] thus, generated electron (e^-)–hole (h^+) pairs are generally bound with higher energy (0.5–1 eV) than thermal energy at a room temperature (approximately 0.025 eV at 298 K).[43,44] For the dissociation of the excitons to free carriers, second materials are required as electron acceptors to break up their Coulomb interaction. The acceptor materials taking up the majority in OSC studies are fullerene (C_{60} or C_{70}) derivatives. Recently, non-fullerene acceptor molecules have also been developed actively to overcome the obstacles associated with fullerenes such as their weak absorption and limited structural tunability.[45–47]

Third, the exciton at donor–acceptor interfaces is dissociated to a hole and an electron by electron transfer from the excited donor to the acceptor material (Process 3 in Figure 1). In this process, the proper paths of the charge carrier transport are necessary for preventing their recombination. In addition, states delocalized π-electron in ordered regions of the donor and acceptor materials would be the key to promote the effective dissociation.[48] It is also noteworthy that the open-circuit voltage (V_{OC}) of OSC device

correlates with the difference of energy levels between the HOMO of donor material and the LUMO of acceptor material. To obtain an improved V_{OC}, a higher LUMO level of acceptor is desirable. At the same time, it should be lower (ideally 0.2–0.3 eV) than the LUMO level of donor material for effective electron transfer.[49]

Fourth, dissociated free electrons and holes are transported toward respective electrodes by diffusion or drifting through the acceptor-rich phase and the donor-rich phase, respectively, to generate power (Process 4 in Figure 1). The efficiency of this process depends on the carrier mobility of materials to the out-of-plane direction and film structures. Localization of the donor and acceptor materials near the anode and cathode, respectively, is also required to maximize the carrier extraction in the respective electrode.

1-1-3. Design of Active Layer

As described above, active layers must achieve not only good absorption but also multistep carrier movements to generate power. Therefore, the active-layer architecture plays a significant role in determining the OCS performance.

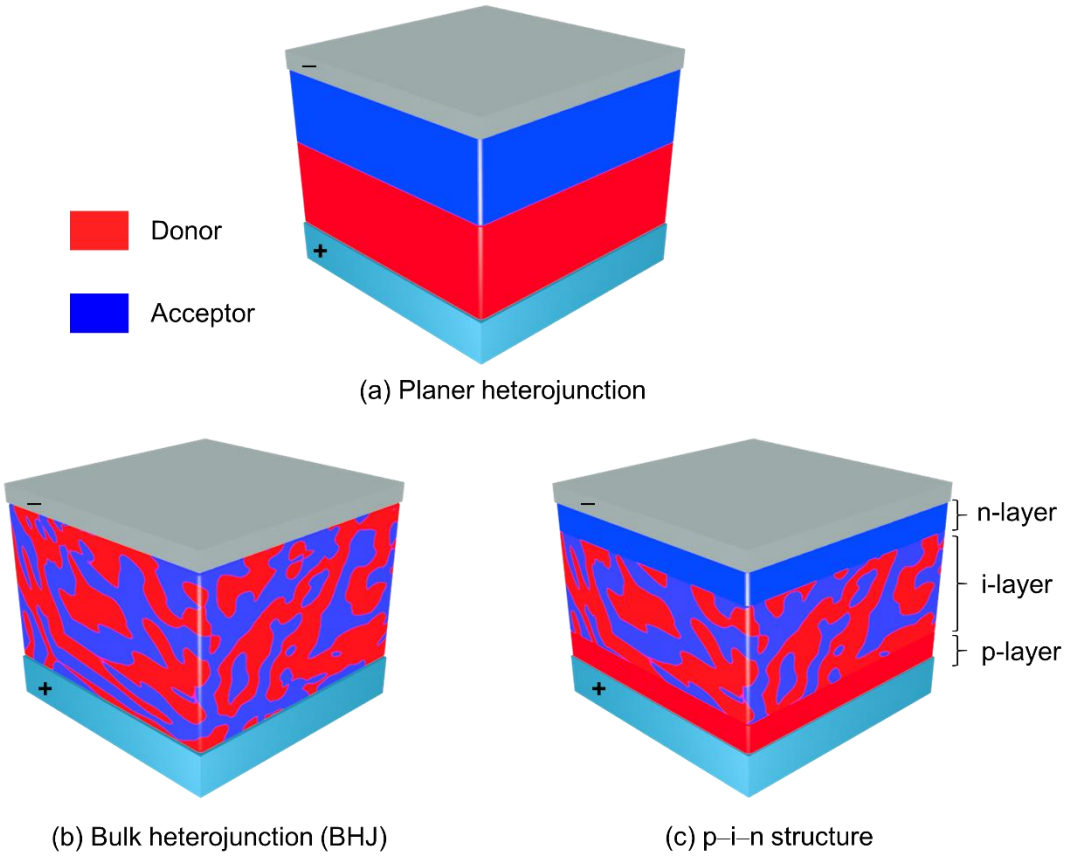

(a) Planer heterojunction

(b) Bulk heterojunction (BHJ)

(c) p–i–n structure

Figure 2. Typical active layer architectures for OSCs.

The planer heterojunction structure, where individual donor- and acceptor-layers are stacked as an active layer, is a pioneering system in the early study of OSCs (Figure 2a).[50] Because of the perfect phase separation in the vertical direction, this structure is beneficial for carrier transport and extraction. However, the planner heterojunction gives a limited area for exciton generation (around 10–20 nm from the donor–acceptor interface). Thus, the power conversion efficiency is also limited. On the other hand, this structure still plays significant roles as ideal model to investigate impacts of interfacial molecular orientation on radiative charge generation, transport, and recombination efficiencies.[51–57]

The bulk heterojunction (BHJ) structure, where donor and acceptor semiconductors are blended together, is the most promising structure and taking up the majority of recent OSC studies (Figure 2b). The powerful capability for a construction of large area donor–acceptor junction for exciton dissociation is providing highl PCEs of over 11% in single cell OSCs.[58–62] A key to obtain the best performance with BHJ structure is the optimization of deposition process (ratio of donor–acceptor components, choice of cast solvents,[63] morphological additives,[63–66] thermal-[67–71] or solvent-annealing,[67,72–79] etc.) to form suitable morphologies depending on selected materials. However, it is often difficult to conserve the optimized BHJ layers because nanometer-scale morphologies of the BHJ are metastable structure.[80–84] Improvements of morphological stability of BHJ structure will be one of the issues to be addressed in the future. Control of vertical phase separation to maximize the charge extraction, in which donor rich layer near the anode and acceptor rich layer near the cathode, is also a challenging task for achieving further improved PCEs.

The p–i–n structure has an internal (i) layer which is sandwiched between neat donor-layer (p-layer) and acceptor-layer (n-layer) in the device (Figure 2c). In this structure, the i-layer plays a roll of effective charge carrier generations same as BHJ structure and then the charge carriers are extracted at the respective electrode through p- and n-layers. This well-defined three-layered structure has been propounded as one of the ideal structures for OSCs.[85–88] In addition, if an interpenetration structure of p- and n-type materials can be constructed in the i-layer (Figure 3), the best PCEs of active layer materials will be achieved in theory. However, the construction of p–i–n structure had been limited to vapor deposition process, because soluble organic semiconductor

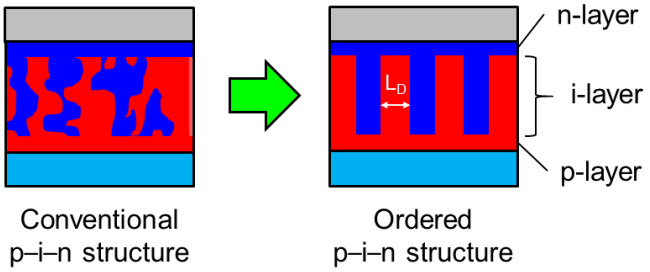

Figure 3. Theoretical optimum morphology for i-layer

films can be washed away easily during the deposition of the upper layer material.

To overcome this problem, a remarkable methodology so-called "precursor approach" has been reported. In this approach, a precursor molecule which is well-soluble and cohesionless can be deposited on a substrate by solution process and the in-situ conversion from the precursor to target semiconducting material is completed by thermal- or photo-stimulation.[89,90] Since the conversion from the precursor to target semiconducting material involves dramatical decrease in solubility owing to the structural change, the upper layer can be solution-deposited to construct the three-layered p–i–n structure. For example, the construction of p–i–n-type device using photo precursor approach has been reported in 2014.[91] OSC performances of the p–i–n devices are higher than the corresponding bilayer or BHJ-type devices. Thus, the superiority of the solution-processed p–i–n structure has been verified experimentally.

1-2. Tetrabenzoporphyrin for Solution-Processable Semiconducting Material

Tetrabenzoporphyrin (BP) is one of the superior semiconducting donor materials and has four fused benzene rings on the *β*-positions of porphyrin. Because of the highly expanded π-conjugated structure, BP exhibits suitable qualities for OSCs material, i.e., strong molar absorbance coefficient (over 10^5 M^{-1} cm^{-1} at 420–550 nm in solution)[92] and excellent chemical stability. BP is hardly soluble in common organic solvents because of the strong π–π interaction. Therefore, the precursor approach using 1,4:8,11:15,18:22,25-tetraethano-*29H*,*31H*-tetrabenzo[*b*,*g*,*l*,*q*]porphyrin (CP)[90] is a powerful tool toward solution-processed BP-based devices. In this approach, well-soluble CP is solution-

deposited on a substrate, and then the obtained CP film is converted to a poly-crystalline BP film in situ by a thermally induced retro-Diels–Alder reaction (Figure 4).

Organic field effect transistors (OFETs) based on free-base and several metal-incorporated BPs have been prepared by using this approach and showed good hole mobilities (0.07–0.22 $cm^2\ V^{-1}\ s^{-1}$).[93–96] By taking advantage of the decrease in solubility upon the thermal conversion from CP to BP, fabricated solution-processed p–i–n-type OSCs have also been reported with findings of interesting BP features. Nguyen and co-workers observed nanoscale mobility of over 10 $cm^2\ V^{-1}\ s^{-1}$ by using the space charge limited current (SCLC) method with conducting-atomic force microscopy (c-AFM) in the p-layer (neat BP film).[97] However, not-so-great performance (PCE = 1.5%) was obtained because of large phase separation and unfavorable vertical morphology due to a formation of the micrometer-size BP grains in the i-layer (blended BP:$PC_{61}BM$ layer). Matsuo and co-workers have also reported similar results about a BP:$PC_{61}BM$-based p–i–n-type OSC with a PCE of 2.0%.[98] At the same time, they have successfully obtained the vertically ordered BP column structure in the i-layer by using a well-designed fullerene derivative named 1,4-bis(silylmethyl)[60]fullerene (SIMEF). The resulting BP:SIMEF-based p–i–n device achieved respectable performance (PCE = 5.2–5.4%) despite the simple molecule structure of BP.[98,99]

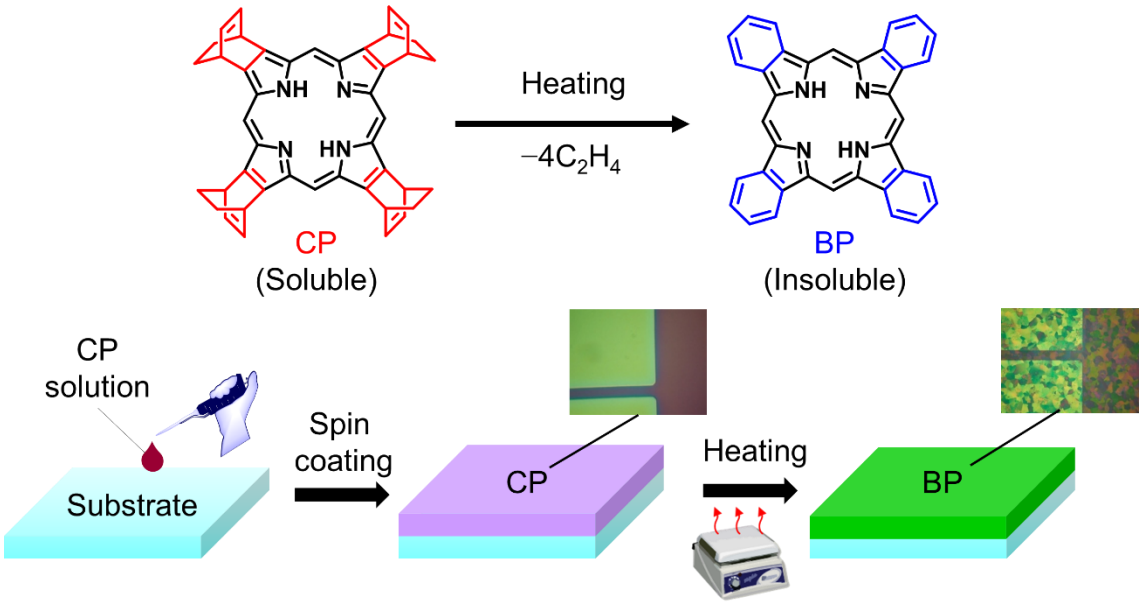

Figure 4. Chemical transformation of CP to BP by heating and schematic description of BP film preparation via the thermal precursor approach.

1-3. Covalent Donor–Acceptor Molecules as OSC Materials

Covalent donor–acceptor (D–A) molecules are designed to have both donor and acceptor units connected via an organic linker moiety in a same molecule. They have been widely studied to understand the charge separation and recombination processes between donor and acceptor units.[100–103] In addition, various D–A compounds have been examined to use as active materials in BHJ OSCs, since direct connection of donor and acceptor components can be beneficial for forming a maximal D–A interface within a film, thereby providing high charge-separation efficiency. Because [6,6]-phenyl-C_{61}-butyric acid methyl ester ($PC_{61}BM$) is the most widely used as an acceptor in OSCs, D–A molecules using fullerene have been designed and synthesized. For example, Hashimoto's group has reported several D–A molecules using C_{60} in their syntheses and investigations of the photovoltaic properties.[104–106] The OSC device using covalent oligothiophene–C_{60} (Th–C_{60}) as the active layer material showed a current density (J_{SC}) of 0.93 mA cm^{-2} and a fill factor (FF) of 0.23 resulting in a PCE of 0.15% (Figure 5a).[104] They assumed that one of the possible factors of the observed low PCE was the inefficient charge transport in the active layer because of an unsuitable molecular packing of the oligothiophene and/or C_{60} moieties. This situation was improved in another D–A molecule using oligo phenyl vinylene (OPV) and C_{60} (OPV–C_{60}) (Figure 5b).[105] The strong π–π interaction of OPV moiety successfully enhanced the charge-carrier transport, resulting in a PCE of 1.28%. In addition, further improvement of the performance (PCE = 1.92%) was achieved by the introduction of C_{70} fullerene instead of C_{60} (OPV–C_{70}) (Figure 5c).[106] This OPV–C_{70} film also showed much higher morphological stability under prolonged annealing (110 °C for 72 h) compared with the mixed BHJ films. More recently, a C_{60}-linked diathiafulvalene-functionalized diketopyrrolopyrrole (DPP–C_{60}) molecule has been reported by Singh et al. as an OSC material (Figure 5d).[107] DPP–C_{60} shows a wide-range absorption reaching up to 1000 nm as film due to the well-designed donor moiety, and the external quantum yield (EQE) spectrum is also broad (400–800 nm) and reaching up to 1000 nm to achieve a PCE of 2.17% in the device. And more performant D–A molecule which has an oligothiophene containing benzodithiophene rhodamine (BDTRh) as donor and two C_{60} as acceptor moiety (BDTRh–C_{60}) has been reported by Gundogdu, Kim, Woo and co-workers (Figure 5e).[108] The fabricated OSC with BDTRh–C_{60} exhibited a PCE of 2.44%,

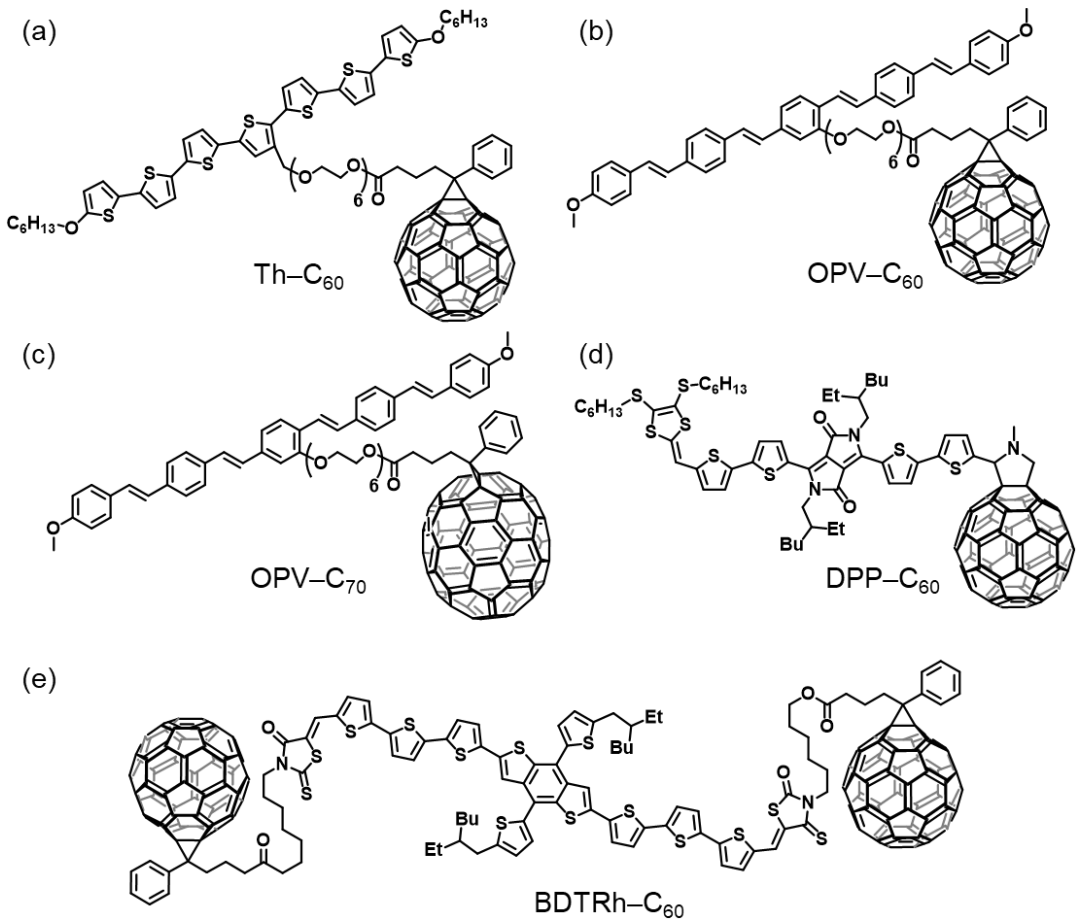

Figure 5. Examples of covalent D–A molecule for OSCs.

which is the highest among the reported efficiencies as single-component devices. In this study, BDTRh–C_{60} showed excellent device and morphological stabilities, showing scarce degradation of PCEs after long-term heating (80 °C for 100 h) compared with the blended BHJ system.

Attempts to fabricate OSCs with covalent D–A molecules are still sporadic and scarce. It is probably because they have not showed enough photovoltaic performances compared with the state-of-the-art OSC studies. However, the D–A architecture which is capable of ensuring the function of light absorption and exciton dissociation in a single molecule would be a key to evade the problems related to the short diffusion length in organic semiconductors. Furthermore, D–A molecules can present several advantages such as considerable simplification of deposition process for device fabrication and stabilization of active layer morphology. Therefore, D–A molecules are promising to be excellent materials toward the combination high OSC performance and long-term stability.

1-4. Aims and Outline

As described above, BP has excellent advantages for the OSC application because of the suitable photo- and electric-properties and accessibility to construction of p–i–n structure. The crystalline blend film of BP and $PC_{61}BM$ tends to have good storage stability, however, it is often difficult to form an ideal morphology because of the strong self-interaction of BP to lead poor miscibility with fullerene. Although BP:SIMEF-based OSC can provide an effective columnar BP structure, the structural region has been limited (ca. 60%). To overcome the problem, the author proposed two strategies toward optimum active layer structure as shown in Figure 6. The strategy A is construction of a proper phase separation with a covalent D–A molecule. This morphological arrange, in which the two phases of donor and acceptor within the bulk heterojunction are interspaced on a length scale of the exciton diffusion length, is expected to provide an effective transport path for both p-type and n-type charge carriers to electrodes, without sacrificing

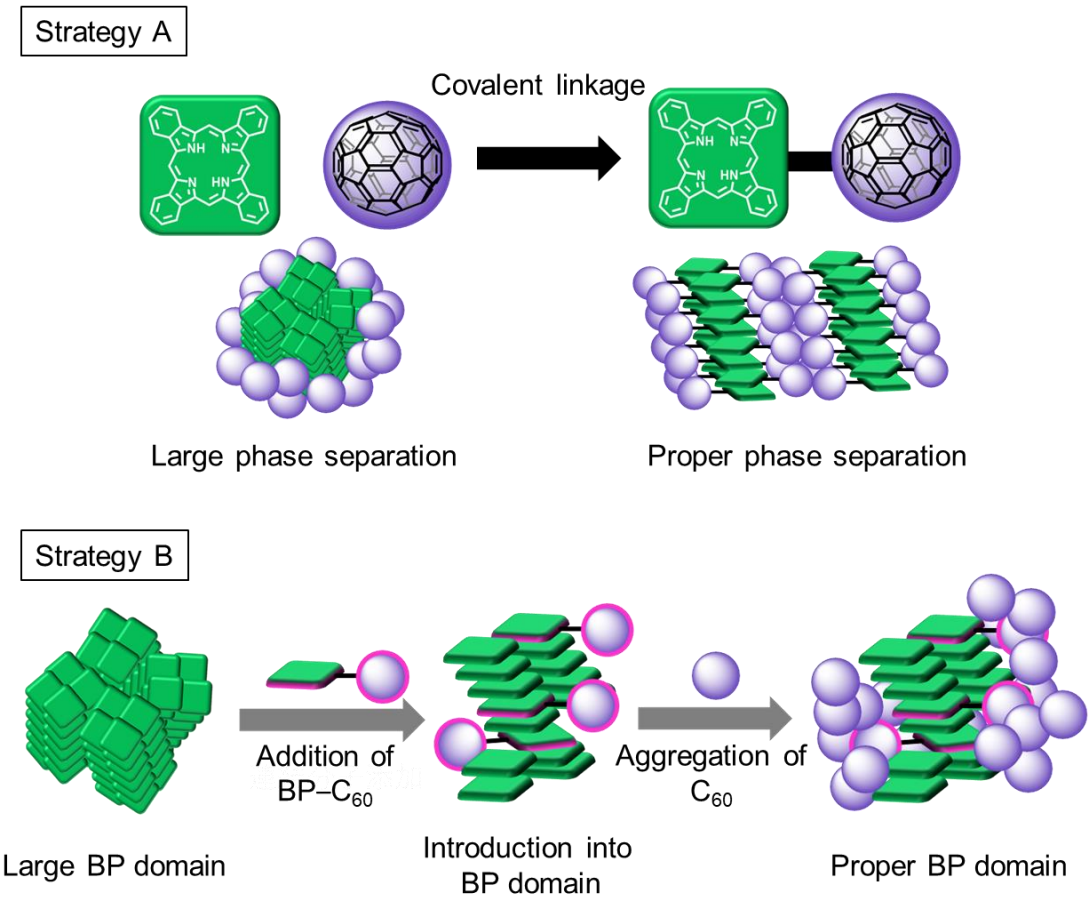

Figure 6. Strategies toward optimum morphologies in this study.

the D–A interfacial contact. The strategy B is domain size control by an addition of BP-based covalent D–A molecule (fullerene-linked tetrabenzoporphyrin: BP–C_{60}) as additive to an active layer composed of BP and $PC_{61}BM$. BP–C_{60} system is promising to improve the miscibility of BP and $PC_{61}BM$, because BP–C_{60} includes both BP and C_{60} natures. Correlation between molecular structure and the film property is necessary to achieve these strategies successful. However, the systematically examined knowledges of covalent D–A molecules for OSCs have been scarce because of their sporadic studies.

In this dissertation, the author aims to develop covalent-linked tetrabenzoporphyrin-fullerene system (BP–C_{60}) in order to perform systematic investigations of strategy A and B toward optimum heterojunction structure in OSCs (Figure 7). Although BP–C_{60} might be hardy soluble in organic solvents, it can be deposited by taking advantage of its soluble precursor (CP–C_{60}). In addition, the three-layered p–i–n structure can be prepared by solution process since the conversion from the CP to BP involves decrease in solubility owing to the structural change.

This study was started with the establishment of effective synthetic procedures for asymmetric BPs as described in Chapter 2. Through these synthetic procedures, three types of covalent BP–C_{60} systems which have flexible linkage with or without an alkyl side chain and rigid linkage were synthesized and their photovoltaic properties have been investigated for Strategy A as described in Chapter 3. Relations between molecular designs of BP–C_{60} systems and photovoltaic behavior in BHJ- or p– i–n-type OSCs were

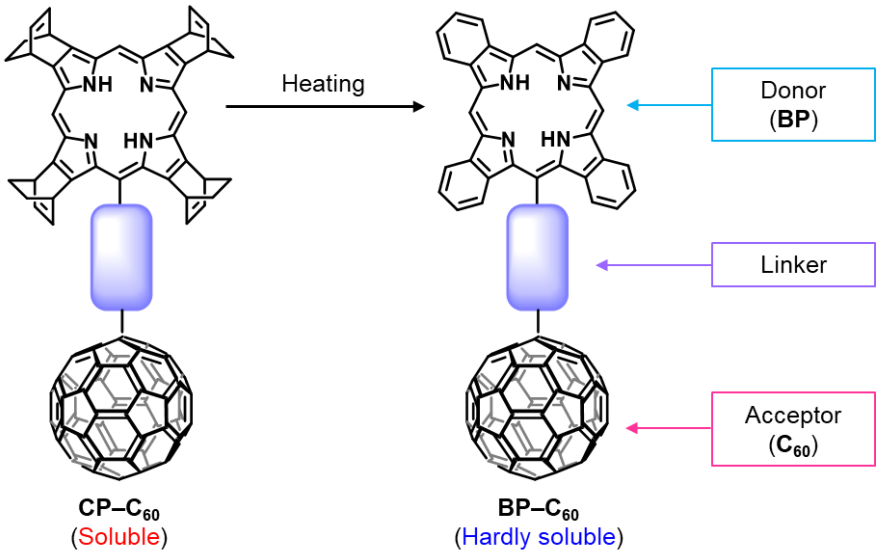

Figure 7. Schematic description of CP–C_{60} and BP–C_{60}.

also discussed. Chapter 4 focused on BP–C_{60} as a morphological additive to obtain the preferable morphology in BP:$PC_{61}BM$ film for Strategy B. Impacts of the covalent BP–C_{60} architecture on morphology of blended BP:$PC_{61}BM$ system were described based on microscopic investigations. Finally, general conclusion of this dissertation and future prospects of the BP–C_{60} system were described in Chapter 5.

1-5. References

(1) Cao, W.; Zheng, Y.; Li, Z.; Wrzesniewski, E.; Hammond, W. T.; Xue, J. Flexible organic solar cells using an oxide/metal/oxide trilayer as transparent electrode. *Organic Electronics* **2012**, *13*, 2221–2228.

(2) O'Connor, T. F.; Zaretski, A. V.; Savagatrup, S.; Printz, A. D.; Wilkes, C. D.; Diaz, M. I.; Sawyer, E. J.; Lipomi, D. J. Wearable organic solar cells with high cyclic bending stability: Materials selection criteria. *Solar Energy Materials and Solar Cells* **2016**, *144*, 438–444.

(3) Zhou, N.; Buchholz, D. B.; Zhu, G.; Yu, X.; Lin, H.; Facchetti, A.; Marks, T. J.; Chang, R. P. H. Ultraflexible Polymer Solar Cells Using Amorphous Zinc-Indium-Tin Oxide Transparent Electrodes. *Adv. mater.* **2014**, *26*, 1098–1104.

(4) Kim, T.; Kim, J. H.; Kang, T. E.; Lee, C.; Kang, H.; Shin, M.; Wang, C.; Ma, B.; Jeong, U.; Kim, T. S.; Kim, B. J. Flexible, highly efficient all-polymer solar cells. *Nat. Commun.* **2015**, *6*, 8647.

(5) Upama, M. B.; Wright, M.; Elumalai, N. K.; Mahmud, M. A.; Wang, D.; Xu, C.; Uddin, A. High-Efficiency Semitransparent Organic Solar Cells with Non-Fullerene Acceptor for Window Application. *ACS Photonics* **2017**, *4*, 2327–2334.

(6) Hsieh, Y.-T.; Chen, J.-Y.; Shih, C.-C.; Chueh, C.-C.; Chen, W.-C. Mechanically robust, stretchable organic solar cells via buckle-on-elastomer strategy. *Organic Electronics* **2018**, *53*, 339–345.

(7) Kaltenbrunner, M.; White, M. S.; Głowacki, E. D.; Sekitani, T.; Someya, T.; Sariciftci, N. S.; Bauer, S. Ultrathin and lightweight rrganic solar cells with high flexibility. *Nat. Commun.* **2012**.

(8) Angmo, D.; Gevorgyan, S. A.; Larsen-Olsen, T. T.; Søndergaard, R. R.; Hösel, M.; Jørgensen, M.; Gupta, R.; Kulkarni, G. U.; Krebs, F. C. Scalability and stability of very thin, roll-to-roll processed, large area, indium-tin-oxide free polymer solar cell modules. *Organic Electronics* **2013**, *14*, 984–994.

(9) Finn, M.; Martens, C. J.; Zaretski, A. V.; Roth, B.; Søndergaard, R. R.; Krebs, F. C.; Lipomi, D. J. Mechanical stability of roll-to-roll printed solar cells under cyclic bending and torsion. *Solar Energy Materials and Solar Cells* **2018**, *174*, 7–15.

(10) dos Reis Benatto, G. A.; Roth, B.; Corazza, M.; Søndergaard, R. R.; Gevorgyan, S. A.; Jørgensen, M.; Krebs, F. C. Roll-to-roll printed silver nanowires for increased stability of flexible ITO-free organic solar cell modules. *Nanoscale* **2016**, *8*, 318–326.

(11) Krebs, F. C. All Solution roll-to-roll processed polymer solar cells free from indium-tin-oxide and vacuum coating steps. *Organic Electronics* **2009**, *10*, 761–768.

(12) Gao, H.; Li, Y.; Wang, L.; Ji, C.; Wang, Y.; Tian, W.; Yang, X.; Yin, L. High performance asymmetrical push–pull small molecules end-capped with cyanophenyl for solution-processed solar cells. *Chem. Commun.* **2014**, *50*, 10251–10254.

(13) Montcada, N. F.; Cabau, L.; Kumar, C. V.; Cambarau, W.; Palomares, E. Indoline as electron donor unit in "push-pull" organic small molecules for solution processed organic solar cells: Effect of the molecular π-bridge on device efficiency. *Organic Electronics* **2015**, *20*, 15–23.

(14) Jiang, Y.; Cabanetos, C.; Allain, M.; Liu, P.; Roncali, J. Manipulation of the band gap and efficiency of a minimalist push–pull molecular donor for organic solar cells. *J. Mater. Chem.*

C **2015**, *3*, 5145–5151.

(15) Nielsen, C. B.; Ashraf, R. S.; Treat, N. D.; Schroeder, B. C.; Donaghey, J. E.; White, A. J. P.; Stingelin, N.; McCulloch, I. 2,1,3-Benzothiadiazole-5,6-Dicarboxylic Imide – A Versatile Building Block for Additive- and Annealing-Free Processing of Organic Solar Cells with Efficiencies Exceeding 8%. *Adv.Mater.* **2015**, *27*, 948–953.

(16) Heintges, G. H. L.; Leenaers, P. J.; Janssen, R. A. J. The effect of side-chain substitution and hot processing on diketopyrrolopyrrole-based polymers for organic solar cells. *J. Mater. Chem. A* **2017**, *5*, 13748–13756.

(17) Labrunie, A.; Josse, P.; Dabos-Seignon, S.; Blanchard, P.; Cabanetos, C. Pentaerythritol based push–pull tetramers for organic photovoltaics. *Sustainable Energy Fuels* **2017**, *1*, 1921–1927.

(18) Kim, Y. J.; Lee, G. B.; Jeon, C. W.; Kim, Y.-H.; Chung, D. S.; Park, C. E. A push–pull organic semiconductor with efficient intramolecular charge transfer for solution-processed small molecule solar cells. *RSC Adv.* **2015**, *5*, 3435–3442.

(19) Yang, D.; Yang, L.; Huang, Y.; Jiao, Y.; Igarashi, T.; Chen, Y.; Lu, Z.; Pu, X.; Sasabe, H.; Kido, J. Asymmetrical Squaraines Bearing Fluorine-Substituted Indoline Moieties for High-Performance Solution-Processed Small-Molecule Organic Solar Cells. *ACS Appl. Mater. Interfaces* **2015**, *7*, 13675–13684.

(20) Gautam, P.; Misra, R.; Siddiqui, S. A.; Sharma, G. D. Unsymmetrical Donor–Acceptor–Acceptor–π–Donor Type Benzothiadiazole-Based Small Molecule for a Solution Processed Bulk Heterojunction Organic Solar Cell. *ACS Appl. Mater. Interfaces* **2015**, *7*, 10283–10292.

(21) Gautam, P.; Misra, R.; Koukaras, E. N.; Sharma, A.; Sharma, G. D. Donor–acceptor–acceptor–donor small molecules for solution processed bulk heterojunction solar cells. *Organic Electronics* **2015**, *27*, 72–83.

(22) Jeux, V.; Segut, O.; Demeter, D.; Rousseau, T.; Allain, M.; Dalinot, C.; Sanguinet, L.; Leriche, P.; Roncali, J. One step synthesis of D-A-D chromophores as active materials for organic solar cells by basic condensation. *Dyes and Pigments* **2015**, *113*, 402–408.

(23) Narayanaswamy, K.; Venkateswararao, A.; Gupta, V.; Chand, S.; Singh, S. P. NIR absorbing D–π–A–π–D structured diketopyrrolopyrrole–dithiafulvalene based small molecule for solution processed organic solar cells. *Chem. Commun.* **2016**, *52*, 210–213.

(24) Leliège, A.; Blanchard, P.; Rousseau, T.; Roncali, J. Triphenylamine/Tetracyanobutadiene-Based D-A-D π-Conjugated Systems as Molecular Donors for Organic Solar Cells. *Org. Lett.* **2011**, *13*, 3098–3101.

(25) Cheng, M.; Chen, C.; Yang, X.; Huang, J.; Zhang, F.; Xu, B.; Sun, L. Novel Small Molecular Materials Based on Phenoxazine Core Unit for Efficient Bulk Heterojunction Organic Solar Cells and Perovskite Solar Cells. *Chem. Mater.* **2015**, *27*, 1808–1814.

(26) Demeter, D.; Rousseau, T.; Leriche, P.; Cauchy, T.; Po, R.; Roncali, J. Manipulation of the Open-Circuit Voltage of Organic Solar Cells by Desymmetrization of the Structure of Acceptor–Donor–Acceptor Molecules. *Adv. Funct. Mater.* **2011**, *21*, 4379–4387.

(27) Zhou, J.; Zuo, Y.; Wan, X.; Long, G.; Zhang, Q.; Ni, W.; Liu, Y.; Li, Z.; He, G.; Li, C.; Kan, B.; Li, M.; Chen, Y. Solution-Processed and High-Performance Organic Solar Cells Using Small Molecules with a Benzodithiophene Unit. *J. Am. Chem. Soc.* **2013**, *135*, 8484–8487.

(28) Kan, B.; Li, M.; Zhang, Q.; Liu, F.; Wan, X.; Wang, Y.; Ni, W.; Long, G.; Yang, X.; Feng, H.; Zuo, Y.; Zhang, M.; Huang, F.; Cao, Y.; Russell, T. P.; Chen, Y. A Series of Simple

Oligomer-like Small Molecules Based on Oligothiophenes for Solution-Processed Solar Cells with High Efficiency. *J. Am. Chem. Soc.* **2015**, *137*, 3886–3893.

(29) Mercier, L. G.; Mishra, A.; Ishigaki, Y.; Henne, F.; Schulz, G.; Bäuerle, P. Acceptor–Donor–Acceptor Oligomers Containing dithieno[3,2-*b*:2′,3′-D]pyrrole and thieno[2,3-*c*]pyrrole-4,6-Dione Units for Solution-Processed Organic Solar Cells. *Org. Lett.* **2014**, *16*, 2642–2645.

(30) Yang, Y.; Liu, Y.; Chen, C. C.; Hong, Z.; Gao, J.; Michael Yang, Y.; Zhou, H.; Dou, L.; Li, G. Solution-processed small-molecule solar cells: Breaking the 10% power conversion efficiency. *Sci. Rep.* **2013**, *3*, 3356.

(31) Mikhnenko, O. V.; Blom, P. W. M.; Nguyen, T.-Q. Exciton diffusion in organic semiconductors. *Energy Environ. Sci.* **2015**, *8*, 1867–1888.

(32) Hebard, A. F.; Haddon, R. C.; Fleming, R. M.; Kortan, A. R. Deposition and characterization of fullerene films. *Appl. Phys. Lett.* **1991**, *59*, 2109–2111.

(33) Loutfy, R. O.; Sharp, J. H. Photovoltaic properties of metal-free phthalocyanines. I. Al/H2Pc Schottky barrier solar cells. *J. Chem. Phys.* **1979**, *71*, 1211–1217.

(34) Zhokhavets, U.; Goldhahn, R.; Gobsch, G.; Al-Ibrahim, M.; Roth, H. K.; Sensfuss, S.; Klemm, E.; Egbe, D. A. M. Anisotropic optical properties of conjugated polymer and polymer/fullerene Films. *Thin Solid Films* **2003**, *444*, 215–220.

(35) Burke, T. M.; McGehee, M. D. How High Local Charge Carrier Mobility and an Energy Cascade in a Three-Phase Bulk Heterojunction Enable >90% Quantum Efficiency. *Adv. Mater.* **2014**, *26*, 1923–1928.

(36) Pandey, R.; Gunawan, A. A.; Mkhoyan, K. A.; Holmes, R. J. Efficient Organic Photovoltaic Cells Based on Nanocrystalline Mixtures of Boron Subphthalocyanine Chloride and C_{60}. *Adv. Funct. Mater.* **2012**, *22*, 617–624.

(37) Gommans, H.; Cheyns, D.; Aernouts, T.; Girotto, C.; Poortmans, J.; Heremans, P. Electro-Optical Study of Subphthalocyanine in a Bilayer Organic Solar Cell. *Adv. Funct. Mater.* **2007**, *17*, 2653–2658.

(38) Dutton, G. J.; Robey, S. W. Exciton Dynamics at CuPc/C_{60} Interfaces: Energy Dependence of Exciton Dissociation. *J. Phys. Chem. C* **2012**, *116*, 19173–19181.

(39) Wilcox, D. E.; Lee, M. H.; Sykes, M. E.; Niedringhaus, A.; Geva, E.; Dunietz, B. D.; Shtein, M.; Ogilvie, J. P. Ultrafast Charge-Transfer Dynamics at the Boron Subphthalocyanine chloride/C_{60} Heterojunction: Comparison between Experiment and Theory. *J. Phys. Chem. Lett.* **2015**, *6*, 569–575.

(40) Klauk, H.; Halik, M.; Zschieschang, U.; Schmid, G.; Radlik, W.; Weber, W. High-mobility polymer gate dielectric pentacene thin film transistors. *J. Appl. Phys.* **2002**, *92*, 5259–5263.

(41) Lee, J.; Kim, S. S.; Kim, K.; Kim, J. H.; Im, S. Correlation between photoelectric and optical absorption spectra of thermally evaporated pentacene films. *Appl. Phys. Lett.* **2004**, *84*, 1701–1703.

(42) Ha, S. D.; Qi, Y.; Kahn, A. Relative permittivity and Hubbard *U* of pentacene extracted from scanning tunneling microscopy studies of *p*-doped films. *Chemical Physics Letters* **2010**, *495*, 212–217.

(43) Shoaee, S. Charge photogeneration in donor/acceptor organic solar cells. *Journal of Photonics for Energy* **2012**, *2*, 21001.

(44) Knupfer, M. Exciton binding energies in organic semiconductors. *Appl. Phys. A* **2003**, *77*, 623–

626.

(45) Lin, Y.; Zhan, X. Non-fullerene acceptors for organic photovoltaics: An emerging horizon. *Materials Horizons* **2014**, *1*, 470.

(46) Lin, Y.; Zhan, X. Designing Efficient Non-Fullerene Acceptors by Tailoring Extended Fused-Rings with Electron-Deficient Groups. *Adv. Energy Mater.* **2015**, *5*, 1501063.

(47) Li, S.; Liu, W.; Li, C.-Z.; Shi, M.; Chen, H. Efficient Organic Solar Cells with Non-Fullerene Acceptors. *Small* **2017**, 1701120.

(48) Gélinas, S.; Rao, A.; Kumar, A.; Smith, S. L.; Chin, A. W.; Clark, J.; Van Der Poll, T. S.; Bazan, G. C.; Friend, R. H. Ultrafast Long-Range Charge Separation in Organic Semiconductor Photovoltaic Diodes. *Science* **2014**, *343*, 512–516.

(49) Brédas, J. L.; Beljonne, D.; Coropceanu, V.; Cornil, J. Charge-Transfer and Energy-Transfer Processes in π-Conjugated Oligomers and Polymers: A Molecular Picture. *Chem. Rev.* **2004**, *104*, 4971–5003.

(50) Tseng, H.-R.; Lin, C.-L. Organic Photovoltaic Cell. *Appl. Phys. Lett.* **2011**, *48*, 183–185.

(51) Kitchen, B.; Awartani, O.; Kline, R. J.; McAfee, T.; Ade, H.; O'Connor, B. T. Tuning Open-Circuit Voltage in Organic Solar Cells with Molecular Orientation. *ACS Appl. Mater. Interfaces* **2015**, *7*, 13208–13216.

(52) Hörmann, U.; Lorch, C.; Hinderhofer, A.; Gerlach, A.; Gruber, M.; Kraus, J.; Sykora, B.; Grob, S.; Linderl, T.; Wilke, A.; Opitz, A.; Hansson, R.; Anselmo, A. S.; Ozawa, Y.; Nakayama, Y.; Ishii, H.; Koch, N.; Moons, E.; Schreiber, F.; Brütting, W. V_{oc} from a Morphology Point of View: The Influence of Molecular Orientation on the Open Circuit Voltage of Organic Planar Heterojunction Solar Cells. *J. Phys. Chem. C* **2014**, *118*, 26462–26470.

(53) Ayzner, A. L.; Nordlund, D.; Kim, D.-H.; Bao, Z.; Toney, M. F. Ultrafast Electron Transfer at Organic Semiconductor Interfaces: Importance of Molecular Orientation. *J. Phys. Chem. Lett.* **2015**, *6*, 6–12.

(54) Ojala, A.; Petersen, A.; Fuchs, A.; Lovrincic, R.; Pölking, C.; Trollmann, J.; Hwang, J.; Lennartz, C.; Reichelt, H.; Höffken, H. W.; Pucci, A.; Erk, P.; Kirchartz, T.; Würthner, F. Merocyanine/C_{60} Planar Heterojunction Solar Cells: Effect of Dye Orientation on Exciton Dissociation and Solar Cell Performance. *Adv. Funct. Mater.* **2012**, *22*, 86–96.

(55) Rand, B. P.; Cheyns, D.; Vasseur, K.; Giebink, N. C.; Mothy, S.; Yi, Y.; Coropceanu, V.; Beljonne, D.; Cornil, J.; Brédas, J. L.; Genoe, J. The Impact of Molecular Orientation on the Photovoltaic Properties of a Phthalocyanine/fullerene Heterojunction. *Adv. Funct. Mater.* **2012**, *22*, 2987–2995.

(56) Ran, N. A.; Roland, S.; Love, J. A.; Savikhin, V.; Takacs, C. J.; Fu, Y. T.; Li, H.; Coropceanu, V.; Liu, X.; Brédas, J. L.; Bazan, G. C.; Toney, M. F.; Neher, Di.; Nguyen, T. Q. Impact of interfacial molecular orientation on radiative recombination and charge generation efficiency. *Nat. Commun.* **2017**, *8*, 1–9.

(57) Graham, K. R.; Erwin, P.; Nordlund, D.; Vandewal, K.; Li, R.; Ndjawa, G. O. N.; Hoke, E. T.; Salleo, A.; Thompson, M. E.; McGehee, M. D.; Amassian, A. Reevaluating the Role of Sterics and Electronic Coupling in Determining the Open Circuit Voltage of Organic Solar Cells. *Adv. Mater.* **2013**, *25*, 6076–6082.

(58) Li, X.; Liu, X.; Zhang, W.; Wang, H. Q.; Fang, J. Fullerene-Free Organic Solar Cells with Efficiency over 12% Based on EDTA-ZnO Hybrid Cathode Interlayer. *Chem. Mater.* **2017**,

29, 4176–4180.

(59) Li, S.; Ye, L.; Zhao, W.; Zhang, S.; Mukherjee, S.; Ade, H.; Hou, J. Energy-Level Modulation of Small-Molecule Electron Acceptors to Achieve over 12% Efficiency in Polymer Solar Cells. *Adv. Mater.* **2016**, *28*, 9423–9429.

(60) Deng, D.; Zhang, Y.; Zhang, J.; Wang, Z.; Zhu, L.; Fang, J.; Xia, B.; Wang, Z.; Lu, K.; Ma, W.; Wei, Z. Fluorination-enabled optimal morphology leads to over 11% efficiency for inverted small-molecule organic solar cells. *Nat. Commun.* **2016**, *7*, 13740.

(61) Zhao, F.; Dai, S.; Wu, Y.; Zhang, Q.; Wang, J.; Jiang, L.; Ling, Q.; Wei, Z.; Ma, W.; You, W.; Wang, C.; Zhan, X. Single-Junction Binary-Blend Nonfullerene Polymer Solar Cells with 12.1% Efficiency. *Adv. Mater.* **2017**, *29*, 1700144.

(62) Zhao, W.; Qian, D.; Zhang, S.; Li, S.; Inganäs, O.; Gao, F. Fullerene-Free Polymer Solar Cells with over 11 % Efficiency and Excellent Thermal Stability. *Adv. Mater.* **2016**, *28*, 4734–4739.

(63) Ruderer, M. A.; Guo, S.; Meier, R.; Chiang, H. Y.; Körstgens, V.; Wiedersich, J.; Perlich, J.; Roth, S. V.; Müller-Buschbaum, P. Solvent-Induced Morphology in Polymer-Based Systems for Organic Photovoltaics. *Adv. Funct. Mater.* **2011**, *21*, 3382–3391.

(64) Suzuki, M.; Yamaguchi, Y.; Takahashi, K.; Takahira, K.; Koganezawa, T.; Masuo, S.; Nakayama, K. I.; Yamada, H. Photoprecursor Approach Enables Preparation of Well-Performing Bulk-Heterojunction Layers Comprising a Highly Aggregating Molecular Semiconductor. *ACS Appl. Mater. Interfaces* **2016**, *8*, 8644–8651.

(65) Liao, H. C.; Ho, C. C.; Chang, C. Y.; Jao, M. H.; Darling, S. B.; Su, W. F. Additives for morphology control in high-efficiency organic solar cells. *Materials Today* **2013**, *16*, 326–336.

(66) Liu, X.; Huettner, S.; Rong, Z.; Sommer, M.; Friend, R. H. Solvent Additive Control of Morphology and Crystallization in Semiconducting Polymer Blends. *Adv. Mater.* **2012**, *24*, 669–674.

(67) Wang, J. L.; Liu, K. K.; Yan, J.; Wu, Z.; Liu, F.; Xiao, F.; Chang, Z. F.; Wu, H. Bin; Cao, Y.; Russell, T. P. Series of Multifluorine Substituted Oligomers for Organic Solar Cells with Efficiency over 9% and Fill Factor of 0.77 by Combination Thermal and Solvent Vapor Annealing. *J. Am. Chem. Soc.* **2016**, *138*, 7687–7697.

(68) Kwon, O. K.; Uddin, M. A.; Park, J. H.; Park, S. K.; Nguyen, T. L.; Woo, H. Y.; Park, S. Y. A High Efficiency Nonfullerene Organic Solar Cell with Optimized Crystalline Organizations. *Adv. Mater.* **2016**, *28*, 910–916.

(69) Yang, X.; Uddin, A. Effect of thermal annealing on P3HT:PCBM bulk-heterojunction organic solar cells: A critical review. *Renewable and Sustainable Energy Reviews* **2014**, *30*, 324–336.

(70) Zhang, Q.; Kan, B.; Liu, F.; Long, G.; Wan, X.; Chen, X.; Zuo, Y.; Ni, W.; Zhang, H.; Li, M.; Hu, Z.; Huang, F.; Cao, Y.; Liang, Z.; Zhang, M.; Russell, T. P.; Chen, Y. Small-molecule solar cells with efficiency over 9%. *Nat. Photonics* **2014**, *9*, 35–41.

(71) Zhao, G. J.; He, Y. J.; Li, Y. 6.5% Efficiency of Polymer Solar Cells Based on poly(3-Hexylthiophene) and Indene-C_{60} Bisadduct by Device Optimization. *Adv. Mater.* **2010**, *22*, 4355–4358.

(72) Wang, J.-L.; Xiao, F.; Yan, J.; Wu, Z.; Liu, K.-K.; Chang, Z.-F.; Zhang, R.-B.; Chen, H.; Wu, H.-B.; Cao, Y. Difluorobenzothiadiazole-Based Small-Molecule Organic Solar Cells with 8.7% Efficiency by Tuning of π-Conjugated Spacers and Solvent Vapor Annealing. *Adv. Funct. Mater.* **2016**, *26*, 1803–1812.

(73) Miao, J.; Chen, H.; Liu, F.; Zhao, B.; Hu, L.; He, Z.; Wu, H. Efficiency Enhancement in Solution-Processed Organic Small Molecule : Fullerene Solar Cells via Solvent Vapor Annealing Efficiency Enhancement in Solution-Processed Organic Small Molecule. *Appl. Phys. Lett.* **2015**, *106*, 183302.

(74) Miller, S.; Fanchini, G.; Lin, Y.-Y.; Li, C.; Chen, C.-W.; Su, W.-F.; Chhowalla, M. Investigation of nanoscale morphological changes in organic photovoltaics during solvent vapor annealing. *J. Mater. Chem.* **2008**, *18*, 306–312.

(75) Gao, K.; Deng, W.; Xiao, L.; Hu, Q.; Kan, Y.; Chen, X.; Wang, C.; Huang, F.; Peng, J.; Wu, H.; Peng, X.; Cao, Y.; Russell, T. P.; Liu, F. New insight of molecular interaction, crystallization and phase separation in higher performance small molecular solar cells via solvent vapor annealing. *Nano Energy* **2016**, *30*, 639–648.

(76) Wang, J. L.; Wu, Z.; Miao, J. S.; Liu, K. K.; Chang, Z. F.; Zhang, R. B.; Wu, H. Bin; Cao, Y. Solution-Processed Diketopyrrolopyrrole-Containing Small-Molecule Organic Solar Cells with 7.0% Efficiency: In-Depth Investigation on the Effects of Structure Modification and Solvent Vapor Annealing. *Chem. Mater.* **2015**, *27*, 4338–4348.

(77) Wang, K.; Azouz, M.; Babics, M.; Cruciani, F.; Marszalek, T.; Saleem, Q.; Pisula, W.; Beaujuge, P. M. Solvent Annealing Effects in Dithieno[3,2-*b*:2′,3′-*d*]pyrrole-5,6-Difluorobenzo[*c*][1,2,5]thiadiazole Small Molecule Donors for Bulk-Heterojunction Solar Cells. *Chem. Mater.* **2016**, *28*, 5415–5425.

(78) Grob, S.; Bartynski, A. N.; Opitz, A.; Gruber, M.; Grassl, F.; Meister, E.; Linderl, T.; Hörmann, U.; Lorch, C.; Moons, E.; Schreiber, F.; Thompson, M. E.; Brütting, W. Solvent vapor annealing on perylene-based organic solar cells. *J. Mater. Chem. A* **2015**, *3*, 15700–15709.

(79) Wei, G.; Wang, S.; Sun, K.; Thompson, M. E.; Forrest, S. R. Solvent-Annealed Crystalline Squaraine: $PC_{70}BM$ (1:6) Solar Cells. *Adv. Energy Mater.* **2011**, *1*, 184–187.

(80) Lee, J. U.; Jung, J. W.; Jo, J. W.; Jo, W. H. Degradation and Stability of Polymer-Based Solar Cells. *J. Mater. Chem.* **2012**, *22*, 24265.

(81) Ciammaruchi, L.; Brunetti, F.; Visoly-Fisher, I. Solvent effects on the morphology and stability of PTB7:PCBM based solar cells. *Solar Energy* **2016**, *137*, 490–499.

(82) Chang, L.; Jacobs, I. E.; Augustine, M. P.; Moulé, A. J. Correlating dilute solvent interactions to morphology and OPV device performance. *Organic Electronics* **2013**, *14*, 2431–2443.

(83) Cardinaletti, I.; Kesters, J.; Bertho, S.; Conings, B.; Piersimoni, F.; D'Haen, J.; Lutsen, L.; Nesladek, M.; Van Mele, B.; Van Assche, G.; Vandewal, K.; Salleo, A.; Vanderzande, D.; Maes, W.; Manca, J. V. Toward bulk heterojunction polymer solar cells with thermally stable active layer morphology. *Journal of Photonics for Energy* **2014**, *4*, 40997.

(84) Treat, N. D.; Brady, M. A.; Smith, G.; Toney, M. F.; Kramer, E. J.; Hawker, C. J.; Chabinyc, M. L. Interdiffusion of PCBM and P3HT Reveals Miscibility in a Photovoltaically Active Blend. *Adv. Energy Mater.* **2011**, *1*, 82–89.

(85) Günes, S.; Neugebauer, H.; Sariciftci, N. S. Conjugated Polymer-Based Organic Solar Cells. *Chem. Rev.* **2007**, *107*, 1324–1338.

(86) Slota, J. E.; He, X.; Huck, W. T. S. Controlling nanoscale morphology in polymer photovoltaic devices. *Nano Today* **2010**, *5*, 231–242.

(87) Neupane, U.; Bahrami, B.; Biesecker, M.; Baroughi, M. F.; Qiao, Q. Kinetic Monte Carlo Modeling on organic solar cells: Domain size, donor-acceptor ratio and thickness. *Nano*

Energy **2017**, *35*, 128–137.

(88) Ray, B.; Alam, M. A. Random vs regularized OPV: Limits of performance gain of organic bulk heterojunction solar cells by morphology engineering. *Solar Energy Materials and Solar Cells* **2012**, *99*, 204–212.

(89) Suzuki, M.; Aotake, T.; Yamaguchi, Y.; Noguchi, N.; Nakano, H.; Nakayama, K. ichi; Yamada, H. Synthesis and photoreactivity of α-diketone-type precursors of acenes and their use in organic-device fabrication. *Journal of Photochemistry and Photobiology C: Photochemistry Reviews* **2014**, *18*, 50–70.

(90) Ito, S.; Murashima, T.; Ono, N.; Uno, H. A new synthesis of benzoporphyrins using 4,7-dihydro-4,7-ethano-*2H*-isoindole as a synthon of isoindole. *Chem. Commun.* **1998**, *16*, 1661–1662.

(91) Yamaguchi, Y.; Suzuki, M.; Motoyama, T.; Sugii, S.; Katagiri, C.; Takahira, K.; Ikeda, S.; Yamada, H.; Nakayama, K. I. Photoprecursor approach as an effective means for preparing multilayer organic semiconducting thin films by solution processes. *Sci. Rep.* **2014**, *4*, 1–8.

(92) Berezin, D. S.; Toldina, O. V; Kudrik, E. V. Complex Formation and Spectral Properties of *meso*-Phenyltetrabenzoporphyrins in Pyridine and *N*,*N*-Dimethylformamide. *Russian Journal of General Chemistry* **2003**, 8, 2003, 1309–1314.

(93) Shea, P. B.; Pattison, L. R.; Kawano, M.; Chen, C.; Chen, J.; Petroff, P.; Martin, D. C.; Yamada, H.; Ono, N.; Kanicki, J. Solution-processed polycrystalline copper tetrabenzoporphyrin thin-film transistors. *Synthetic Metals* **2007**, *157*, 190–197.

(94) Shea, P. B.; Kanicki, J.; Pattison, L. R.; Petroff, P.; Kawano, M.; Yamada, H.; Ono, N. Solution-processed nickel tetrabenzoporphyrin thin-film transistors. *J. Appl. Phys.* **2006**, *100*, 034502.

(95) Shea, P. B.; Yamada, H.; Ono, N.; Kanicki, J. Solution-processed zinc tetrabenzoporphyrin thin-films and transistors. *Thin Solid Films* **2012**, *520*, 4031–4035.

(96) Noguchi, N.; Junwei, S.; Asatani, H.; Matsuoka, M. Control of Morphology and Orientation of a Thin Film Tetrabenzoporphyrin (TBP) Organic Semiconductor by Solid-State Crystallization. *Crystal Growth and Design* **2010**, *10*, 1848–1853.

(97) Guide, M.; Dang, X. D.; Nguyen, T. Q. Nanoscale Characterization of Tetrabenzoporphyrin and Fullerene-Based Solar Cells by Photoconductive Atomic Force Microscopy. *Adv. Mater.* **2011**, *23*, 2313–2319.

(98) Matsuo, Y.; Sato, Y.; Niinomi, T.; Soga, I.; Tanaka, H.; Nakamura, E. Columnar Structure in Bulk Heterojunction in Solution-Processable Three-Layered p-i-n Organic Photovoltaic Devices Using Tetrabenzoporphyrin Precursor and silylmethyl[60]fullerene. *J. Am. Chem. Soc.* **2009**, *131*, 16048–16050.

(99) Tanaka, H.; Abe, Y.; Matsuo, Y.; Kawai, J.; Soga, I.; Sato, Y.; Nakamura, E. An Amorphous Mesophase Generated by Thermal Annealing for High-Performance Organic Photovoltaic Devices. *Adv. Mater.* **2012**, *24*, 3521–3525.

(100) Imahori, H.; Sakata, Y. Donor-Linked Fullerenes: Photoninduced Electron Transfer and Its Potential Application. *Adv. Mater.* **1997**, *9*, 537–546.

(101) Gust, D.; Moore, T. A.; Moore, A. L. Molecular Mimicry of Photosynthetic Energy and Electron Transfer. *Acc. Chem. Res.* **1993**, *26*, 198–205.

(102) Wasielewski, M. R. Photoinduced Electron Transfer in Supramolecular Systems for Artificial

Photosynthesis. *Chem. Rev.* **1992**, *92*, 435–461.

(103) Kashiwagi, Y.; Ohkubo, K.; McDonald, J. A.; Blake, I. M.; Crossley, M. J.; Araki, Y.; Ito, O.; Imahori, H.; Fukuzumi, S. Long-Lived Charge-Separated State Produced by Photoinduced Electron Transfer in a Zinc Imidazoporphyrin-C_{60} dyad. *Org. Lett.* **2003**, *5*, 2719–2721.

(104) Nishizawa, T.; Tajima, K.; Hashimoto, K. Supramolecular formation of fibrous nanostructure in donor–acceptor dyad film. *J. Mater. Chem.* **2007**, *17*, 2440–2445.

(105) Nishizawa, T.; Lim, H. K.; Tajima, K.; Hashimoto, K. Efficient dyad-based organic solar cells with a highly crystalline donor group. *Chem. Commun.* **2009**, 18, 2469–2471.

(106) Izawa, S.; Hashimoto, K.; Tajima, K. Morphological stability of organic solar cells based upon an oligo(*p*-phenylenevinylene)–C_{70} Dyad. *Phys. Chem. Chem. Phys.* **2012**, *14*, 16138–16142.

(107) Narayanaswamy, K.; Venkateswararao, A.; Nagarjuna, P.; Bishnoi, S.; Gupta, V.; Chand, S.; Singh, S. P. An Organic Dyad Composed of Diathiafulvalene-Functionalized Diketopyrrolopyrrole–Fullerene for Single-Component High-Efficiency Organic Solar Cells. *Angew. Chem. Int. Ed.* **2016**, *55*, 12334–12337.

(108) Nguyen, T. L.; Lee, T. H.; Gautam, B.; Park, S. Y.; Gundogdu, K.; Kim, J. Y.; Woo, H. Y. Single Component Organic Solar Cells Based on Oligothiophene-Fullerene Conjugate. *Adv. Funct. Mater.* **2017**, *27*, 1–9.

Chapter 2.

Development of Effective Synthetic Routes for Asymmetric *meso*-Substituted Tetrabenzoporphrins

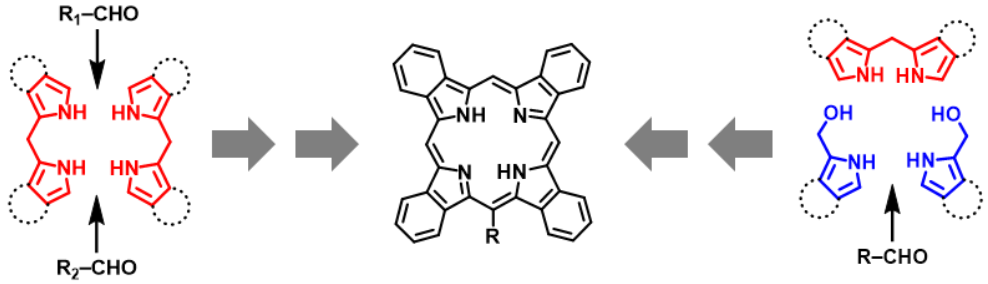

In this chapter, effective synthetic procedures for asymmetric *meso*-substituted BCOD-fused porphyrins (CPs) and their reactivities with heating to corresponding tetrabenzoporphyrins (BPs) are described.

2-1. Introduction

The aims of this chapter are establishment of effective synthetic route of asymmetric *meso*-substituted CPs with various chemical groups and investigation of their thermal conversion properties to corresponding asymmetric BPs. Although there are a lot of works on thermal precursor approach of BPs,[1–8] investigation of substituted BPs toward semiconducting materials has been performed only in the limited structures.[9–11] Especially, no asymmetric *meso*-substituted BP which can be used as an effective building block for donor–acceptor systems has been reported, to the best of our knowledge. Thus, fundamental understanding of the nature of mono-*meso*-substituted CPs with their corresponding BPs is important work to utilize them for well-designed donor–acceptor systems as OSCs material. However, effective synthetic procedure for asymmetric *meso*-substituted CPs is limited because of the poor synthetic efforts. In fact, the mono-substituted BPs have hardly been reported as far as we know, except a selective halogenation of the precursor CP followed by a thermal conversion to BP.[12]

To pave the way for an effective synthetic route toward asymmetric *meso*-substituted CPs, enormous studies of porphyrin derivatives should be referred. A lot of syntheses of asymmetric porphyrins have been reported before: Acid catalyzed condensation reaction,[13–17] the reaction of tripyrranes with mono-substituted pyrrole (Scheme 1a),[13,18] and the oxidation of pentapyrrane (Scheme 1b).[19] The *meso*-substitution of porphyrin with organolithium reagents (Scheme 1c),[13,20,21] the Vilsmeier formylation of copper porphyrin (Scheme 1d),[22] and chlorination of octaethylporphyrin by *N*-chlorosuccinimide(Scheme 1e)[12] also gave mono-*meso*-substituted porphyrins. By taking knowledge of these great works, an effective synthetic route for asymmetric *meso*-substituted CPs will be achieved.

In this chapter, synthetic efforts to obtain asymmetric *meso*-substituted CPs using condensation reaction (Figure 1) are described. These reactions are selected because of their good versatility to introduce various substituent groups with one pot process. Availability of obtained substituted-BPs is also discussed with their thermal behaviors and calculated optimal structures.

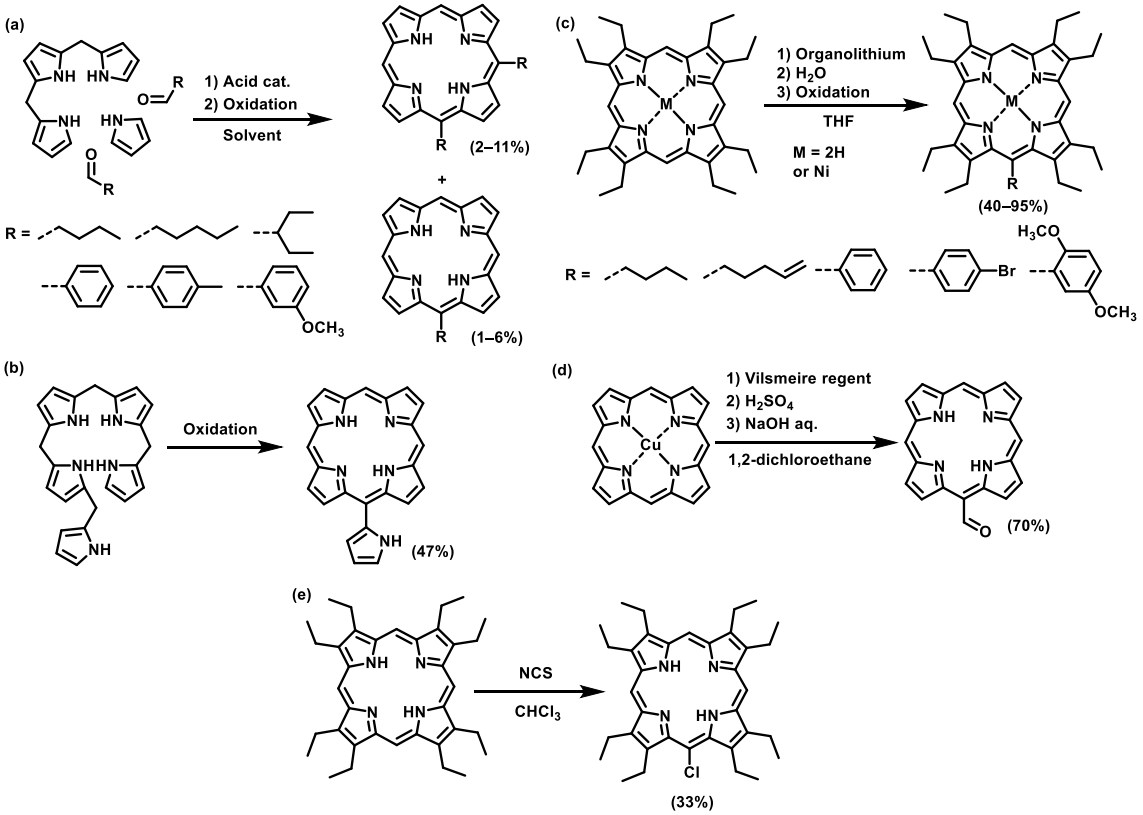

Scheme 1. Examples of synthetic procedure for asymmetric *meso*-substituted porphyrins.[12,20,21,24]

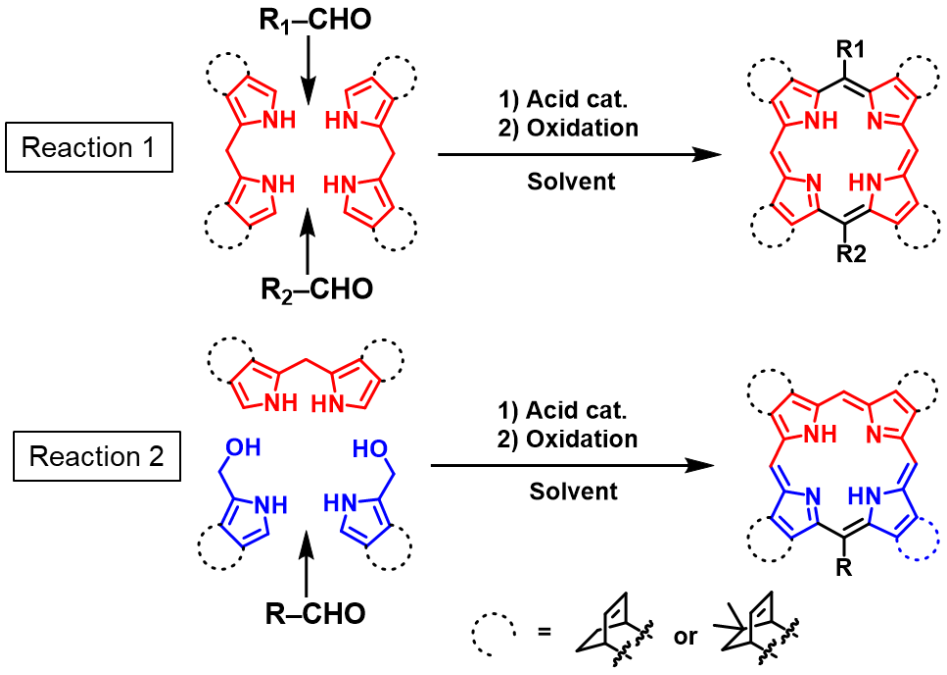

Figure 1. Schematic description of Reaction 1 and 2 to obtain asymmetric CPs.

2-2. Synthetic Effort to Obtain an Asymmetric CPs (1)

As an initial synthetic approach, Reaction 1 using BCOD-fused α-free dipyrromethane **1**[23] and aldehyde derivatives was selected because of the simplest handling (Scheme 2). At first, an acid-catalyzed condensation of BCOD-fused dipyrromethane **1**[23], *n*-pentanal **2**, and 4-methoxycarbonylpentane-1-al **3**[24] was performed followed by oxidation with *p*-chloranil (Scheme 2a). After insertion of a zinc ion to make the purification of the products easy, the zinc porphyrin monoester **4** was obtained in 22% yield with small amount of symmetrical 5-15-substituted CPs (DiBu-CP in 4% yield and Diester-CP in 11%yield). In the same manner, 5-substiruted CPs (**6** and **7**) were obtained in 28–36% yield when commercially available paraformaldehyde **5** was used (Scheme 2b and 2c). As mentioned in Chapter 3, ester groups at *meso*-positions are key structure to

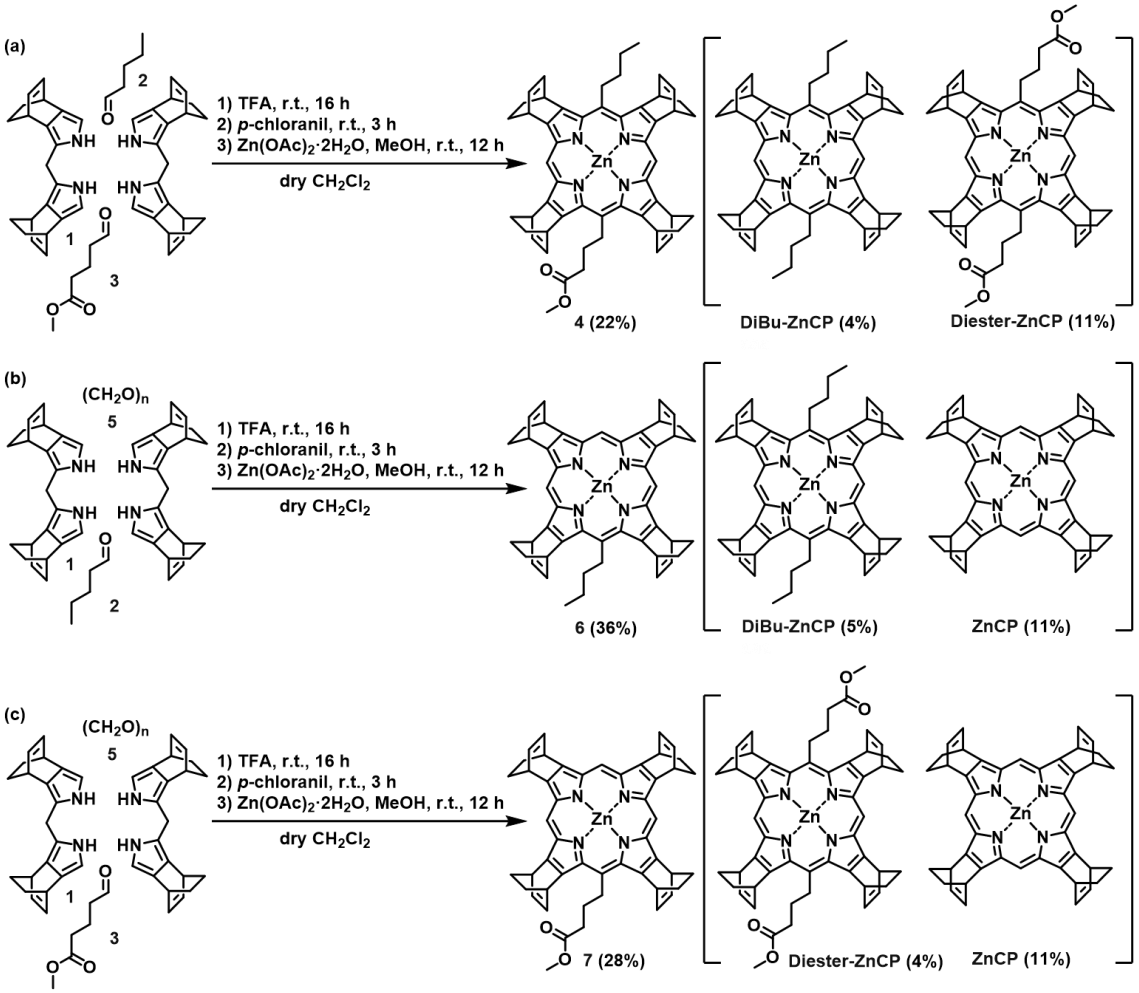

Scheme 2. Synthetic procedures to obtain the asymmetric alkyl-substituted CP of (a) **4**, (b) **6**, and (c) **7**.

prepare donor–acceptor molecules.

Next, encouraged by the successful results in Reaction 1 using paraformaldehyde **5** (Scheme 2b and 2c), *p*-[(trimethylsilyl)ethynyl]benzaldehyde **9**[25] and (triisopropylsilyl)ethynylaldehyde **11** were used instead of aldehydes **2** and **3** as shown in Scheme 3. Expecting the low solubility of the *meso*-alkynyl- or *meso*-alkynylphenyl-substited CP derivatives, dimethylBCOD-fused dipyrromethene **8**[2] was used instead of the BCOD-fused dipyrromethene **1**. However, no 5-substituted CPs (**10a** and **12a**) were obtained in both reactions with the main product of 5-15-disubstituted CP (**10b** and **12b**) and minor product of zinc complex of methyl-CP (ZnMeCP).

The one of the reasons of this result was assumed to be the stabilization of porphyrinogen cation intermediates A of **10b** and **12b** with double phenyl- or ethynyl-groups more than intermediates B for **10a** and **12a** (Figure 2). On the other hand, both reactions generated a slight amount of non-substituted CP (MeZnCP). Thus, porphyrinogene intermediates of **10a** and **12a** must be generated during these reactions. The synthesis of target compounds **10a** and **12a** probably can be achieved from more

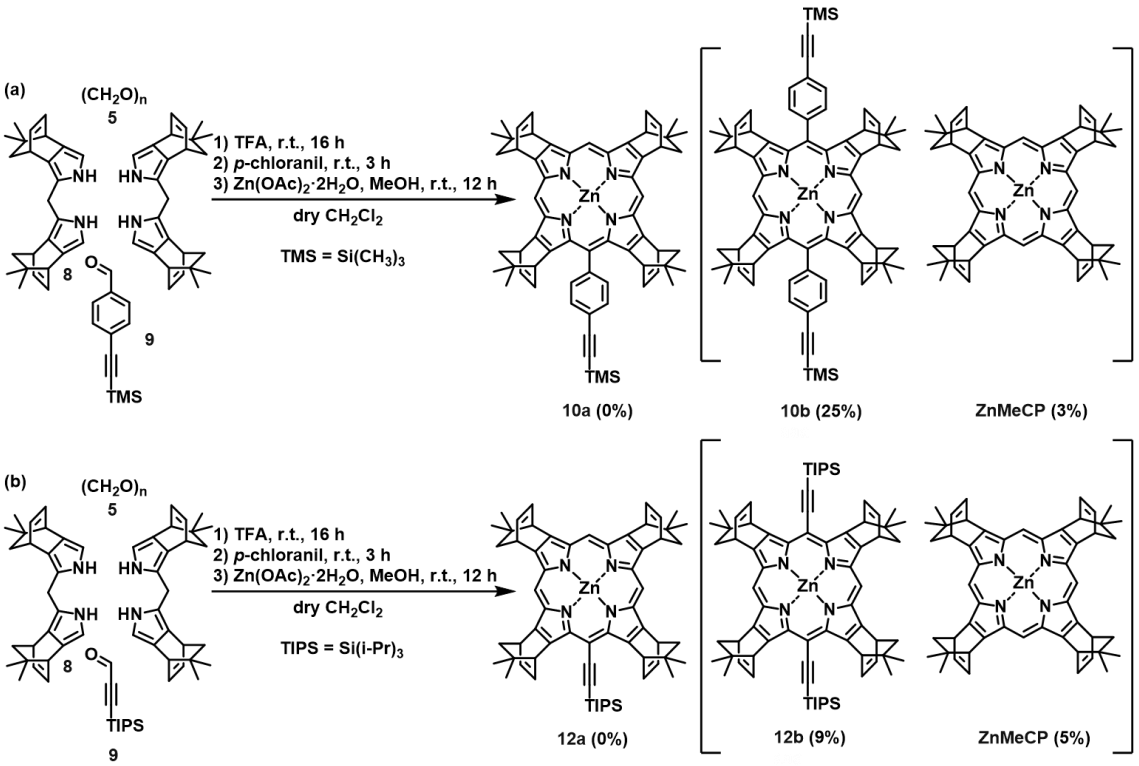

Scheme 3. Efforts of Reaction 1 to obtain asymmetric aryl- or ethynyl-substituted CP of (a) **10a** and (b) **12a**.

careful modification of reaction time and select of reagents. However, our group found that Reaction 1 using dimethylBCOD-fused dipyrromethene **8**[2] generates insoluble CP derivatives[9] in between, therefore, our synthetic effort moved to another approach as follows.

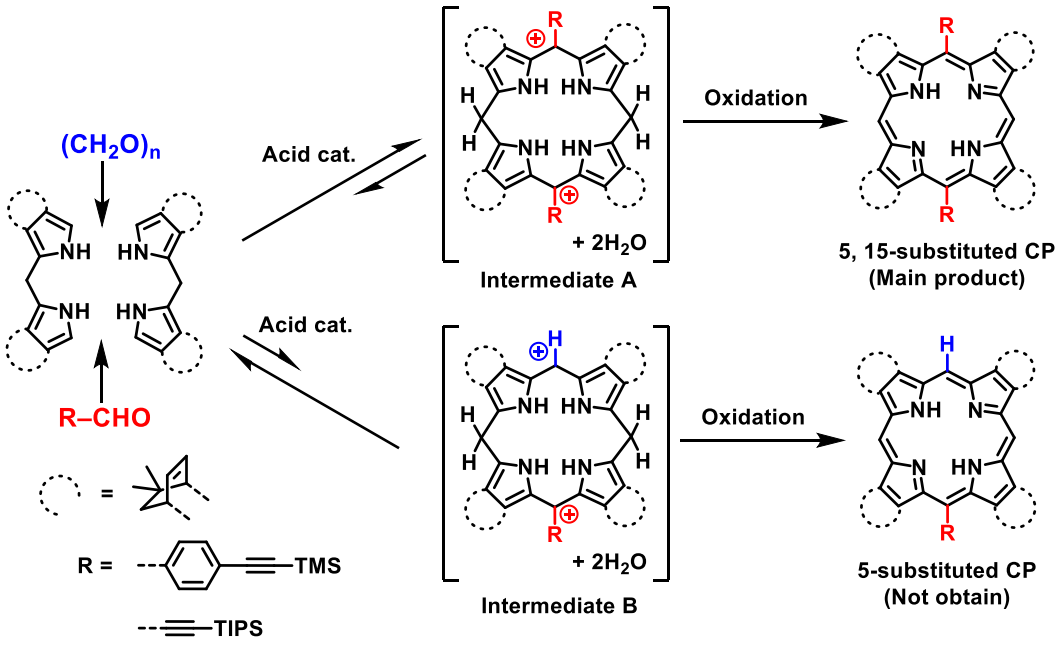

Figure. 2 Speculated reaction mechanisms of Reaction 1 using *p*-formaldehyde and benzaldehyde or ethynylaldehyde.

2-3. Synthetic Effort to Obtain an Asymmetric CPs (2)

Reaction 2 with careful optimizations of reaction reagent and solvent was performed to obtain mono-*meso*-aryl- or ethynyl-CP, as shown in Scheme 4. By acid condensation of α-hydroxymethylpyrrole **13**,[2] dipyrromethane **8**[2], and aldehyde **9**[25] followed by oxidation with 2,3-dichloro-5,6-dicyano-*p*-benzoquinone (DDQ) and zinc complexation, 5-substituted-MeCP **10a** was obtained in a 54% yield. The yields of 5,15-disubstituted porphyrin **10b** and non-substituted MeCP (ZnMeCP) were only 1% and trace, respectively (Scheme 4a). In addition, 5-ethynyl-MeCP **12a** was obtained by using methanol (MeOH) as the reaction solvent and boron trifluoride etherate ($BF_3 \cdot OEt_2$)[9,23] as the Lewis acid catalysis in a 22% yield (Scheme 4b). This reaction also gave 5,15-ethynyl porphyrin **12b** and ZnMeCP in 9% and trace, respectively.

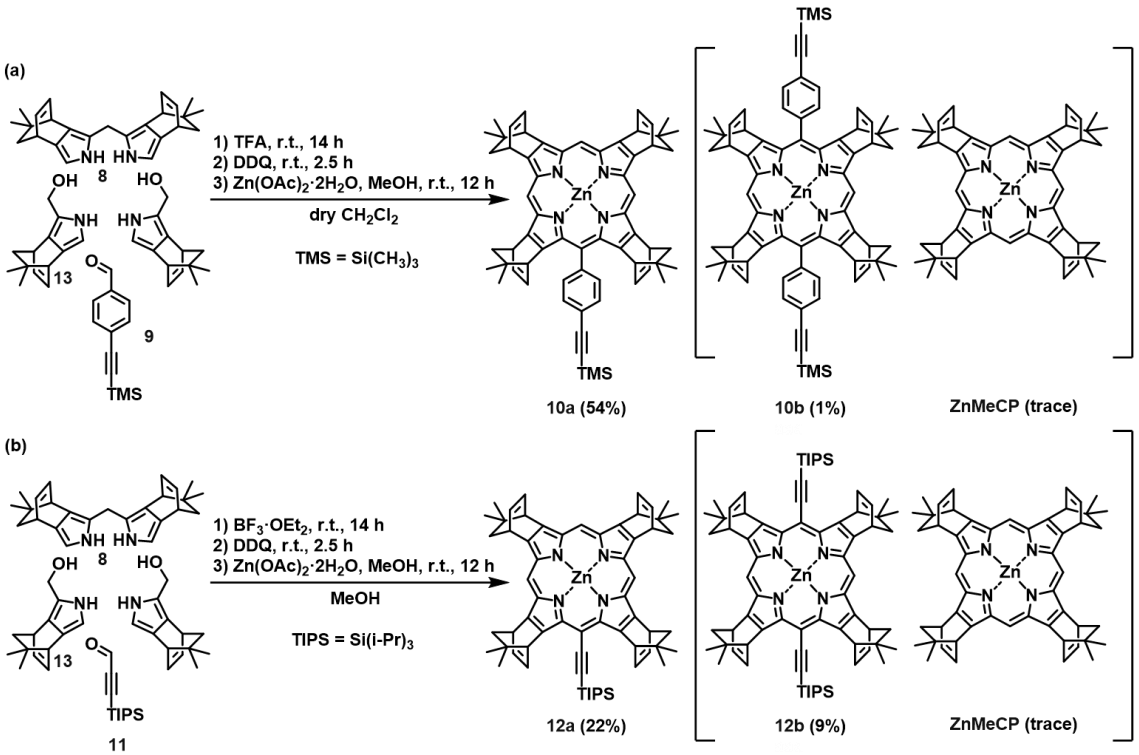

Scheme 4. Synthetic procedures of Reaction 2 to obtain the asymmetric aryl- or ethynyl-substituted CPs of (a) **10a**, (b) 1**2a**.

2-4. Thermal Properties of Asymmetric *meso*-Substituted CPs

In order to investigate the thermal conversion behavior of the asymmetric *meso*-substituted CPs, the zinc ions of **6**, **10a**, and **12a** were removed by treatment with TFA to prepare the 5-butyl-CP (Bu-CP), 5-trimetylsilylphenyl-CP (TMS-CP), and 5-(triisopropylsilyl)ethynyl-CP (TIPS-CP), respectively (Scheme 5).

Thermal conversion of Bu-CP, TMS-CP, and TIPS-CP to Bu-BP, TMS-BP, and TIPS-BP was observed by thermogravimetric analysis (TGA), as shown in Figure 3. During these TGA measurements, all of CPs showed two kinds of mass loss behavior corresponding to the retro-Deals Alder (r-DA) reaction from BCOD structure to BP structure and the decomposition of molecules. The beginning temperatures of the r-DA reaction (T_r) and decomposition (T_d) were summarized with theoretical and observed mass loss value due to the r-DA reaction in Table 1 with reference normal CP. The r-DA reaction is started around 130–150 ºC and stopped around 200 ºC in all of CP derivatives. Observed mass loss of all of CP derivatives during the r-DA reaction were in accordance

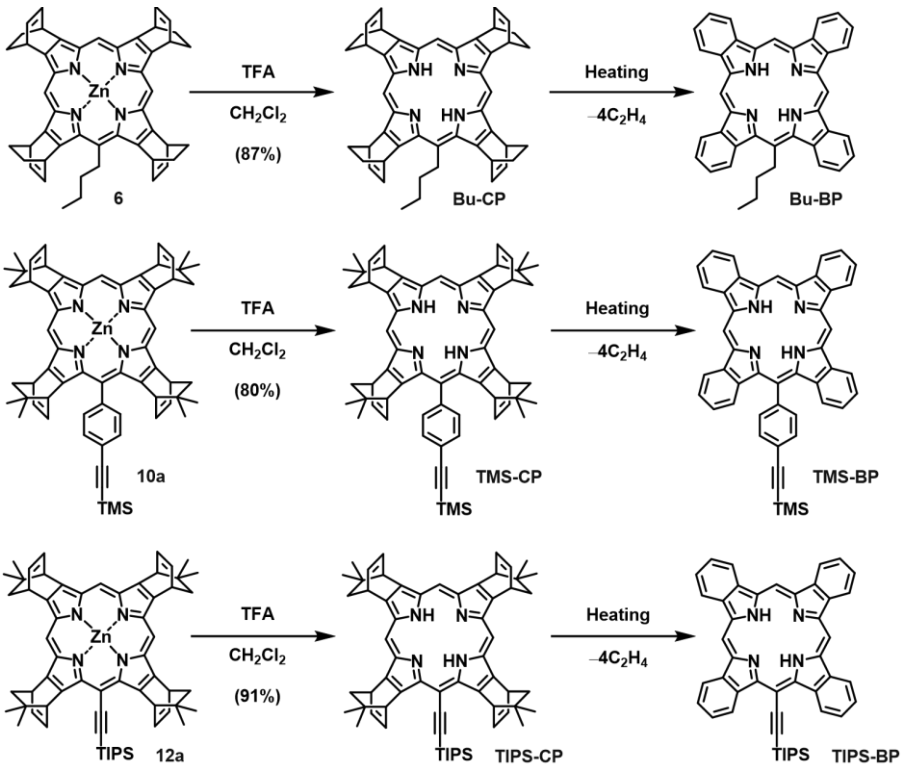

Scheme 5. Preparation of three types of free-base CP derivatives (Bu-CP, TMS-CP, and TIPS-CP) and their chemical transformation to BP derivatives (Bu-BP, TMS-BP, and TIPS-BP) by heating.

well with the theoretical value which corresponds the elimination of four ethylene or isobutene molecules. These results suggest that quantitative r-DA reaction can be carried out in these 5-substituted CP derivatives to obtain the 5-substituted BP derivatives. On the other hand, the T_d of these 5-substituted BPs (T_d = 380–400 ºC) is lower than normal BP (T_d = 527 ºC). This trend of the decreased thermal stability is also observed in other studies of *meso*-substituted BP[9], thus these lower T_d's are attributable to the substituent introduction to *meso* position. After the r-DA reaction, the MALDI spiral-TOF mass spectra of the obtained Bu-, TMS-, and TIPS-BP were in good agreement with the simulated values (Figure. S2-1–2-3 in Support Information). However, the solubility of these BP compounds was not enough for NMR measurement.

Table 1. Summary of TGA

Sample	T_r / °C	Mass loss (theoretical) / %	Mass loss (observed) / %	T_d / °C
Bu-CP	145	16.5	15.9	383
TMS-CP	131	24.7	25.0	400
TIPS-CP	133	25.0	25.6	352
CP	146	18.0	18.3	527

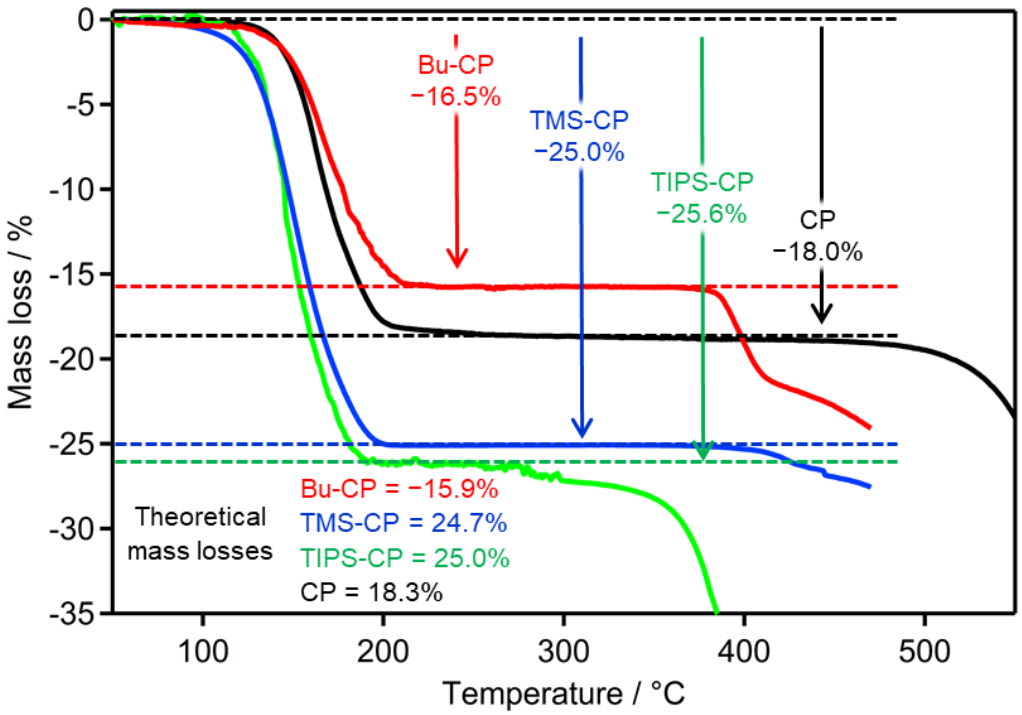

Figure 3. TGA curves of Bu-CP, TMS-CP, TIPS-CP, and CP under nitrogen gas flowing with heatup time of 5 ºC min^{-1}.

2-5. Molecular Orbital Calculations

Optimized molecular structures of non-substituted BP, Bu-, TMS-, and TIPS-BP compounds were calculated by the density functional theory (DFT) with their highest occupied molecular orbital (HOMO) and lowest unoccupied molecular orbital (LUMO) as shown in Figure 4. All of the 5-sustituted BPs have very flat BP planes as same as non-substituted BP. This is important point for an effective BP packing which can induce a good conductibility and significant switching of solubility via thermal precursor approach. *Meso*-butyl group in Bu-BP showed stuck-out structure from porphyrin plane because of steric repulsion of butyl group and with peripheral hydrogen atoms on BP. *Meso*-phenyl group in TMS-BP also showed steric repulsion with peripheral hydrogen atoms on BP to

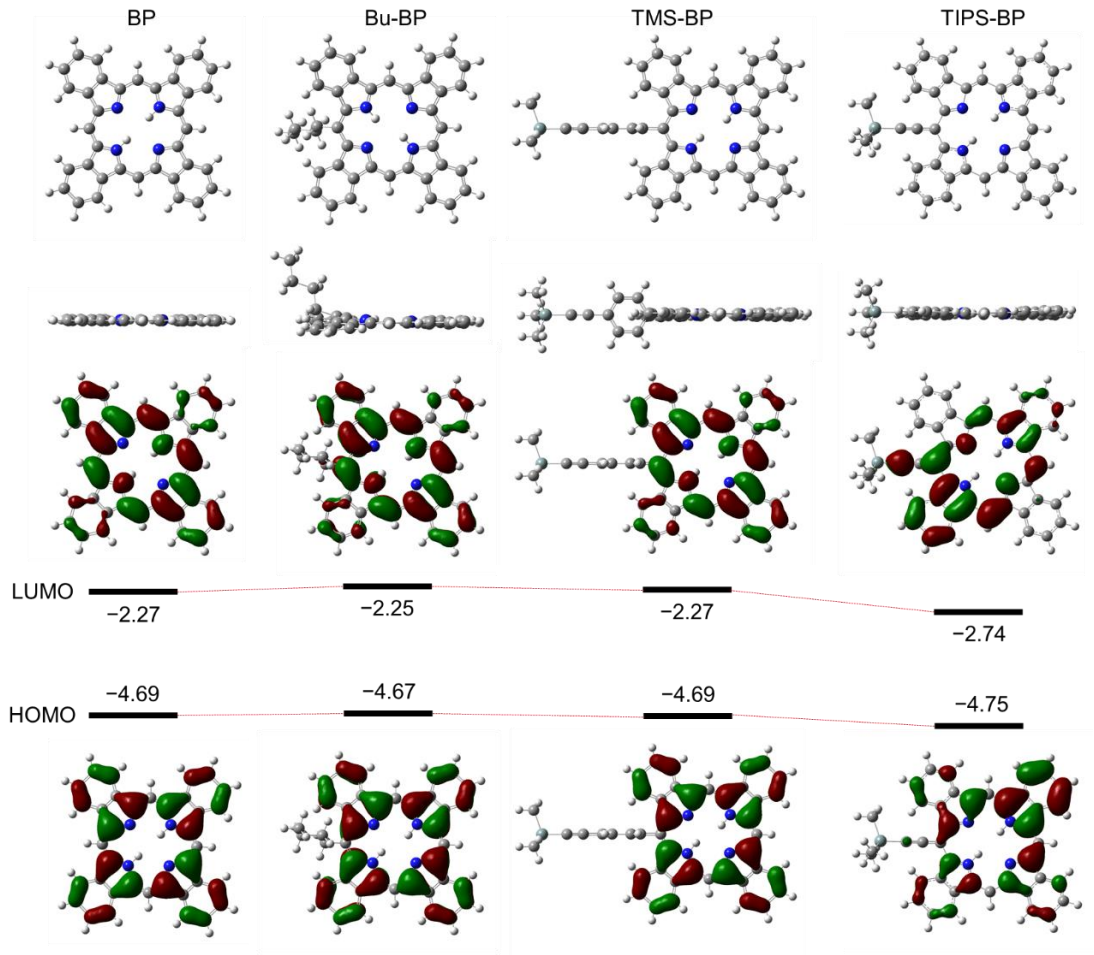

Figure 4. (a) Optimized molecular structure of Bu-, TMS-, and TIPS-BP with non-substituted BP.; (b) Geometry of HOMO and LUMO for the optimized structure of Bu-, TMS-, and TIPS-BP with non-substituted BP.

make the porphyrin ring and *moso*-phenyl planes perpendicular. On the other hand, *meso*-ethynyl group in TIPS-BP can be expanded straight structure.

Due to the structural features of the substituents described above, there are few electronic interactions between *meso*-substituents and BP framework in Bu- and TMS-BP. The frontier orbital energies of Bu-BP (HOMO = −4.65 eV, LUMO = −2.25 eV) and TMS-BP (HOMO = −4.69 eV, LUMO = −2.27 eV) are same as BP (HOMO = −4.69 eV, LUMO = −2.27 eV). On the other hand, different electronic structure was observed in TIPS-BP because of the conjugation with *moso*-ethynyl group. HOMO level of TIPS-BP (−4.75 eV) was slightly lower than BP due to the partially delocalized electron density on the ethynyl moiety. LUMO level of TIPS-BP (−2.72 eV) was also low compared with the other BPs because of the delocalized electron density on the ethynyl moiety. Thus, TIPS-BP might be used as a building-block for further tuning for optical or electrical-properties of BP.

From these results, asymmetric *meso*-substituted BP must be able to be developed as useful building blocks for semiconducting materials.

2-6. Summary

The author established a synthetic method for asymmetric *meso*-substituted BPs in moderate yields. To obtain the asymmetric alkyl-substituted CPs, Reaction 1 must be useful. When commercially available paraformaldehyde was used as the paired aldehyde, mono-alkylated CPs can be synthesized. However, this method was not suitable to prepare 5-aryl- or 5-ethynyl-CPs because of the preferential prepration of 5, 15-aryl- or 5, 15-ethynyl-CPs. Instead of the Reaction 1, Reaction 2 with DDQ oxidation showed good superiority for the reactants.

5-substituted BPs (Bu-BP, TMS-BP, and TIPS-BP) were successfully prepared by r-DA reaction of their precursors. Their decomposition temperatures (352–400 ºC) were lower than that of non-substituted BP (> 500 ºC), but r-DA reactions occurred between 131–200 ºC. Therefore, quantitative r-DA reaction of their precursor (Bu-CP, TMS-CP, and TIPS-CP) can be achieved. From DFT calculations, optimized 5-substituted BPs were expected to have flat BP planes as same as non-substituted BP. Because of steric repulsion with phenyl hydrogen atoms on BP, *meso*-butyl group was bended and *moso*-phenyl planes were crossed to be perpendicular with porphyrin ring. Thus, they have frontier orbital energies similar to non-substituted BP. On the other hand, lower frontier orbital energies of TIPS-BP were expected due to the electron delocalization on both BP and *meso*-ethynyl group.

From these result, the author concludes that asymmetric *meso*-substituted BP derivatives can be prepared easily and be applied for semiconducting materials with the advantage of thermal precursor approach.

2-7. Support Information

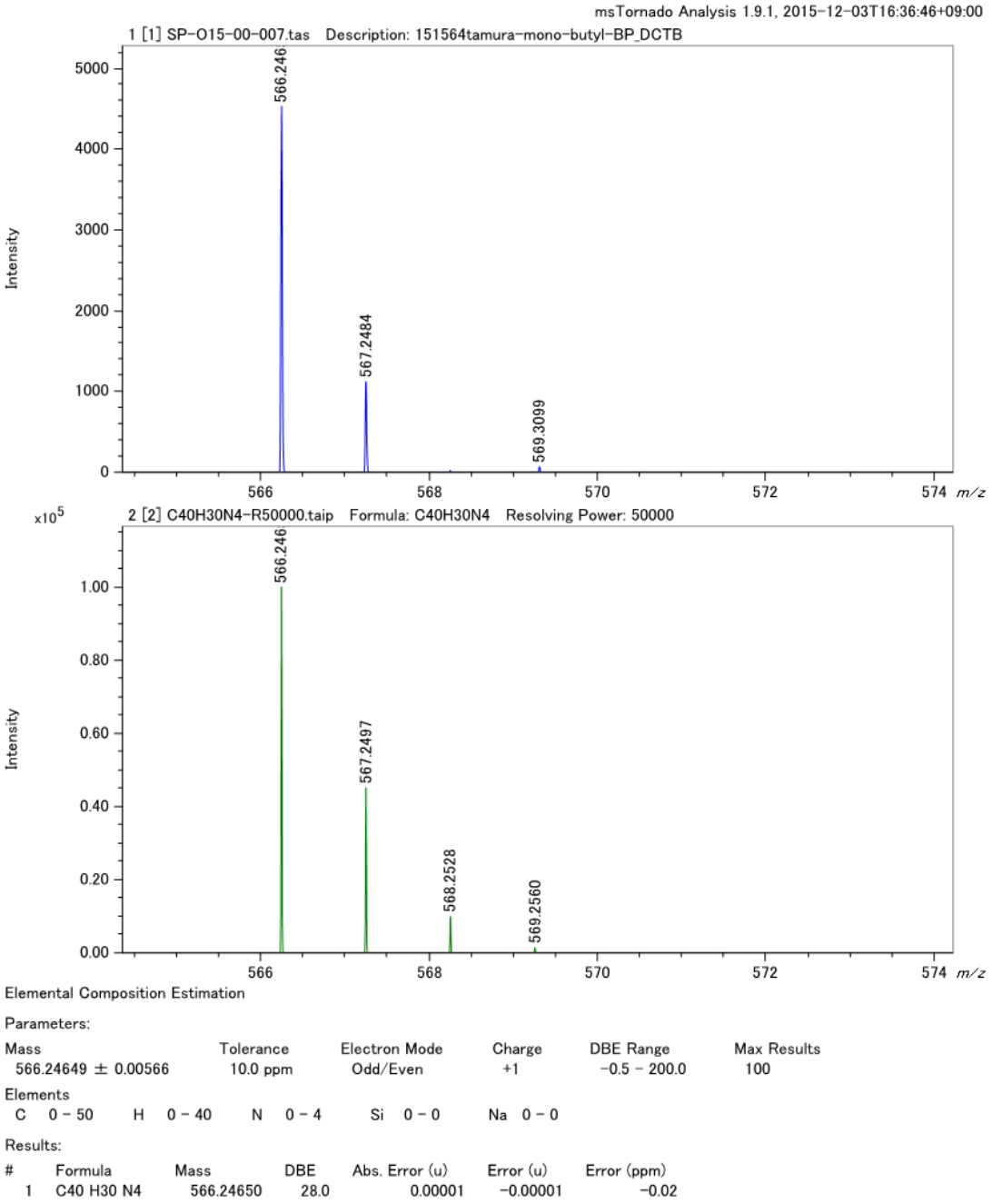

Figure S2-1. HR MALDI spiral-TOF mass spectrum of Bu-BP. Upper is the obtained spectrum and lower is simulation for $C_{40}H_{30}N_4$.

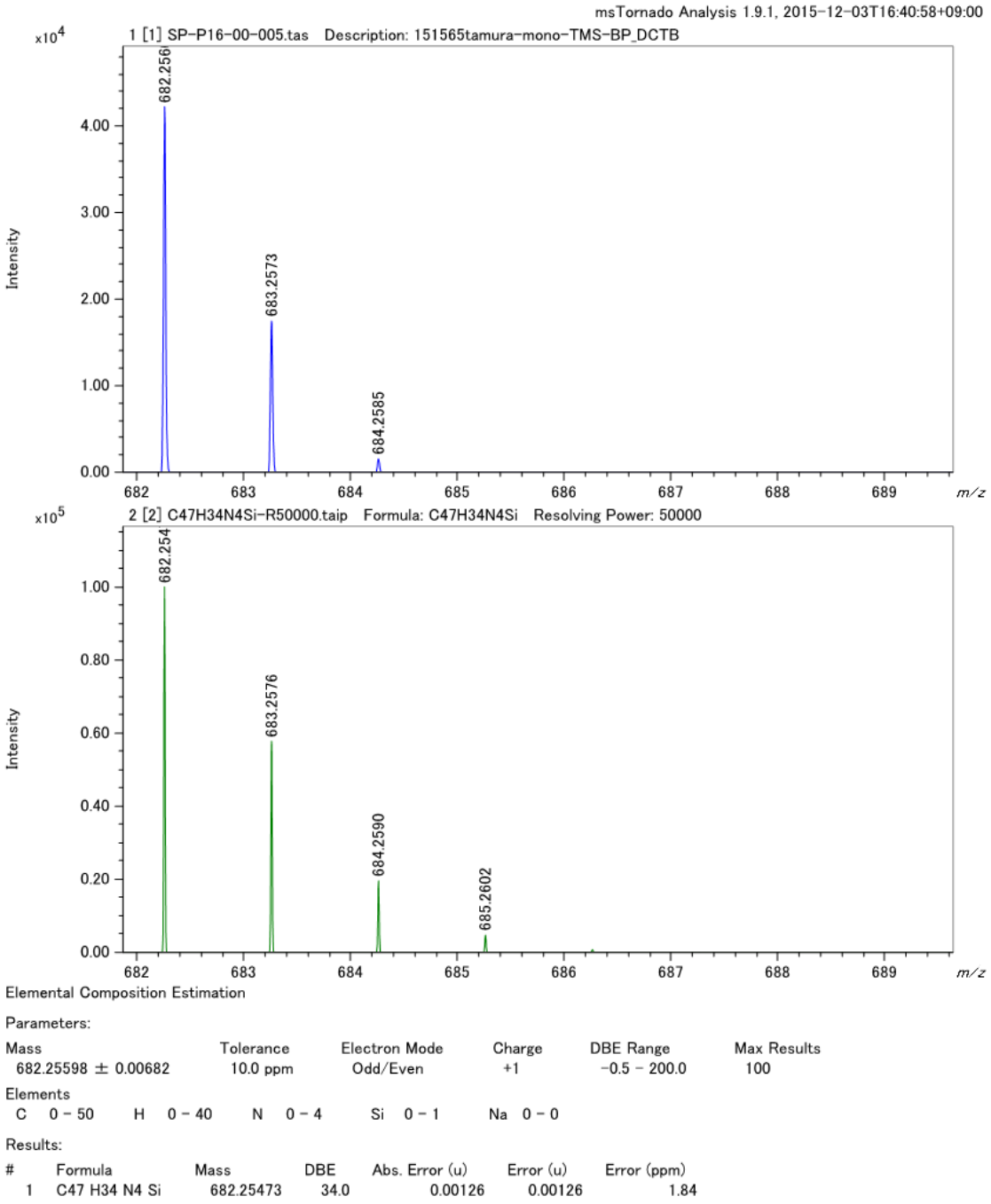

Figure S2-2. HR MALDI spiral-TOF mass spectrum of TMS-BP. Upper is the obtained spectrum and lower is simulation for $C_{47}H_{34}N_4Si$.

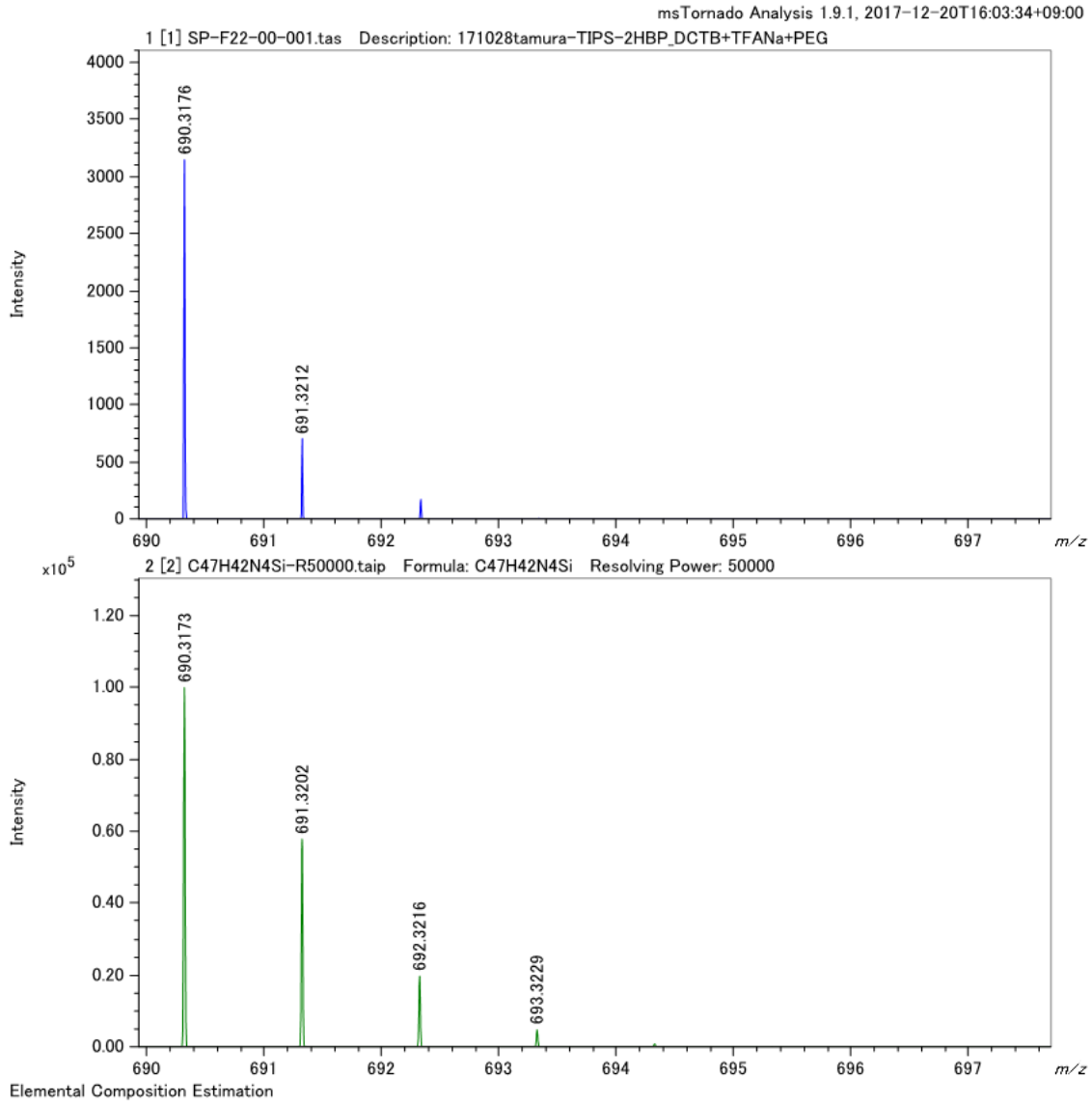

Figure S2-3. HR MALDI spiral-TOF mass spectrum of TIPS-BP. Upper is the obtained spectrum and lower is simulation for $C_{47}H_{42}N_4Si$.

2-8. Experimental Section

2-8-1. General

Materials

Solvents and chemicals were reagent grade quality, obtained commercially and used without further purification except as noted. Bis(4,7-dihydro-4,7-ethano-*2H*-isoindol-1-yl)methane (**1**),[23] 4-methoxycarbonylpentan-1-al (**3**),[24] Bis(4,7-dihydro-8,8-dimethyl-4,7-ethano-*2H*-isoindol-1-yl)methane (**9**),[2] *p*-[(trimethylsilyl)ethynyl]benzaldehyde (**10**),[25] and CP[23] were synthesized as described in literatures. Dimethyl-4,7-dihydro-*2H*-4,7-ethanoisoindol-1-yl)methanol (**13**)[2] was synthesized from ethyl 4,7-dihydro-8,8-dimethyl-4,7-ethano-*2H*-isoindole-1-carboxylate[2] as described in the literature. Because **13** is unstable compound under ambient condition, fresh **13** should be prepared every time for a reaction and directly used without further purification.

Purification and Characterization of Materials

Room temperature, or r.t., means 20–25 ºC. Thin-layer chromatography (TLC) was conducted on Art. 5554 (Merck KGaA) with visualization using UV light at 254 or 365 nm. Material purifications were performed by gravity column chromatography on Silica Gel 60N, 60 Å, 63–210 μm (Kanto Chemical Co.), Alumina Activated 200, Particle size: approx. 200mesh, Specially Prepared Reagent (NACALAI TESQUE, INC.), and gel permeation chromatography (GPC) using JAILC-9225NEXT equipped with JAIGEL 1H and 2H polystyrene gel columns (600 × 40 mm; bead size = 16 μm; pore size = 20–30 (1H) and 40–50 (2H) Å) at room temperature using $CHCl_3$ as an eluent. ^1H NMR and $^{13}C\{^1H\}$ NMR spectra were recorded on a JNM-ECX400 spectrometer using tetramethylsilane or solvent as an internal standard. The thermogravimetric analysis (TGA) was carried out on a Seiko Exstar 6000 TG/DTA 6200 instrument under a nitrogen gas flow with a heating rate of 5 ºC min^{-1}. Materials converted by heating (200 ºC, 30 min) were investigated by MALDI-TOF mass spectra. ESI and MALDI-TOF mass spectra were measured on a JEOL JMST100LC AccuTOF spectrometer and JEOL spiral TOF JMS-S3000 spectrometer, respectively.

DFT Calculation

The geometries of compounds were fully optimized using the density functional theory (DFT). The functional and basis set used in the DFT calculations were the Becke's three-parameter hybrid functional combined with the Lee-Yang-Parr correlation functional (B3LYP) and the 6-31G(d) basis set, respectively. Equilibrium geometries were verified by the frequency calculations, where no imaginary frequency was found. All the calculations were carried out using the Gaussian 09 suite of programs.

2-8-2. Synthetic Procedures

[5-(4-methoxycarbonylpentyl)-15-butyl-tetrakis(BCOD)porphyrin]zinc(II) (4)

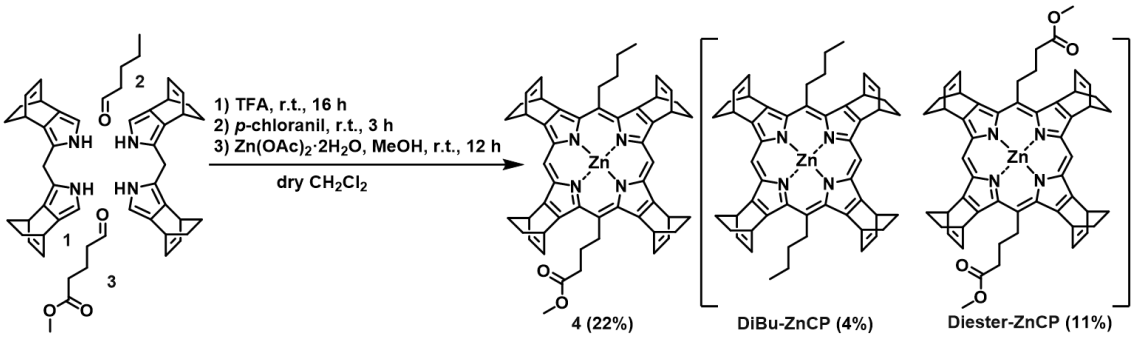

BCOD-fused dipyrromethane **1** (1.04 g, 3.46 mmol), pentanal **2** (86 mg, 1.04 mmol), and 4-methoxycarbonylpentan-1-al **3** (320 mg, 2.42 mmol) and dry-CH_2Cl_2 (600 mL) were placed to a 1000-mL three-necked round-bottom flask under Ar atmosphere. After Ar gas bubbling for 25 min, trifluoroacetic acid (TFA, 19 μm) was added to the solution and the solution was stirred at room temperature with protection from light for 16 h. After the addition of *p*-bchliranil (1.42 g, 5.75 mmol), the solution was stirred at room temperature for 3 h and was neutralized with triethylamine. After removing soluvent, 100 mL of CH_2Cl_2 and $Zn(OAc)_2 \cdot 2H_2O$ (379 mg, 1.73 mmol) in methanol (20 mL) was added to the residue. The solution was stirred at room temperature for 12 h. Then, the solvent was removed under reduced pressure. The crude product was purified by silica gel column chromatography with ethyl acetate/hexane (1:6) as an eluent and recrystallization from $CHCl_3/CH_3CN$ to afford the target products **5** in 22% (320 mg, 0.38 mmol) as red powder. At the same time, by-product of **DiBu-CP** in 4% (55 mg, 0.07 mmol), and **Diester-ZnCP** in 11% (168 mg, 0.19 mmol) also obtained, respectively.

4: ^{1}H NMR ($CDCl_3$, 400 MHz): δ (ppm) = 10.15–10.33 (m, 2H), 7.06–7.23 (m, 8H), 5.06–5.85 (8H), 5.13–5.53 (m, 4H), 3.28–3.90 (m, 2H), 2.59–3.28 (m, 4H), 1.77–2.32 (m, 18H), 1.24–1.41 (m, 3H).; ^{13}C NMR ($CDCl_3$, 100 MHz): δ (ppm) = 173.92, 173.86, 151.46, 151.34, 148.02, 147.65, 143.87, 143.77, 140.50, 136.98, 120.40, 120.23, 118.35, 118.16, 96.61, 95.87, 52.12, 51.75, 41.38, 41.20, 40.92, 40.05, 36.00, 34.57, 33.87, 33.66, 33.37, 33.00, 32.61, 28.16, 27.66, 27.58, 27.46, 27.07, 23.81, 14.83, 14.69. HR-MS (ESI): calcd for $C_{53}H_{53}N_4O_2Zn$, 841.3460 $[M + H]^+$; found, 841.3454.

DiBu-ZnCP: ^{1}H NMR ($CDCl_3$, 400 MHz): δ (ppm) = 10.23–10.13 (m, 2H), 7.23–7.05 (m, 2H), 5.85–5.69 (m, 8H), 5.52–5.10 (m, 4H), 3.09–2.60 (m, 4H), 2.36–1.77 (m, 20H),

1.43–1.22 (m, 6H).; ^{13}C NMR ($CDCl_3$, 100 MHz): δ (ppm) = 151.28, 147.88, 143.85, 140.50, 137.03, 120.15, 96.51, 41.49, 40.91, 36.47, 36.03, 34.57, 28.17, 27.63, 27.49, 27.13, 23.85, 14.86; HR-MS (ESI): calcd. for $C_{52}H_{53}N4Zn$, 797.3562 $[M + H]^+$; found, 797.3563.

Diester-ZnCP: ^{1}H NMR ($CDCl_3$, 400 MHz): δ (ppm) = 10.26–10.20 (m, 2H), 7.25–7.11 (m, 8H), 5.85–5.68 (m, 8H), 5.52–5.29 (m, 4H), 3.86–3.73 (m, 6H), 3.16–2.87 (m, 8H), 2.33–1.85 (m, 16H); ^{13}C NMR ($CDCl_3$, 100 MHz): δ (ppm) =173.95, 151.58, 147.84, 143.87, 140.60, 136.99, 118.67, 96.75, 51.81, 40.97, 36.03, 34.74, 33.30, 28.19, 27.67, 27.47, 27.05; HR-MS (ESI): calcd. for $C_{54}H_{53}N_4O_2Zn$, 885.3362 $[M + H]^+$; found, 885.3358.

[5-butyl-tetrakis(BCOD)porphyrin]zinc(II) (6)

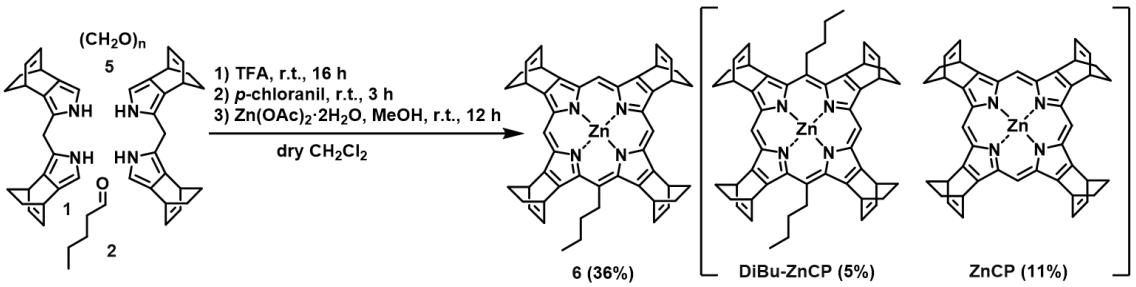

BCOD-fused dipyrromethane **1** (1.04 g, 3.46 mmol), pantanal **2** (149 mg, 1.73 mmol), paraformaldehyde **5** (0.52 mg, 1.73 mmol), and dry-CH_2Cl_2 (600 mL) were placed to a 1000-mL three-necked round-bottom flask under Ar atmosphere. After Ar gas bubbling for 25 min, trifluoroacetic acid (TFA, 19 μm) was added to the solution and the solution was stirred at room temperature with protection from light for 16 h. After the addition of *p*-bchliranil (1.42 g, 5.75 mmol), the solution was stirred at room temperature for 3 h and was neutralized with triethylamine. After removing soluvent, 100 mL of CH_2Cl_2 and $Zn(OAc)_2{\cdot}2H_2O$ (379 mg, 1.73 mmol) in methanol (20 mL) was added to the residue. The solution was stirred at room temperature for 12 h. Then, the solvent was removed under reduced pressure. The crude product was purified by passing through a pad of aluminum using CH_2Cl_2 as an eluent and GPC using $CHCl_3$ as an eluent to afford the target products **6** in 36% (462 mg, 0.62 mmol) as red powder. At the same time, by-product of **DiBu-CP** in 5% (69 mg, 0.08 mmol) and **ZnCP** in 11% (130 mg, 0.19 mmol) also obtained, respectively.

6: ^{1}H NMR ($CDCl_3$, 400 MHz): δ (ppm) = 10.36–10.23 (m, 3H), 7.23–7.08 (m, 8H), 5.88–5.70 (m, 8H), 5.60–5.26 (m, 2H), 3.00–2.72 (m, 2H), 2.33–1.82 (m, 18H), 1.42–1.28 (m, 3H); ^{13}C NMR ($CDCl_3$, 100 MHz): δ (ppm) = 151.32, 149.86, 149.84, 149.81, 149.66, 148.07, 148.03, 143.36, 142.89, 141.86, 140.92, 136.95, 121.73, 97.28, 97.34, 96.85, 41.55, 41.06, 36.46, 36.11, 34.84, 28.21, 27.99, 27.64, 27.50, 27.15, 23.87, 14.88, 1.90; HR-MS (ESI): calcd. for $C_{48}H_{44}N_4Zn$, 740.2838 $[M]^{\bullet+}$; found, 740.2852.

[5-(methyester)butyl-tetrakis(BCOD)porphyrin]zinc(II) (7)

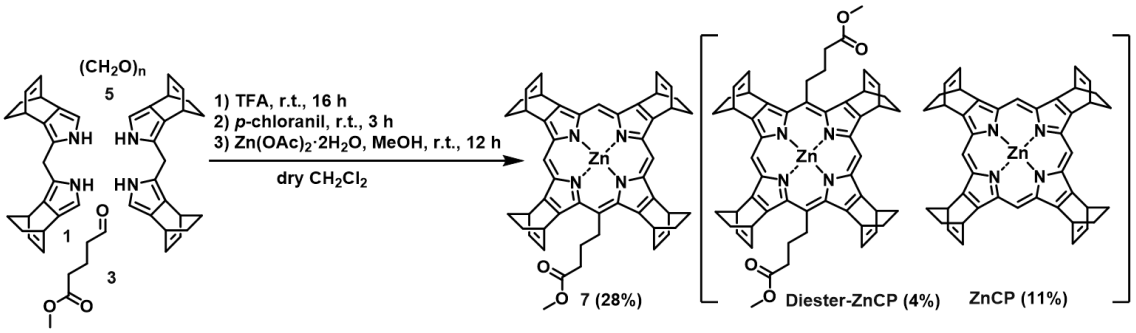

BCOD-fused dipyrromethane **1** (1.04 g, 3.46 mmol), 4-methoxycarbonylpentan-1-al **3** (230 mg, 1.73 mmol), paraformaldehyde **5** (0.52 mg, 1.73 mmol), and dry-CH_2Cl_2 (600 mL) were placed to a 1000-mL three-necked round-bottom flask under Ar atmosphere. After Ar gas bubbling for 25 min, trifluoroacetic acid (TFA, 19 μm) was added to the solution and the solution was stirred at room temperature with protection from light for 16 h. After the addition of *p*-bchliranil (1.42 g, 5.75 mmol), the solution was stirred at room temperature for 3 h and was neutralized with triethylamine. After removing soluvent, 100 mL of CH_2Cl_2 and $Zn(OAc)_2{\cdot}2H_2O$ (379 mg, 1.73 mmol) in methanol (20 mL) was added to the residue. The solution was stirred at room temperature for 12 h. Then, the solvent was removed under reduced pressure. The crude product was purified by silica gel column chromatography with ethyl acetate/hexane (1:6) as an eluent and recrystallization from $CHCl_3/CH_3CN$ to afford the target products **7** in 28% (380 mg, 0.48 mmol) as red powder. At the same time, by-product of **Diester-CP** in 6% (92 mg, 0.10 mmol) and **ZnCP** in 11% (130 mg, 0.19 mmol) also obtained, respectively.

7: ^{1}H NMR ($CDCl_3$, 400 MHz): δ (ppm) = 10.38–10.36 (m, 3H), 7.23–7.08 (m, 8H), 5.87–5.67 (m, 8H), 5.62–5.39 (m, 2H), 3.88–3.75 (m, 3H), 3.29–2.91 (m, 4H), 2.40–1.76 (m, 16H); ^{13}C NMR ($CDCl_3$, 100 MHz): δ (ppm) = 173.92, 151.50, 149.92, 149.88, 149.79, 143.29, 142.94, 142.92, 141.94, 140.95, 137.13, 136.92, 119.98, 97.47, 97.43,

97.09, 51.80, 41.08, 36.45, 36.08, 34.74, 33.39, 31.587, 28.25, 27.97, 27.71, 27.52, 27.078, 22.654, 14.130; HR-MS (ESI): calcd. for $C_{49}H_{44}N_4NaO_2Zn$, 807.2653 $[M + Na]^+$; found, 807.2656.

[5-(4-trimethylsilylethynyl)phenyl-tetrakis(dimethylBCOD)porphyrin]zinc(II) (10a)

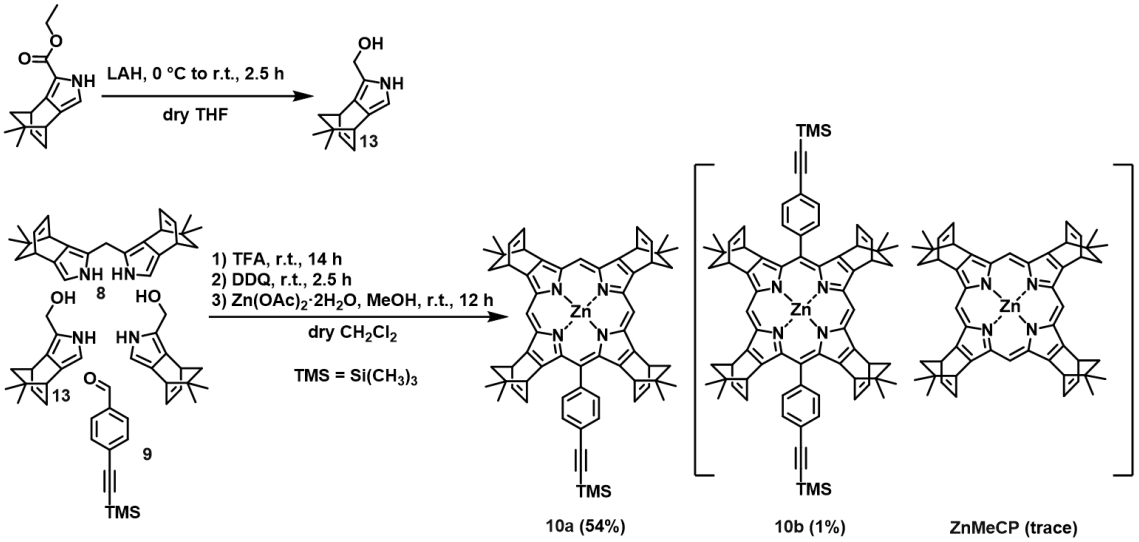

Ethyl 4,7-dihydro-8,8-dimethyl-4,7-ethano-*2H*-isoindole-1-carboxylate[2] (700 mg, 2.85 mmol) was dissolved in dry THF (20 mL), then lithyumaluminiumhydride (LAH, 530 mg, 13.95 mmol) was added to the solution slowly at 0 ºC. The mixture was stirred at room temperature with protection from light for 2.5 h. After quenching the reaction with water at 0 ºC, the reaction mixture was filtrated on Celite. The filtrate was extracted by AcOEt and washed with brine, dried over Na_2SO_4. Then solvent was removed to prepare compound **13**. The resulting compound **13**, dimethylBCOD-fused dipyrromethane **8** (500 mg, 1.39 mmol), *p*-[(trimethylsilyl)ethynyl]benzaldehyde **9** (281 mg, 1.39 mmol), and dry CH_2Cl_2 (600 mL) were placed to a 1000-mL three-necked round-bottom flask under Ar atmosphere. After Ar gas bubbling for 25 min, trifluoroacetic acid (TFA, 50 μm) was added to the solution and the solution was stirred at room temperature under protection from light for 14 h. After the addition of 2,3-dichloro-5,6-dicyano-*p*-benzoquinone (DDQ, 790 mg, 3.48 mmol), the solution was stirred at room temperature for 2.5 h and was neutralized with triethylamine. After removing solvent, the residue was dissolved in CH_2Cl_2 (50 mL) and a solution of $Zn(OAc)_2 \cdot 2H_2O$ (310 mg, 1.39 mmol) in methanol (20 mL) was added. The solution was

stirred at room temperature for 12 h. Then, the solvent was removed under reduced pressure. The crude product was purified by passing through a pad of aluminum using CH_2Cl_2 as an eluent and GPC using $CHCl_3$ as an eluent to afford to afford the target products **10a** in 54% (728 mg, 0.75 mmol) as red powder. At the same time, by-product of **10b** in 1% (16 mg, 0.014 mmol) and **ZnMeCP** in trace also obtained, respectively.

10a: ^{1}H NMR ($CDCl_3$, 400 MHz): δ (ppm) = 10.38–10.24 (m, 3H), 8.35–7.82 (m, 4H), 7.24– 6.59 (m, 8H), 5.69–5.51 (m, 3H), 5.21–5.05 (m, 3H), 3.64–3.20 (m, 2H), 2.19–1.10 (m, 21H), 0.92–0.30 (m, 20H); ^{13}C NMR ($CDCl_3$, 100 MHz): δ (ppm) = 149.75, 148.06, 147.02, 143.49, 143.22, 139.82, 138.10, 137.94, 137.56, 137.16, 137.06, 136.41, 136.11, 135.97, 135.91, 135.72, 134.98, 134.01, 133.57, 133.32, 130.30, 129.97, 129.58, 123.22, 123.02, 122.97, 116.64, 116.45, 105.46, 97.27, 96.85, 96.64, 94.99, 50.90, 50.61, 50.33, 49.44, 49.06, 43.96, 43.87, 43.53, 43.30, 40.59, 40.55, 40.50, 40.23, 40.01, 39.97, 39.89, 39.51, 39.42, 37.73, 37.65, 37.43, 37.39, 31.68, 31.47, 31.26, 31.14, 30.71, 0.43, 0.15, 0.13; HR-MS (ESI): calcd. for $C_{63}H_{65}N_4SiZn$, 969.4270 $[M + H]^+$; found, 969.4265.

10b: ^{1}H NMR ($CDCl_3$, 400 MHz): δ (ppm) = 10.37–10.25 (m, 2H), 8.32–7.87 (m, 8H), 7.20– 6.72 (m, 8H), 5.64–5.52 (m, 4H), 3.30–3.20 (m, 4H), 2.12–0.17 (m, 54H); ^{13}C NMR ($CDCl_3$, 100 MHz): δ (ppm) = 151.52, 151.44, 151.38, 151.25, 150.20, 150.06, 149.91, 144.37, 144.26, 143.79, 143.58, 141.85, 141.79, 138.25, 138.13, 135.89, 134.98, 134.69, 134.62, 133.81, 130.16, 129.75, 128.99, 123.05, 122.92, 122.87, 117.45, 105.48, 98.22, 98.09, 94.77, 94.69, 51.27, 51.21, 50.82, 43.90, 43.75, 4.34, 40.31, 40.24, 40.21, 40.03, 39.99, 39.93, 39.49, 37.39, 31.52, 31.37, 31.29, 31.24, 30.83, 30.63, 0.46, 0.18; HR-MS (ESI): calcd. for $C_{74}H_{76}N_4Si_2Zn$, 1140.4900 $[M + H]^+$; found, 1140.4895.

[5-triisopropylsilylethynyl-tetrakis(dimethylBCOD)porphyrin]zinc(II) (12a)

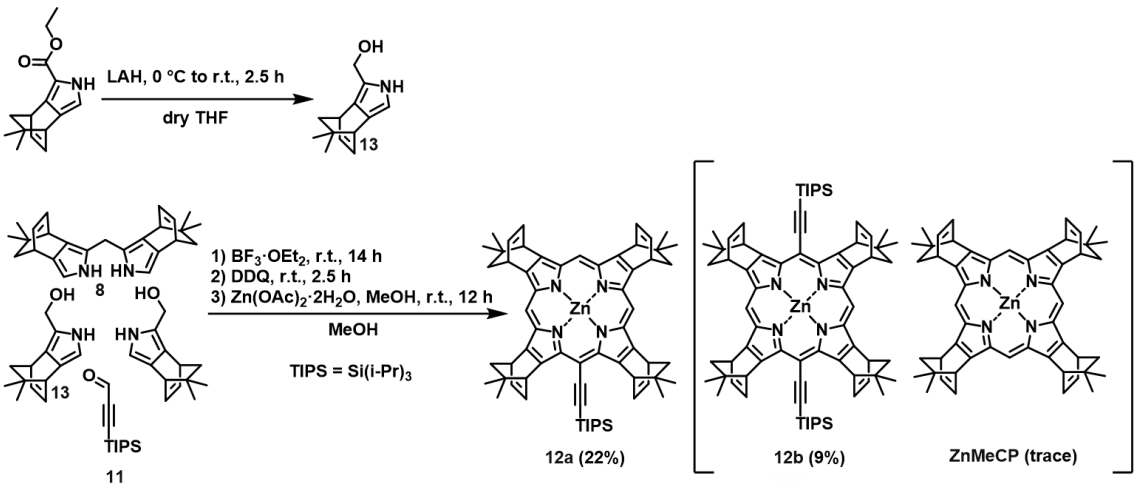

Ethyl 4,7-dihydro-8,8-dimethyl-4,7-ethano-*2H*-isoindole-1-carboxylate[2] (700 mg, 2.85 mmol) was dissolved in dry THF (20 mL), then lithyumaluminiumhydride (LAH, 530 mg, 13.95 mmol) was added to the solution slowly at 0 ºC. The mixture was stirred at room temperature with protection from light for 2.5 h. After quenching the reaction with water at 0 ºC, the reaction mixture was filtrated on Celite. The filtrate was extracted by AcOEt and washed with brine, dried over Na_2SO_4. Then solvent was removed to prepare compound **13**. The resulting compound **13**, dimethylBCOD-fused dipyrromethane **8** (500 mg, 1.39 mmol), *p*-[(triisopropylsilyl)ethynyl]aldehyde **11** (290 mg, 1.39 mmol), and MeOH (500 mL) were placed to a 1000-mL three-necked round-bottom flask under Ar atmosphere. After Ar gas bubbling for 25 min, boron trifluoride-diethyl ether complex ($BF_3{\cdot}OEt_2$, 50 μm) was added to the solution and the solution was stirred at room temperature under protection from light for 14 h. After the addition of 2,3-dichloro-5,6-dicyano-*p*-benzoquinone (DDQ, 790 mg, 3.48 mmol), the solution was stirred at room temperature for 2.5 h and was neutralized with triethylamine. After removing soluvent, the residue was dissolved in CH_2Cl_2 (50 mL) and a solution of $Zn(OAc)_2{\cdot}2H_2O$ (310 mg, 1.39 mmol) in methanol (20 mL) was added. The solution was stirred at room temperature for 12 h. Then, the solvent was removed under reduced pressure. The crude product was purified by passing through a pad of aluminum using CH_2Cl_2 as an eluent and GPC using $CHCl_3$ as an eluent to afford to afford the target products **12a** in 22% (292 mg, 0.31 mmol) as purple powder. At the same time, by-product of **12b** reported by Takahashi et al.[9] in 9% (139 mg, 0.12 mmol) and **ZnMeCP** in trace also obtained, respectively.

12a: ^{1}H NMR ($CDCl_3$): δ (ppm) = 10.33–10.19 (3H, m), 7.24–7.02 (8H, m), 6.75–5.06 (8H, m), 2.14–1.23 (41H, m), 0.88–0.12 (12H, m); ^{13}C NMR ($CDCl_3$, 100 MHz): δ (ppm) = 153.16, 153.12, 153.10, 153.05, 151.54, 151.42, 150.94, 150.77, 150.75, 150.59, 148.84, 148.80, 148.78, 148.39, 148.32, 148.12, 148.02, 147.98, 146.25, 144.87, 144.61, 144.42, 144.40, 144.33, 142.71, 142.70, 142.65, 142.45, 142.41, 142.32, 142.24, 142.20, 140.59, 138.52, 137.77, 137.11, 137.00, 136.83, 136.04, 135.93, 135.39, 110.82, 110.64, 99.29, 99.21, 98.99, 98.77, 97.76, 97.55, 51.72, 49.51, 49.29, 44.53, 44.05, 43.48, 40.68, 40.64, 40.57, 40.53, 40.51, 39.86, 39.82, 39.79, 39.75, 39.68, 37.76, 37.71, 37.63, 31.62, 31.34, 31.25, 31.10, 30.90, 19.39, 19.34, 19.08, 18.97, 12.39, 12.14; HRMS (ESI): calcd for $C_{74}H_{95}N_4Si_2$ $[M + H]^+$, 1095.7095; found, 1095.7091.

5-butyl-tetrakis(BCOD)porphyrin (Bu-CP)

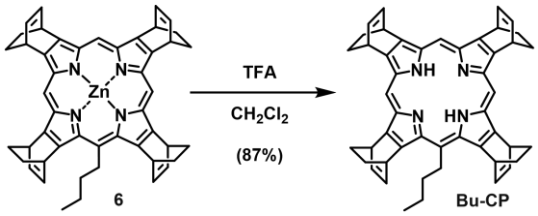

Excess TFA (1 mL) was added to the solution of **6** (200 mg, 0.27 mmol) in CH_2Cl_2 (10 mL). After stirring 12 h at the room temperature, the solution was washed with saturated $NaHCO_3$ aq, water, and brine. Then the organic layer was dried over Na_2SO_4, and the solvent was removed under reduced pressure. The crude product was purified by recrystallization from $CHCl_3$/MeOH to afford the target compound **Bu-CP** in 87% as dark brown powder (159 mg, 0.23 mmol).

^{1}H NMR ($CDCl_3$, 400 MHz): δ (ppm) = 10.40–10.08 (m, 3H), 7.18–7.01 (m, 8H), 5.93–5.58 (m, 8H), 5.50–5.19 (m, 2H), 2.90–2.59 (m, 2H), 2.32–1.74 (m, 17H), 1.42–1.13 (m, 4H), −3.87–−4.21 (m, 2H); ^{13}C NMR ($CDCl_3$, 100 MHz): δ (ppm) = 150.89, 150.83, 149.52, 149.50, 148.20, 148.15, 146.51, 140.45, 140.10, 137.61, 136.91, 136.74, 120.74, 120.71, 120.68, 96.41, 95.75, 41.03, 40.41, 36.45, 36.39, 36.30, 36.08, 33.93, 27.98, 27.87, 27.57, 27.11, 23.80, 14.77, 14.75; HR-MS (ESI): calcd. for $C_{48}H_{47}N_4$, 679.3801 $[M + H]^+$; found, 679.3807.

5-trimethylsilyl-tetrakis(dimethylBCOD)porphyrin (TMS-CP)

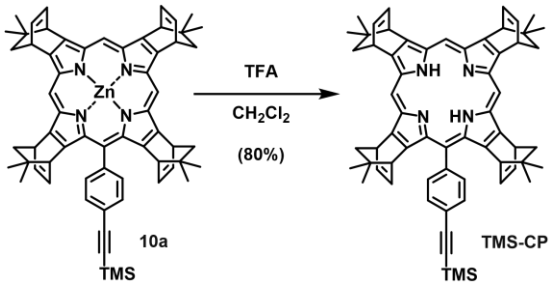

Excess TFA (1 mL) was added to a solution of **10a** (200 mg, 0.21 mmol) in CH_2Cl_2 (10 mL). After stirring at room temperature for 12 h, the solution was washed with saturated $NaHCO_3$ aq, water, and brine. Then the organic layer was dried over Na_2SO_4, and the solvent was removed under reduced pressure. The crude product was purified by reprecipitation (CH_3CN and water) to afford the target compound **TMS-CP** in 80% as brown powder (152 mg, 0.17 mmol).

^{1}H NMR ($CDCl_3$, 400 MHz): δ (ppm) = 10.36–10.15 (m, 3H), 8.37–7.80 (m, 8H), 7.24–6.58 (m, 8H), 5.67–5.52 (m, 3H), 5.20–5.03 (m, 3H), 3.67–3.55 (m, 1H), 3.38–3.55 (m, 1H), 2.16–1.00 (m, 22H), 0.91–0.15 (m, 21H), −4.1–−4.42 (m, 2H); ^{13}C NMR ($CDCl_3$, 100 MHz): δ (ppm) = 149.75, 147.03, 143.49, 143.22, 138.10, 137.94, 137.57, 137.17, 137.06, 136.41, 136.11, 135.97, 135.91, 135.86, 135.72, 134.14, 134.01, 133.78, 133.57, 133.32, 130.30, 129.97, 129.59, 123.06, 123.02, 166.64, 116.45, 105.46, 97.27, 96.64, 96.51, 94.99, 50.90, 50.70, 50.61, 50.33, 49.44, 49.07, 43.96, 43.87, 43.54, 43.30, 40.59. 40.55, 40.50, 40.23, 40.01, 39.97, 39.89, 39.51, 39.42, 37.73, 37.65, 37.43, 37.39, 31.68, 31.47, 31.26, 31.14, 31.10, 31.02, 30.71, 0.15, 0.13; HR-MS (ESI): calcd. for $C_{63}H_{67}N_4Si$, 907.5135 $[M + H]^+$; found, 907.5132.

5-triisopropylsilyl-tetrakis(dimethylBCOD)porphyrin (TIPS-CP)

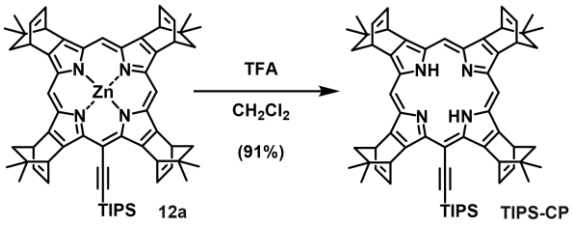

Excess TFA (1 mL) was added to a solution of **12a** (200 mg, 0.20 mmol) in CH_2Cl_2 (10 mL). After stirring at room temperature for 12 h, the solution was washed with saturated $NaHCO_3$ aq., water, and brine. Then the organic layer was dried over Na_2SO_4, and the solvent was removed under reduced pressure. The crude product was

purified by reprecipitation (CH_3CN and water) to afford the target compound **TIPS-CP** in 91% as dark purple powder (166 mg, 0.18 mmol).

^1H NMR ($CDCl_3$, 400 MHz): δ (ppm) = 10.30–10.06 (3H, m), 7.24–7.02 (8H, m), 6.65–5.00 (8H, m), 2.15–1.29 (41H, m), 0.88–0.19 (12H, m), −3.60–−3.97 (2H, m).; ^{13}C NMR ($CDCl_3$, 100 mHz): δ (ppm) = 152.60, 152.48, 150.55, 150.04, 149.10, 147.95, 146.66, 141.77, 138.26, 137.57, 136.92, 136.69, 136.56, 135.82, 135.72, 135.22, 130.51, 109.92, 109.82, 99.66, 98.43, 98.04, 97.96, 96.64, 77.32, 77.20, 77.00, 76.68, 51.05, 49.35, 49.26, 44.41, 43.95, 43.36, 40.59, 40.56, 40.52, 40.48, 40.45, 40.10, 40.00, 39.90, 39.88, 39.86, 39.82, 39.78, 37.60, 31.49, 31.22, 31.18, 31.09, 31.05, 30.63, 19.23, 19.09, 19.05, 18.97, 18.95, 12.28, 12.06, 12.00; HR-MS (MALDI): calcd. For $C_{63}H_{75}N_4Si$, 915.5756 $[M]^{\bullet+}$; found, 915.5755.

2-8-3. NMR Spectra

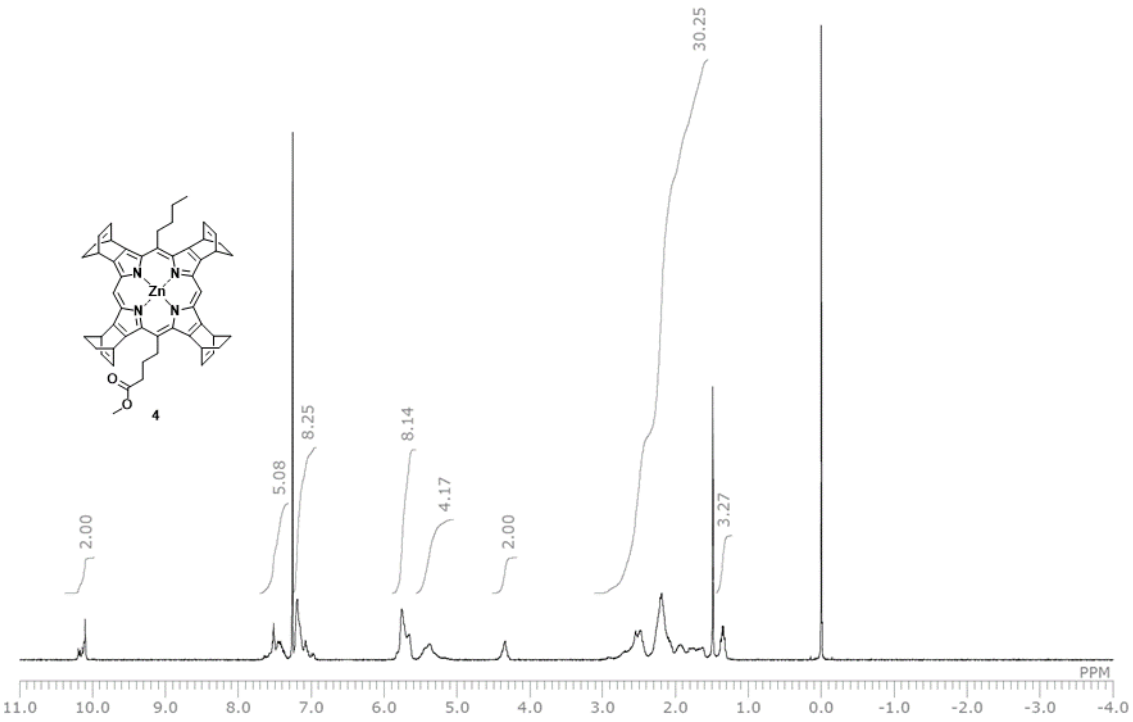

Figure S2-4-1. ^{1}H NMR spectrum of **4** in $CDCl_3$.

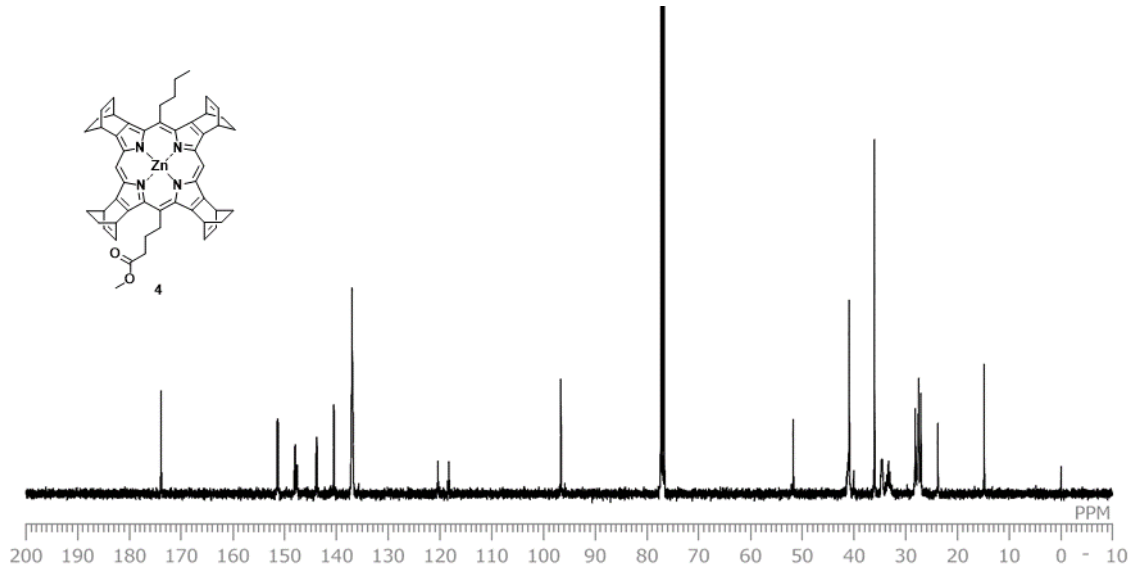

Figure S2-4-2. ^{13}C NMR spectrum of **4** in $CDCl_3$. (Minor peaks are occasionally observed alongside of the main peaks, which are presumably from the structural isomers differing in the orientation of bicycle[2.2.2]octadieno-units. The minor peaks are also listed in the spectroscopic characterization data above.)

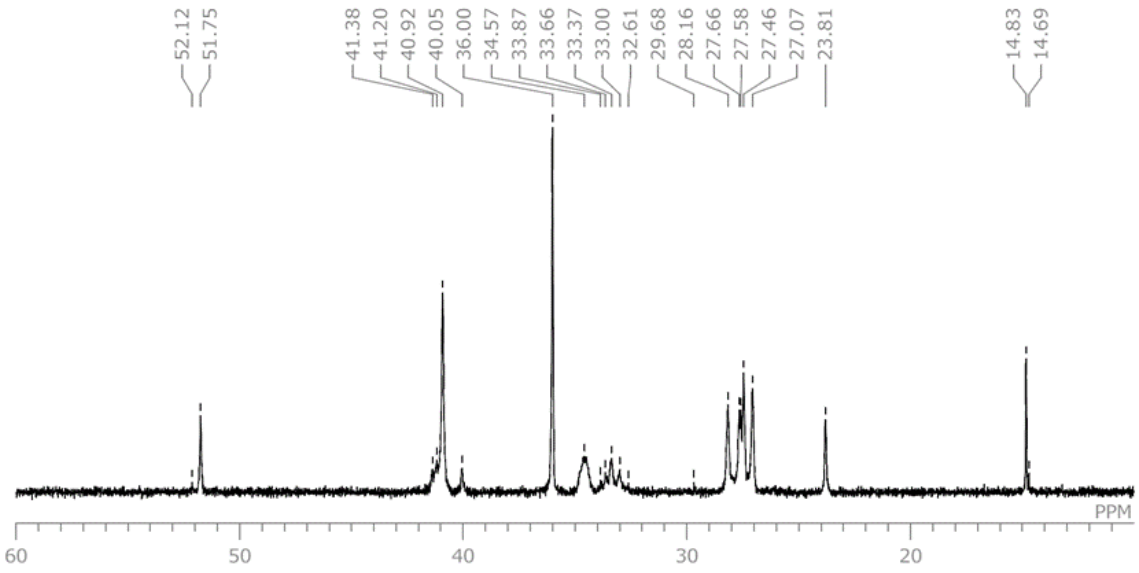

Figure S2-4-3. ^{13}C NMR spectrum of **4** in $CDCl_3$ (10–60 ppm).

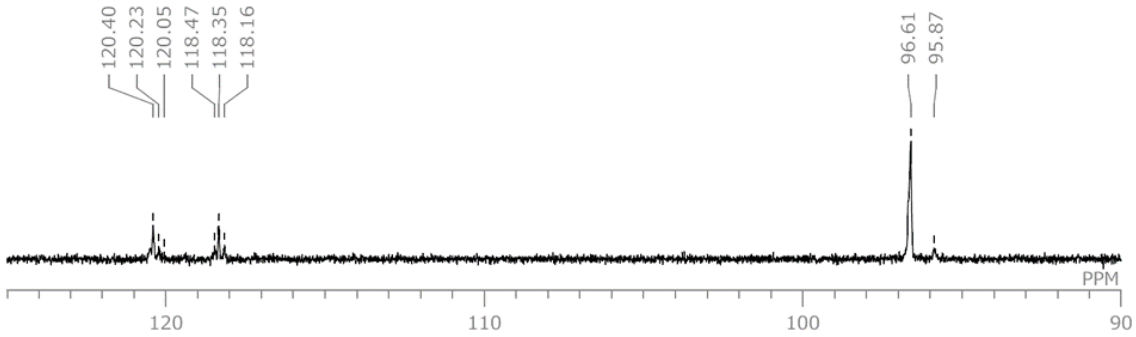

Figure S2-4-4. ^{13}C NMR spectrum of **4** in $CDCl_3$ (90–125 ppm).

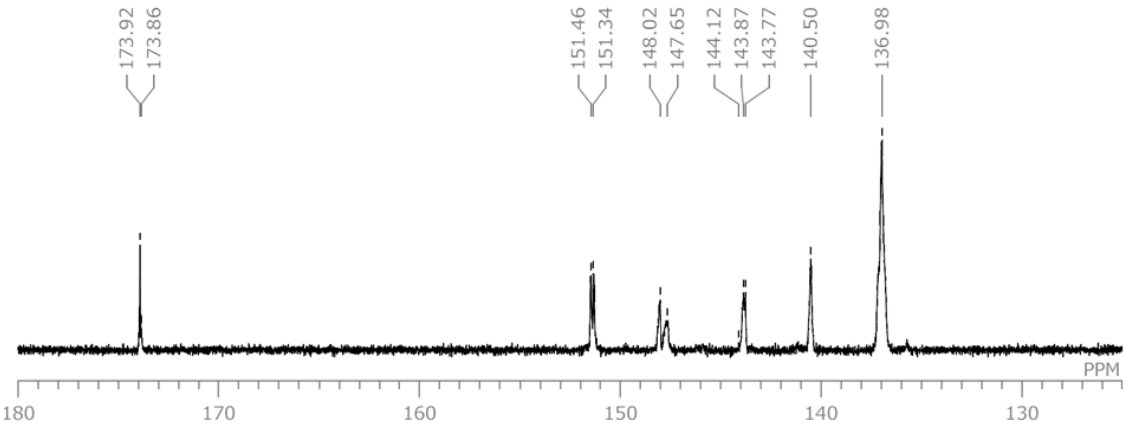

Figure S2-4-5. ^{13}C NMR spectrum of **4** in $CDCl_3$ (125–180 ppm).

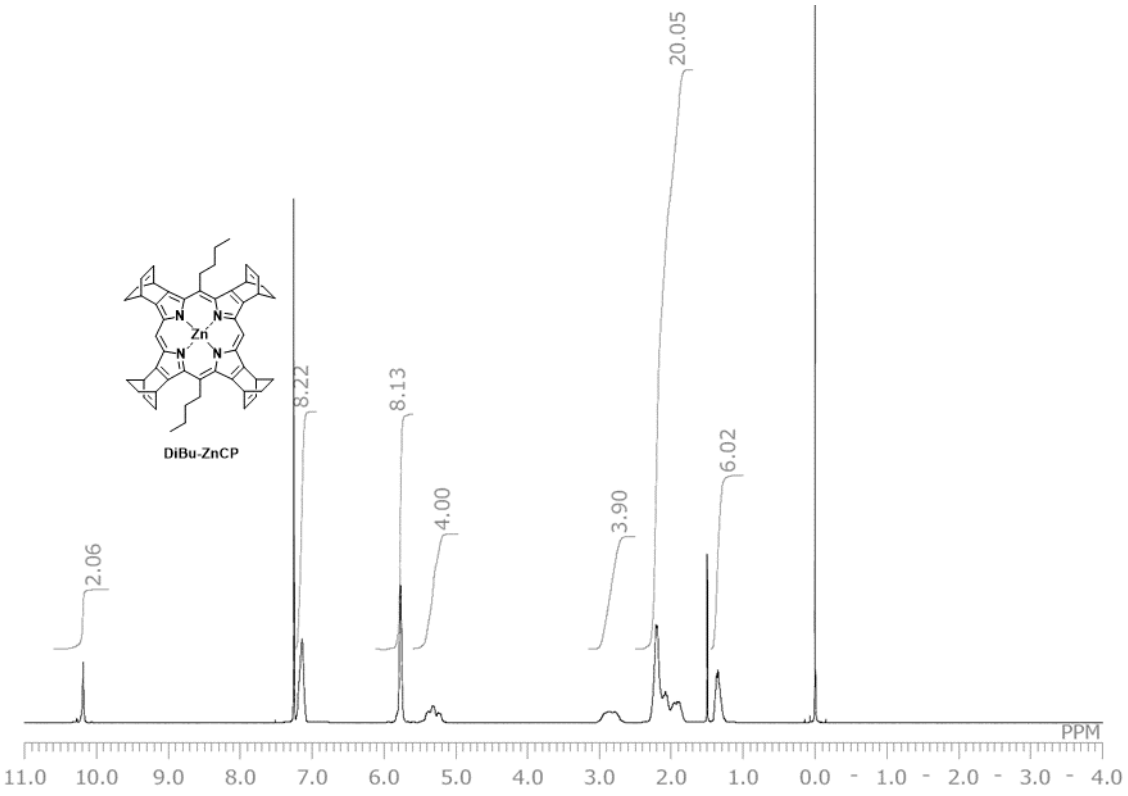

Figure S2-5-1. ^{1}H NMR spectrum of DiBu-ZnCP in $CDCl_3$.

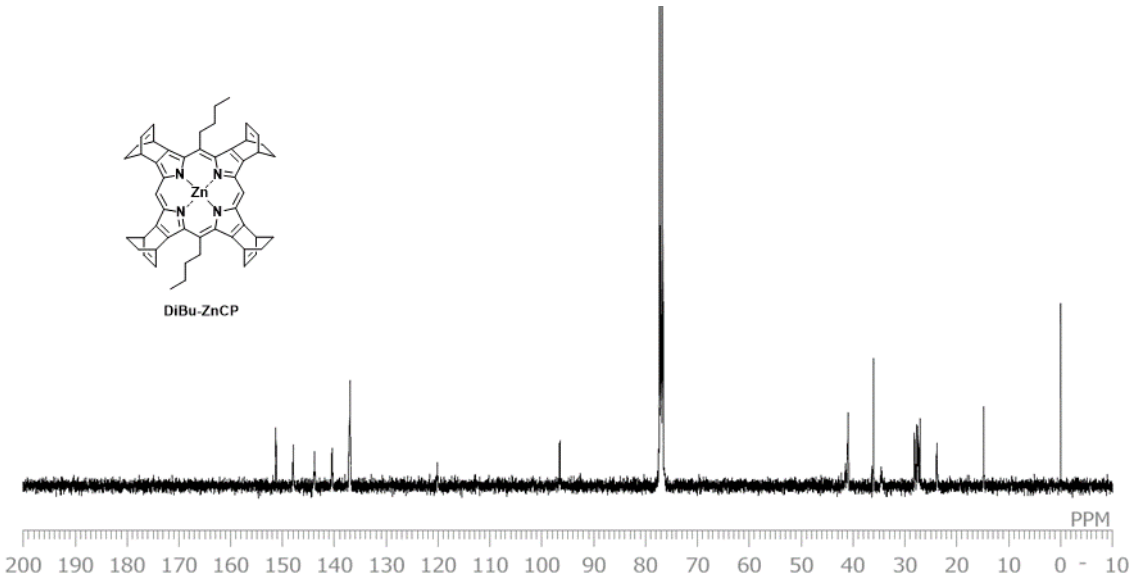

Figure S2-5-2. ^{13}C NMR spectrum of DiBu-ZnCP in $CDCl_3$. (Minor peaks are occasionally observed alongside of the main peaks, which are presumably from the structural isomers differing in the orientation of bicycle[2.2.2]octadieno-units. The minor peaks are also listed in the spectroscopic characterization data above.)

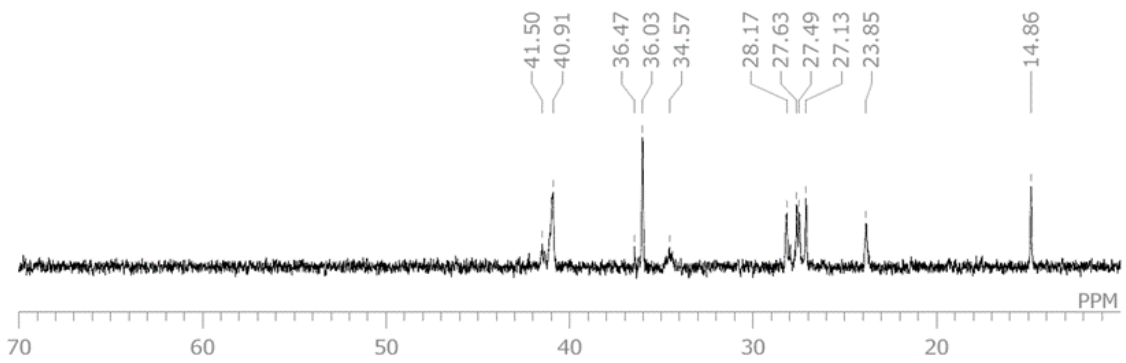

Figure S2-5-3. ^{13}C NMR spectrum of DiBu-ZnCP in $CDCl_3$ (10–70 ppm).

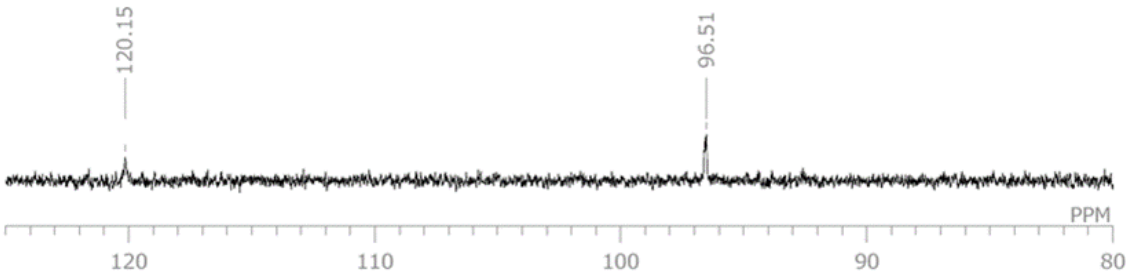

Figure S2-5-4. ^{13}C NMR spectrum of DiBu-ZnCP in $CDCl_3$ (80–125 ppm).

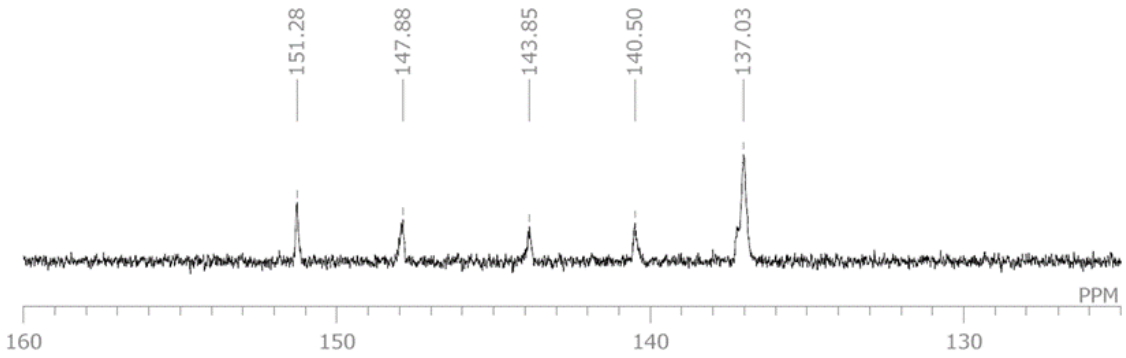

Figure S2-5-6. ^{13}C NMR spectrum of DiBu-ZnCP in $CDCl_3$ (125–160 ppm).

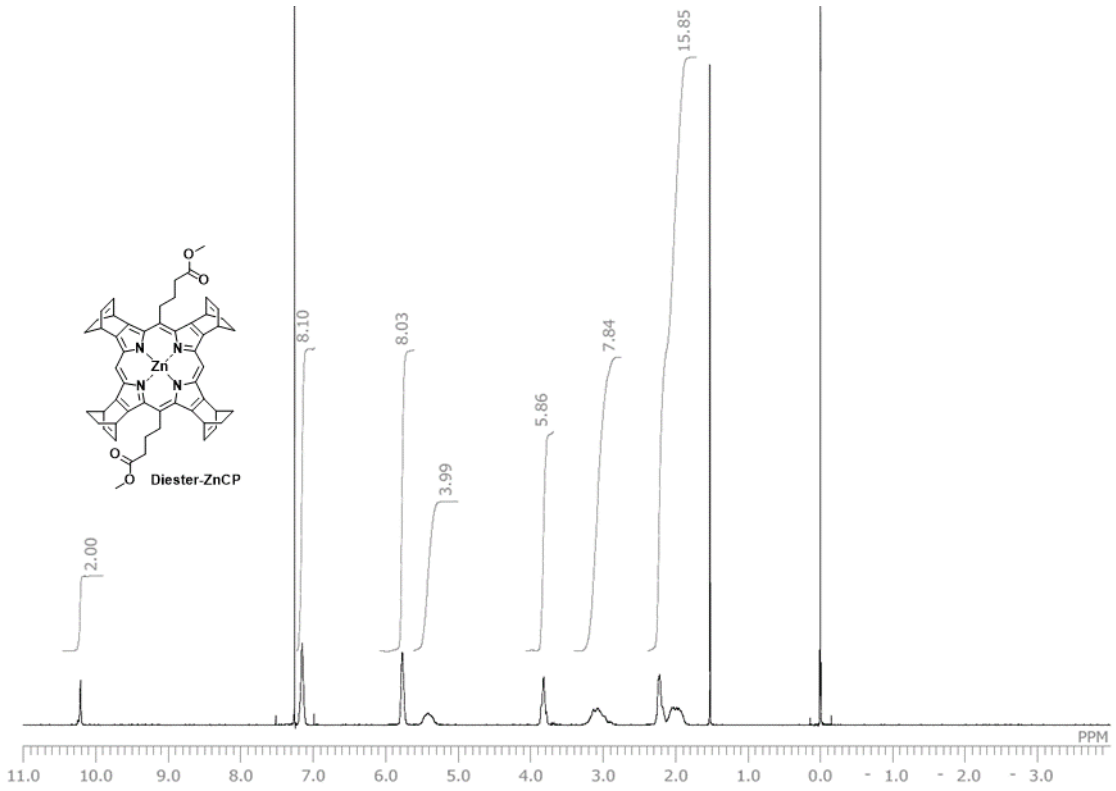

Figure S2-6-1. ^{1}H NMR spectrum of **Diester-ZnCP** in $CDCl_3$.

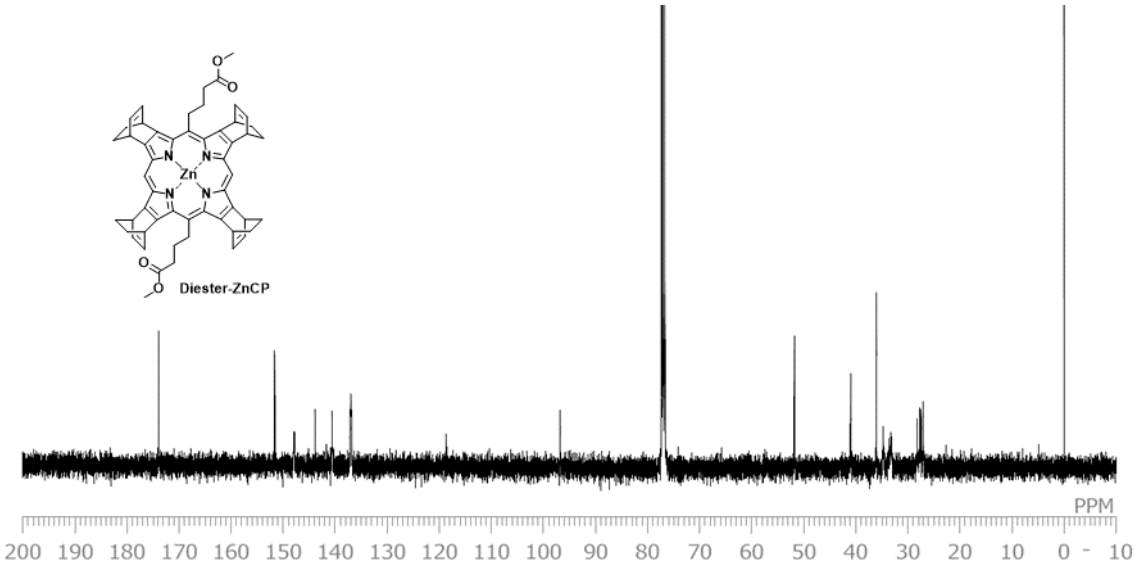

Figure S2-6-2. ^{13}C NMR spectrum of **Diester-ZnCP** in $CDCl_3$. (Minor peaks are occasionally observed alongside of the main peaks, which are presumably from the structural isomers differing in the orientation of bicycle[2.2.2]octadieno-units. The minor peaks are also listed in the spectroscopic characterization data above.)

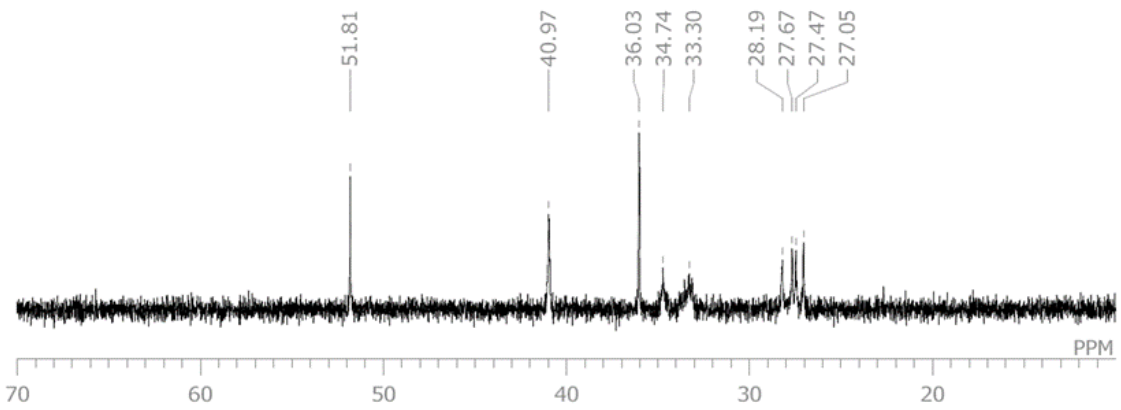

Figure S2-6-3. ^{13}C NMR spectrum of **Diester-ZnCP** in $CDCl_3$ (10–70 ppm).

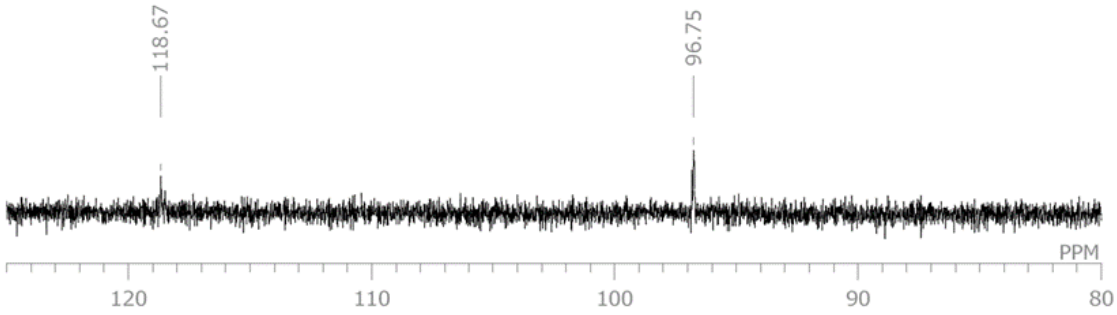

Figure S2-6-4. ^{13}C NMR spectrum of **Diester-ZnCP** in $CDCl_3$ (80–125 ppm).

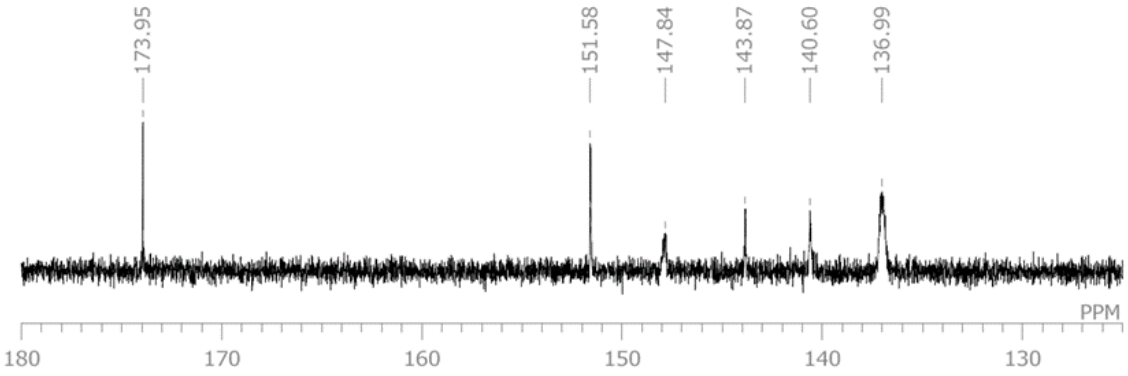

Figure S2-6-5. ^{13}C NMR spectrum of **Diester-ZnCP** in $CDCl_3$ (125–180 ppm).

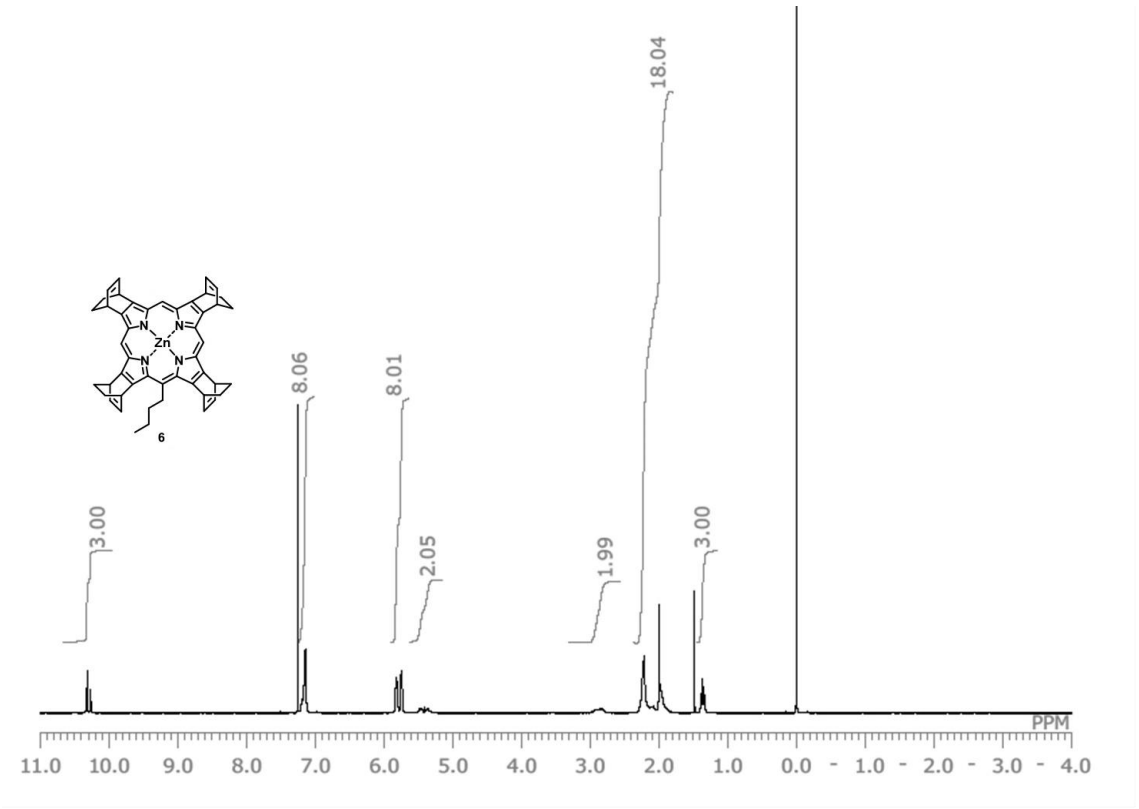

Figure S2-7-1. ^{1}H NMR spectrum of **6** in $CDCl_3$.

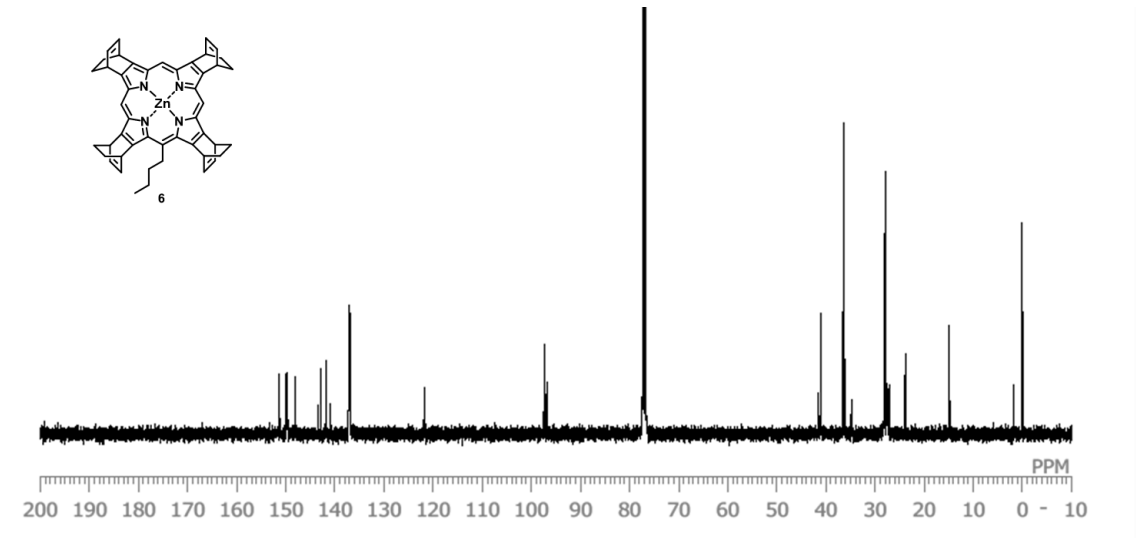

Figure S2-7-2. ^{13}C NMR spectrum of **6** in $CDCl_3$. (Minor peaks are occasionally observed alongside of the main peaks, which are presumably from the structural isomers differing in the orientation of bicycle[2.2.2]octadieno-units. The minor peaks are also listed in the spectroscopic characterization data above.)

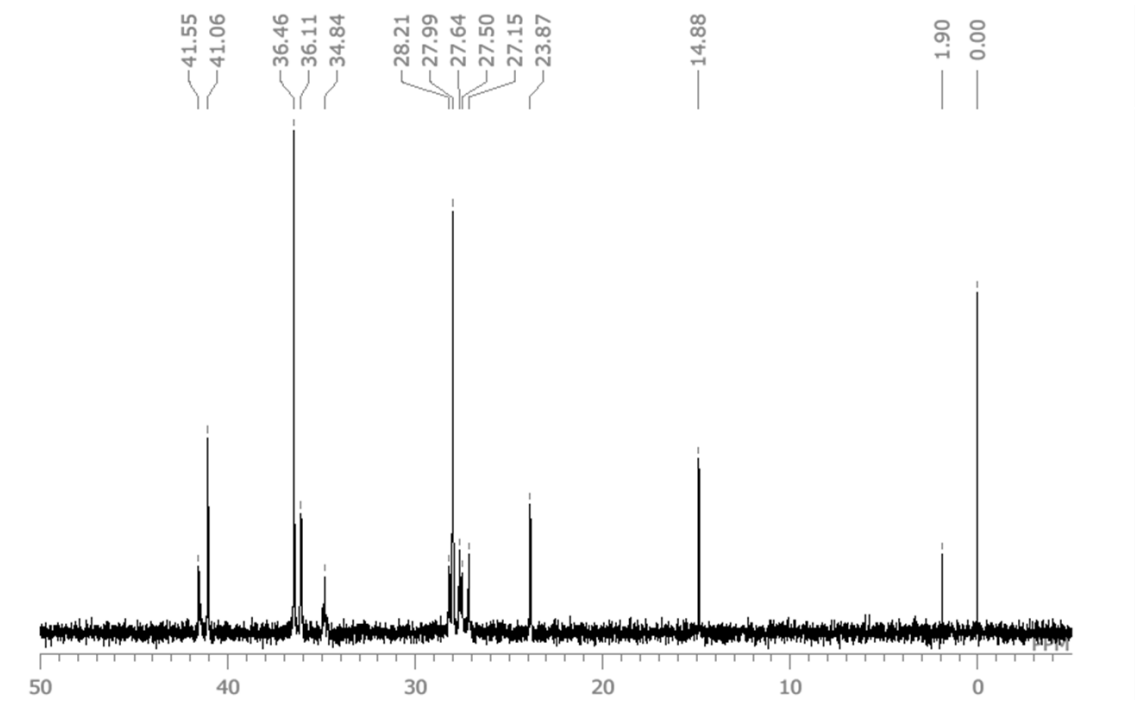

Figure S2-7-3. ^{13}C NMR spectrum of **6** in $CDCl_3$ (−5–50 ppm).

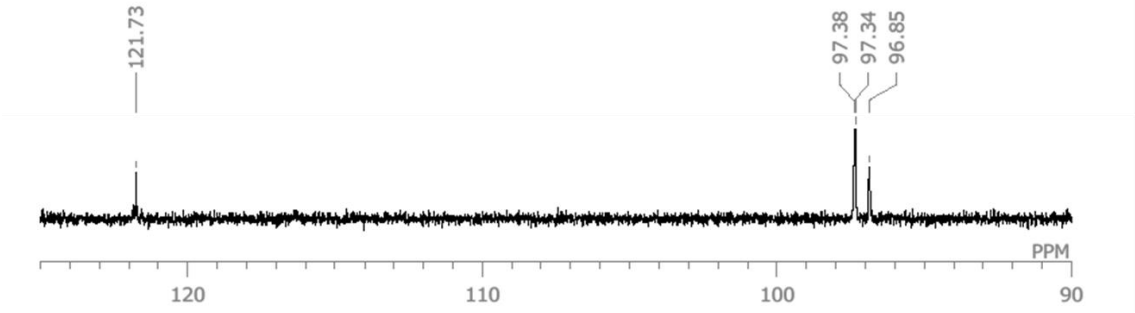

Figure S2-7-4. ^{13}C NMR spectrum of **6** in $CDCl_3$ (90–125 ppm).

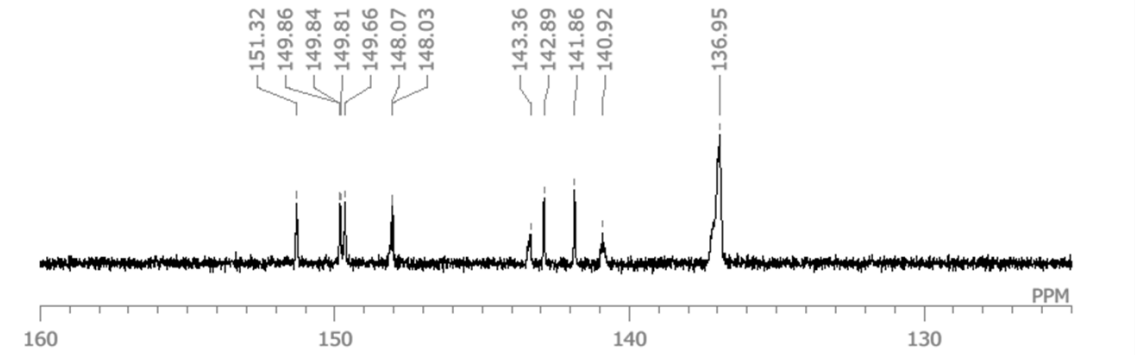

Figure S2-7-5. ^{13}C NMR spectrum of **6** in $CDCl_3$ (125–160 ppm).

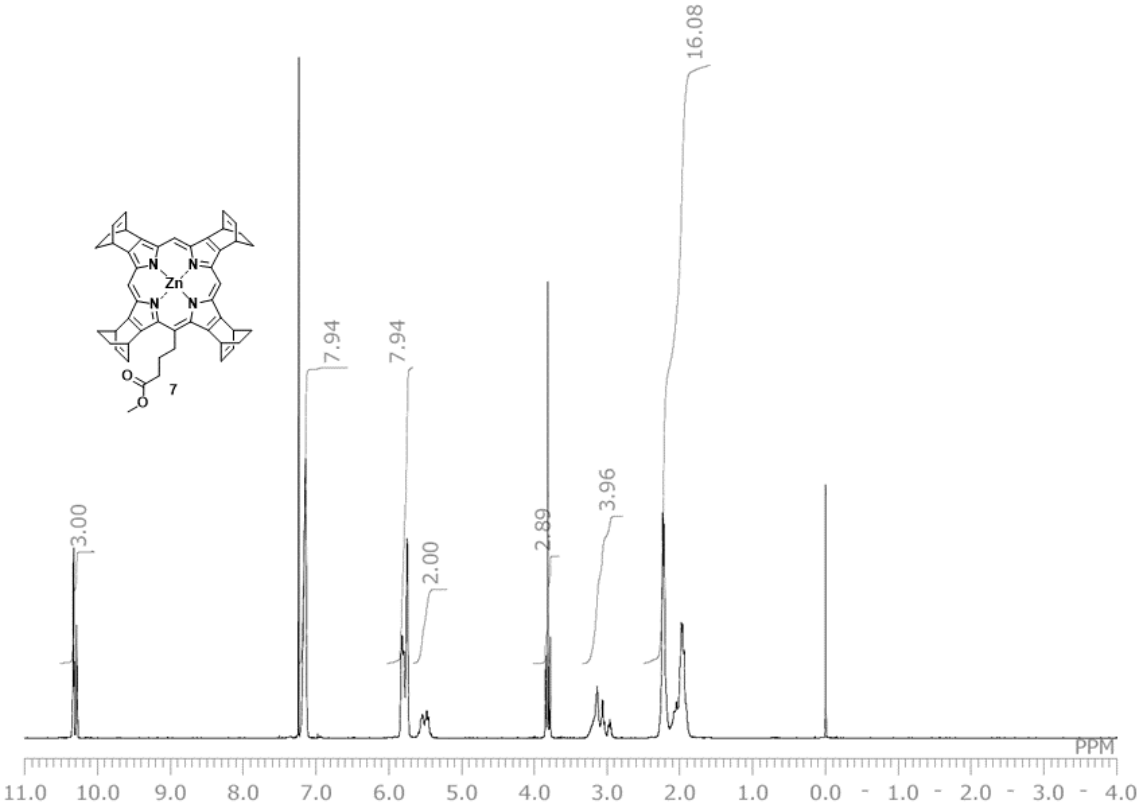

Figure S2-8-1. ^{1}H NMR spectrum of **7** in $CDCl_3$.

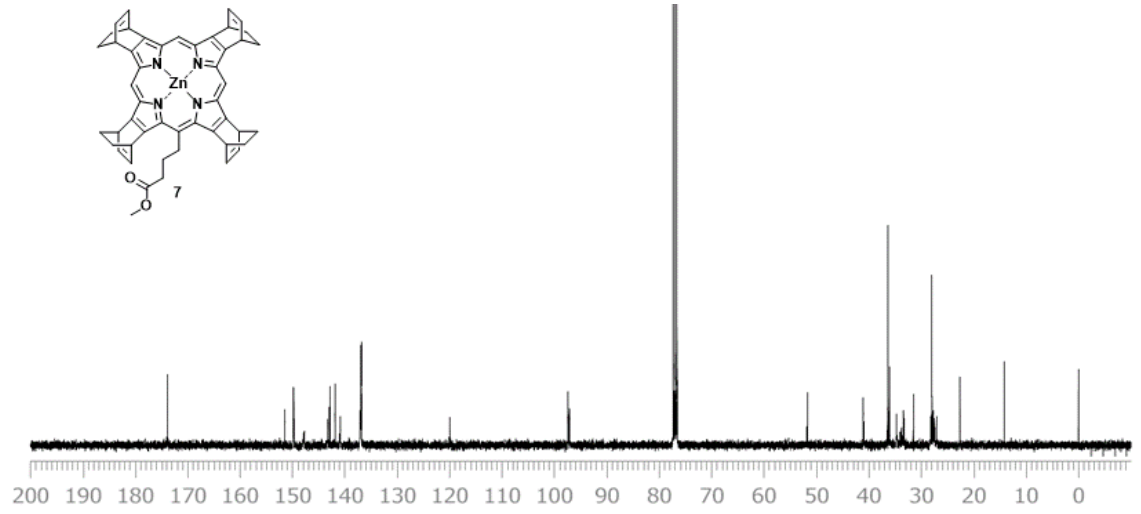

Figure S2-8-2. ^{13}C NMR spectrum of **7** in $CDCl_3$. (Minor peaks are occasionally observed alongside of the main peaks, which are presumably from the structural isomers differing in the orientation of bicycle[2.2.2]octadieno-units. The minor peaks are also listed in the spectroscopic characterization data above.)

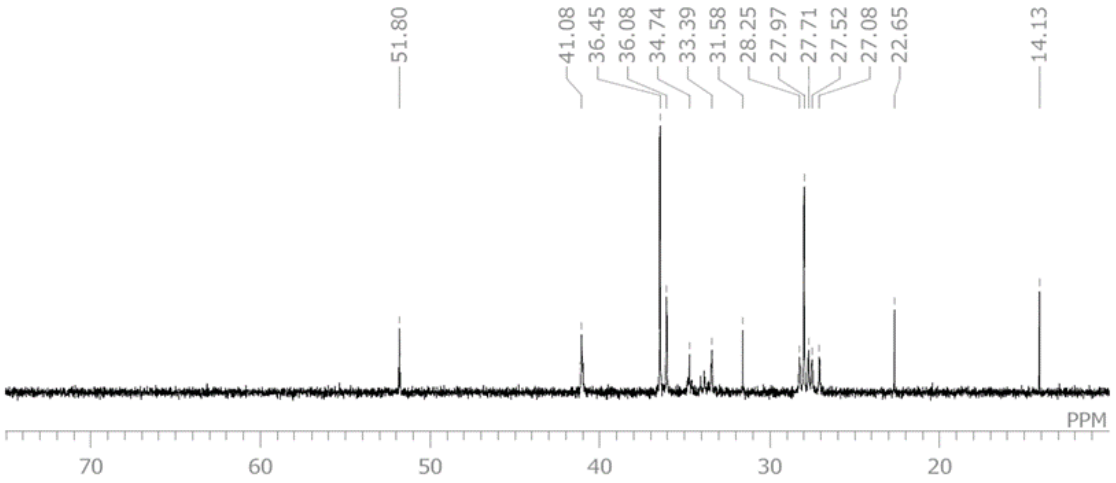

Figure S2-8-3. ^{13}C NMR spectrum of **7** in $CDCl_3$ (10–75 ppm).

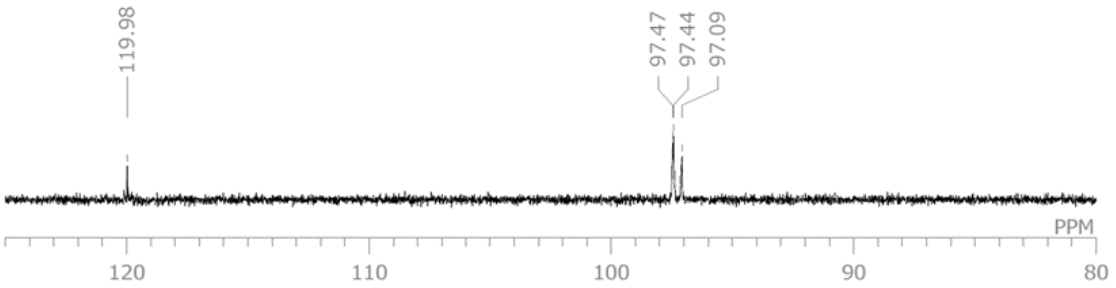

Figure S2-8-4. ^{13}C NMR spectrum of **7** in $CDCl_3$ (80–125 ppm).

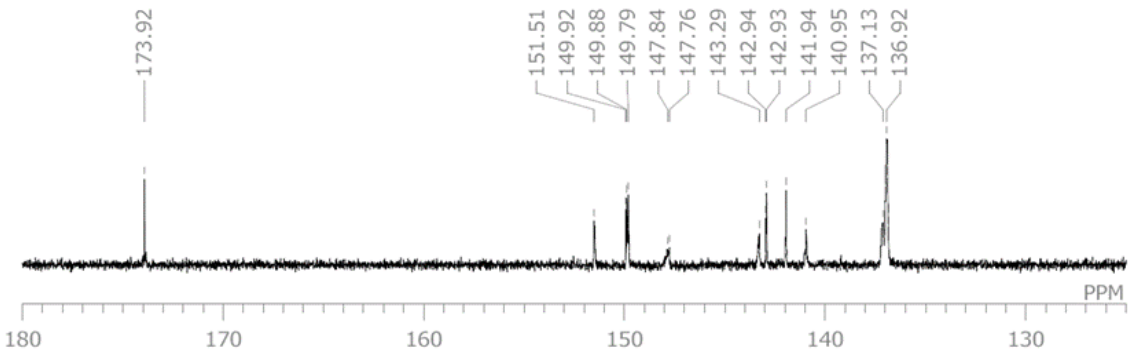

Figure S2-8-5. ^{13}C NMR spectrum of **7** in $CDCl_3$ (125–180 ppm).

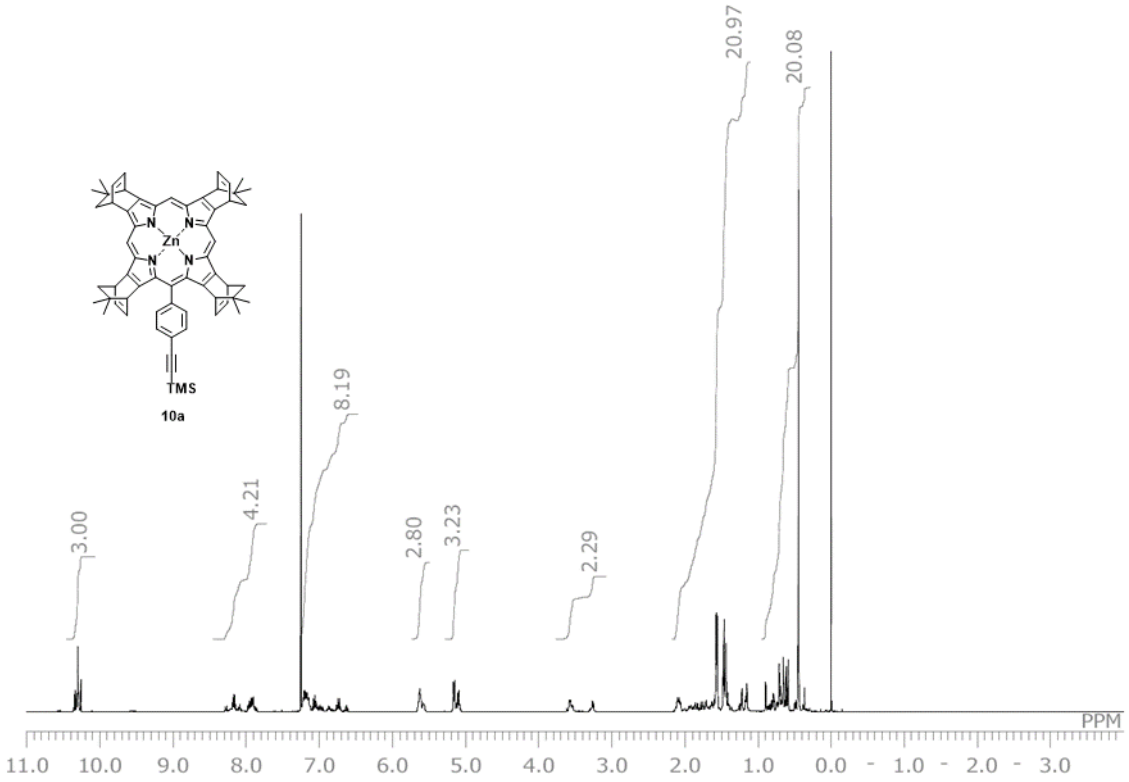

Figure S2-9-1. ^{1}H NMR spectrum of **10a** in $CDCl_3$.

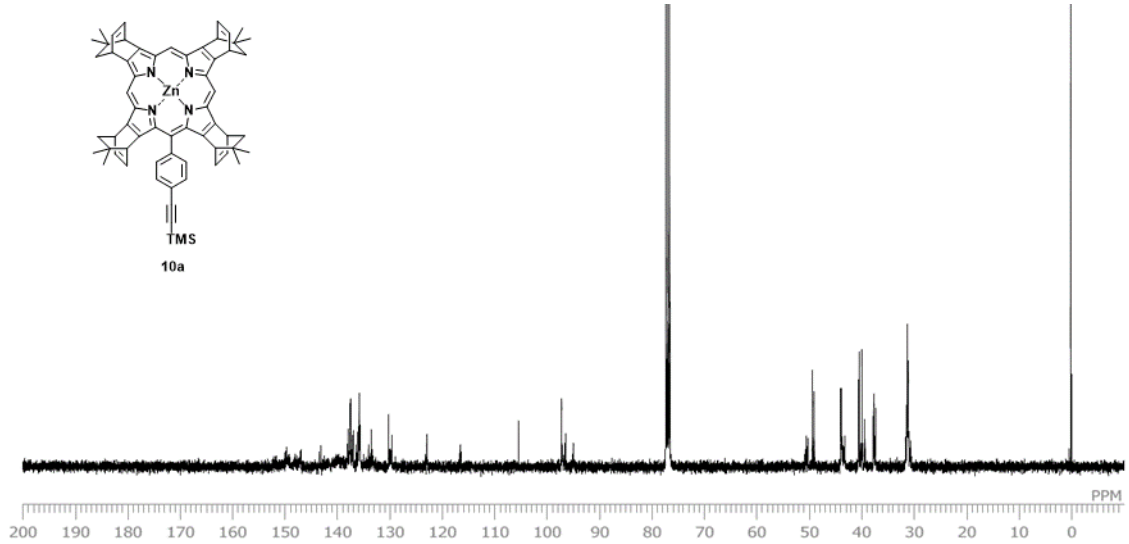

Figure S2-9-2. ^{13}C NMR spectrum of **10a** in $CDCl_3$. (Minor peaks are occasionally observed alongside of the main peaks, which are presumably from the structural isomers differing in the orientation of dimethyl-bicycle[2.2.2]octadieno-units. The minor peaks are also listed in the spectroscopic characterization data above.)

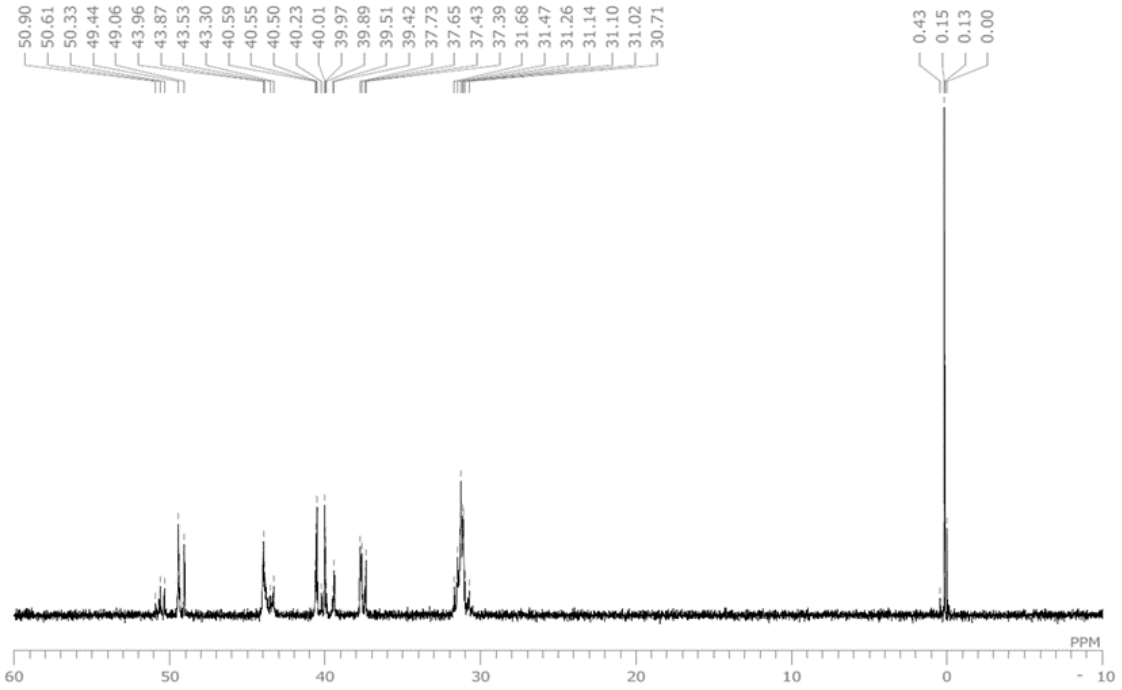

Figure S2-9-3. ^{13}C NMR spectrum of **10a** in $CDCl_3$ (−10–60 ppm).

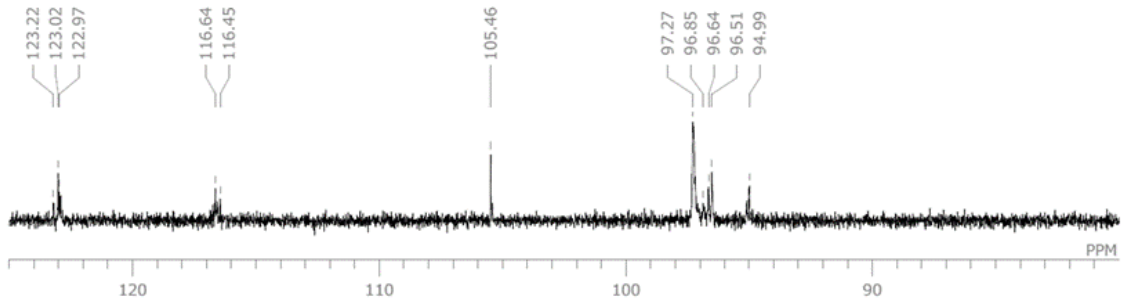

Figure S2-9-4. ^{13}C NMR spectrum of **10a** in $CDCl_3$ (80–125 ppm).

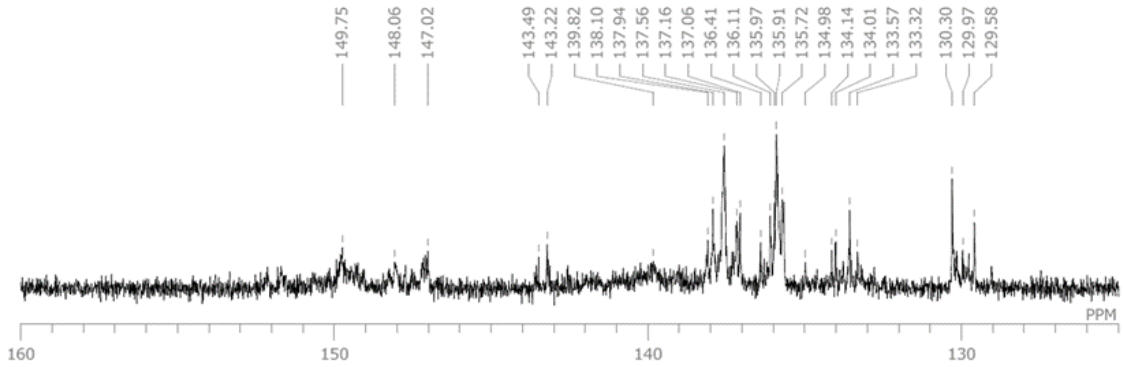

Figure S2-9-5. ^{13}C NMR spectrum of **10a** in $CDCl_3$ (125–160 ppm).

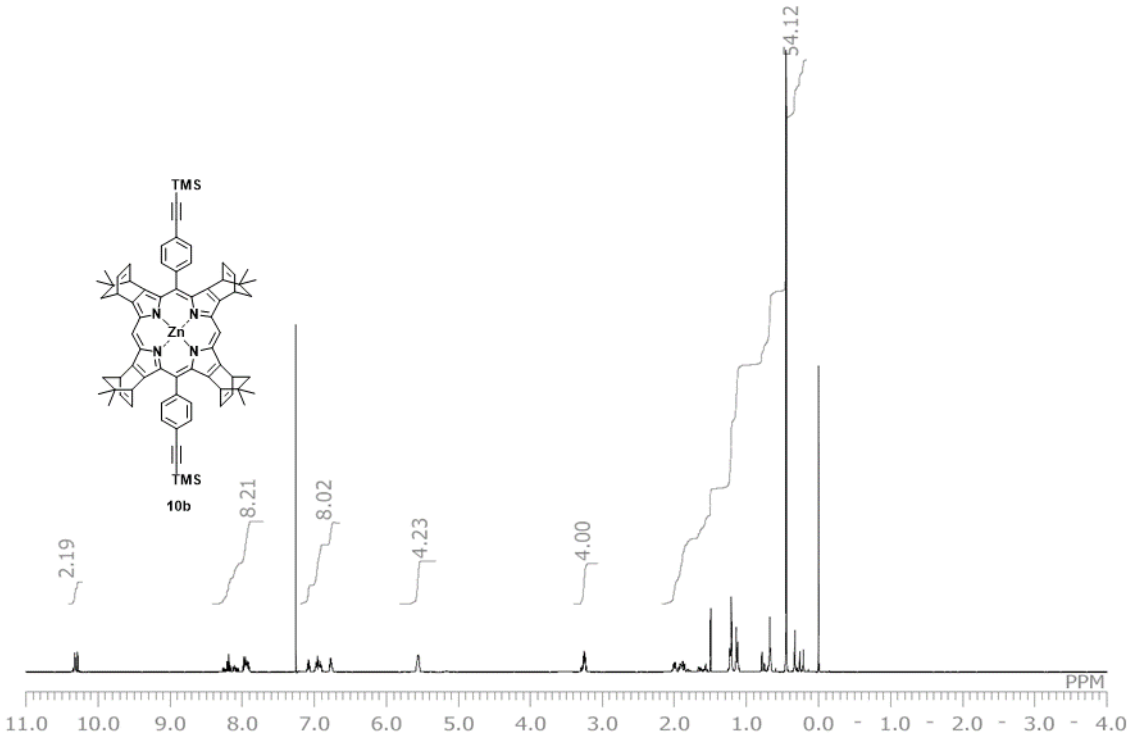

Figure S2-10-1. ^{1}H NMR spectrum of **10b** in $CDCl_3$.

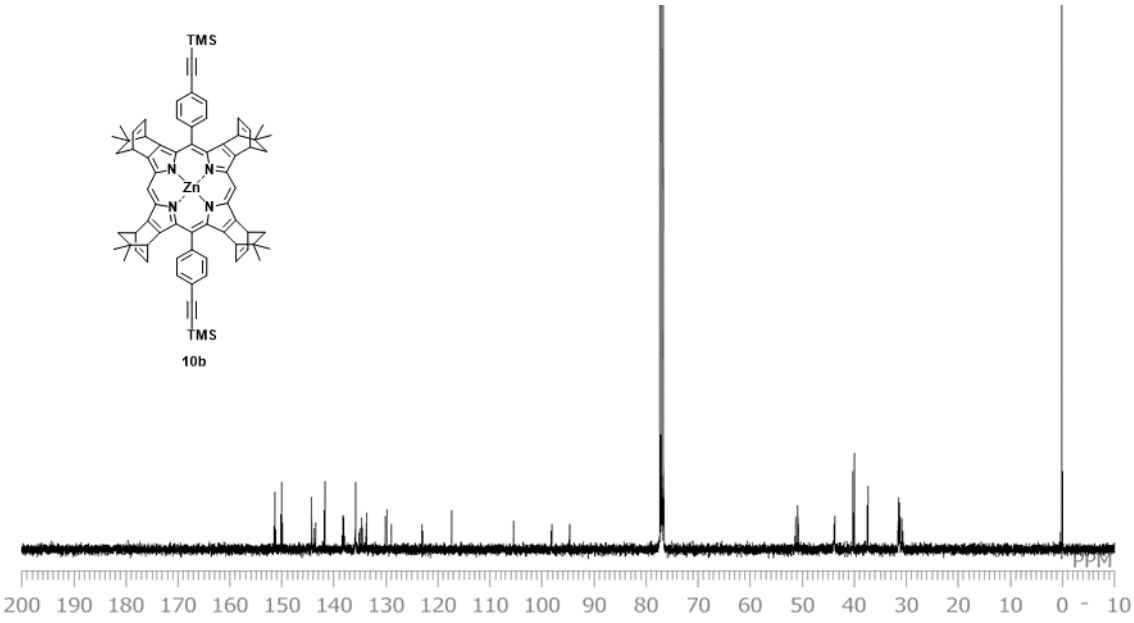

Figure S2-10-2. ^{13}C NMR spectrum of **10b** in $CDCl_3$. (Minor peaks are occasionally observed alongside of the main peaks, which are presumably from the structural isomers differing in the orientation of dimethyl-bicycle[2.2.2]octadieno-units. The minor peaks are also listed in the spectroscopic characterization data above.)

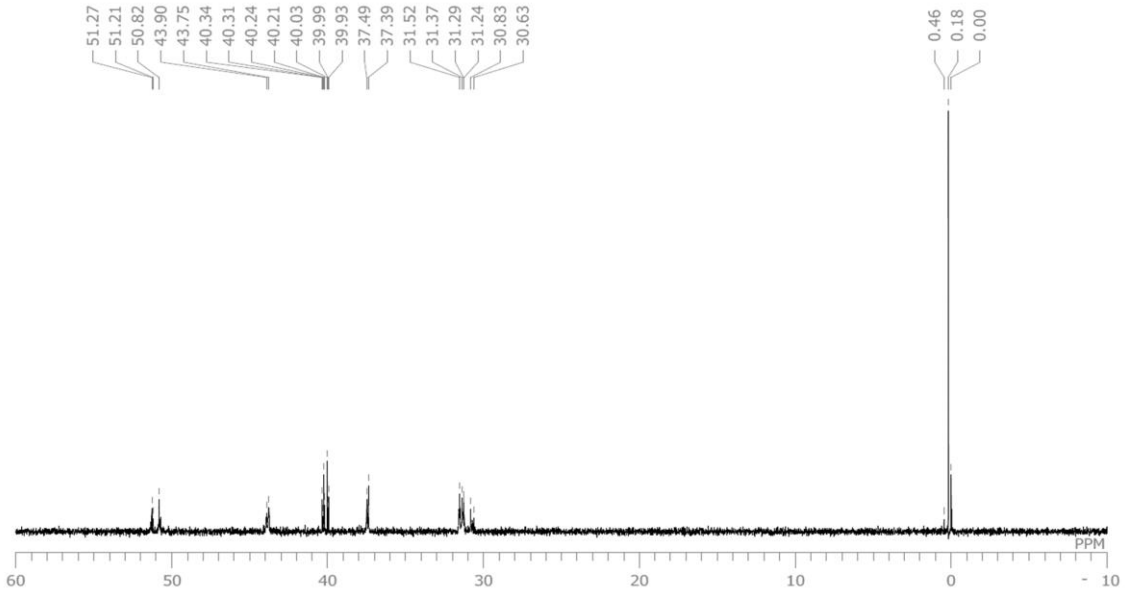

Figure S2-10-3. ^{13}C NMR spectrum of **10b** in $CDCl_3$ (−10–60 ppm).

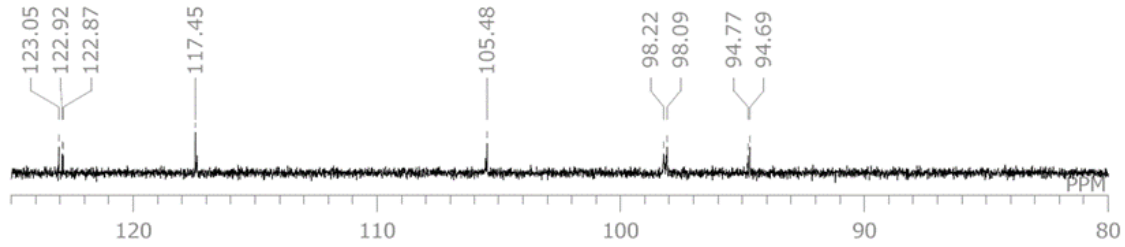

Figure S2-10-4. ^{13}C NMR spectrum of **10b** in $CDCl_3$ (80–125 ppm).

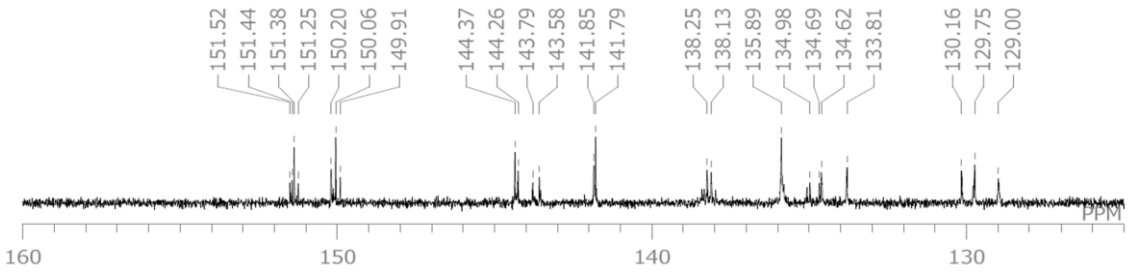

Figure S2-10-5. ^{13}C NMR spectrum of **10b** in $CDCl_3$ (125–160 ppm).

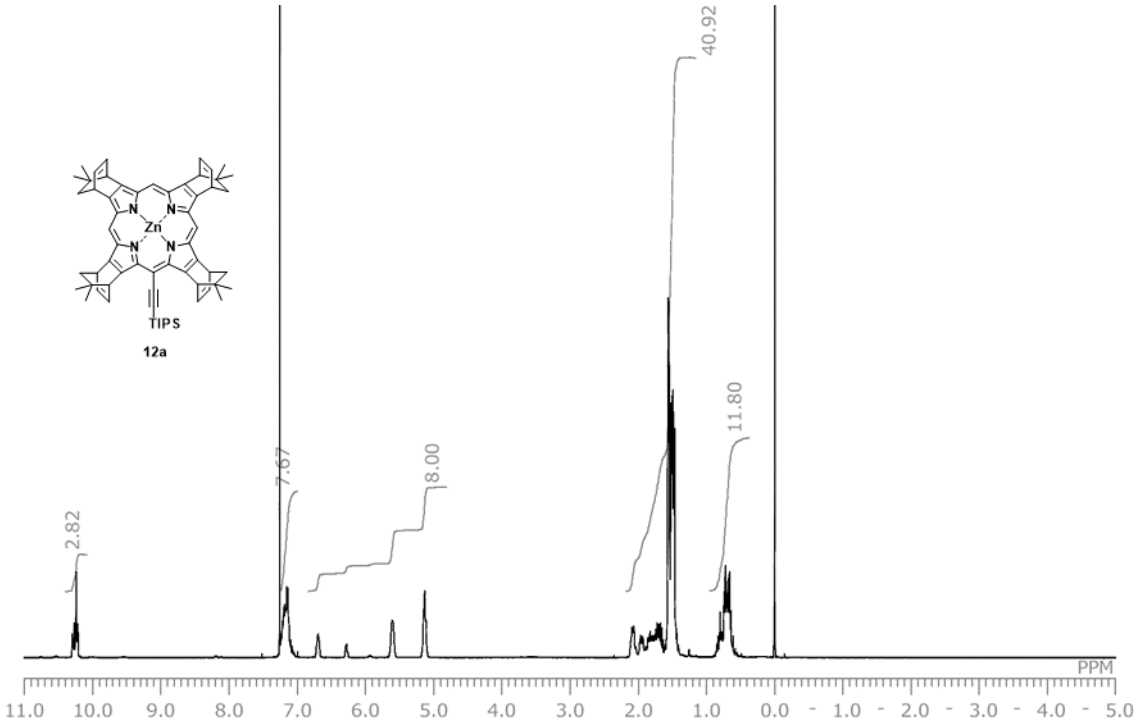

Figure S2-11-1. ^{1}H NMR spectrum of **12a** in $CDCl_3$.

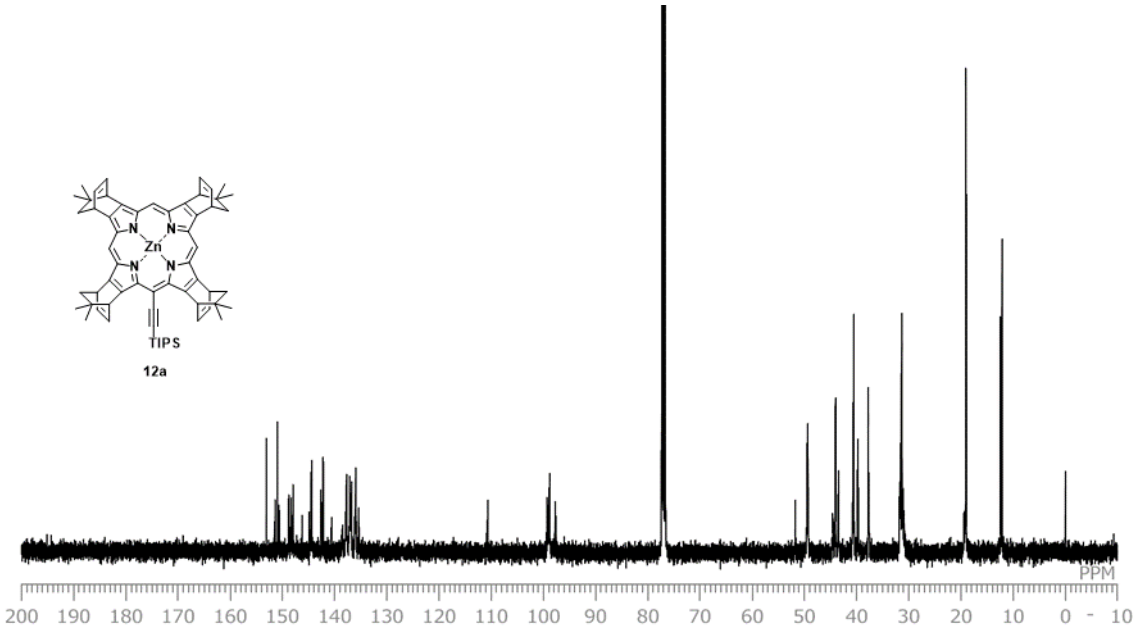

Figure S2-11-2. ^{13}C NMR spectrum of **12a** in $CDCl_3$. (Minor peaks are occasionally observed alongside of the main peaks, which are presumably from the structural isomers differing in the orientation of dimethyl-bicycle[2.2.2]octadieno-units. The minor peaks are also listed in the spectroscopic characterization data above.)

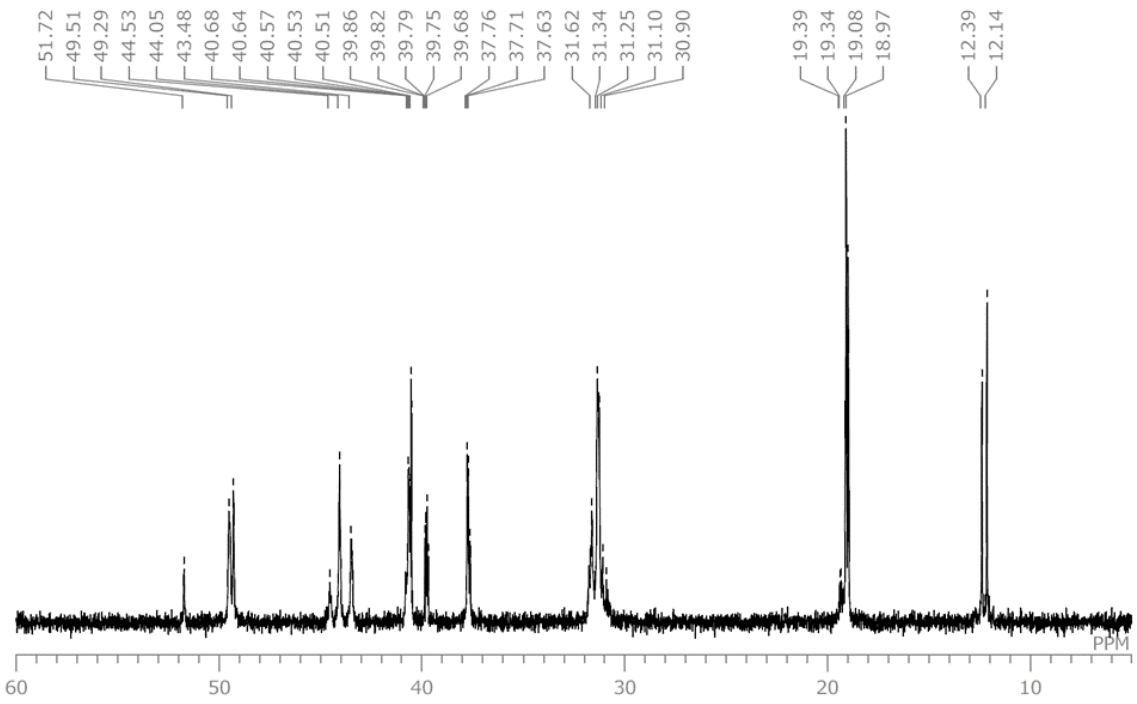

Figure S2-11-3. ^{13}C NMR spectrum of **12a** in $CDCl_3$ (5–60 ppm)

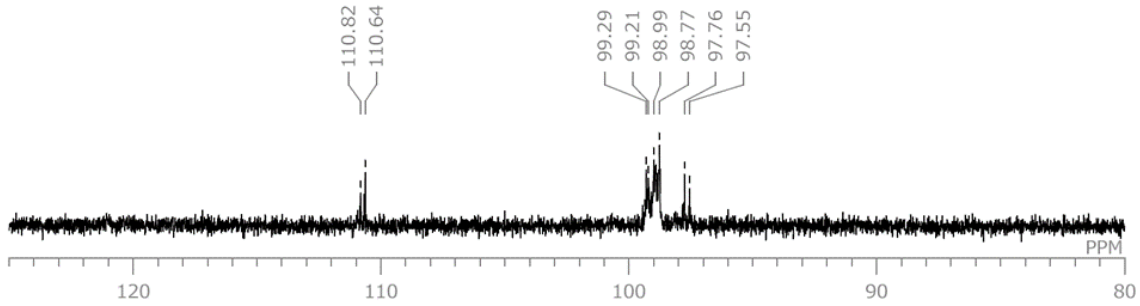

Figure S2-11-4. ^{13}C NMR spectrum of **12a** in $CDCl_3$ (80–125 ppm)

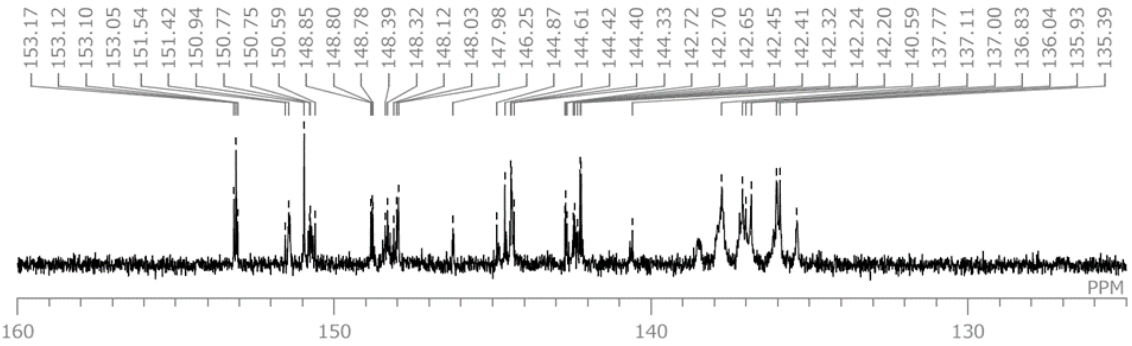

Figure S2-11-5. ^{13}C NMR spectrum of **12a** in $CDCl_3$ (125–160 ppm)

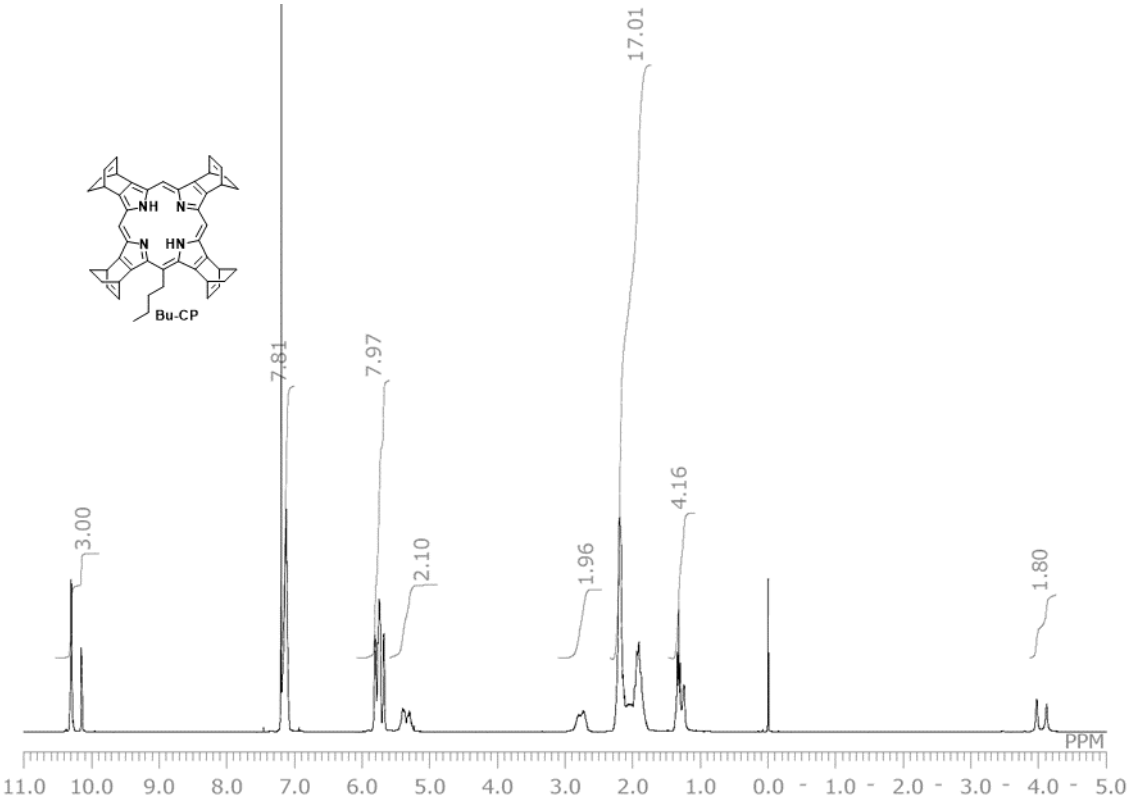

Figure S2-12-1. ^{1}H NMR spectrum of **Bu-CP** in $CDCl_3$.

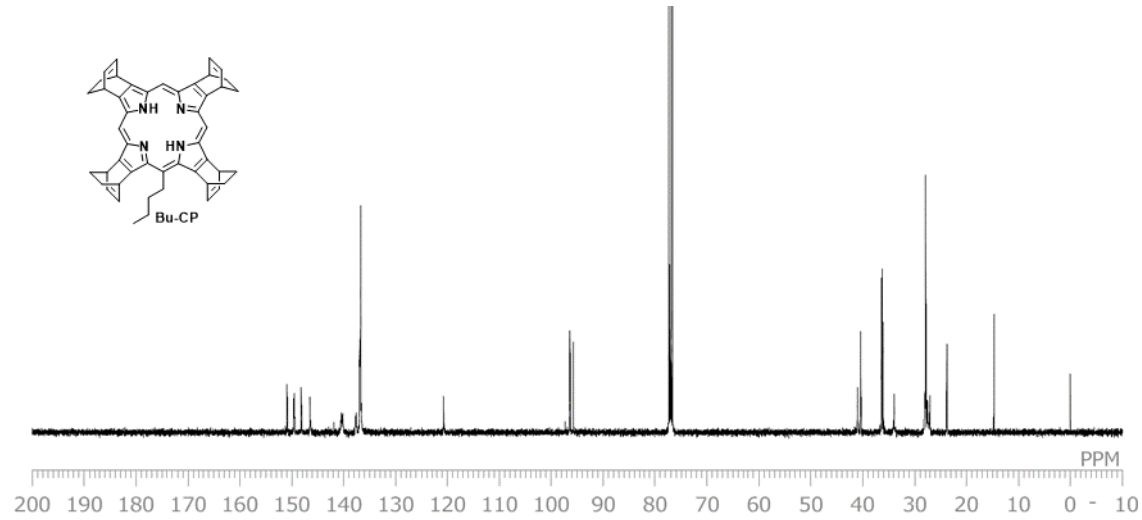

Figure S2-11-2. ^{13}C NMR spectrum of **12a** in $CDCl_3$. (Minor peaks are occasionally observed alongside of the main peaks, which are presumably from the structural isomers differing in the orientation of dimethyl-bicycle[2.2.2]octadieno-units. The minor peaks are also listed in the spectroscopic characterization data above.)

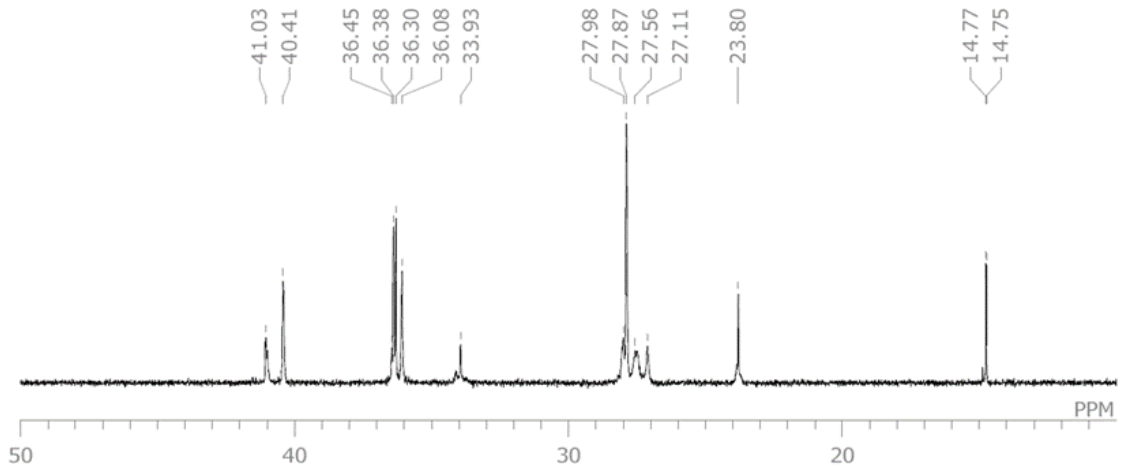

Figure S2-12-3. ^{13}C NMR spectrum of **Bu-CP** in $CDCl_3$ (10–50 ppm)

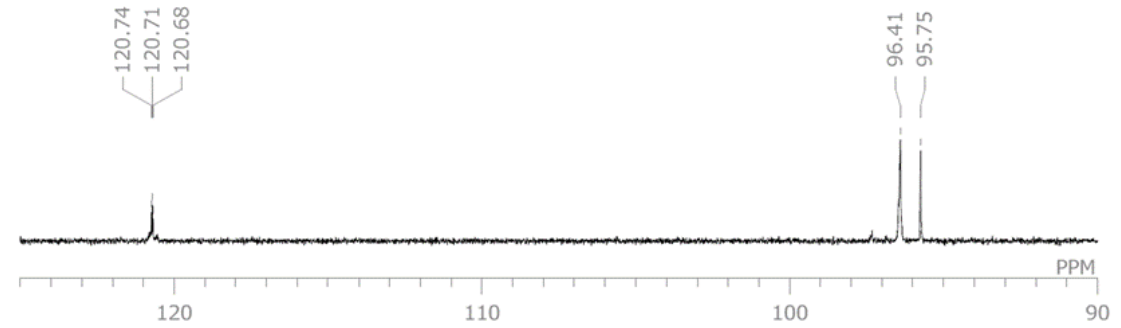

Figure S2-12-4. ^{13}C NMR spectrum of **Bu-CP** in $CDCl_3$ (90–125 ppm)

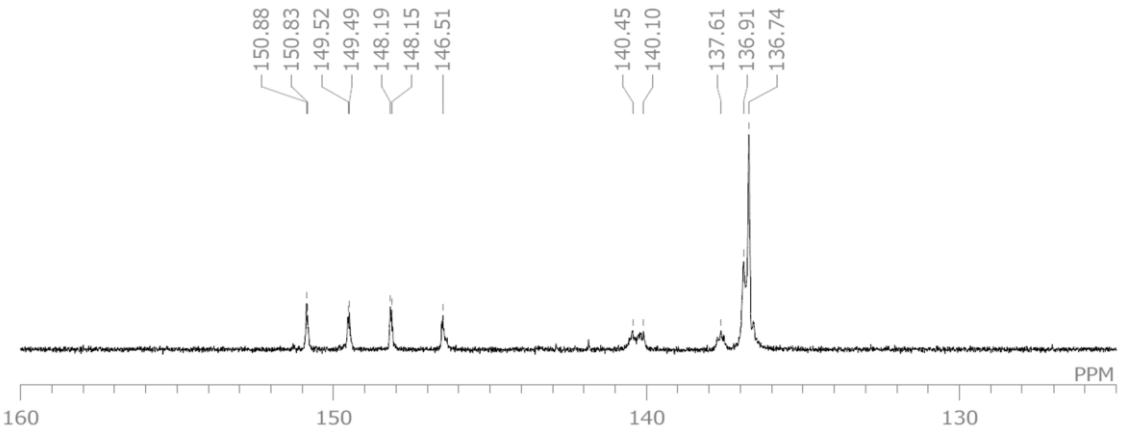

Figure S2-12-5. ^{13}C NMR spectrum of **Bu-CP** in $CDCl_3$ (125–160 ppm)

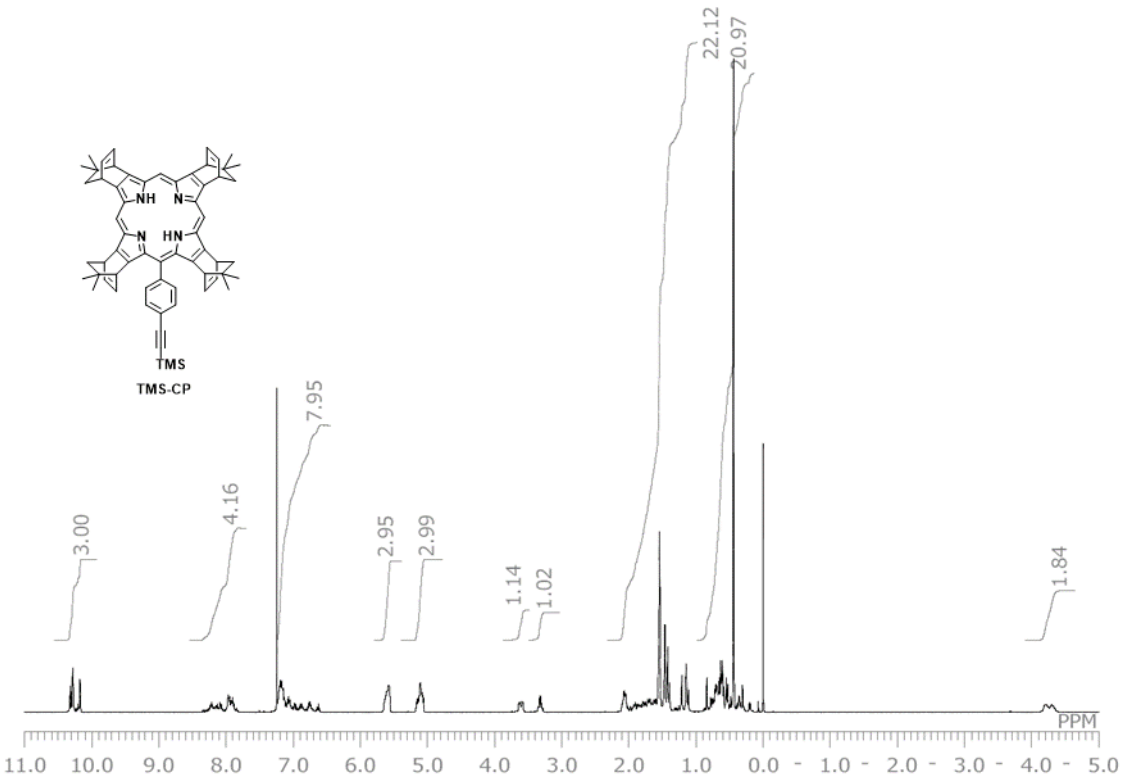

Figure S2-13-1. ^{1}H NMR spectrum of **TMS-CP** in $CDCl_3$.

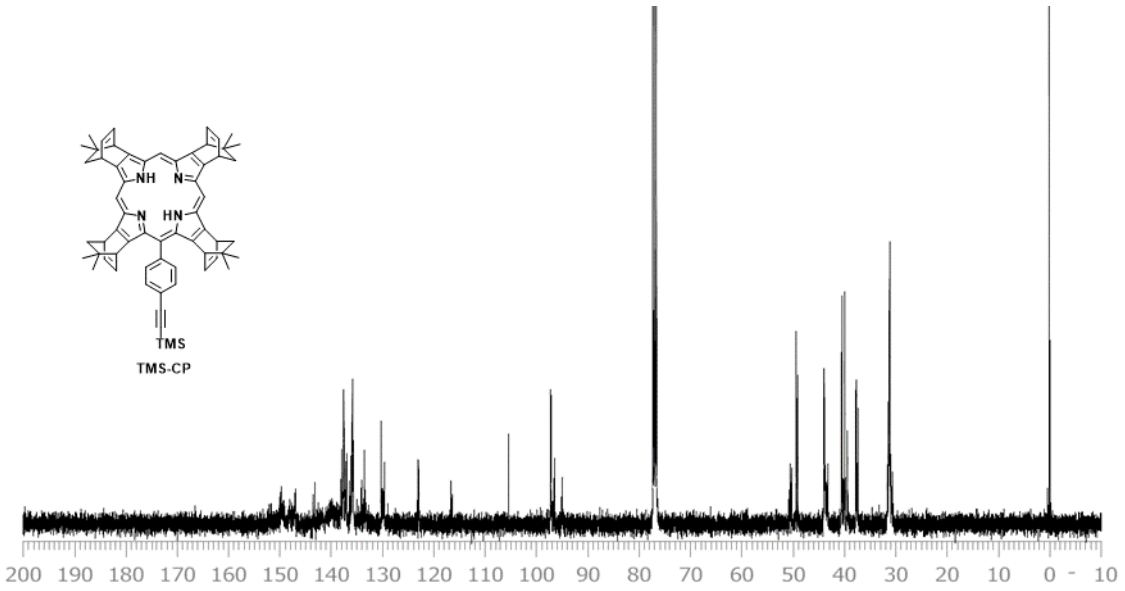

Figure S2-13-2. ^{13}C NMR spectrum of **TMS-CP** in $CDCl_3$. (Minor peaks are occasionally observed alongside of the main peaks, which are presumably from the structural isomers differing in the orientation of dimethyl-bicycle[2.2.2]octadieno-units. The minor peaks are also listed in the spectroscopic characterization data above.)

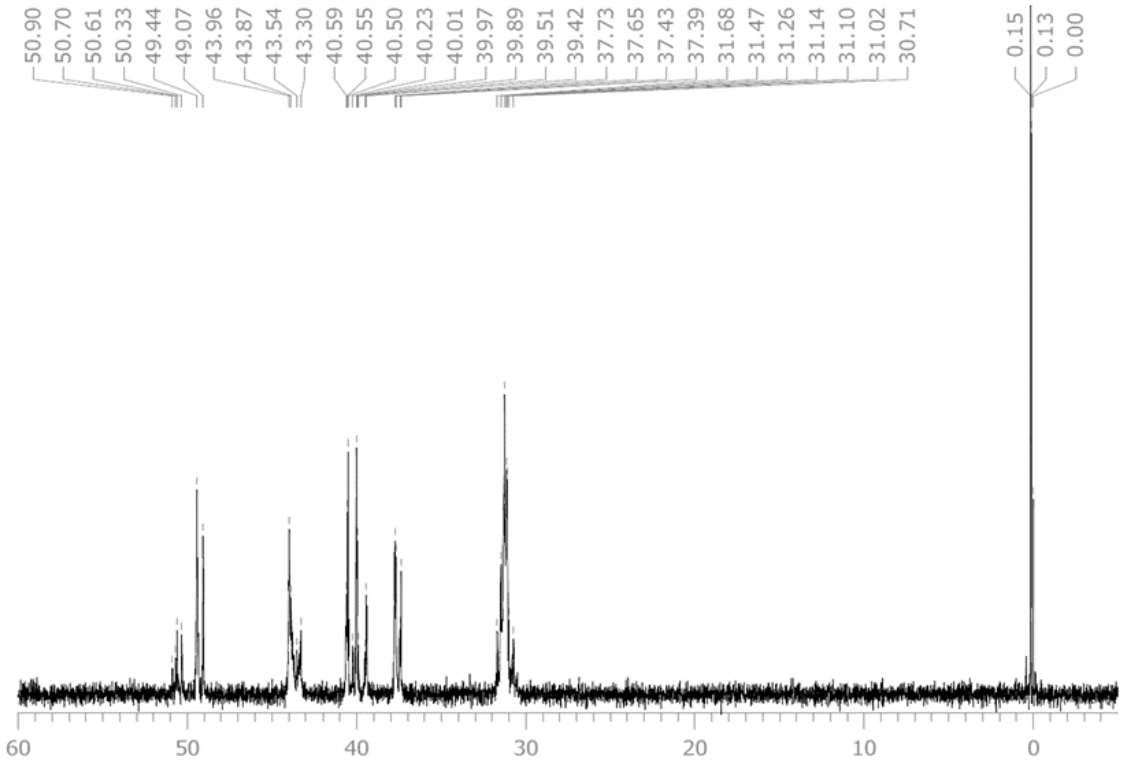

Figure S2-13-3. ^{13}C NMR spectrum of **TMS-CP** in $CDCl_3$ (−5–60 ppm)

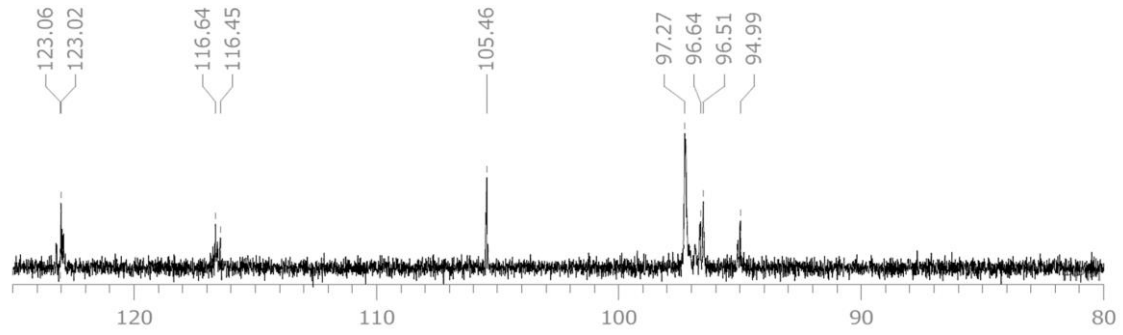

Figure S2-13-4. ^{13}C NMR spectrum of **TMS-CP** in $CDCl_3$ (80–125 ppm)

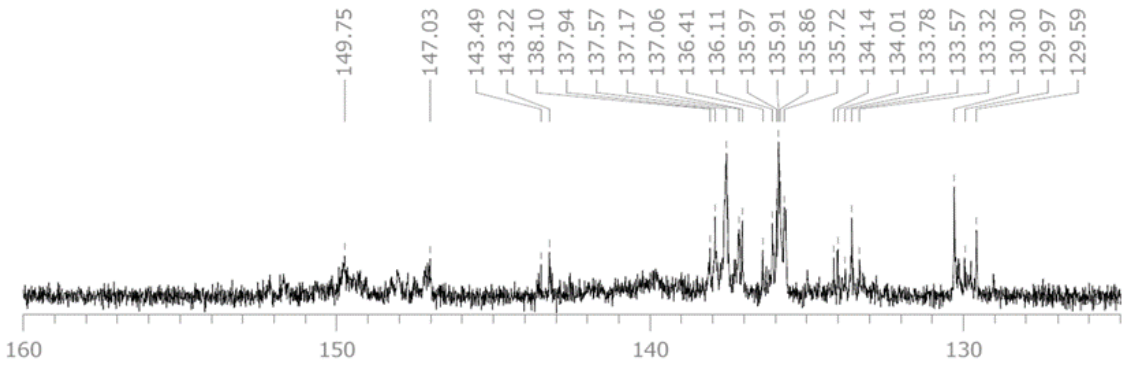

Figure S2-13-5. ^{13}C NMR spectrum of **TMS-CP** in $CDCl_3$ (125–160 ppm)

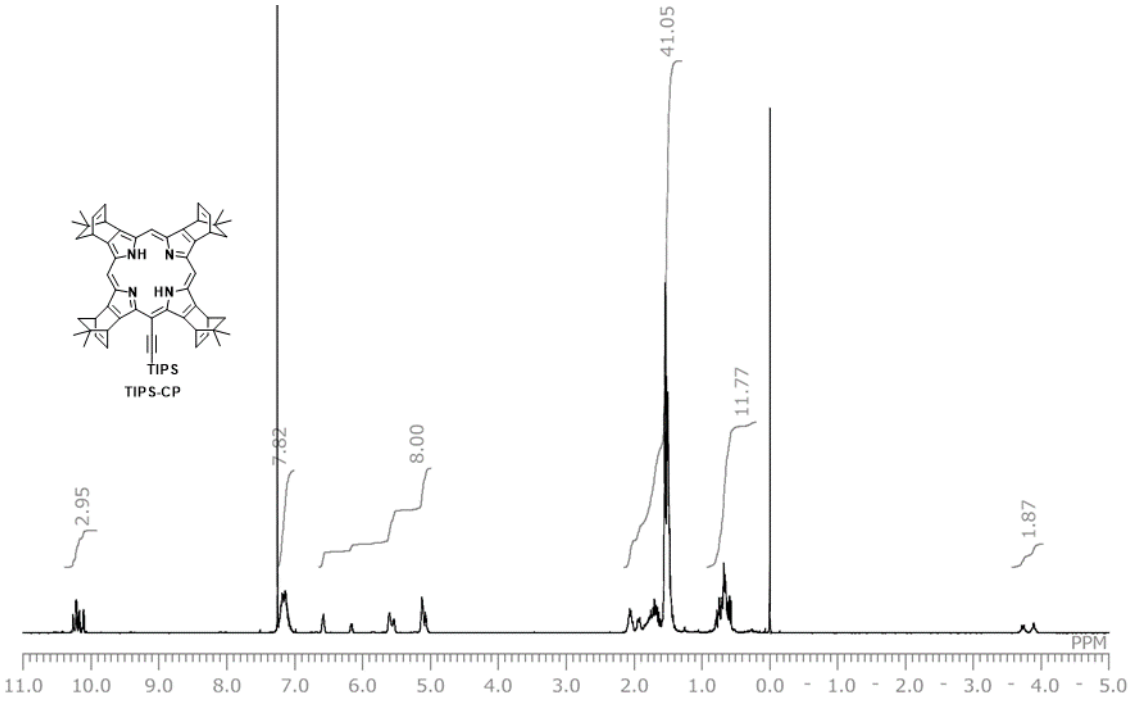

Figure S2-14-1. ^{1}H NMR spectrum of **TIPS-CP** in $CDCl_3$.

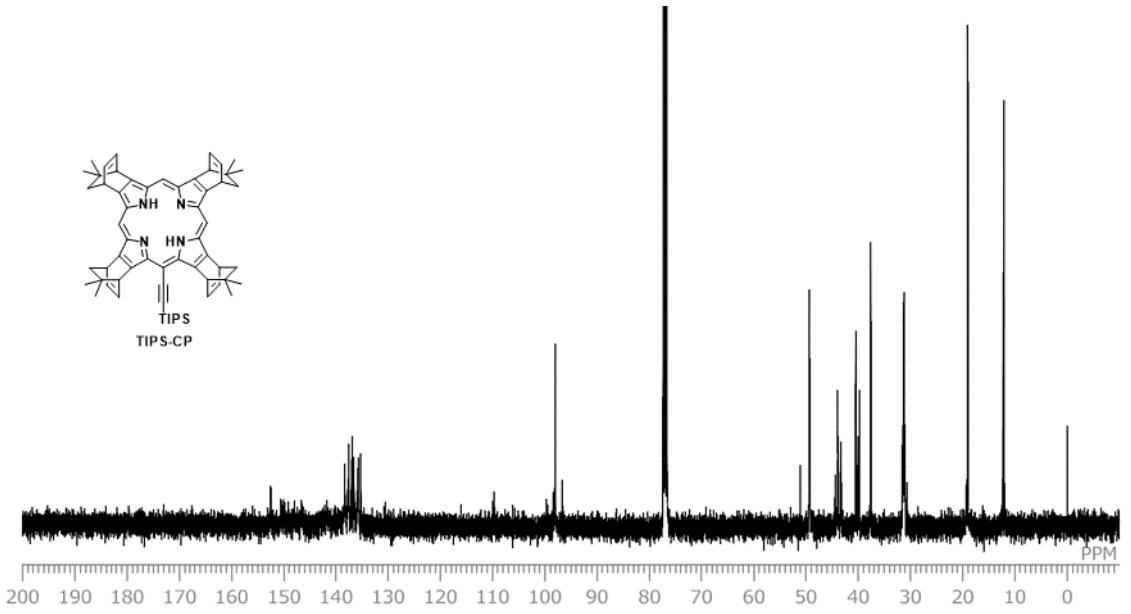

Figure S2-14-2. ^{13}C NMR spectrum of **TIPS-CP** in $CDCl_3$. (Minor peaks are occasionally observed alongside of the main peaks, which are presumably from the structural isomers differing in the orientation of dimethyl-bicycle[2.2.2]octadieno-units. The minor peaks are also listed in the spectroscopic characterization data above.)

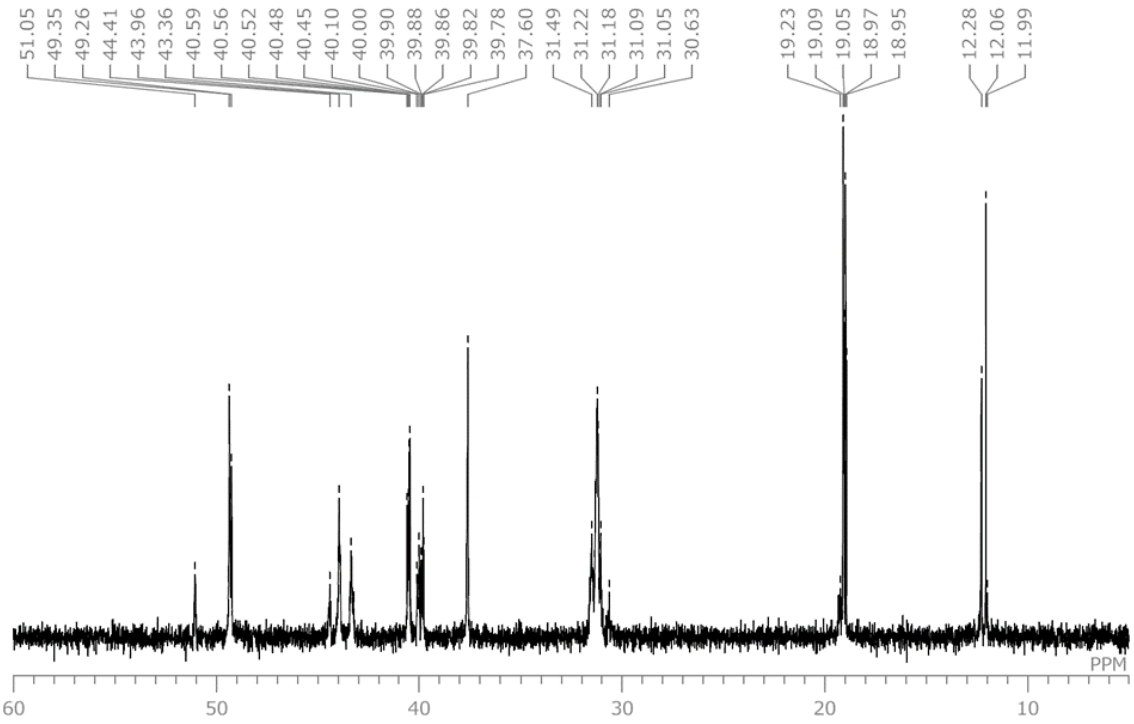

Figure S2-14-3. ^{13}C NMR spectrum of **TIPS-CP** in $CDCl_3$ (5–60 ppm)

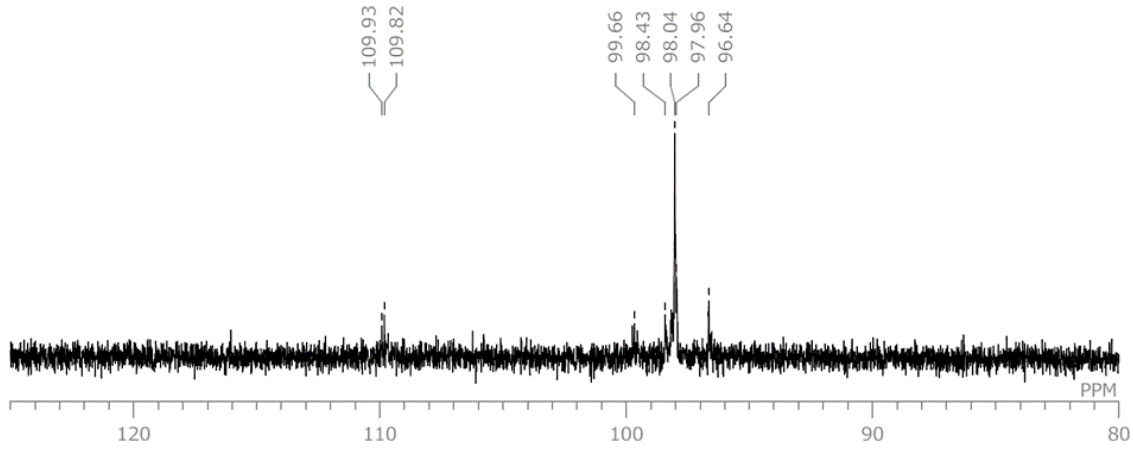

Figure S2-14-4. ^{13}C NMR spectrum of **TIPS-CP** in $CDCl_3$ (80–125 ppm)

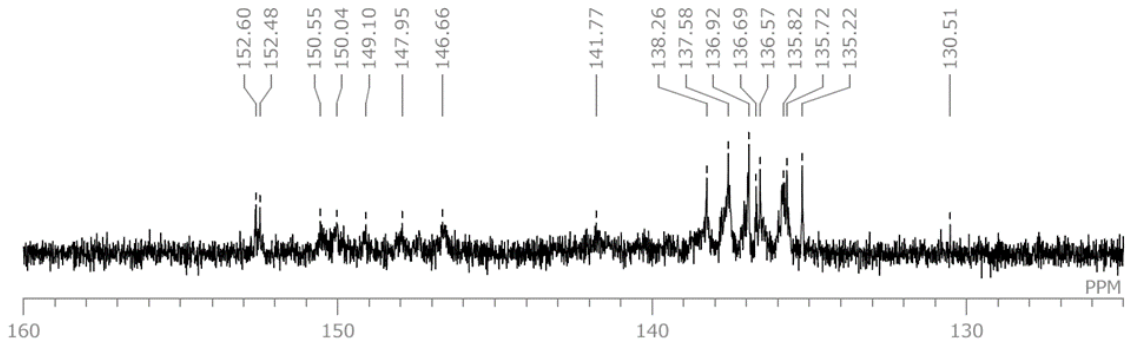

Figure S2-14-5. ^{13}C NMR spectrum of **TIPS-CP** in $CDCl_3$ (125–160 ppm)

2-9. References

(1) Ito, S.; Murashima, T.; Ono, N.; Uno, H. A new synthesis of benzoporphyrins using 4,7-dihydro-4,7-ethano-*2H*-isoindole as a synthon of isoindole. *Chem. Commun.* **1998**, 16, 1661–1662.

(2) Okujima, T.; Hashimoto, Y.; Jin, G.; Yamada, H.; Uno, H.; Ono, N. Synthesis of extremely soluble precursors of tetrabenzoporphyrins. *Tetrahedron* **2008**, *64*, 2405–2411.

(3) Ito, S.; Uno, H.; Murashima, T.; Ono, N. Synthesis of benzoporphyrins functionalized with octaester groups. *Tetrahedron Letters* **2001**, *42*, 45–47.

(4) Dhoot, A. S.; Aramaki, S.; Moses, D.; Heeger, A. J. Metal-Insulator Transition in Solution-Processible Porphyrinic Field-Effect Transistors. *Adv Mater* **2007**, *19*, 2914–2918.

(5) Shea, P. B.; Yamada, H.; Ono, N.; Kanicki, J. Solution-processed zinc tetrabenzoporphyrin thin-films and transistors. *Thin Solid Films* **2012**, *520*, 4031–4035.

(6) Noguchi, N.; Junwei, S.; Asatani, H.; Matsuoka, M. Control of Morphology and Orientation of a Thin Film Tetrabenzoporphyrin (TBP) Organic Semiconductor by Solid-State Crystallization. *Crystal Growth and Design* **2010**, *10*, 1848–1853.

(7) Shea, P. B.; Kanicki, J.; Pattison, L. R.; Petroff, P.; Kawano, M.; Yamada, H.; Ono, N. Solution-processed nickel tetrabenzoporphyrin thin-film transistors. *J. Appl. Phys.* **2006**, *100*, 034502.

(8) Guide, M.; Dang, X. D.; Nguyen, T. Q. Nanoscale Characterization of Tetrabenzoporphyrin and Fullerene-Based Solar Cells by Photoconductive Atomic Force Microscopy. *Adv. Mater.* **2011**, *23*, 2313–2319.

(9) Takahashi, K.; Kumagai, D.; Yamada, N.; Kuzuhara, D.; Yamaguchi, Y.; Aratani, N.; Koganezawa, T.; Koshika, S.; Yoshimoto, N.; Masuo, S.; Suzuki, M.; Nakayama, K.; Yamada, H. Side-chain engineering in a thermal precursor approach for efficient photocurrent generation. *J. Mater. Chem. A* **2017**, *5*, 14003–14011.

(10) Takahashi, K.; Shan, B.; Xu, X.; Yang, S.; Koganezawa, T.; Kuzuhara, D.; Aratani, N.; Suzuki, M.; Miao, Q.; Yamada, H. Engineering Thin Films of a Tetrabenzoporphyrin toward Efficient Charge-Carrier Transport: Selective Formation of a Brickwork Motif. *ACS Appl. Mater. and Interfaces* **2017**, *9*, 8211–8218.

(11) Takahashi, K.; Yamada, N.; Kumagai, D.; Kuzuhara, D.; Suzuki, M.; Yamaguchi, Y.; Aratani, N.; Nakayama, K.; Yamada, H. Effect of alkyl substituents: 5,15-bis(trimethylsilylethynyl) *vs*. 5,15-bis(triisopropylsilylethynyl)- tetrabenzoporphyrins and their metal complexes. *J. Porphyrins Phthalocyanines* **2015**, *19*, 465–478.

(12) Ito, S.; Phong, L. T.; Komatsu, T.; Igarashi, N.; Otsubo, S.; Sakai, Y.; Ohno, A.; Aramaki, S.; Tanaka, Y.; Uno, H.; Oba, T.; Hiratani, K. First Synthesis of *meso*-Chlorinated Tetrabenzoporphyrins. *Eur. J. Org. Chem.* **2009**, 31, 5373–5382.

(13) Ryppa, C.; Senge, M. O.; Hatscher, S. S.; Kleinpeter, E.; Wacker, P.; Schilde, U.; Wiehe, A. Synthesis of Mono- and Disubstituted Porphyrins: A- and 5,10-A_2-Type Systems. *Chem. Eur. J.* **2005**, *11*, 3427–3442.

(14) Rowland, G. B.; Barnett, K.; Dupont, J. I.; Akurathi, G.; Le, V. H.; Lewis, E. A. The effect of pyridyl substituents on the thermodynamics of porphyrin binding to G-quadruplex DNA.

Bioorg. Med. Chem. **2013**, *21*, 7515–7522.

(15) Fan, D.; Taniguchi, M.; Yao, Z.; Dhanalekshmi, S.; Lindsey, J. S. 1,9-Bis(*N*,*N*-dimethylaminomethyl)dipyrromethanes in the synthesis of porphyrins bearing one or two *meso* Substituents. *Tetrahedron* **2005**, *61*, 10291–10302.

(16) Dogutan, D. K.; Ptaszek, M.; Lindsey, J. S. Rational or Statistical Routes from 1-Acyldipyrromethanes to *meso*-Substituted Porphyrins. Distinct Patterns, Multiple Pyridyl Substituents, and Amphipathic Architectures. *J. Org. Chem.* **2008**, *73* , 6187–6201.

(17) Otte, F. L.; Lemke, S.; Schütt, C.; Krekiehn, N. R.; Jung, U.; Magnussen, O. M.; Herges, R. Ordered Monolayers of Free-Standing Porphyrins on Gold. *J. Am. Chem. Soc.* **2014**, *136*, 11248–11251.

(18) Saltsman, I.; Goldberg, I.; Balasz, Y.; Gross, Z. Porphine and pyrrole-substituted porphyrin from cyclocondensation of tripyrrane with mono-substituted pyrroles. *Tetrahedron Letters* **2007**, *48*, 239–244.

(19) Saltsman, I.; Gross, Z. Microwave-Assisted Synthesis of non-substituted tripyrrane, tetrapyrrane and pentapyrrane. *Tetrahedron Letters* **2008**, *49*, 247–249.

(20) Feng, X.; Bischoff, I.; Senge, M. O. Mechanistic Studies on the Nucleophilic Reaction of Porphyrins with Organolithium Reagents. *J. Org. Chem.* **2001**, *66*, 8693–8700.

(21) Senge, M. O. Nucleophilic Substitution as a Tool for the Synthesis of Unsymmetrical Porphyrins. *Acc. Chem. Res.* **2005**, *38*, 733–743.

(22) Liu, P. P.; Feng, Y. Q.; Gu, C. Z.; Meng, S. X.; Zhang, B. The facile synthesis of 5-formylporphyrin. *Chinese Chemical Letters* **2012**, *23*, 505–508.

(23) Yamada, H.; Kushibe, K.; Okujima, T.; Uno, H.; Ono, N. Novel one-pot synthesis of 5-alkenyl-15-alkynylporphyrins and their derivatisation to a butadiyne-linked benzoporphyrin dimer. *chem. commun.* **2006**, *42*, 383–390.

(24) Hickmann, V.; Kondoh, A.; Gabor, B.; Alcarazo, M.; Fürstner, A. Catalysis-Based and Protecting-Group-Free Total Syntheses of the Marine Oxylipins Hybridalactone and the Ecklonialactones A, B, and C. *J. Am. Chem. Soc.* **2011**, *133*, 13471–13480.

(25) Aakeröy, C. B.; Sinha, A. S.; Epa, K. N.; Spartz, C. L.; Desper, J. A versatile and green mechanochemical route for aldehyde–oxime conversions. *Chem. Commun.* **2012**, *48*, 11289–11291.

Chapter 3.

Development of Donor–Acceptor Systems with Thermal Precursor Approach for Solution-Processed Organic Solar Cells

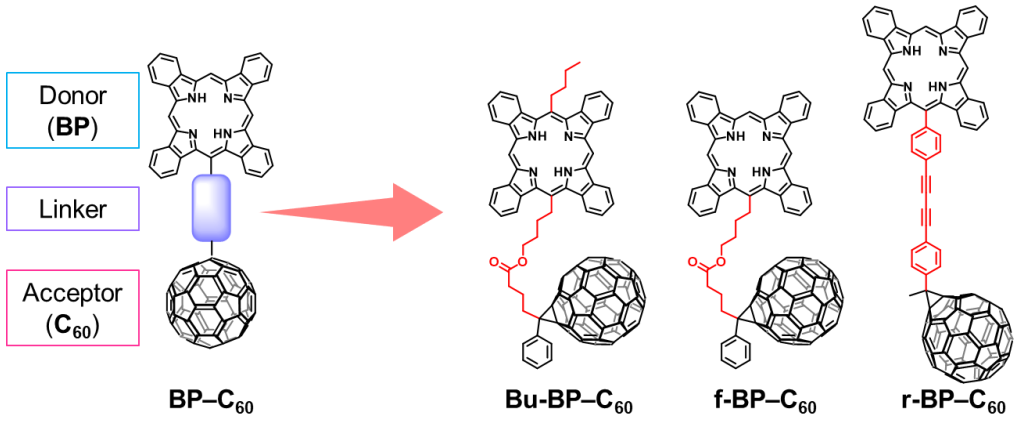

This chapter focuses on the development of covalently linked donor–acceptor (D–A) molecules, tetrabenzoporphyrin (BP)–fullerene (C_{60}) dyads as OSCs materials.

In the first effort, direct comparison of BP–C_{60} dyad and a 1:1 mixture of BP and C_{60} as organic photovoltaic materials is described. In the second effort, to investigate the effect of the covalent connection of the donor and acceptor units on the film morphology and on the OPV performances, the BP and fullerene units were connected by a flexible or rigid linker (f-BP–C_{60} or r-BP–C_{60}). These systematic investigations provide the proof that covalently-linked D–A system can be one of the strong way to improve the miscibility of BP and $PC_{61}BM$ with a construction of modified surface for layer-by-layer structure, and the flexibility of the linker between the BP and C_{60} units is important to design the BP–C_{60} system as active-layer materials.

3-1. Introduction

As the author mentioned in Chapter 1, BP has a substantial potential for realization of practical use of OSCs. However, the poor miscibility with fullerene derivatives should be improved to form proper phase separation in an active layer. This chapter focused on covalently-linked D–A molecular system to control a phase-separation structure of BP. Several types of covalently linked D–A molecules have been reported as active-layer materials for single component OSCs with better miscibility than the blended system.[1–11] However, they have still been underdeveloped in the OSC community compared to blended component system, probably because of the scarce systematically examined knowledges. In fact, covalent D–A molecule materials which were investigated with various linker structures for the same donor and acceptor units have been scarce to date. In addition, no p–i–n-type device with a covalent D–A molecule has been reported as far as we know, although the employment of the p–i–n structure may lead to enhanced efficiencies.

In the meantime, effective synthetic routes for unsymmetrical *meso*-substituted BPs have been established in the Chapter 2. By using this knowledge, fullerene-linked tetrabenzoporphyrin (BP–C_{60}) was designed as original D–A system for OSCs material as described in Chapter 1. Although BP–C_{60} might be hardy soluble in the organic solvents, it can be deposited by solution process without losing the solution-processability via its soluble precursor (CP–C_{60}). In addition, a three-layered p–i–n structure[12–14] achieving the vertical phase separation for an effective charge extraction can be prepared by solution process since the conversion from the CP to BP involves solubility decrease, owing to the structural change.

In this chapter, two systematized investigations were performed to discuss BP–C_{60} systems as OSC materials. Concretely, the author performed (1) direct comparison of a covalently-linked BP–C_{60} molecule and a 1:1 mixture of BP and C_{60} as organic photovoltaic materials and (2) investigation of fullerene-linked tetrabenzoporphyrins for solution processed organic photovoltaics: flexible vs. rigid linkers. From the following section, the syntheses and photovoltaic performances of three types of covalent BP–C_{60} molecules with their optical- and electrical-properties will be described.

3-2. Direct Comparison of a Covalently-Linked BP–C_{60} Molecule and a 1:1 Mixture of BP and C_{60} as Organic Photovoltaic Materials

3-2-1. Molecular Design and Synthesis

Although thermal precursor of BP was first reported by Ono and co-workers in 1998[15], fullerene-linked CP or BP has not been scarcely reported. Thus, fullerene-linked 5-butyl-BP (Bu-BP–C_{60}) which has normal butyl on 5-popsition of BP and alkyl ester linker between BP and C_{60} was designed to obtain an enough solubility of the precursor (Bu-CP–C_{60}) for solution-process deposition as shown in Figure 2.

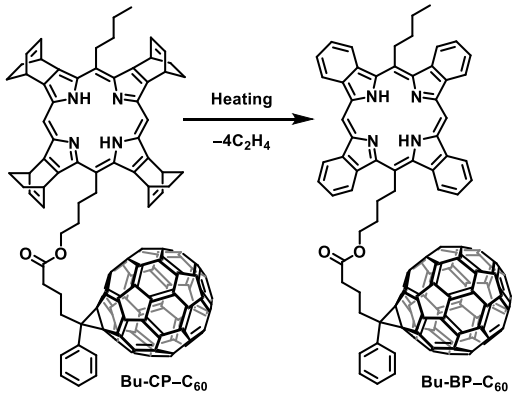

Figure 2. Chemical structures of Bu-CP–C_{60} and Bu-BP–C_{60}.

The synthetic route of Bu-CP–C_{60} is shown in Scheme 1 (see Experimental Section for practical reaction conditions and purifications). By taking a same condensation reaction in Chapter 1, the zinc porphyrin monoester **1** was prepared. Reduction of **1** by $LiAlH_4$ in 76% yield afforded the corresponding alcohol **2** and then coupling with [6,6]-phenyl-C_{61}-butyric acid **3**[8] did Bu-ZnCP–C_{60} in 64% yield. Bu-ZnCP–C_{60} was treated with trifluoroacetic acid (TFA) to afford Bu-CP–C_{60} in 86% yield. 5,15-Dibulyl-CP (DiBu-CP) was also prepared from dipyrrylmethane **4**[15] and *n*-pentanal **5** in 42% yield as a precursor of the reference compound 5,15-dibutylbenzoporphyrin (DiBu-BP). The CPs of Bu-CP–C_{60} and DiBu-CP were obtained as mixtures of stereo-isomers at the BCOD moieties. In thermogravimetric analyses (TGA), mass loss due to the retro-Deals–Alder (r-DA) reaction started at around 150 ºC and ended at around 200

ºC for both Bu-CP–C_{60} and DiBu-CP. The decreased weights corresponded well to four ethylene units per molecule as shown in Figure 3. Thus, quantitative thermal conversion from CP to BP unit was observed in both Bu-CP–C_{60} and DiBu-CP. Bu-BP–C_{60} showed lower decomposed temperature (320 ºC) than DiBu-BP (390 ºC). This might be attributed to the presence of reactive moieties such as flexible alkyl chain connected with ester group in Bu-BP–C_{60}. After the r-DA reaction, the MALDI spiral-TOF mass spectra of the obtained Bu-BP–C_{60} was in good agreement with the simulated values (Figure S3-1 and S3-2, Support information), and the solubility of the BP–C_{60} compounds was not enough for NMR measurement.

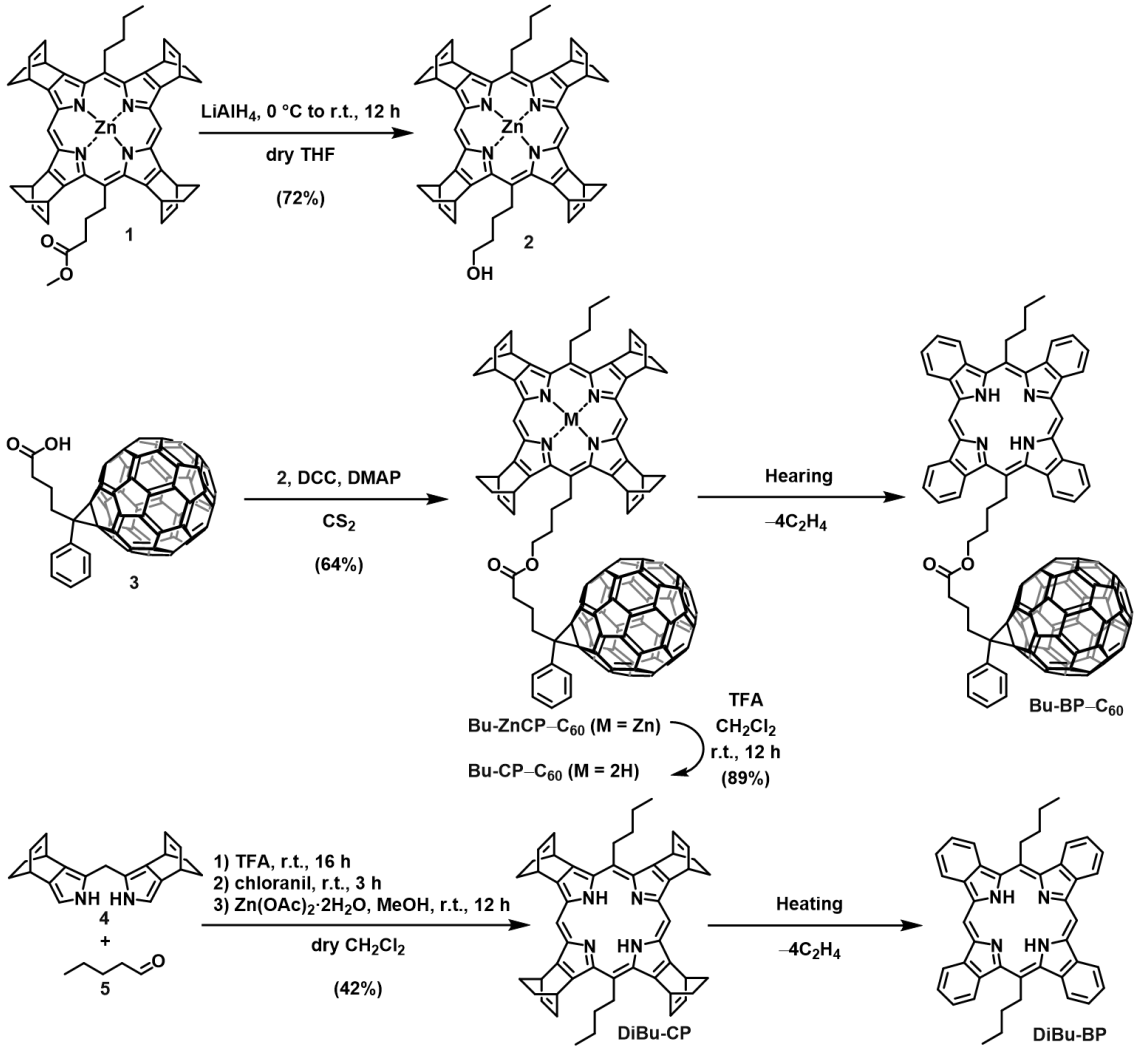

Scheme 1. Synthesis route of Bu-BP–C_{60} and DiBu-BP

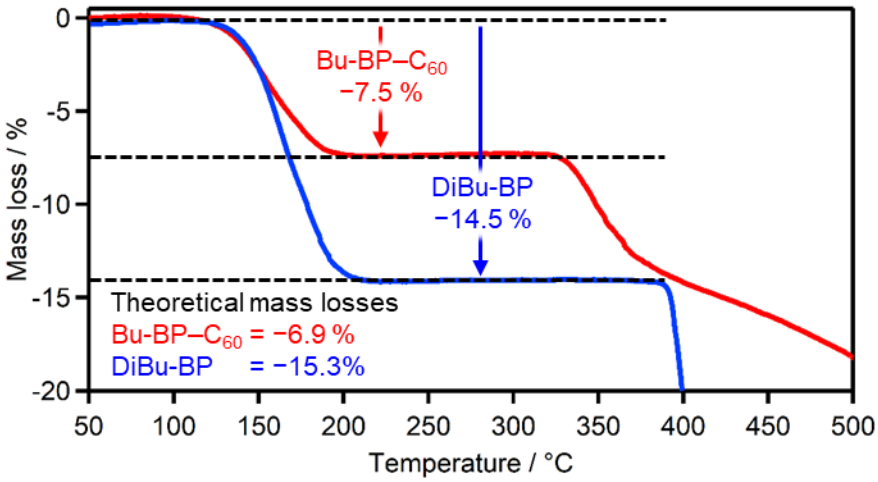

Figure 3. TGA curves of Bu-CP–C_{60} and DiBu-CP measured under nitrogen gas flowing with heatup time of 5 ºC min^{-1}.

3-2-2. Optical and Electronic Properties

The UV–vis absorption spectra of Bu-CP–C_{60} and Bu-BP–C_{60} in CH_2Cl_2 are shown in Figure 4. The spectrum of BP–C_{60} has peaks at 442, 573, 614 and 671 nm, which were red-shifted compared to the corresponding peaks of CP–C_{60} at 420, 512, 542 and 579 nm. These results also support the justified chemical transformation of CP–C_{60} to BP–C_{60} by r-DA reaction.

The spectrum of Bu-CP–C_{60} was compared to that of a 1:1 mixture of DiBu-CP and $PC_{61}BM$ as shown in Figure 4 (left side). The Soret peak of CP–C_{60} (420 nm) is red-shifted by 10 nm from that of DiBu-CP (410 nm) and broadened. The spectrum of CP–C_{60} does not show the concentration dependency; thus, the intramolecular interaction between the CP and C_{60} units might be the cause of the red shift and broadening. Similarly, the spectrum of Bu-BP–C_{60} showed the broadening and red shift of the Soret band compared to the spectrum of a 1:1 mixture of DiBu-BP and $PC_{61}BM$ (Figure 4, right side).

Fluorescence of Bu-CP–C_{60} and Bu-BP–C_{60} is quenched drastically compared to those of DiBu-CP and DiBu-BP as shown in Figure 5. The fluorescence quantum yields of Bu-CP–C_{60}, DiBu-CP, Bu-BP–C_{60} and DiBu-BP were 0.36, 3.1, 1.1 and 11.3%, respectively. This observation again suggests the existence of intramolecular interaction for the dyads in solution, where the C_{60} moiety can effectively quench the fluorescence from the porphyrin moiety through the photo-induced electron transfer[16–18]. This interaction must be enabled by the flexibility of the linkage.

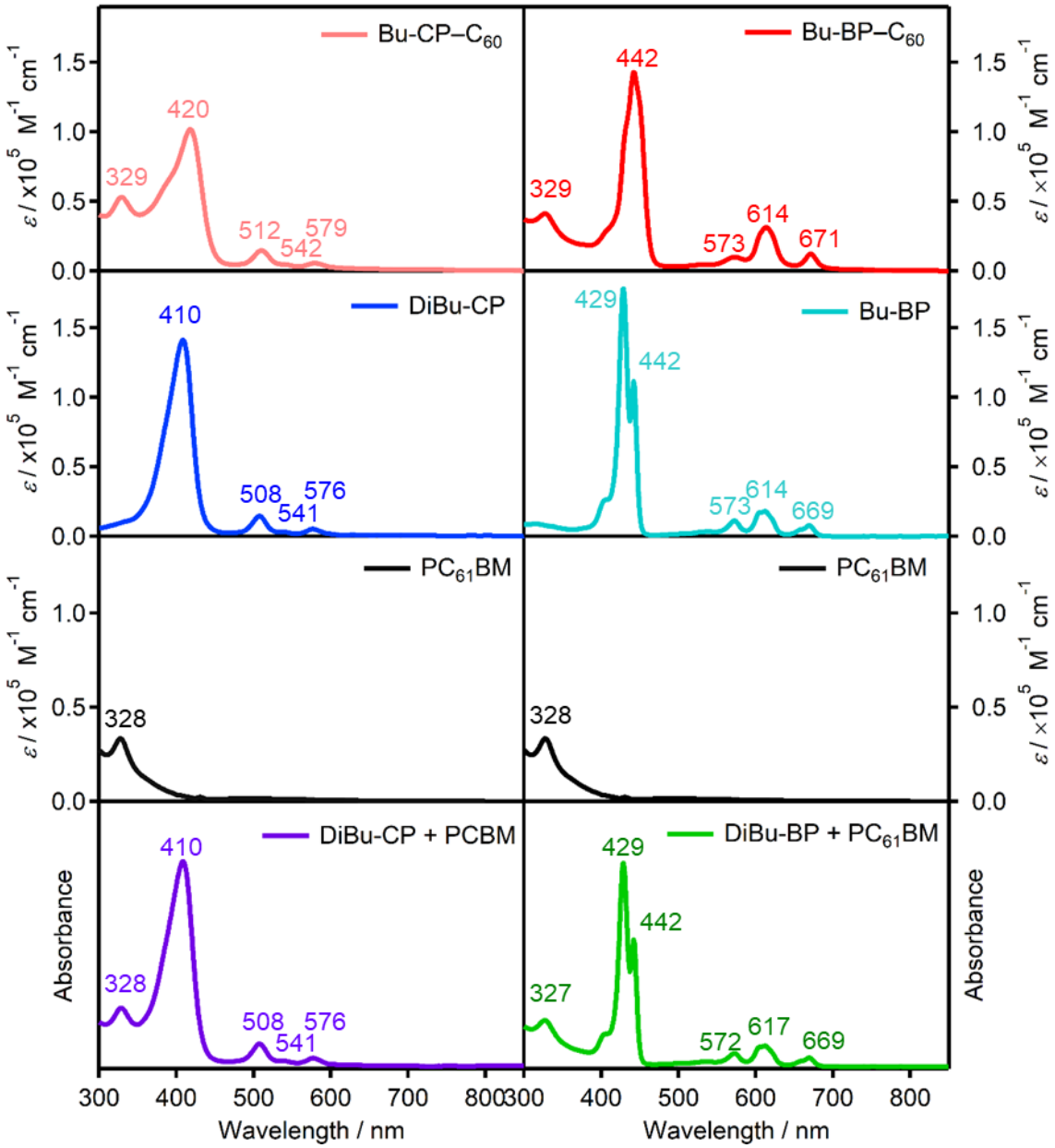

Figure 4. The UV–vis absorption spectra of Bu-CP–C_{60}, DiBu-CP, $PC_{61}BM$, a 1:1 mixture of DiBu-CP and $PC_{61}BM$ (mol/mol), Bu-BP–C_{60}, DiBu-BP, and a 1:1 mixture of DiBu-BP and $PC_{61}BM$ (mol/mol) in CH_2Cl_2.

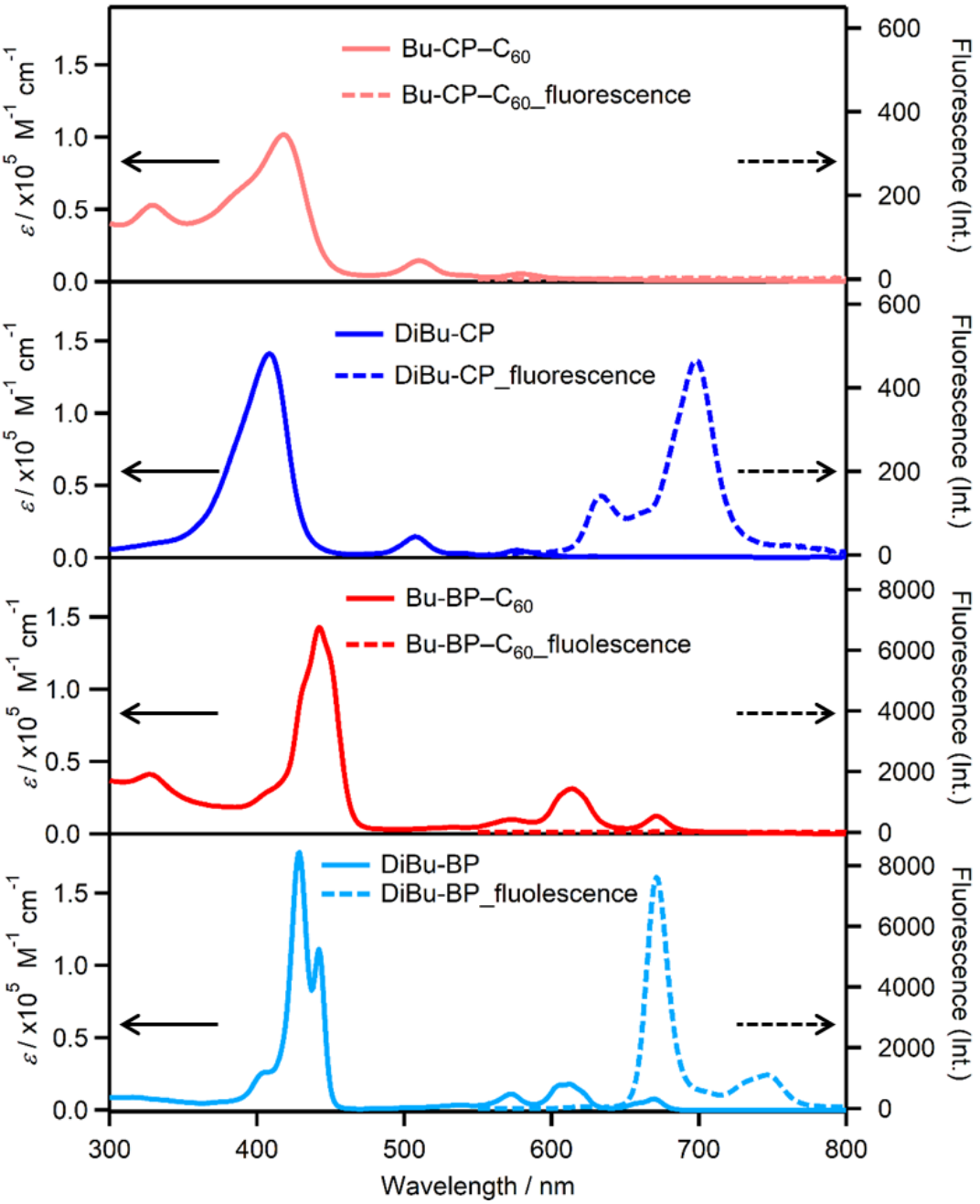

Figure 5. The UV–vis absorption (solid lines) and fluorescence spectra (dot lines) of Bu-CP–C_{60}, DiBu-CP, Bu-BP–C_{60}, and DiBu-BP in CH_2Cl_2. The excitation wavelengths of Bu-CP–C_{60}, DiBu-CP, Bu-BP–C_{60}, and DiBu-BP are 420, 410, 442 and 429 nm, respectively. All of fluorescence spectra were measured with low concentration of sample solution (lower than 0.98 μM at least).

The absorption spectra of Bu-CP–C_{60} and Bu-BP–C_{60} films are shown in Figure 6. The Bu-BP–C_{60} film was prepared by heating of Bu-CP–C_{60} film at 200 ºC for 20 min under nitrogen atmosphere. The film of Bu-BP–C_{60} shows redshifted Soret and Q band peaks (433, 631 and 681 nm) compared with Bu-CP–C_{60} (424, 514 and 583 nm), thus, it is definite that the thermal conversion of Bu-CP–C_{60} to Bu-BP–C_{60} is performable as a film on the substrate. In addition, broader peaks of Bu-BP–C_{60} film compared to those seen in CH_2Cl_2 also observed because of the increased aggregation of Bu-BP–C_{60} in a solid state.

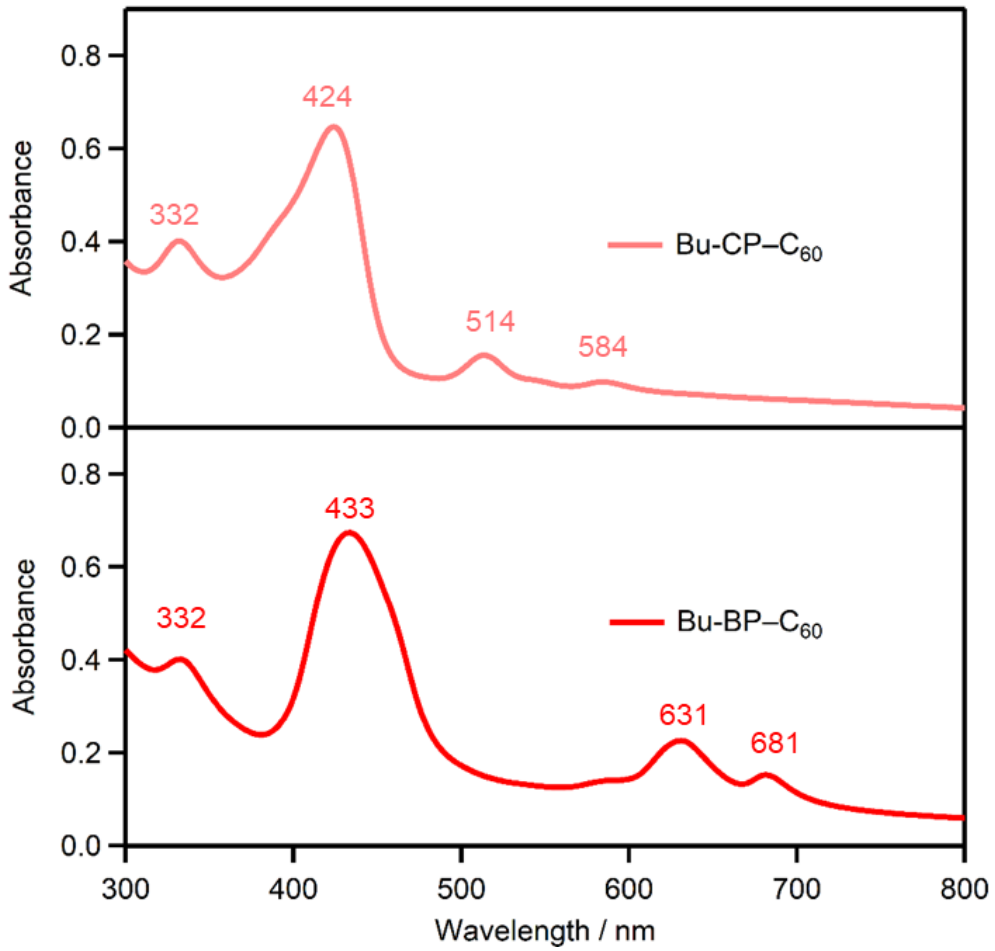

Figure 6. The UV–vis absorption spectra of Bu-CP–C_{60} and Bu-BP–C_{60} films.

The normalized absorption spectrum of Bu-BP–C_{60} film was also compared with those of BP, $PC_{61}BM$, and the 1:1-blend films as shown in Figure 7. The BP film showed a strong Q band at 693 nm, which is typical for crystalline BP films.[19] On the other hand, the shape of the Q band of Bu-BP–C_{60} film indicates that BP units are not effectively stacked with each other within the film. The spectrum of blend film has a larger peak at 690 nm and a broader peak at around 640 nm as compared to the Bu-BP–C_{60} film, suggesting partial stacking of BP units. The Soret peak of the blend film is also broadened compared to the Bu-BP–C_{60} and BP film.

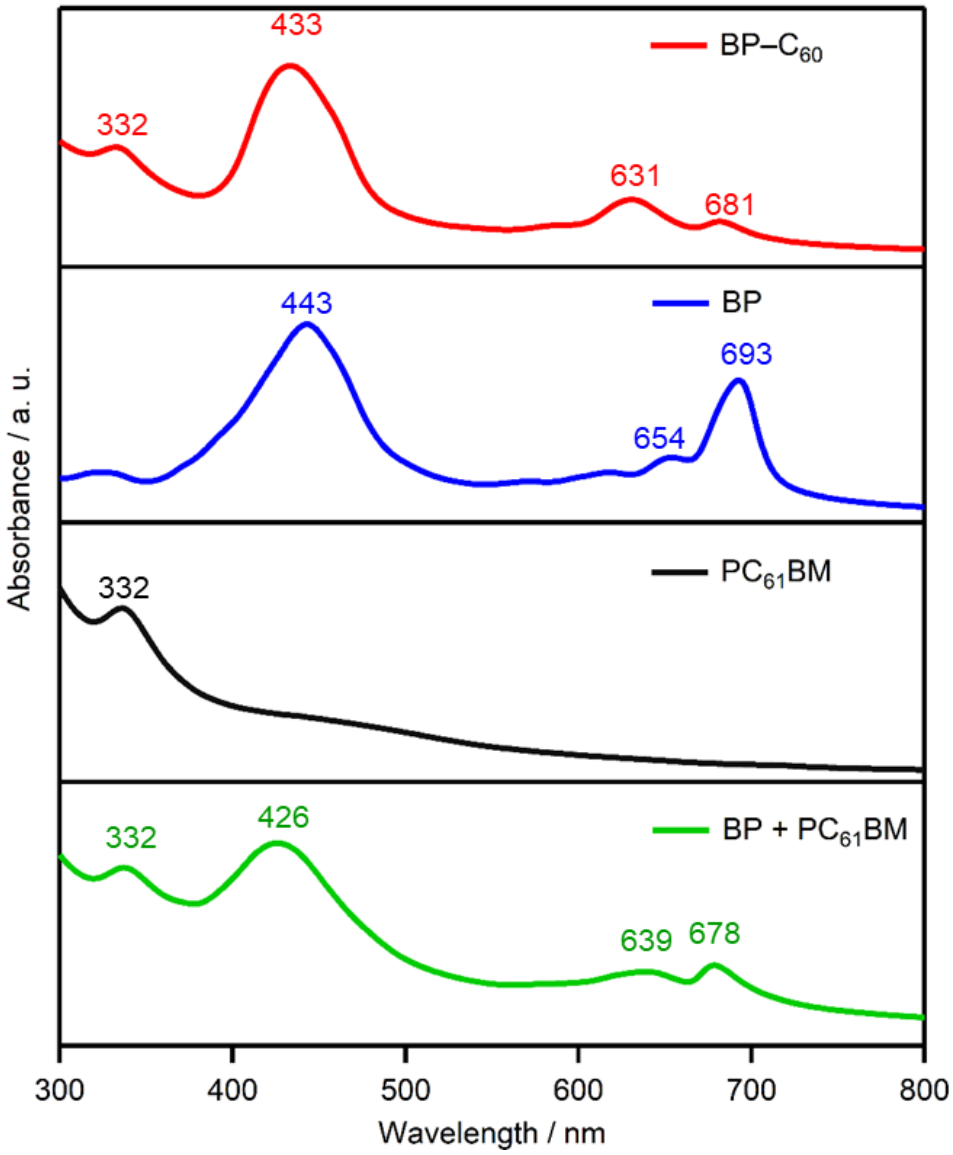

Figure 7. Normalized UV–vis absorption spectra of Bu-BP–C_{60}, BP:$PC_{61}BM$ (1:1 mol/mol) blend, BP, and $PC_{61}BM$ as film.

The electronic property of Bu-BP–C_{60} was investigated by cyclic voltammetry in benzonitrile with reference compounds of DiBu-BP and $PC_{61}BM$ as shown in Figure 8. In the cyclic voltammogram (CV) of Bu-BP–C_{60}, oxidation waves and third-reduction waves assigned to BP moiety and first- and second-reduction waves assigned to the C_{60} moiety were observed by the comparison with reference DiBu-BP and $PC_{61}BM$. The CV of Bu-BP–C_{60} shows reversible waves which suggests that Bu-BP–C_{60} is stable toward consecutive exchange of electrons in the solution. On the other hand, the CV of Bu-BP–C_{60} showed split first oxidation waves. In this regard, effect of the aggregation of BP moiety in benzonitrile is suggested from differential pulse voltammograms (DPV) measurements of low concentration Bu-BP–C_{60} solutions and estimation of these components ratio (Figure 9).

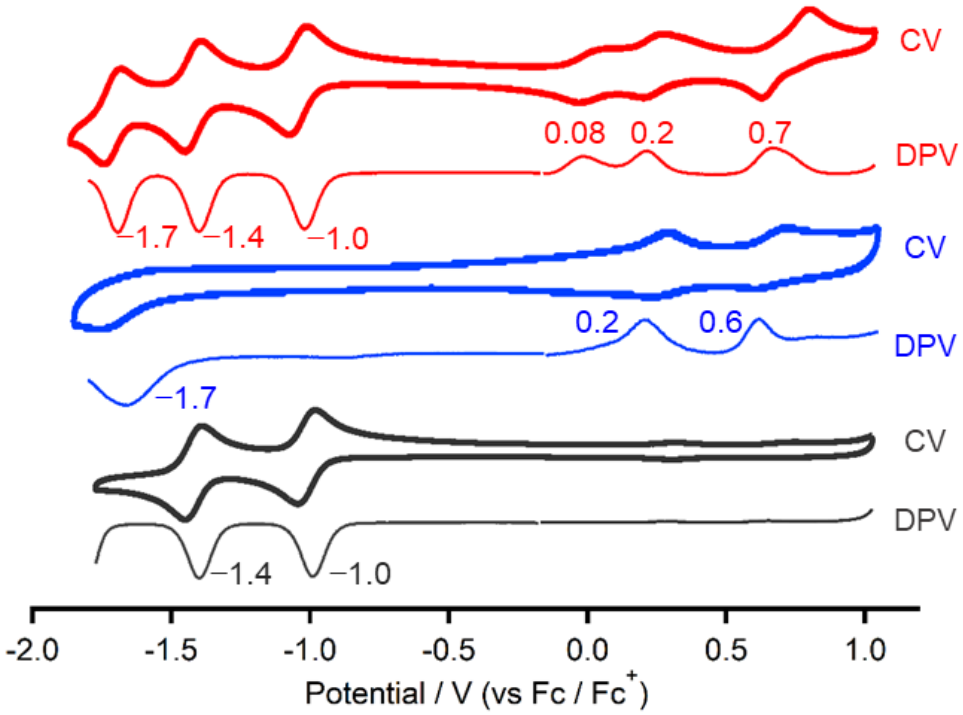

Figure 8. Cyclic voltammograms (CVs) and differential pulse voltammograms (DPVs) of Bu-BP–C_{60} (red), DiBu-BP (blue) and $PC_{61}BM$ (black) in benzonitrile.

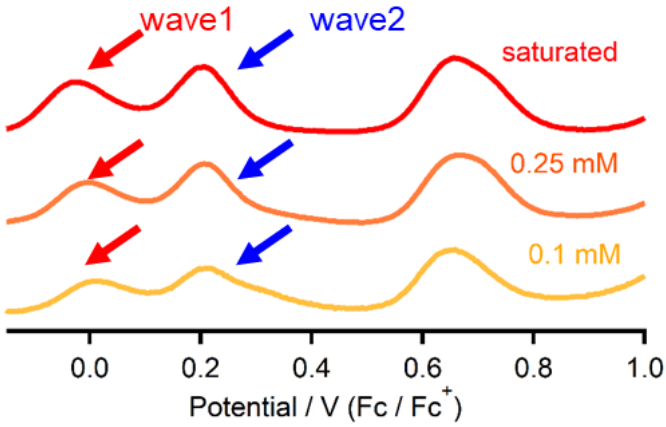

Bu-BP–C_{60} Solution	Ratio of components	
	Wave 1	Wave 2
Saturated	0.87	1.0
0.25 mM	0.49	1.0
0.1 mM	0.45	1.0

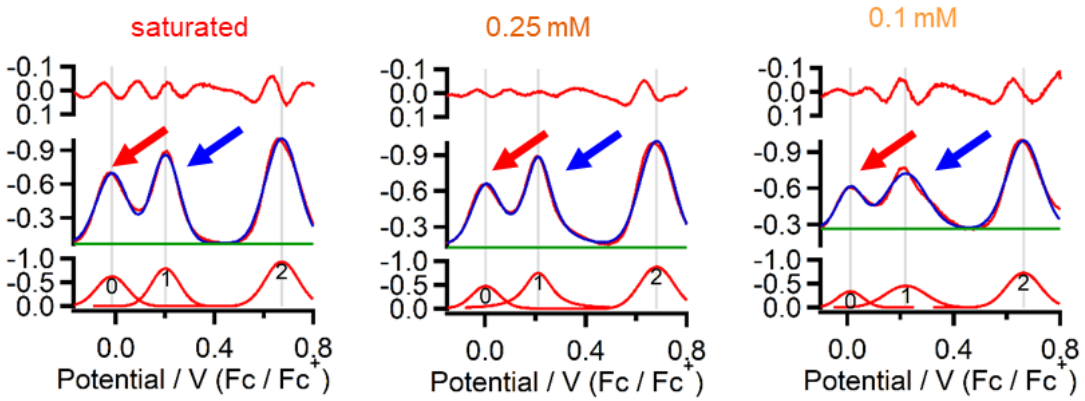

Figure 9. DPV measurements of Bu-BP–C_{60} in different concentrations. The Gaussian function is used for these fitting to estimate components ratio of split first oxidation wave. Estimated components-ratio values were summarized in the table.

The experimentally determined optical band gap (E_{gap}) and frontier-orbital energies of Bu-BP–C_{60} are summarized in Table 1 with those of BP and $PC_{61}BM$ films. To obtain these frontier-orbital energies, cyclic voltammetry and photoemission yield spectroscopy (Figure 10) were measured. Comparison of these values shows that the difference between the LUMO energy level of $PC_{61}BM$ as measured by cyclic voltammetry and the HOMO energy level of BP as measured by photoemission yield spectroscopy is same as the HOMO–LUMO difference in the Bu-BP–C_{60} dyad estimated with the same methods. Thus, the linkage with alkyl ester in Bu-BP–C_{60} has contributed little to HOMO energy level of BP moiety and LUMO energy levels of C_{60} moiety.

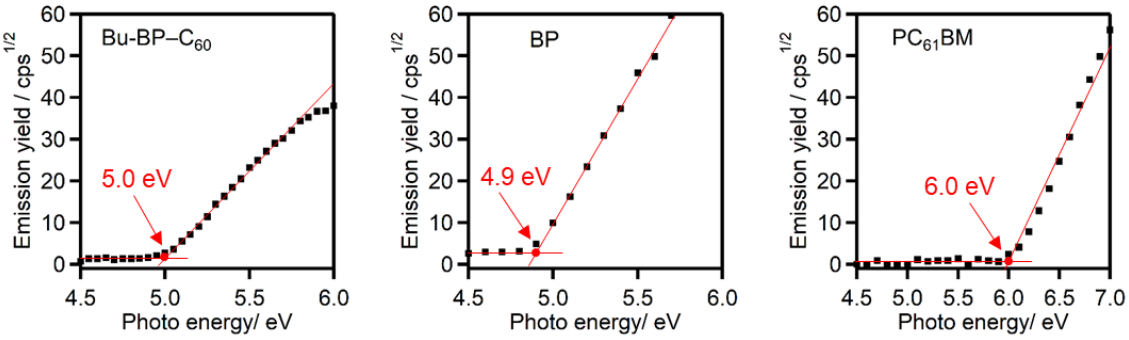

Figure 10. Photoemission yield spectroscopy in air of the films based on Bu-BP–C_{60}, BP, and $PC_{61}BM$ on the ITO coated glass substrate.

Table 1. HOMO and LUMO energy level of examined materials

	E_{gap} [a] / eV	$E_{1/2}^{ox}$ [b] / V	$E_{1/2}^{red}$ [b] / V	HOMO [c] / eV	HOMO [d] / eV	LUMO [e] / eV	LUMO [f] / eV
Bu-BP–C_{60}	1.6	0.08*	−1.0	−5.0	−4.0*	−3.4	−3.8
BP	1.7	–	–	−4.9	–	−3.2	–
DiBu-BP	–	0.2	−1.7	–	−4.6	–	−3.1
$PC_{61}BM$	1.8	–	−1.0	−6.0	–	−4.2	−3.8

[a] Determined by absorption edge of the film.; [b] Determined from the oxidation and reduction peaks obtained by cyclic voltammetry, V vs Fc/Fc^+.; [c] Determined by photoemission yield spectroscopy in air.; [d] HOMO = – (4.8 + $E_{1/2}^{ox}$).; [e] Estimated from E_{gap} and HOMO[c] levels (LUMO = E_{gap} + HOMO); [f] LUMO = – (4.8 + $E_{1/2}^{red}$).; * Probably not true values because of the split oxidation wave as shown in Figure 9 and 10.

3-2-3. Photovoltaic Performance

Schematic descriptions of the bulk heterojunction (BHJ) and p–i–n devices are shown in Figure 11. The deposition conditions of organic active layer is described in the Experimental Section. The BHJ (Bu-BP–C_{60}) device has a Bu-BP–C_{60} active layer, which was prepared by spin-coating of a Bu-CP–C_{60} solution followed by heating at 160 ºC for 20 min. BHJ (BP:$PC_{61}BM$) is a 1:1 blend film of BP and $PC_{61}BM$ deposited similarly using a mixed solution of CP and $PC_{61}BM$. The p–i–n (Bu-BP–C_{60}) film was prepared by sequential deposition of BP, Bu-BP–C_{60} and $PC_{61}BM$ as p-, i-, and n-layers, respectively. The p–i–n (BP:$PC_{61}BM$) device has a 1 : 1 mixture film of BP and $PC_{61}BM$ in the i-layer instead of Bu-BP–C_{60}.

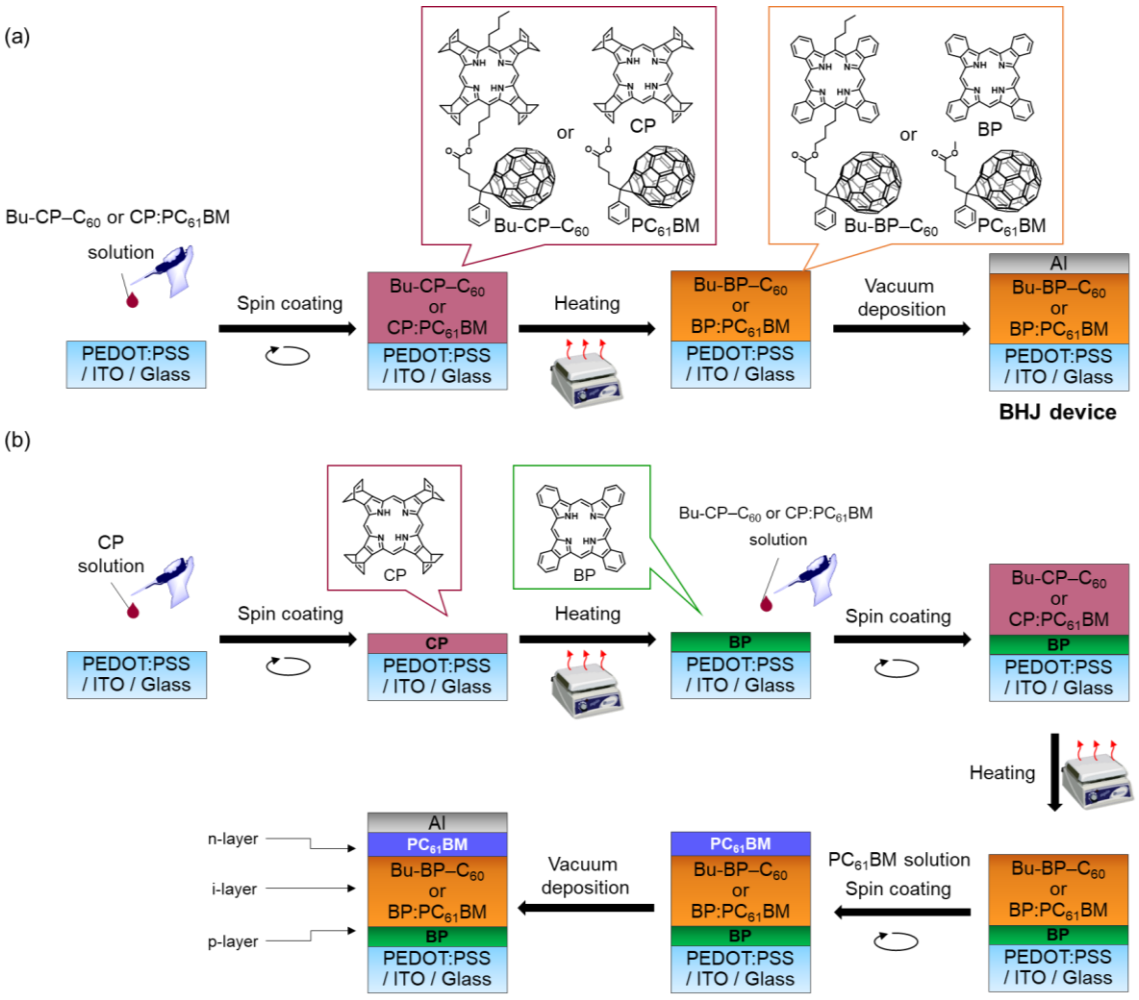

Figure 11. Device fabrication of (a) BHJ devices and (b) p–i–n devices.

The *J–V* characteristics of BHJ and p–i–n devices are shown in Figure 12a and 12b, and the device performances are summarized in Table 2. The BHJ (Bu-BP–C_{60}) device showed a better performance (PCE = 0.15%) with a short circuit current density (J_{SC}) of 1.12 mA cm^{-2}, an open circuit voltage (V_{OC}) of 0.45 V and a fill factor (FF) of 0.29 compared to the BHJ (BP:$PC_{61}BM$) device (J_{SC} = 0.57 mA cm^{-2}, V_{OC} = 0.14 V, FF = 0.23, PCE = 0.02%). Although the BHJ (Bu-BP–C_{60}) device is better than the BHJ (BP:$PC_{61}BM$), the dark *J–V* characteristics of both devices show current leakage. The performance of p–i–n (Bu-BP–C_{60}) and p–i–n (BP:$PC_{61}BM$) is much improved; J_{SC} = 5.18 mA cm^{-2}, V_{OC} = 0.62 V, FF = 0.61 and PCE = 1.98% for p–i–n (Bu-BP–C_{60}) and J_{SC} = 5.92 mA cm^{-2}, V_{OC} = 0.59 V, FF = 0.46, and PCE = 1.63% for p–i–n (BP:$PC_{61}BM$). The highest FF of p–i–n (Bu-BP–C_{60}) is associated with the lowest series resistance (R_s)

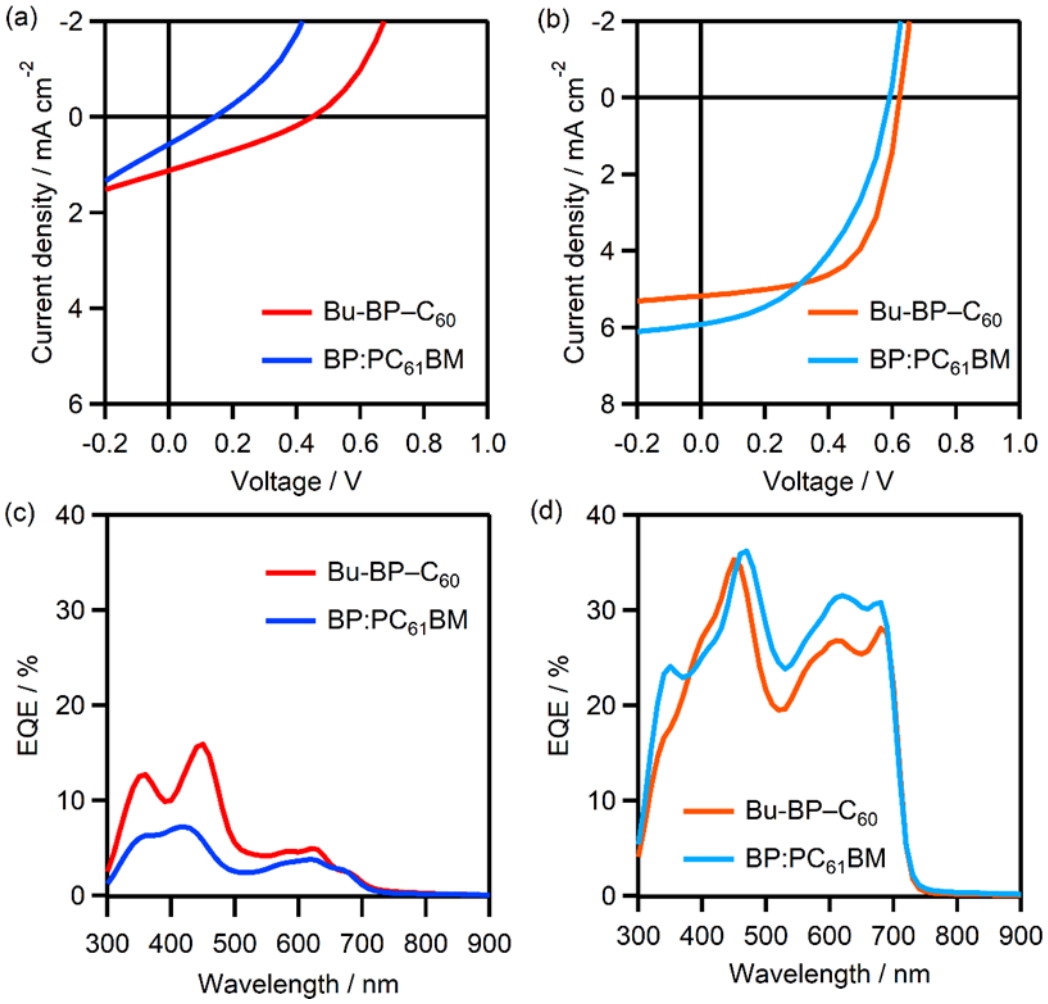

Figure 12. *J–V* and EQE curves of BHJ devices ((a) and (c)) and p–i–n devices ((b) and (d)). *J–V* curves were measured under illuminated (solid line) and dark (dot line) conditions, respectively.

and the highest shunt resistance (R_{sh}), which suggests the best semiconducting properties of the p–i–n (Bu-BP–C_{60}) device among those examined here. Figure 12c and 12d show external quantum efficiency (EQE) spectra of the devices. The better EQE of BHJ (Bu-BP–C_{60}) than BHJ (BP:$PC_{61}BM$) suggests that the carrier generation in the dyad film is more effective than in BHJ (BP:$PC_{61}BM$). The spectrum of BHJ (Bu-BP–C_{60}) shows two peaks at 350 and 440 nm corresponding to C_{60} and BP, respectively, which indicates that both units work as sensitizers. The broader and less defined peaks in the EQE spectrum of BHJ (BP:$PC_{61}BM$) could be attributed to the stacking of BP molecules in the blend films—a similar tendency was observed between the UV–vis absorption spectra of these films (Figure 8). The EQEs of the p–i–n (Bu-BP–C_{60}) and p–i–n (BP:$PC_{61}BM$) are much enhanced as compared to the BHJ devices. The peak at 350 nm for p–i–n (Bu-BP–C_{60}) is lower than that for p–i–n (BP:$PC_{61}BM$), thus the C_{60} moieties do not work effectively as sensitizers in the former device. This seems to reflect the relatively low absorption at this wavelength in the film of Bu-BP–C_{60} (Figure 8).

Table 2. Device performances of BHJ and p–i–n devices.

Device	PCE (ave.*) / %	J_{SC} / mA cm^{-2}	V_{OC} / V	FF	R_s / Ω cm^2	R_{sh} / Ω cm^2
BHJ (Bu-BP–C_{60})	0.15 (0.10 ± 0.03)	1.12	0.45	0.29	163	490
BHJ (BP:$PC_{61}BM$)	0.02 (0.01 ± 0.005)	0.57	0.14	0.23	219	261
p–i–n (Bu-BP–C_{60})	1.98 (1.89 ± 0.03)	5.18	0.62	0.61	12	1436
p–i–n (BP:$PC_{61}BM$)	1.63 (1.40 ± 0.15)	5.92	0.59	0.46	16	721

* At least four devices in all.

3-2-4. Film Morphology

The tapping-mode atomic force microscopy (AFM) height and phase images of a neat Bu-BP–C_{60} film and a 1:1 blend film of BP and $PC_{61}BM$ are shown in Figure 13. The two films are similar in surface roughness, with the root-mean square (RMS) values of 0.43 and 0.50 nm for the dyad and blend films, respectively. On the other hand, the phase images showed an obvious difference: the dyad film has a smooth surface, but the blend film shows large grains of 1–2 mm diameters. In addition, a dyad film formed on a BP layer showed a much smoother surface with fewer grains as compared to a corresponding blend film on BP as shown in Figure 14. And probably, these morphological differences can affect to form flat and homogenous n-layer in case of Bu-BP–C_{60} or inhomogeneous n-layer in case of BP:$PC_{61}BM$ as shown in Figure 15. Thus, the covalent linkage between the BP and C_{60} units prevents the formation of grains, which may have led to the improvement of the FF. The out-of-plane XRD patterns, on the other hand, did not show the specific peaks for both the dyad and blend films as shown in Figure 16. The crystallinity of BP and $PC_{61}BM$ in these films is not so high, although large grains are observed in the AFM phase image of p–i–n (BP:$PC_{61}BM$) and the Q band of the blend film suggested the partial π–π interaction of BP in the blend film.

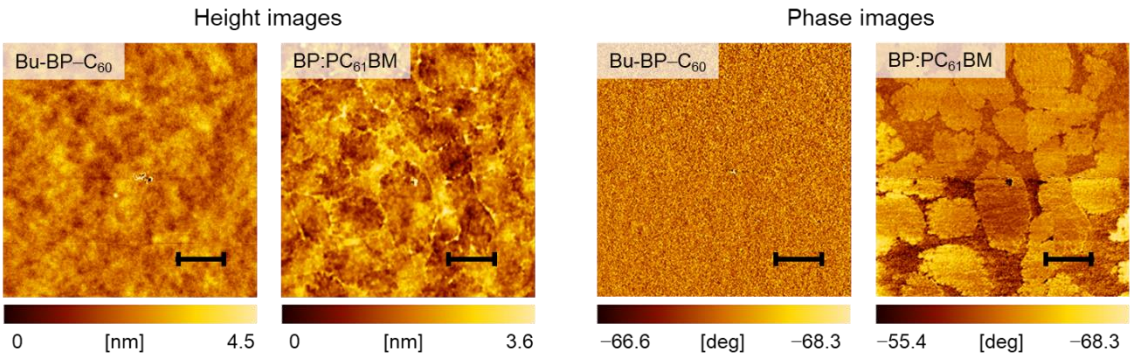

Figure 13. Tapping-mode AFM height and phase images of Bu-BP–C_{60} film and blended BP:$PC_{61}BM$. RMS values of height images are 0.43 and 0.50 nm for BP–C_{60} and BP:$PC_{61}BM$. The scale bars correspond to 1 μm.

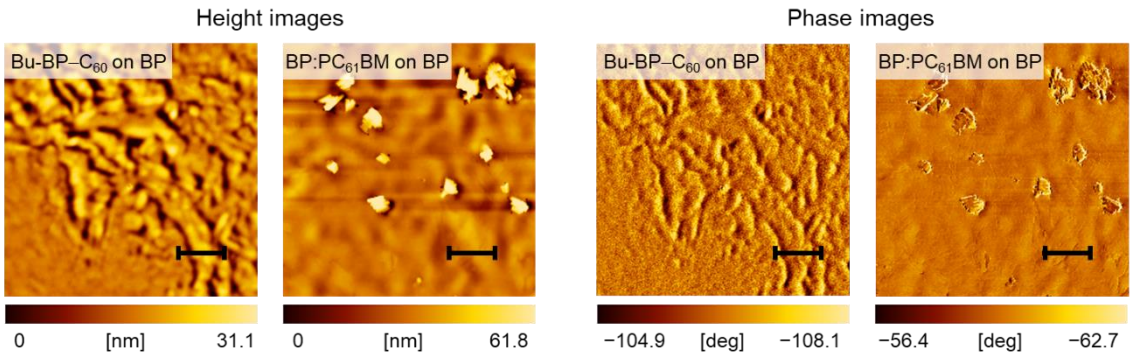

Figure 14. Tapping–mode AFM height and phase images of Bu-BP–C_{60} film on BP layer and blended BP:$PC_{61}BM$ film on BP layer. RMS values of height images are 4.88 and 8.83 nm for Bu-BP–C_{60} on BP and BP:$PC_{61}BM$ on BP. The scale bars correspond to 1 μm.

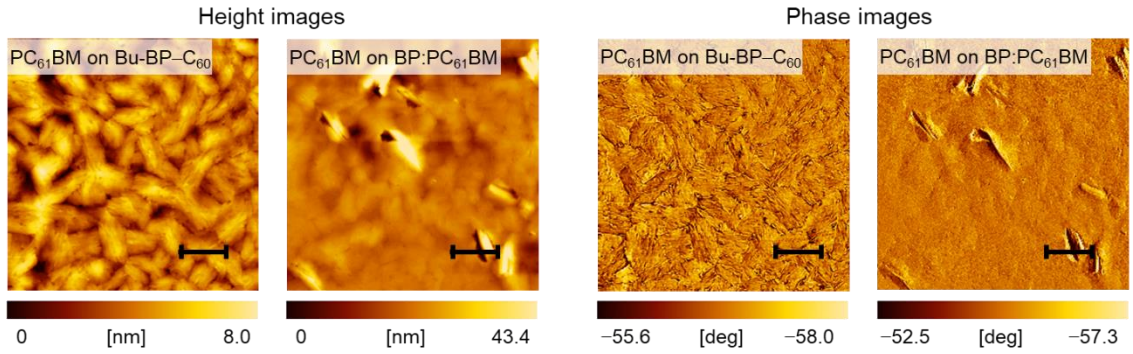

Figure 15. Tapping–mode AFM height and phase images of $PC_{61}BM$-layers on p-i–layer with Bu-BP–C_{60} or BP:$PC_{61}BM$. RMS values of height images are 1.23 and 6.42 nm for $PC_{61}BM$ on Bu-BP–C_{60} and $PC_{61}BM$ on BP:$PC_{61}BM$. The scale bars correspond to 1 μm.

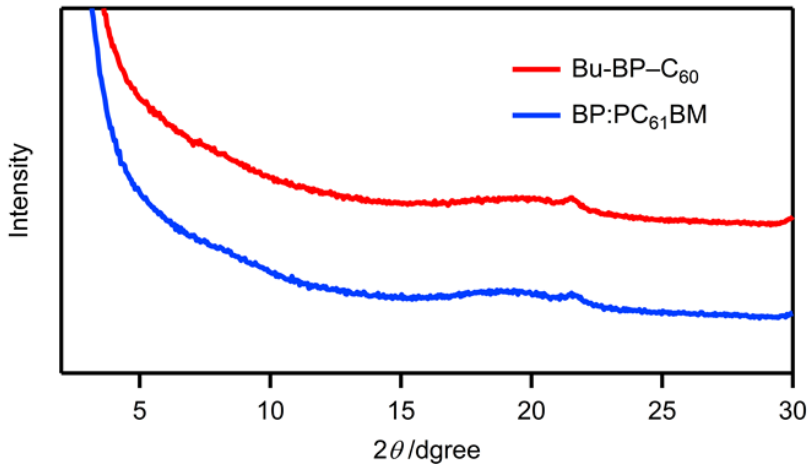

Figure 16. Out-of-plane XRD patterns of Bu-BP–C_{60} layer and BP:$PC_{61}BM$ layer on PEDOT:PSS/ITO/glass.

3-3. Investigation of Fullerene-Linked Tetrabenzoporphyrins for Solution-Processed Organic Photovoltaics: Flexible vs. Rigid Linkers

3-3-1. Molecular Design and Syntheses

As indicated above, Bu-BP–C_{60} suggested the solid significance of morphological advantages as OSCs material. For construction of more performant BP–C_{60} system, we hypothesized that the flexible spacer between BP and C_{60} might accelerate the electron recombination as well as the charge separation between BP and C_{60}. To verify the hypothesis, we designed a mono-substituted BP–C_{60} connected by a flexible linker (f-BP–C_{60}) and rigid linker (r-BP–C_{60}) as shown in Figure 17. The butyl group of the Bu-BP–C_{60} was removed to exclude the effect of the insulating alkyl group on BP, if any. The carrier mobility and OPV performance of BHJ and p–i–n devices with these materials will be discussed.

A flexible precursor (f-CP–C_{60}) of mono-substituted free-base BP–C_{60} was prepared as shown in Scheme 2. The synthetic details are described in the Experimental section. The 5-substituted-ZnCP **6** obtained via same condensation reaction as we shown in Chapter 1 was converted to the flexible free-base CP–C_{60} (f-CP–C_{60}) following a previously reported procedure: reduction of the ester group to give porphyrin **7**, coupling

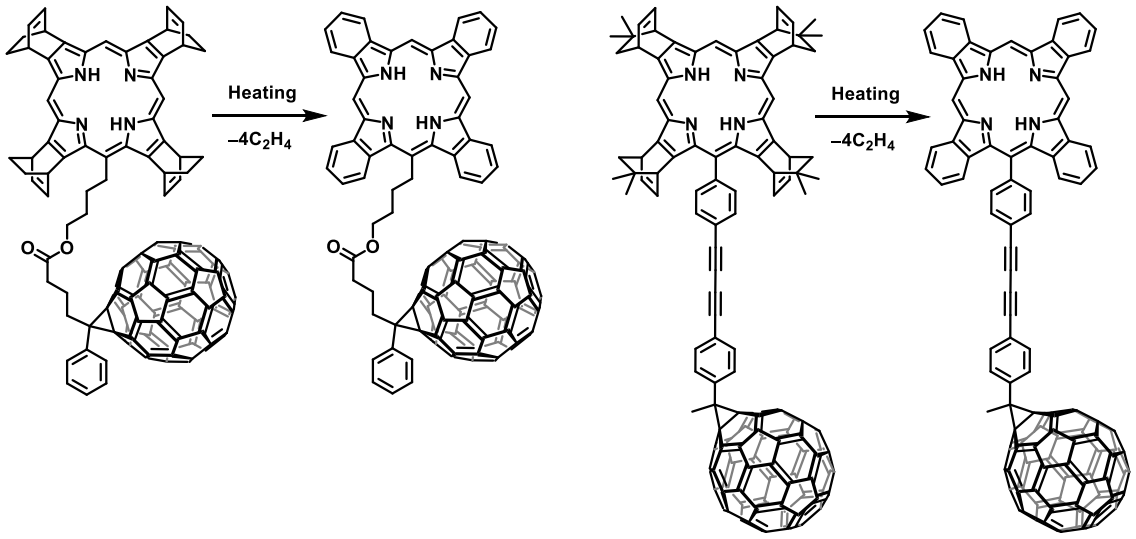

Figure 17. Chemical Structures of f-CP–C_{60}, f-BP–C_{60}, r-CP–C_{60}, and r-BP–C_{60}.

with [6,6]-phenyl-C_{61}-butyric acid (PCBA)[8] **6** to give f-ZnCP–C_{60}, and demetallation by trifluoroacetic acid (TFA). As a reference compound, 5-butyl-CP (Bu-CP) and 5-butyl-BP (Bu-BP) reported in the Chapter 2 were also prepared.

Next, rigidly-linked CP–C_{60} (r-CP–C_{60}) was prepared as shown in Scheme 3. To bypass the low solubility of r-CP–C_{60} due to the rigid-linked structure, a dimethylBCOD-fused pyrrole[20] **8** was used instead of the BCOD-pyrrole. By acid condensation of dimethylBCOD-fused pyrrole[20] **8**, α-hydroxymethylpyrrole[20] **9**, and 4-bromoalkynyl-benzaldehyde **10**,[21] 5-substituted-MeCP **11** was obtained in a 33% yield. 5-Substituted MeCP **11** was a mixture of stereoisomers, but it was used for the following reactions without further purification. MeCP **11** was reacted with fullerene **15** which was prepared from 4-(trimethylsilylethynyl)acetophenone[22] **12** in 3 steps to give the rigid dyad r-ZnCP–C_{60} in 46% yield. The zinc ion of r-ZnCP–C_{60} was removed by treatment with TFA to give r-CP–C_{60} in 88% yield. In a same manner of Chapter 2, a

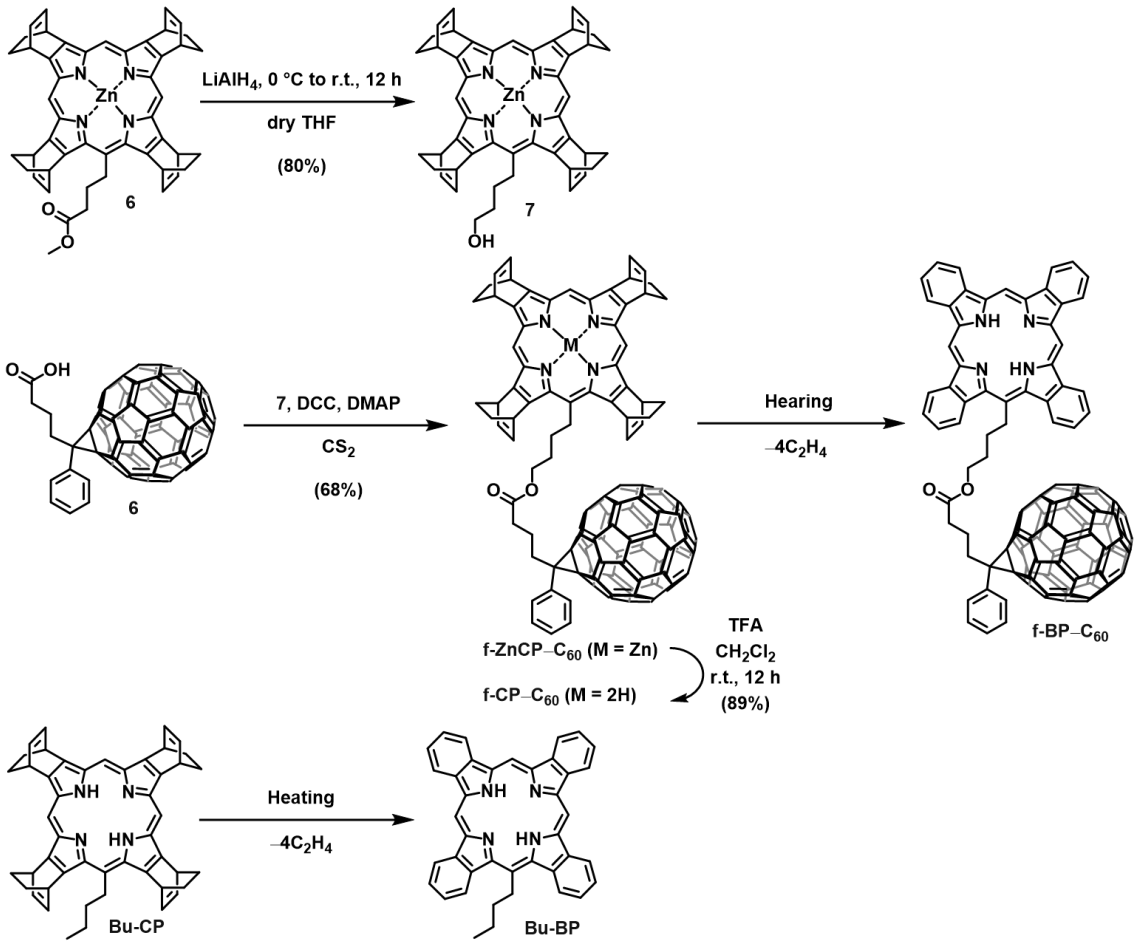

Scheme 2. Synthetic routes of f-BP–C_{60} and Bu-BP.

precursor (TMS-CP) of the reference compound (TMS-BP) was prepared as a reference compound. The zinc complex of r-BP–C_{60} (r-ZnBP–C_{60}) was also prepared to obtain single crystals suitable for X-ray crystallography.

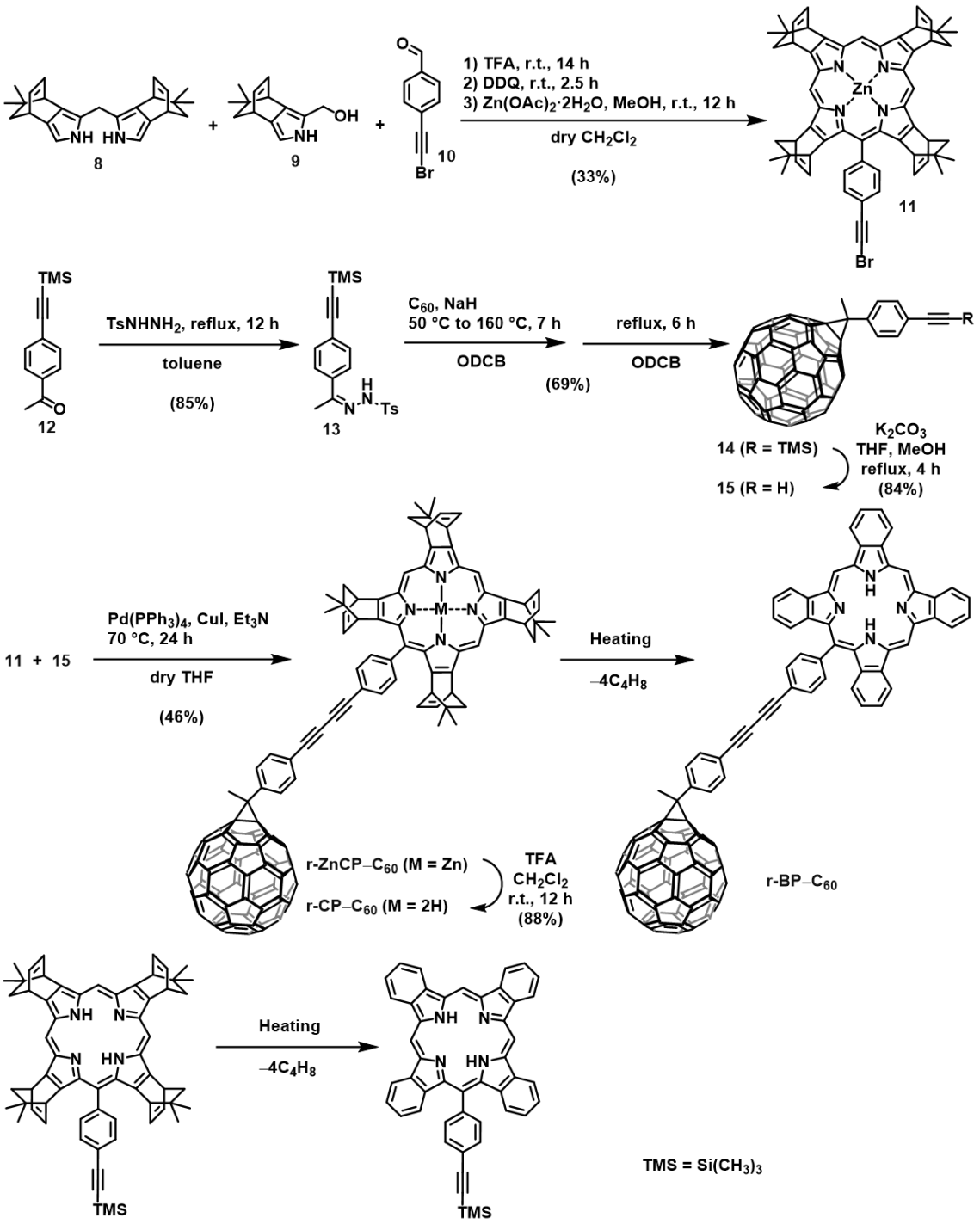

Scheme 3. Synthetic routes of r-BP–C_{60} and TMS-BP.

The thermogravimetric analysis of CP–C_{60} is shown in Figure 18. The observed mass loss of f-CP–C_{60} (−7.2%), r-CP–C_{60} (−13.3%), and r-ZnCP–C_{60} (−13.7%) in TGA curves of the obtained r-BP–C_{60}, r-BP–C_{60} and r-ZnBP–C_{60} were in good agreement with the simulated values. The retro-Diels–Alder reaction of f-CP–C_{60} started at 120 ºC and finished around 220 ºC, while that of r-CP–C_{60} started around 140 ºC and finished around 200 ºC. The decomposition temperatures of f-CP–C_{60} and r-CP–C_{60} are around 358, and 472 ºC, respectively. r-CP–C_{60} showed higher thermal stability than f-CP–C_{60} the flexible linker. This result suggests that decomposition temperature of our BP–C_{60} system is presumably depended by linkage structure. After the retro-Diels–Alder reaction, the MALDI spiral-TOF mass spectra obtained r-BP–C_{60}, r-BP–C_{60} and r-ZnBP–C_{60} could be found the simulated mass spectra (Fig. S3-3–S3-5, Support information). But, the solubility of the BP–C_{60} compounds was not enough for NMR measurement.

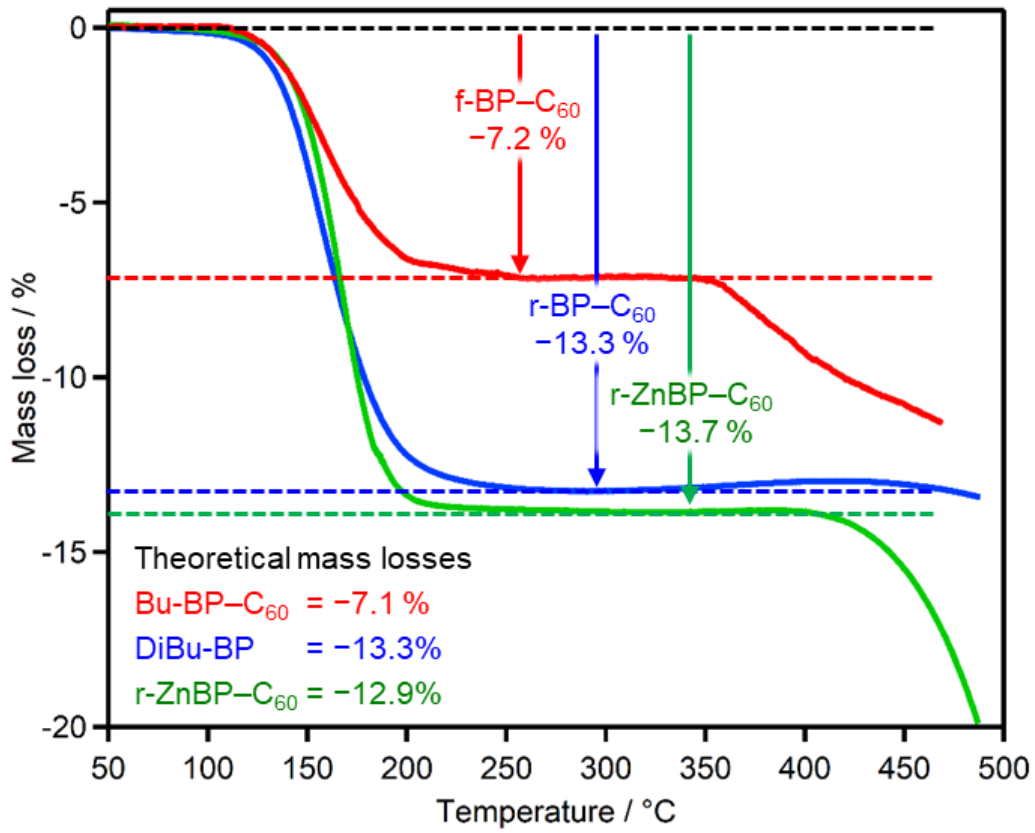

Figure 18. TGA curves of (a) f-CP–C_{60}, (b) r-CP–C_{60}, and (c) r-ZnCP–C_{60} measured under nitrogen gas flowing with heatup time of 5 ºC min^{-1}.

The single crystals of r-ZnBP–C_{60} were obtained by slow diffusion of either acetonitrile into a chlorobenzene solution. The single crystal structure of r-ZnBP–C_{60} was determined with synchrotron X-ray radiation (Figure. 19 and Table S1).[21] Since the tiny crystals contained many severely disordered solvent molecules, they gave only weak diffractions, especially in the high q range. The molecule is extended straight and the porphyrin and meso-phenyl planes are perpendicular to each other. The porphyrin plane is slightly ruffled. The intramolecular center-to-center distance (d_{cc}) between the porphyrin and C_{60} units is about 22 Å and the edge-to-edge distance (d_{ee}) is about 14 Å. In a unit cell, two molecules are alternately placed, and the intermolecular distance between the porphyrin and C_{60} units is less than the van der Waals distance. This structure is suitable for effective charge separation, but charge recombination is also expected to be fast. The packing structure is shown in Figure 20. The top and side views suggest that the fullerenes are arranged in line with an edge-to-edge distance of 3.5 Å, which is suitable for electron transport, while the porphyrins only overlap at the edge of the benzene rings.

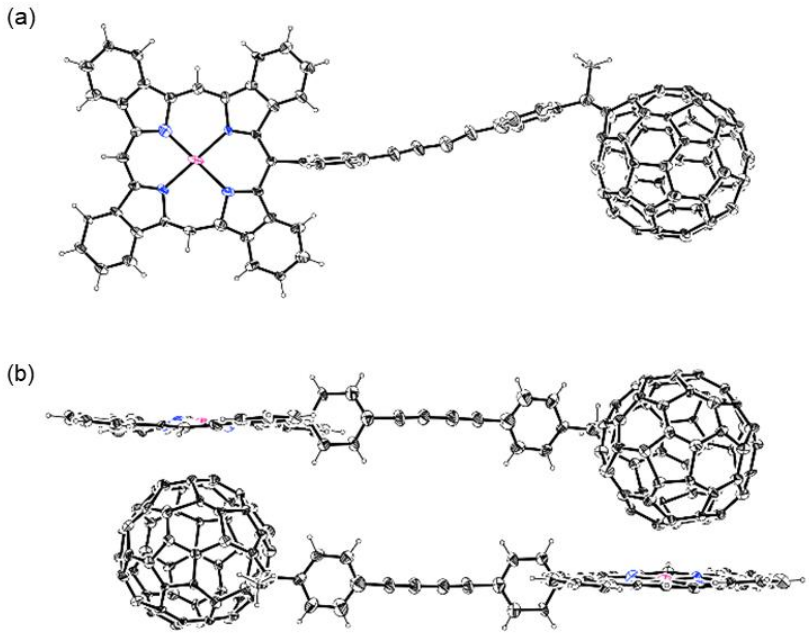

Figure 19. The single crystal structure of r-ZnBP–C_{60}. (a) Top view and (b) side view with packing structure. The ellipsoid is scaled to 20% prpbability.

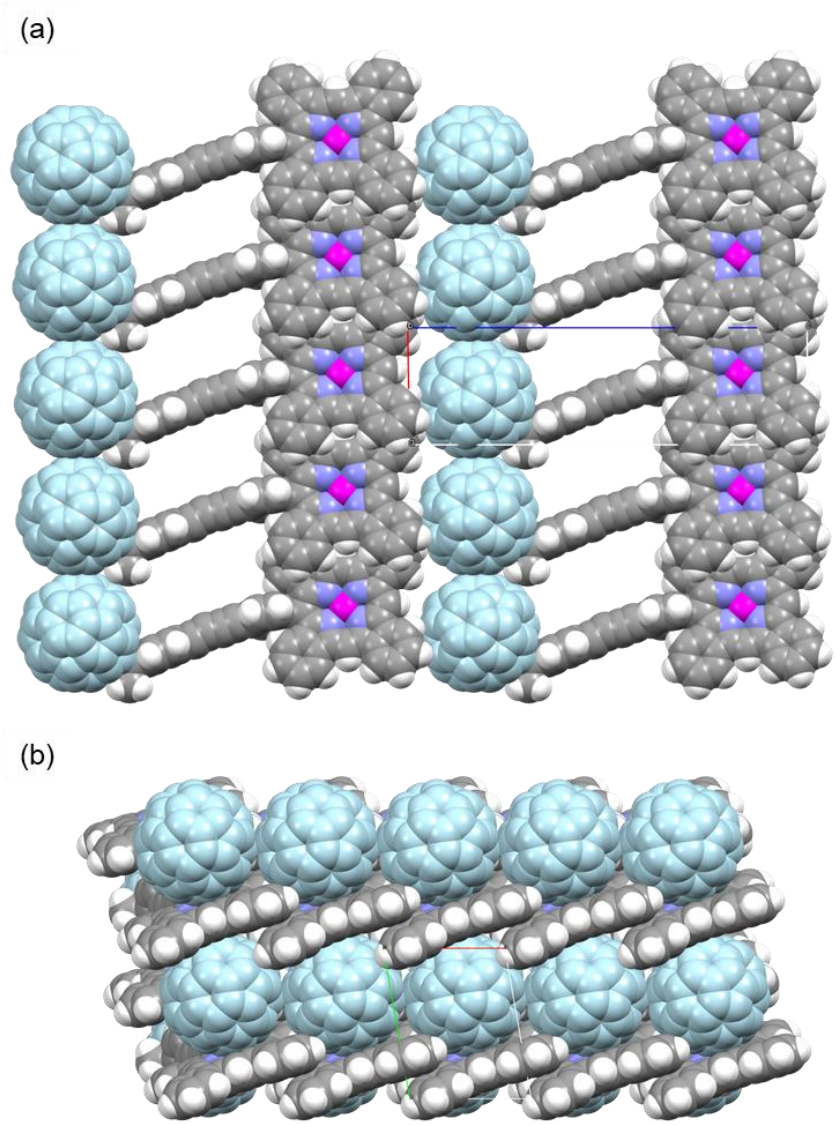

Figure 20. Packing structure in single crystal of r-ZnBP–C_{60}. (a) Top view and (b) side view.

3-3-2. Optical and Electronic Properties

The absorption and fluorescence spectra of f-BP–C_{60}, r-BP–C_{60} and their reference compounds (Bu-BP and TMS-BP) are shown in Figure 21, and the related data are summarized in Table 3. Flexible f-BP–C_{60} has a Soret band at 436 nm with a shoulder at 428 nm, Q bands at 568, 609, and 667 nm, and a broad absorption from fullerene at 310–350 nm. The absorption peaks are similar to those of the reference Bu-BP except for the peaks of fullerene. The solubility of r-BP–C_{60} was not enough to obtain the absorption coefficients. Rigid r-BP–C_{60} has Soret bands at 419 and 434 nm, Q bands at 568, 601, 608 and 664 nm with a shoulder at 615 nm and a broad absorption from fullerene at 310–350 nm. The absorption of the porphyrin moiety is similar to the reference TMS-BP: Soret bands at 418 and 433 nm and Q bands at 567, 603, 608, and 664 nm with a shoulder at 615 nm. Due to the lower symmetry of the electronic structure of the porphyrin moiety with a monosubstituent at the 5-position, the Soret and Q bands of the porphyrins show splitting. The absorption band of f-BP–C_{60} shows the broadening of porphyrin and fullerene peaks compared to the peaks of r-BP–C_{60}. The broadening of f-BP–C_{60} might come from the intramolecular interaction between BP and C_{60}. The fluorescence spectra of Bu-BP and TMS-BP, the reference BPs, showed a relatively high fluorescence intensity at 665–668 nm with fluorescence quantum yields (Φ_f) of 18.5 and 26.6%, respectively. The Φ_f values of the dyads, f-BP–C_{60} and r-BP–C_{60}, in CH_2Cl_2 were 1.0 and 2.5%, respectively. This result suggested that the fullerene moieties effectively intramolecularly quench the fluorescence of porphyrins, even though the d_{ee} of r-BP–C_{60} is 14 Å. The fluorescence lifetimes (τ_f) of f-BP–C_{60} and r-BP–C_{60} were analyzed in two components: 0.61 ns (96.2%) and 9.38 ns (3.8%) for f-BP–C_{60} and 1.16 ns (99.4%) and 11.97 ns (0.6%) for r-BP–C_{60} (Figure 22 and Table 3). Those of the reference compounds, Bu-BP and TMS-BP, were analyzed as a single component, 8.74 and 9.91 ns, respectively. The short lifetimes of f-BP–C_{60} and r-BP–C_{60} are characterized by the intramolecular electron transfer from BP to C_{60}. The fluorescence lifetimes of f-BP–C_{60} were analyzed in two components on average, although f-BP–C_{60} could take multiple conformations in solution with a flexible linkage. Intramolecular fluorescence quenching of r-BP–C_{60} (τ_f = 1.16 ns) is not so effective as f-BP–C_{60} (0.61 ns) because of the rigid spacer with d_{cc} = 22 Å. The absorption spectra of the f-BP–C_{60} and r-BP–C_{60} films are shown in Figure 23 and

the related data are summarized in Table 3. The films of BP–C_{60} were prepared by spin-coating CP–C_{60} followed by heating on a hotplate at 200 ºC for 20 min. The details of the film preparation are described in the Experimental Section. The film of f-BP–C_{60} shows absorption peaks at 427, 628, and 677 nm, while r-BP–C_{60} shows peaks at 436, 628, and 677 nm. The spectra of the BP–C_{60} films are broader compared to the spectra in CH_2Cl_2 because of the π–π stacking of the porphyrins. The Q band peaks of the films are similarly red-shifted for f-BP–C_{60} and r-BP–C_{60} from those in solution, while the Soret band of r-BP–C_{60} is 9 nm red shifted compared to the f-BP–C_{60} film. This probably can be attributed that a intermolecular complex formation of r-BP–C_{60} in film same as the reported study about other porphyrin–C_{60} dyad in a solid film[23].

Table 3. Optical properties of fullerene-linked BPs and reference molecules

	λ_{abs} [a] / nm	λ_{abs} [b] / nm	λ_f / nm	Φ_f / %	τ_f [c] / ns
f-BP–C_{60}	327, 428 (sh), 436, 568, 609, 667	334, 427, 628, 678	668	1.0	0.61 (96.2), 9.38 (3.8)
Bu-BP	395, 421, 435, 568, 608, 665		665	18.5	8.74
r-BP–C_{60}	319, 390, 419, 434, 568, 601, 608, 615 (sh), 664	327, 436, 628, 679	668	2.5	1.16 (99.4), 11.97 (0.6)
TMS-BP	391, 418, 433, 567, 603, 608, 615 (sh), 664		666	26.6	9.91

[a] In CH_2Cl_2. [b] As film. [c] τ_f was measured by excitation at 405 nm in CH_2Cl_2. Emission was monitored at 670 nm.

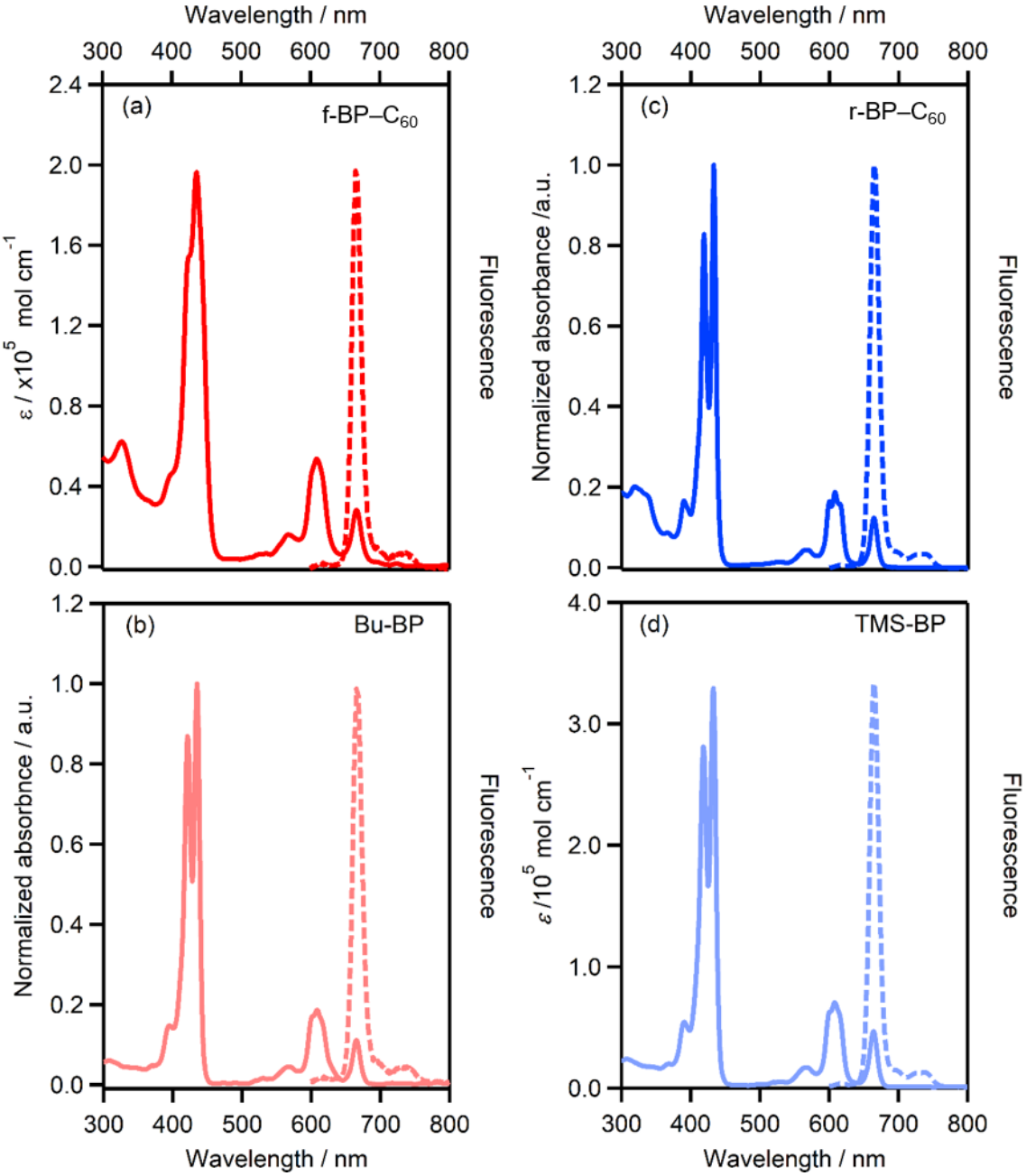

Figure 21. The UV–vis absorption and fluorescence spectra of (a) f-BP–C_{60}, (b) Bu-BP, (c) r-BP–C_{60} and (d) TMS-BP in CH_2Cl_2. All of fluorescence spectra were measured with low concentration of sample solution (lower than 0.50 μM at least). The excitation wavelengths of f-BP–C_{60}, Bu-BP, r-BP–C_{60}, and TMS-BP in CH_2Cl_2 are 436, 435, 434, and 433 nm, respectively.

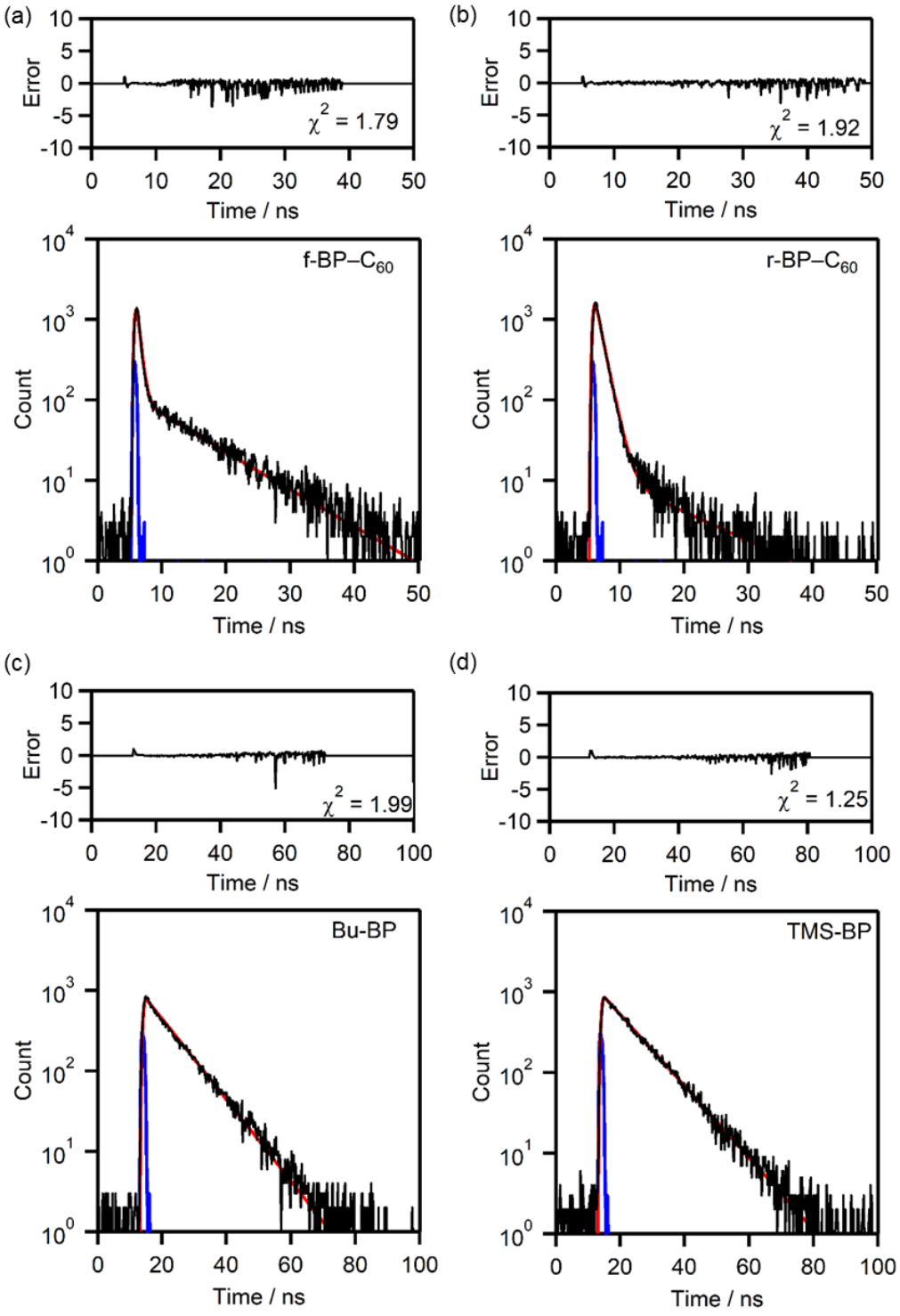

Figure 22. Florescence decays of (a) f-BP–C_{60}, (b) r-BP–C_{60}, (c) Bu-BP and (d) TMS-BP in CH_2Cl_2. The excitation light wavelength was 405 nm. The figure shows the experimental fluorescence decay (black line), the fitted curve (red line), and the response from the excitation light (blue line) on a semilogarithmic scale. The fitting was accomplished over the complete rise and decay curve. The recovered fluorescence lifetime contains the reduced χ^2 (i.e., fitting criterion) amounted to less than 2.

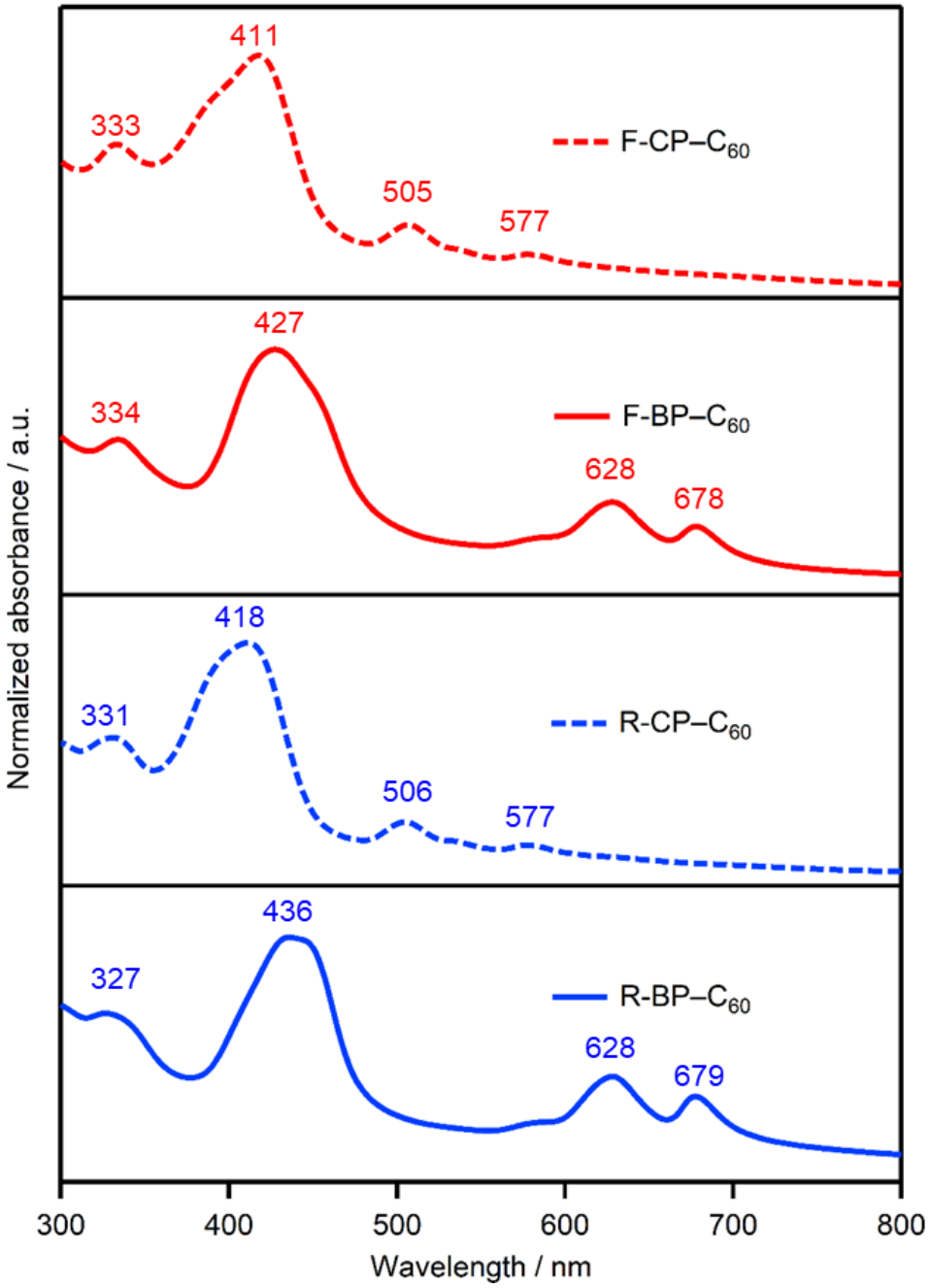

Figure 23. The UV–vis absorption spectra of f-CP–C_{60}, f-BP–C_{60}, r-CP–C_{60}, and r-BP–C_{60} as films.

The optical band gap (E_{gap}) obtained from the absorption edge (estimated from Figure 23) is summarized in Table 4. The highest occupied molecular orbital (HOMO) energies of f-BP–C_{60} and r-BP–C_{60} were estimated by photoelectron spectroscopy (PES) of the film in air (Figure 24). The lowest unoccupied molecular orbital (LUMO) energies were estimated from the onset of the cyclic voltammograms (CVs) according to the known empirical equation LUMO = – (4.8 + E^{red}_{onset}), where E^{red}_{onset} is referenced to the ferrocene/ferrocenium (Fc/Fc^+) standard (Figure 25). The estimated values are also summarized in Table 4 with the values of the BP and $PC_{61}BM$ films. The HOMO energies of the r-BP–C_{60} film was −0.1 eV lower than f-BP–C_{60}. The LUMO energies of the f-BP–C_{60} and f-BP–C_{60} films the same although the structures of the linkages between the porphyrin and fullerene are different.

Table 4. The optical band gap, HOMO and LUMO levels of examined compounds.

	E_{gap} [a] / eV	E^{ox}_{onset} [b] / eV	E^{red}_{onset} [b] / eV	HOMO [c] / eV	LUMO [d] / eV	HOMO [e] / eV	LUMO [f] / eV
f-BP–C_{60}	1.6	0.04*	−1.0	−5.0	−3.4	−4.76*	−3.8
r-BP–C_{60}	1.7	0.1*	−1.0	−5.1	−3.4	−4.9*	−3.8
Bu-BP	–	0.04*	−1.8	–	–	−4.76*	−3.0
TMS-BP	–	0.08*	−1.7	–	–	−4.72*	−3.1
BP	1.7	–	–	−4.9	−3.2	–	–
$PC_{61}BM$	1.8	–	−1.0	−6.0	−4.2	–	−3.8

[a] Determined by absorption edge of the film; [b] Determined from the oxidation and reduction peaks obtained by cyclic voltammetry, V vs Fc/Fc^+; [c] Determined by photoemission yield spectroscopy in air; [d] Estimated from E_{gap} and HOMO levels. LUMO = E_{gap} + HOMO; [e] HOMO = – (4.8 + E^{ox}_{onset}); [f] LUMO = – (4.8 + E^{red}_{onset}). In 0.1 M $TBAPF_6$ / PhCN. Scan rate 0.1 Vs^{-1}. [Sample] = 5mM (TMS-BP and $PC_{61}BM$) or saturated (f-BP–C_{60}, r-BP–C_{60} and Bu-BP); W.E.: glassy carbon; C.E.: Pt; R.E.: Ag/Ag^+. *Probably not true values because of the split oxidation wave as shown in Figure 26.

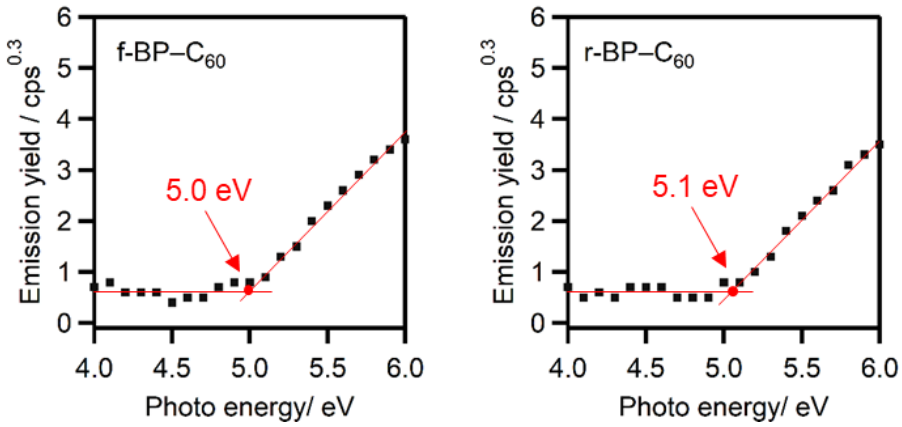

Figure 24. Photoelectron spectroscopy in air of f-BP–C_{60} and r-BP–C_{60} films.

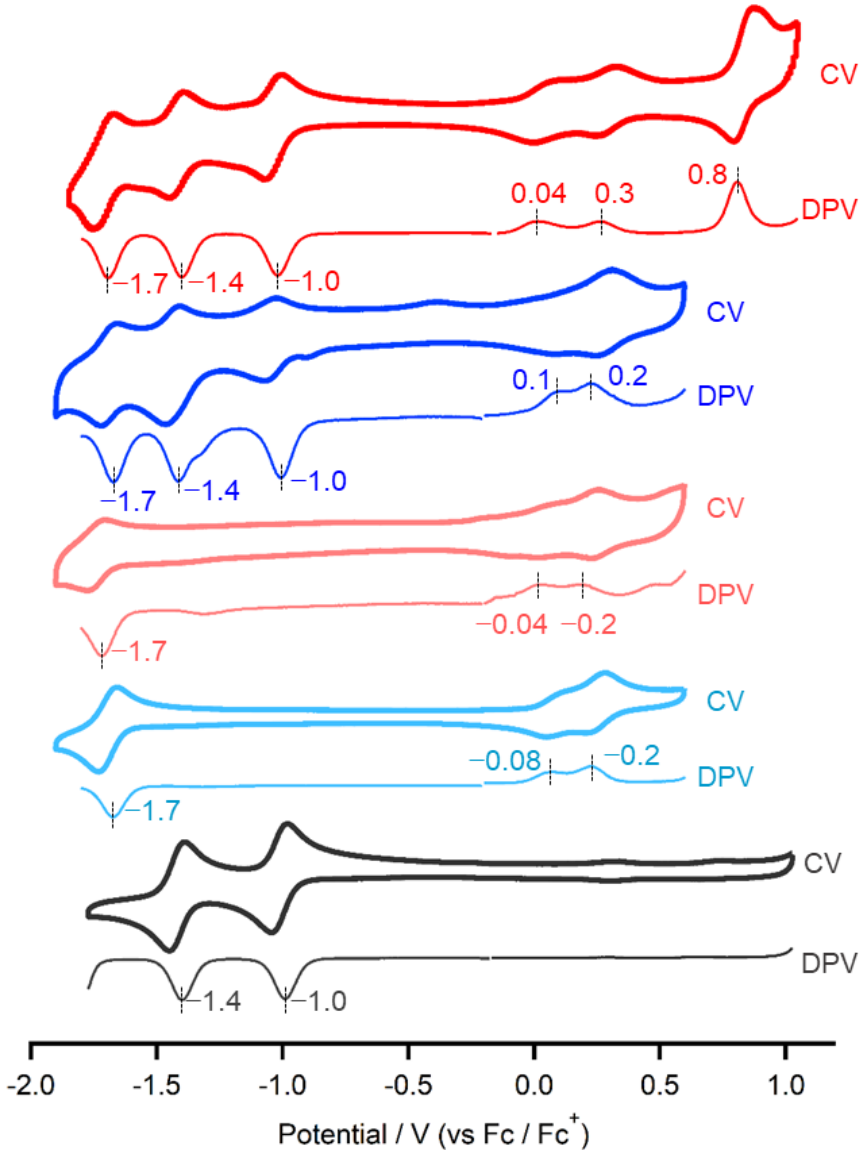

Figure 25. Cyclic voltammograms (CVs) and differential pulse voltmmograms (DPVs) of f-BP–C_{60} (Red), r-BP–C_{60} (Blue), Bu-BP (Pink), TMS-BP (Aqua) and $PC_{61}BM$ (black) in benzonitrile.

3-3-3. Device Performance and Film Morphology

To evaluate the electrical properties of BP−C_{60} compounds, the charge carrier mobilities of the f-BP–C_{60} and r-BP–C_{60} films were measured by the space-charge-limited-current (SCLC) technique as shown in Figure 26. Hole-only devices with the structure of [ITO/MoO_3/f-BP–C_{60} or r-BP–C_{60}/MoO_3/Al] and electron-only devices with [ITO/ZnO/f-BP–C_{60} or r-BP–C_{60}/LiF/Al] were fabricated with these same devices using Bu-BP–C_{60} as their reference. As shown in Table 5, the hole (μ_h) and electron (μ_e) mobilities of the f-BP–C_{60} film were 2.3×10^{-5} cm^2 V^{-1} s^{-1} and 4.4×10^{-5} cm^2 V^{-1} s^{-1}, while those of the r-BP–C_{60} film were 6.8×10^{-5} and 5.8×10^{-5} cm^2 V^{-1} s^{-1}, respectively. These results are around single-digit increased mobilities compared with Bu-BP–C_{60} film ($\mu_h = 2.3\times10^{-6}$ and $\mu_e = 3.1\times10^{-6}$ cm^2 V^{-1} s^{-1}). From these SCLC measurement, the butyl group in Bu-BP–C_{60} can be indicated as insulating moiety in BP–C_{60} system. The hole and electron mobilities in the f-BP–C_{60} and r-BP–C_{60} films were roughly balanced, respectively, and seemed to be suitable for the BHJ layer than Bu-BP–C_{60}. The hole mobility of r-BP–C_{60} is three times larger than that of the f-BP–C_{60} film, while their electron mobilities are almost the same. Note that both f- and r-BP–C_{60} film prepared by thermal conversion of f- and r-CP–C_{60} films did not show any crystallinity as shown in Figure 30. However, we suppose that observed better hole mobility of r-BP–C_{60} could be due to difference of interaction extent between BP and C_{60} in a solid state. In fact, experimental results of single crystal structure of r-ZnBP-C_{60} and UV–vis absorption spectra as film are suggesting an increased interaction between BP and C_{60} moieties than f-BP–C_{60} film. Thus, r-BP–C_{60} structure might be able to partly form the beneficial charge pass like single crystal r-ZnBP–C_{60} in the film to exhibit the improved hole mobility.

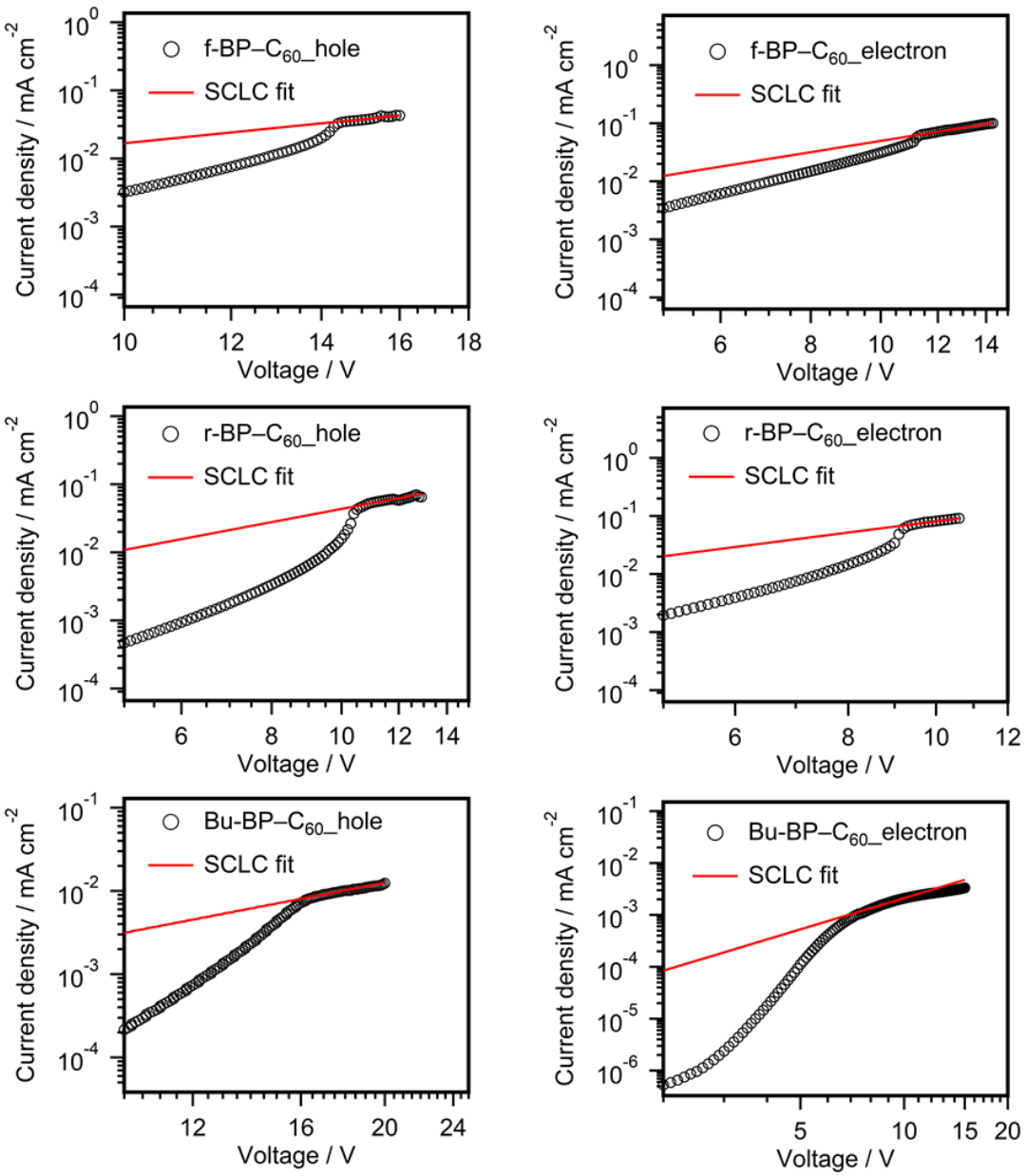

Figure 26. SCLC hole and electron measurements of f-BP–C_{60}, r-BP–C_{60} and Bu-BP–C_{60}.

Table 5. Carrier motility values of f-BP–C_{60}, r-BP–C_{60}, and Bu-BP–C_{60}.

Active layer	μ_h / cm^2 V^{-1} s^{-1} (Active layer thickness /nm)	μ_e / cm^2 V^{-1} s^{-1} (Active layer thickness /nm)
f-BP–C_{60}	2.3×10^{-5} (118)	4.4×10^{-5} (102)
r-BP–C_{60}	6.8×10^{-5} (123)	5.8×10^{-5} (95)
Bu-BP–C_{60}	2.3×10^{-6} (99)	3.1×10^{-6} (120)

To investigate the OPV performances of the BHJ-type devices with a [ITO/PEDOT:PSS/f-BP–C_{60} or r-BP–C_{60}/Ca/Al] structure, the f-BP–C_{60} or r-BP–C_{60} active layer was prepared by spin-coating a f-CP–C_{60} or r-CP–C_{60} solution followed by heating at 180 ºC for 20 min (Figure 27 (a)). The details of the device performance are summarized in Experimental section. The current density–voltage (*J*–*V*) curve and external quantum efficiency (EQE) are shown in Figure 27 (b), and the OPV performances are summarized in Table 6. The performance of the previously reported Bu-BP–C_{60} was also studied to investigate the influence of additional butyl groups at the *meso*-position.

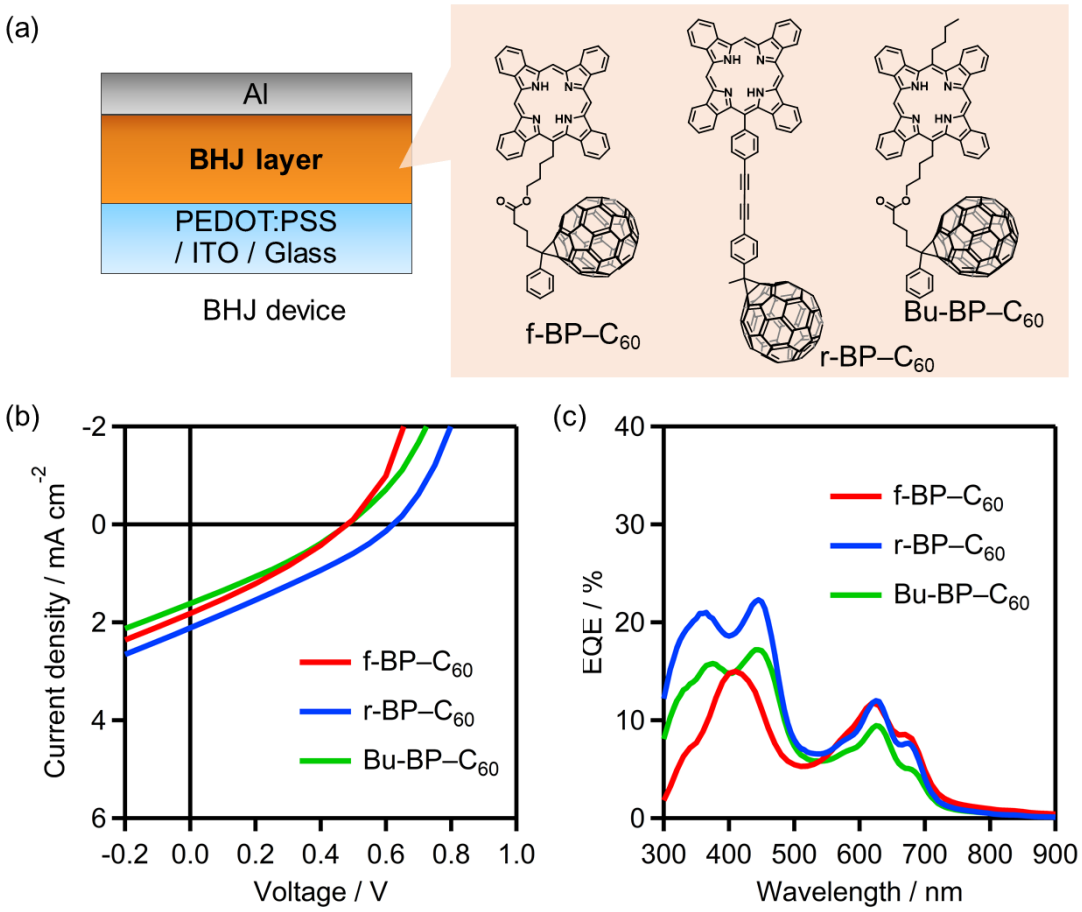

Figure 27. (a) BHJ device structure using f-, r- and Bu-BP–C_{60} as BHJ layer with (b) *J*–*V* curves and (c) EQE spectra of these BHJ devices.

With the removal of the butyl group from Bu-BP–C_{60} to f-BP–C_{60}, the J_{SC} of the BHJ device was improved from J_{SC} = 1.60 mA cm^{-2} to 1.82 mA cm^{-2} with an improvement in the series resistance (R_S), while V_{OC} and FF did not change. The PCE was almost the same for f-BP–C_{60} and Bu-BP–C_{60} at 0.23 and 0.26%, respectively. This result suggests the butyl group at the *meso*-position has little influence on the OPV performance. With the rigid linker, r-BP–C_{60} showed a better J_{SC} and V_{OC}, which improved the PCE to 0.38%. These results are in good agreement with the SCLC performance, where the r-BP–C_{60} film has a better carrier mobility than the f-BP–C_{60} film. In addition, BHJ (r-BP–C_{60}) device showed specific improvement in V_{OC} to achieve 0.64 V, the highest value in all of BHJ devices. One of the reasons that r-BP–C_{60} showed the best V_{OC} value can be attributed the difference of HOMO energy levels compared with flexible BP–C_{60} molecules. As mentioned above, the HOMO energy level of −5.1 eV observed in r-BP–C_{60} film is −0.1 eV lower than flexible BP–C_{60}. These results are comparatively coincided with difference of V_{OC} values.

Table 6. Summary of BHJ device performance.

BHJ layer	PCE (ave*) / %	J_{SC} / mA cm^{-2}	V_{OC} / V	FF	R_s / Ω cm^2	R_{sh} / Ω cm^2
f-BP–C_{60}	0.26 (0.26 ± 0.00)	1.82	0.48	0.29	163	490
r-BP–C_{60}	0.38 (0.35 ± 0.03)	2.11	0.62	0.29	121	361
Bu-BP–C_{60}	0.23 (0.22 ± 0.01)	1.60	0.49	0.29	197	384

* At least four devices in all.

The microscopic surface morphology of the films was investigated by tapping-mode atomic-force microscopy (AFM), as shown in Figure 28. Both f-BP–C_{60} and r-BP–C_{60} films showed relatively smooth surfaces with root-mean square (RMS) roughness of 0.41 and 0.81 nm. The crystallinity of the films was examined by out-of-plane X-ray diffraction (XRD) analysis, but no signal peaks were observed (Figure 29), which suggested that the films are amorphous. The annealing temperature changed from 160 to 220 ºC, but the results were the same. Although the r-BP–C_{60} film has a better carrier mobility than the f-BP–C_{60} film, we could not find the apparent difference in the film morphology of these films.

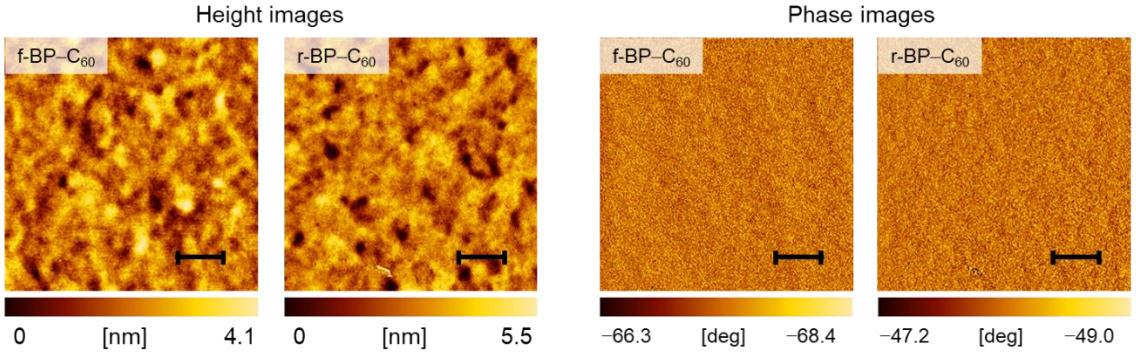

Figure 28. Tapping-mode AFM height and phase images of f-BP–C_{60} film and r-BP–C_{60} film. RMS values estimated from height images are 0.41 and 0.81 nm for f-BP–C_{60} film and r-BP–C_{60} film. The scale bars correspond to 1 μm.

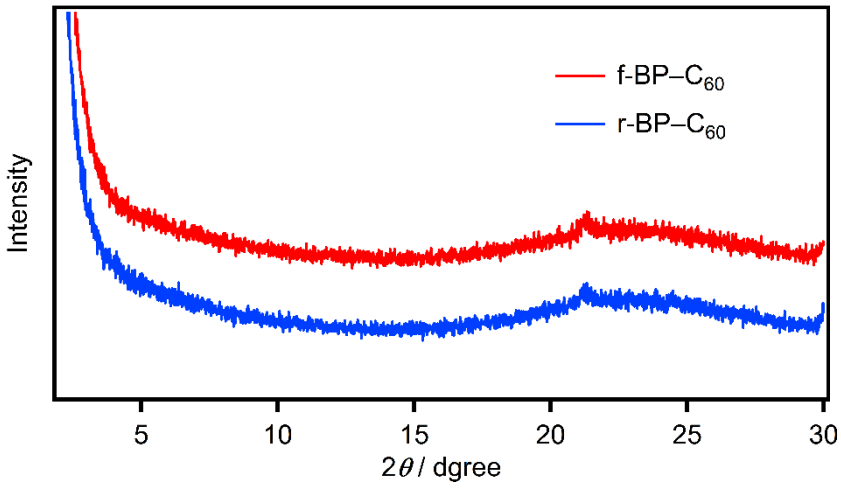

Figure 29. Out-of-plane XRD patterns of f-BP–C_{60} and r-BP–C_{60} layer on PEDOT:PSS/ITO/glass.

Next the p–i–n devices were prepared by sequential fabrication of the BP-, BP–C_{60}- and $PC_{61}BM$-layers as the p-, i-, and n-layers, respectively (Figure 30 (a)). The *J*–*V* curves and EQE spectra are also shown in Figure 30b and 30c. And photovoltaic performances are summarized in Table 7 with those of the p–n device using BP and $PC_{61}BM$ as a reference. The optimization of the film thickness of i-layers is summarized in Tables 8 and 9, while the p-layer and n-layer were fixed to 23 and 45 nm, respectively. With f-BP–C_{60} for the i-layer, the film thickness of the i-layer changed from 46 to 30 nm, and the best PCE performance of the p–i–n device was obtained as J_{SC} = 5.27 mA cm^{-2},

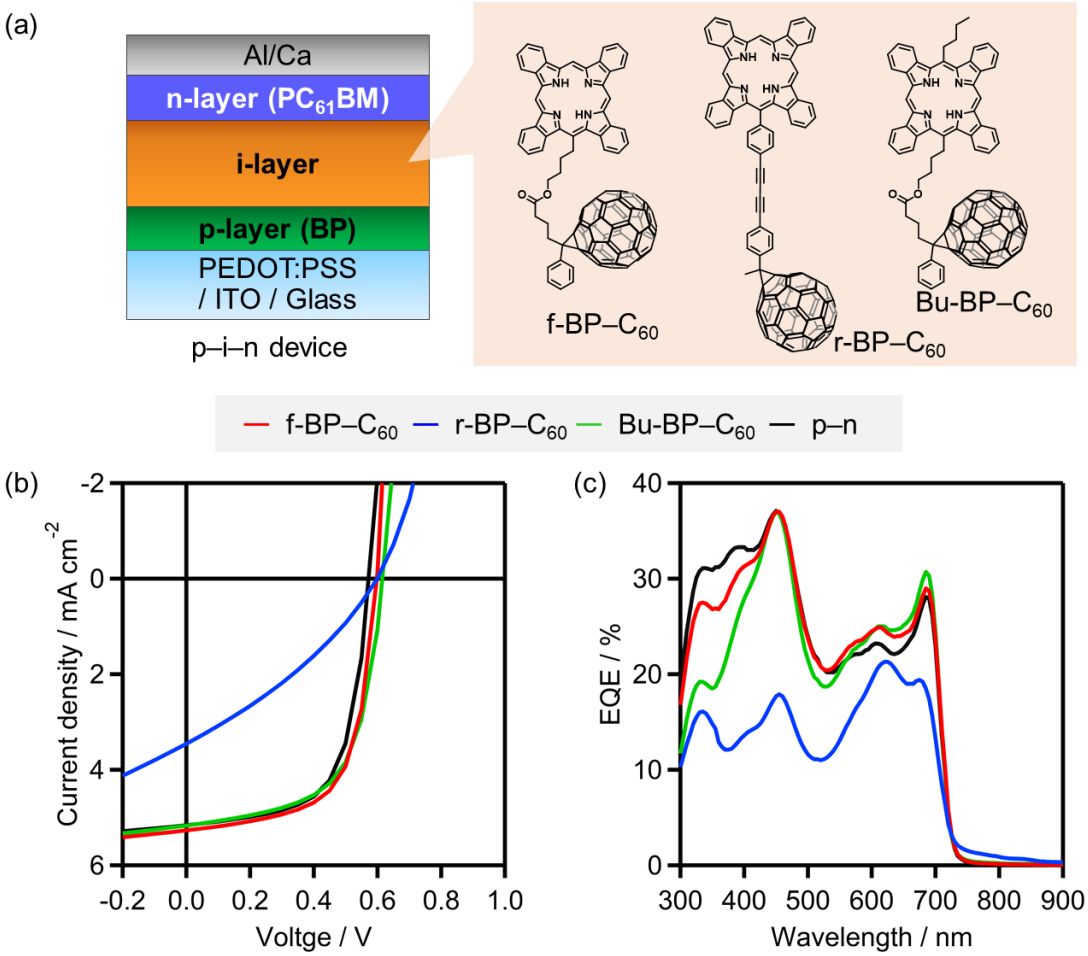

Figure 30. (a) p–i–n device structure using f-, r- and Bu-BP–C_{60} as i-layer with (b) *J*–*V* curves and (c) EQE spectra of these p–i–n devices.

V_{OC} = 0.60 V, FF = 0.63 and PCE = 2.00% at a 35 nm thickness. The performance is comparable to that of Bu-BP–C_{60}, and the removal of the butyl group on the *meso*-position of the BP did not affect the PCE performance of the p–i–n device. For the p–i–n device using r-BP–C_{60}, J_{SC} and FF did not improve from the BHJ device,and the best PCE was only 0.67% at a 46 nm i-layer thickness. It is interesting that the PCE performance of the BHJ device for r-BP–C_{60} is better, while that of the p–i–n device was worse than f-BP–C_{60}. The OPV performance of p–i–n with F-BP–C_{60} for the i-layer was only slightly improved from the p–n device of BP and $PC_{61}BM$.

Table 6. Summary of p–i–n and p–n device performance

p–i–n device (i-layer)	PCE (ave*) / %	J_{SC} / mA cm^{-2}	V_{OC} / V	FF	R_s / Ω cm^2	R_{sh} / Ω cm^2
f-BP–C_{60}	2.00 (1.97 ± 0.03)	5.27	0.60	0.63	8	1254
r-BP–C_{60}	0.67 (0.66 ± 0.01)	3.46	0.60	0.32	72	280
Bu-BP–C_{60}	1.98 (1.89 ± 0.03)	5.17	0.62	0.61	12	1105
p–n device	1.89 (1.78 ± 0.10)	5.16	0.57	0.64	10	1396

* At least four devices in all.

Table 7. Effect of i-layer condition for p–i–n devices using f–BP–C_{60}

i-Layer thickness / nm	PCE / %	J_{SC} / mA cm^{-2}	V_{OC} / V	FF	R_s / Ω cm^2	R_{sh} / Ω cm^2
46	1.82	5.26	0.59	0.59	9	650
45	1.91	5.15	0.60	0.60	12	1101
41	1.93	5.23	0.59	0.63	10	1092
39	1.98	5.28	0.58	0.65	7	1335
35	2.00	5.27	0.60	0.63	8	1254
30	1.81	4.94	0.57	0.64	6	1189

Table 8. Effect of i-layer condition for p–i–n devices using r–BP–C_{60}

i-Layer thickness / nm	PCE / %	J_{SC} / mA cm^{-2}	V_{OC} / V	FF	R_s / Ω cm^2	R_{sh} / Ω cm^2
50	0.42	2.20	0.62	0.31	148	423
46	0.67	3.46	0.60	0.32	72	280
43	0.48	2.63	0.57	0.32	107	340
39	0.42	2.35	0.59	0.31	138	363
38	0.26	2.32	0.40	0.28	136	204
34	0.15	2.19	0.26	0.26	108	129

To investigate the morphology of the i-layer, AFM images of i-layers on the p-layer (BP film) were measured. The AFM of BP film is shown in Figure 31. The RMS roughness is relatively high at 12.4 nm because of the high crystallinity of BP. The RMS roughness of the f-BP–C_{60} films on a BP layer is 4.88 nm, while the RMS of r-BP–C_{60} on BP layer is 7.75 nm (Figure 32). The flexible f-BP–C_{60} can level and smooth the rough p-layer surface, but the rigid r-BP–C_{60} could not offset the roughness of the lower layer. The surface of the n-layers on the i-layers shows similar AFM images for the three devices, and the RMS roughness of the $PC_{61}BM$ layers on the f-BP–C_{60}, and r-BP–C_{60} layers are 1.73 and 1.08 nm, respectively (Figure 33). The similarity of the roughness of the two systems seems to come from the amorphous property of $PC_{61}BM$. Thus, the rigid r-BP–C_{60} layer on the BP layer does not have a good interface morphology, and the f-BP–C_{60} can even out the surface of the p-layer because of the flexibility. Since the r-BP–C_{60} is rigid and could not smooth the roughness of the p-layer, as shown in the AFM image, the rigid structure might have a worse effect on carrier injection between the p-layer and i-layer. Since the mobility of the r-BP–C_{60} film is higher than that of the f-BP–C_{60}, the combination with a smooth p-layer might improve the performance. The p–n device of BP and $PC_{61}BM$ showed a relatively high performance, which was almost comparable to the p–i–n structure with f-BP–C_{60}. This is because the rough surface of BP was covered with amorphous $PC_{61}BM$, and a pseudo-p–i–n structure was constructed in a p–n device.[13]

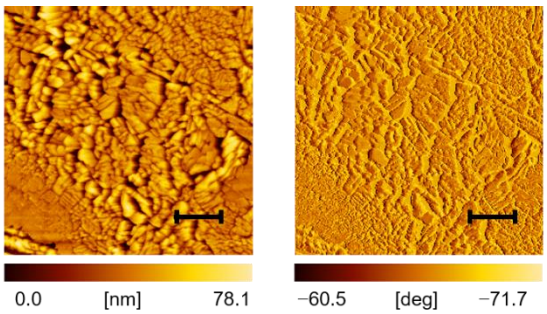

Figure 31. Tapping-mode AFM height (left) and phase (right) images of BP-layer. The RMS value of the height image is 12.4 nm. The scale bars correspond to 1 μm.

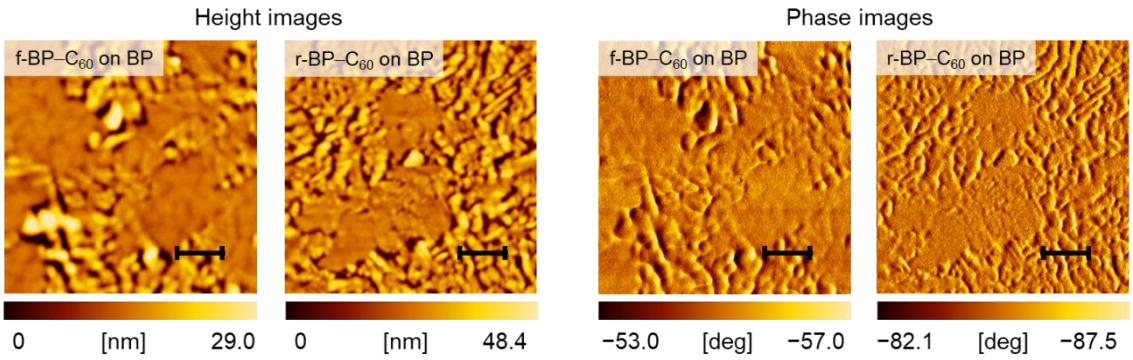

Figure 32. Tapping-mode AFM height and phase images of f-BP–C_{60} and r-BP–C_{60} on the BP-layer. The RMS values of height images are 4.33 and 7.75 nm for f-BP–C_{60} on the BP-layer and r-BP–C_{60} on the BP-layer. The scale bars correspond to 1 μm.

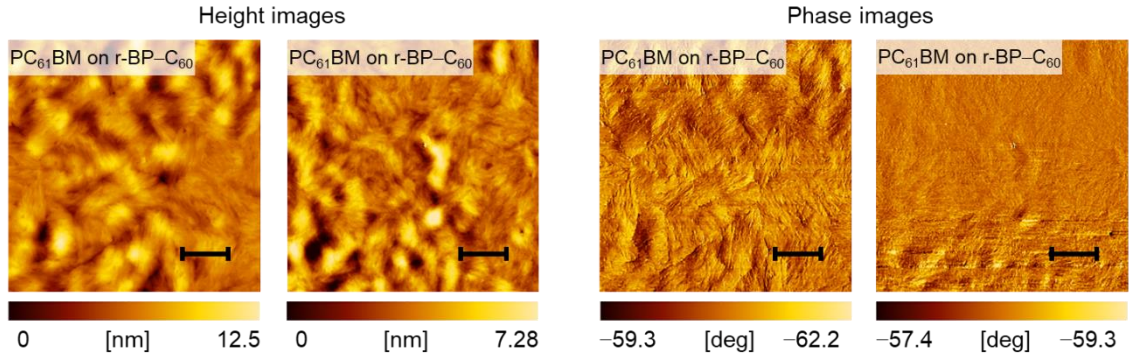

Figure 33. Tapping-mode AFM height and phase images of $PC_{61}BM$-layer on f-BP–C_{60} and r-BP–C_{60}. The RMS values of height images are 1.73 and 1.08 nm for $PC_{61}BM$ on f-BP–C_{60} and $PC_{61}BM$ on r-BP–C_{60}. The scale bars correspond to 1 μm.

3-4. Summary

Studies in this chapter were successful in constructing OSC devices composed of BP–C_{60} for BHJ- and i-layer, respectively, using the in situ thermal conversion from solution-deposited CP–C_{60} to BP–C_{60}.

The Bu-BP–C_{60} film showed better performance in a p–i–n device associated with a higher FF compared to the 1:1 blend film of BP and $PC_{61}BM$. The grain boundaries in the blend film could have increased the resistance in the film and therefore lowered the FF values. In contrast, the Bu-BP–C_{60} did not form grains and the resultant p–i–n device showed lower series resistances than the corresponding device based on the blend film. Moreover, flexible and rigid linkage structure of f-BP–C_{60} and r-BP–C_{60} exhibited recognizable difference in optical- and photovoltaic-properties. The fluorescence of BP was quenched more efficiently in f-BP–C_{60} than in r-BP–C_{60} in CH_2Cl_2 because of the intramolecular through-space approach of C_{60} to BP by the flexible spacer. In the film, r-BP–C_{60} showed higher hole and electron carrier mobilities than f-BP–C_{60}. The well-balanced carrier mobility of the r-BP–C_{60} film resulted in a twice better performance of the BHJ-type OPV than the f-BP–C_{60}. However, when the molecules were used for i-layers in p–i–n devices, the trend was reversed. The OPV performance of the p–i–n device with f-BP–C_{60} in the i-layer was 2.0%, while that with r-BP–C_{60} was 0.67%. The flexible structure of the f-BP–C_{60} smoothed the rough surface of the p-layer and kept the good FF of the p–n device even in the p–i–n device. On the other hand, the FF of the p–i–n with r-BP–C_{60} was depressed to 0.32. The rigid and long molecule might not be suitable to smooth the surface of a high roughness p-layer.

As mentioned above, the interface of the p–n device with BP and $PC_{61}BM$ is rough, and it will be an intrinsically pseudo p–i–n structure with a crystalline BP-layer and amorphous $PC_{61}BM$-layer. To improve the p–n device of BP and $PC_{61}BM$ by p–i–n structure using the BP–C_{60} dyad for the i-layer, p- and n-materials in the i-layer should be well-mixed, and the interface area of the p- and n-materials has to be spread for the effective charge separation. This result suggests that the proper crystallinity gives better carrier mobilities, but at the same time, a smooth interface between each layer is required.

3-5. Outlook

These works suggested good morphological availability of BP–C_{60} system as OSCs material compared with simple mixing BP:$PC_{61}BM$ system. However, their photovoltaic performances are still limited to 2.0 %, and the effect of the i-layer is not promising. To achieve advanced BP–C_{60} systems, interface area of i-layer has to be spread for the effective charge separation and crystallinity should be achieved for the better hole and electron transport. In fact, over 10^{-4} cm^2 V^{-1} s^{-1} hole and electron mobilities at least with good balance were reported in state-of-the-art OSC materials which can show over 10% of PCE.[24–26] For the better charge separation, short face-to-edge distance between BP and C_{60} is necessary. For the better crystallinity, appropriate rigidity, but not expanded shape, is probably important. Considering these points, another idea is an introduction of the hydrophilic or semi-flexible linker to promote the phase separation of donor and acceptor result in a higher crystallinity (Figure 34). The hydrophilic flexible linker such as ethylene glycol chain has been reported in dyad molecules for a single-component OSC.[5–8] The comparing hydrophilic flexible linker with hydrophobic linker (e.g. alkyl linker as we used) has scarcely known. But effective phase separation of donor and acceptor components result in constructions of fiber-like nanostructure and crystallization

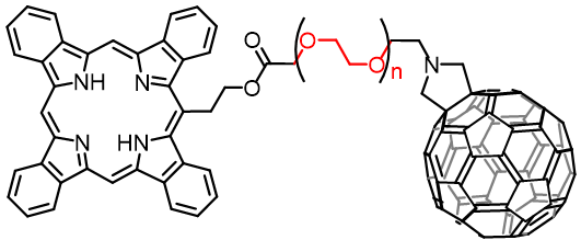

Flexible linkage with hydrophilic linker

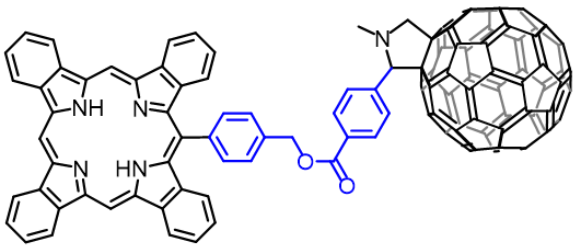

Semi-flexible linkage with phenyl–ester linker

Figure 34. Molecular design of BP–C_{60} conjugated with semi-flexible or the hydrophilic flexible linker.

of donor component of dyad molecules in the film have been reported. On the other hand, semi-flexible linker such as phenyl group linked with ester coupling is not majority as linkage structure for dyad based OSC materials. However, interesting coaxially segregated porphyrin and C_{60} nanodomains with ambipolar carrier transport properties was achieved [27].

Our synthetic development for unsymmetrical *meso*-substituted BP will be favorable access to these BP–C_{60} molecules. Note that D–A linked molecule based OSC materials which investigated with various linker structures for the same donor and acceptor unit have been scarce to date. Therefore, these studies will lead to more useful knowledge for D–A molecular design and will be help to pave the way toward realizing our goal.

3-6. Support Information

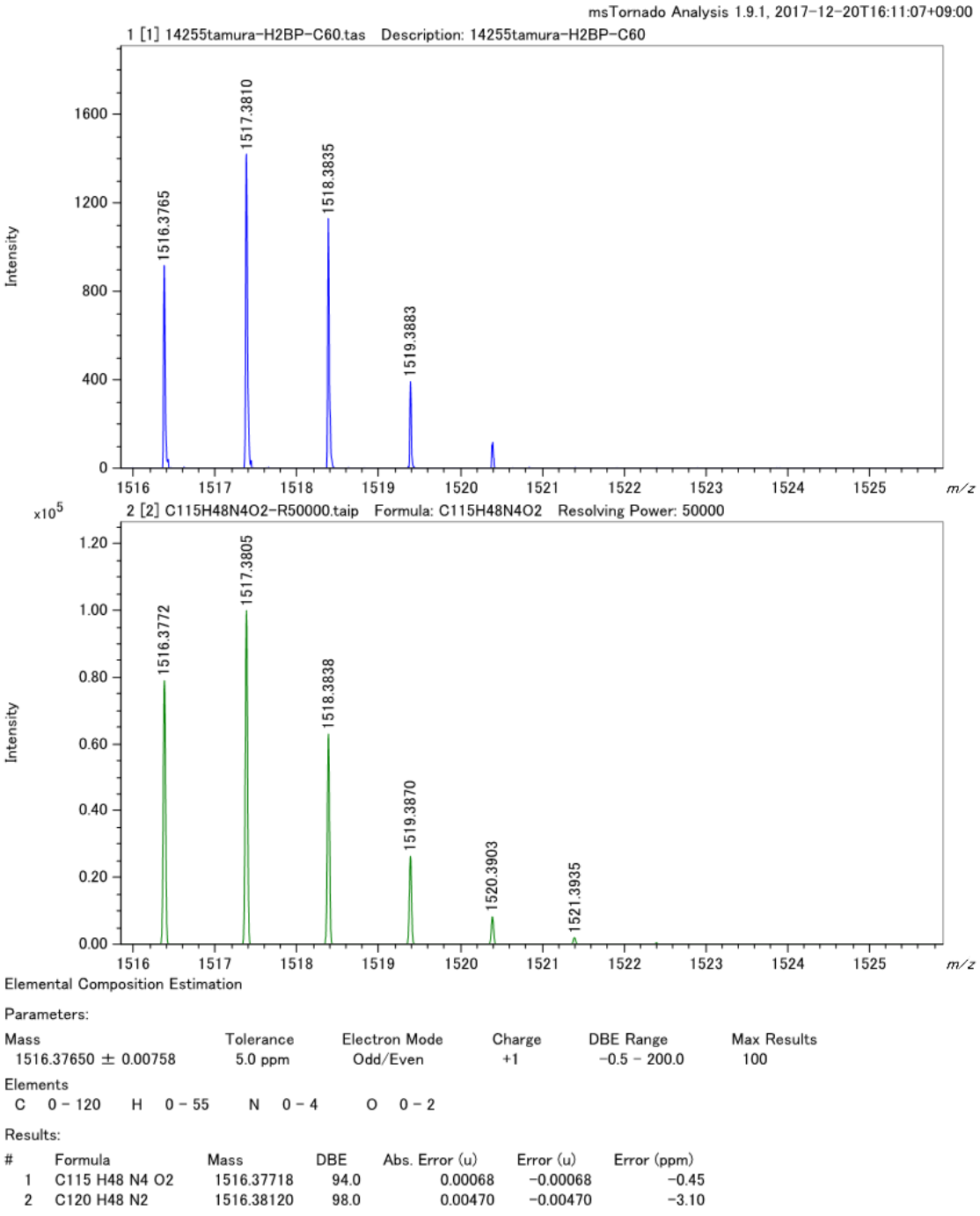

Figure S3-1. HR-MALDI spiral-TOF mass spectrum of Bu-BP–C_{60}. Upper is simulation for $C_{115}H_{48}N_4O_2$ and lower is the obtained spectrum.

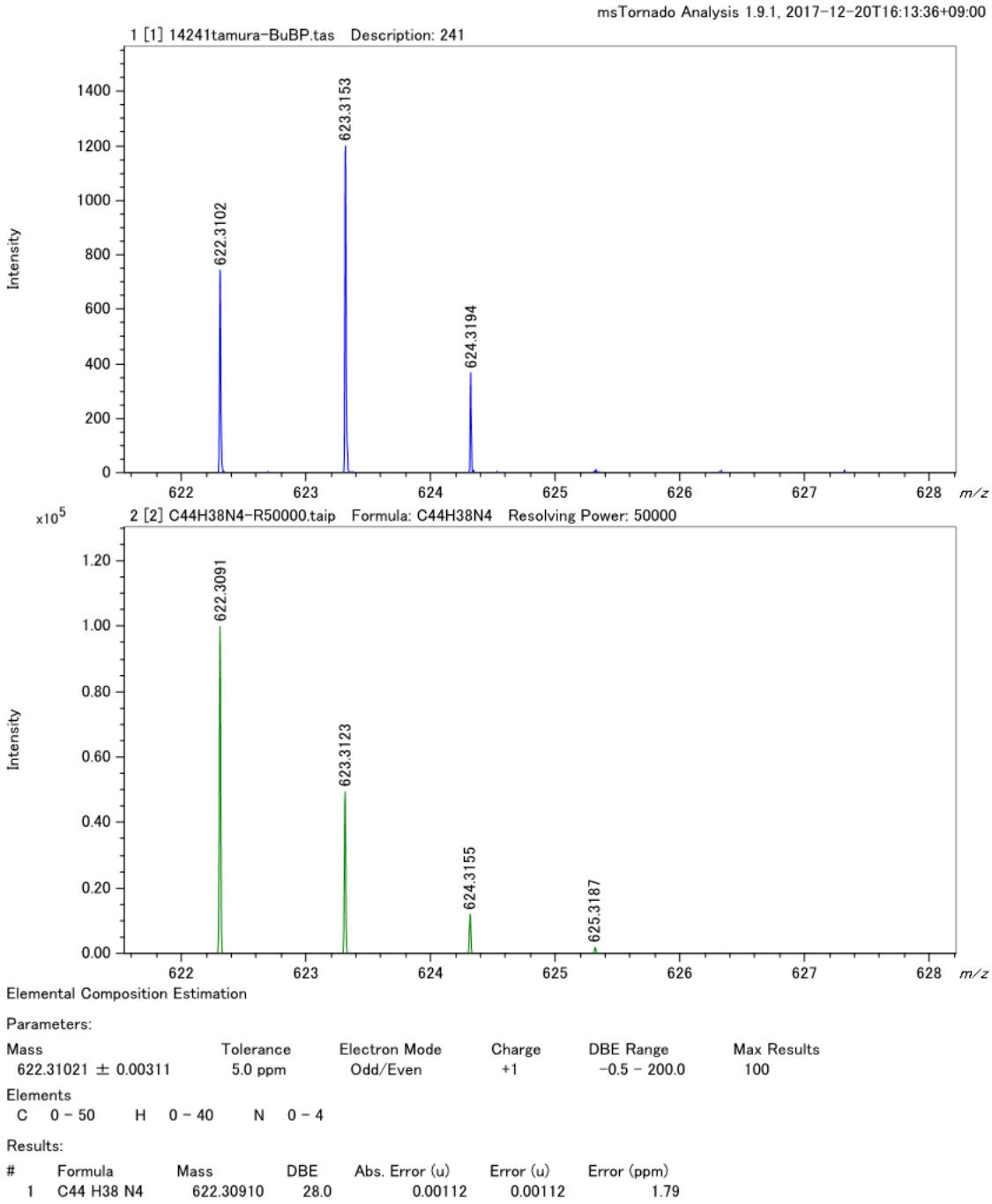

Figure S3-2. HR-MALDI spiral-TOF mass spectrum of DiBu-BP. Upper is simulation for $C_{44}H_{38}N_4$ and lower is the obtained spectrum.

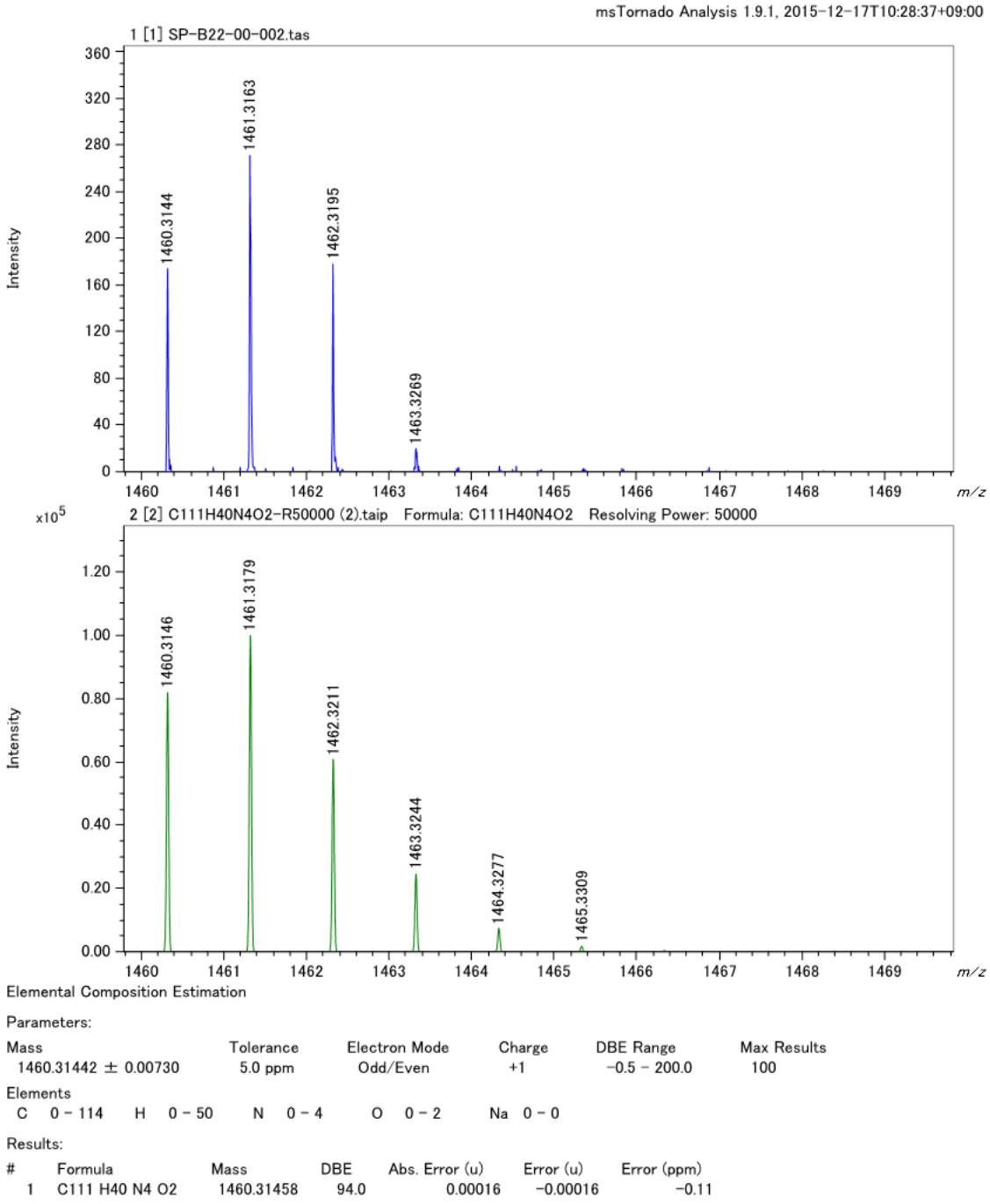

Figure S3-3. HR-MALDI spiral-TOF mass spectrum of f-BP–C_{60}. Upper is the obtained spectrum and lower is simulation for $C_{111}H_{40}N_4O_2$.

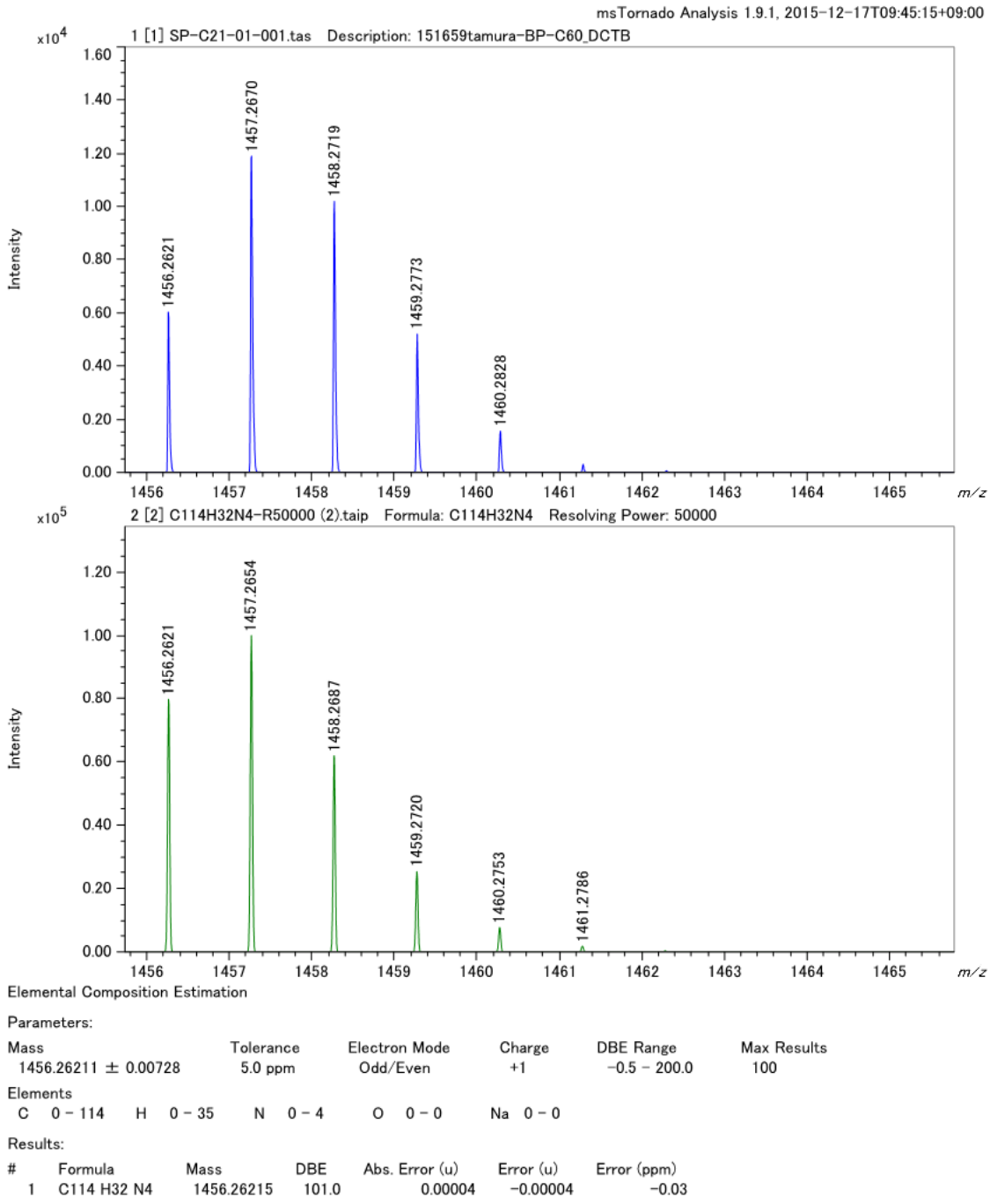

Elemental Composition Estimation

Parameters:

Mass	Tolerance	Electron Mode	Charge	DBE Range	Max Results
1456.26211 ± 0.00728	5.0 ppm	Odd/Even	+1	−0.5 – 200.0	100

Elements

C 0 – 114 H 0 – 35 N 0 – 4 O 0 – 0 Na 0 – 0

Results:

#	Formula	Mass	DBE	Abs. Error (u)	Error (u)	Error (ppm)
1	C114 H32 N4	1456.26215	101.0	0.00004	−0.00004	−0.03

Figure S3-4. HR-MALDI spiral-TOF mass spectrum of r-BP–C_{60}. Upper is the obtained spectrum and lower is simulation for $C_{114}H_{32}N_4$.

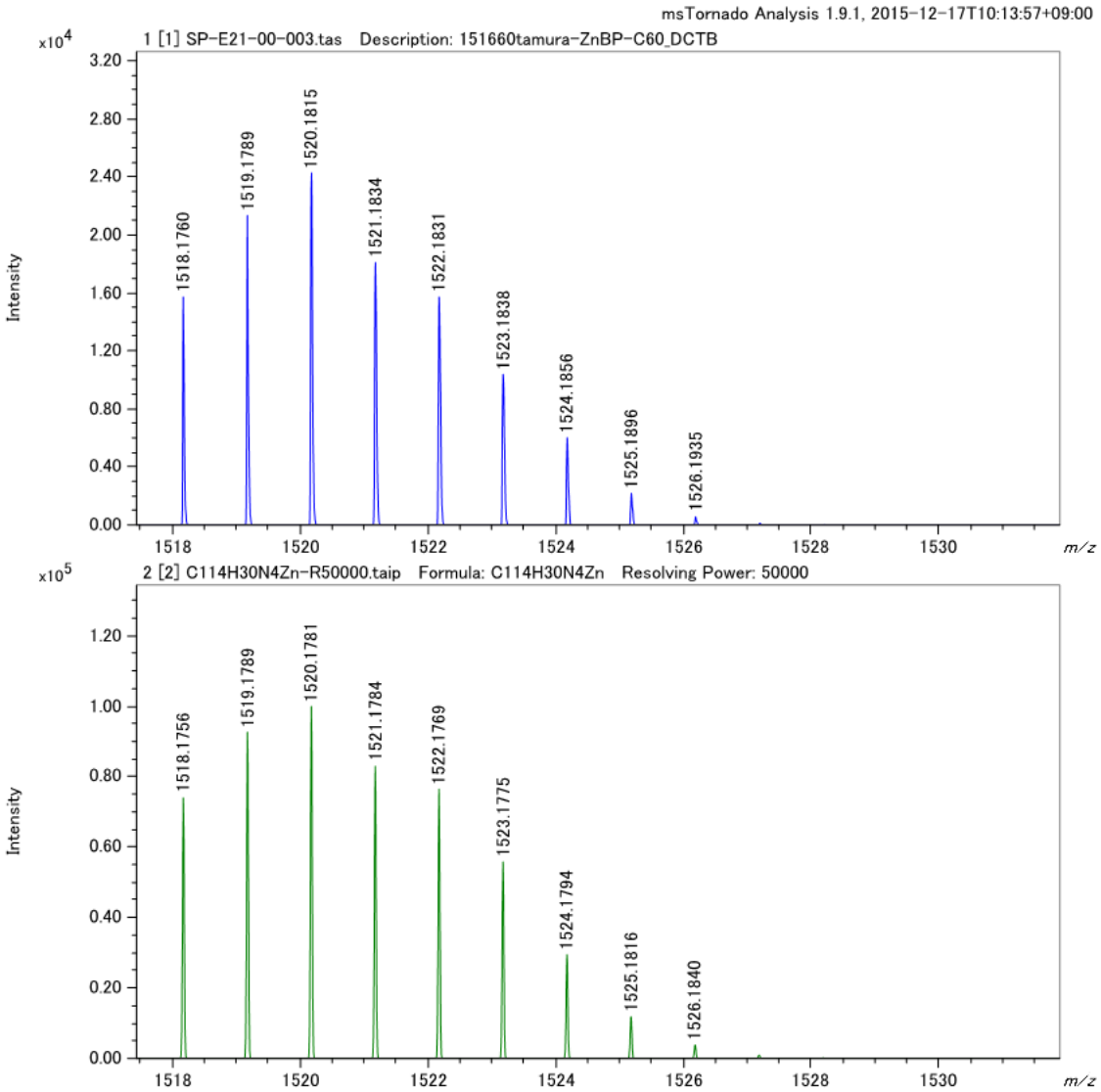

Elemental Composition Estimation

Parameters:

Mass	Tolerance	Electron Mode	Charge	DBE Range	Max Results
1518.17601 ± 0.00759	5.0 ppm	Odd/Even	+1	−0.5 – 200.0	100

Elements

C	H	N	Zn	Na
0 – 114	0 – 50	0 – 4	0 – 1	0 – 0

Results:

#	Formula	Mass	DBE	Abs. Error (u)	Error (u)	Error (ppm)
1	C114 H30 N4 Zn	1518.17565	102.0	0.00037	0.00037	0.24

Figure S3-5. HR-MALDI spiral-TOF mass spectrum of r-ZnBP–C_{60}. Upper is the obtained spectrum and lower is simulation for $C_{114}H_{30}N_4Zn$.

Table S1. Crystal data and structure refinement for r-ZnBP–C_{60}.

Empirical formula	C114 H30 N4 Zn	
Formula weight	1520.79	
Temperature	90(2) K	
Wavelength	0.78203 Å	
Crystal system	Triclinic	
Space group	*P*-1	
Unit cell dimensions	a = 10.040(6) Å	α = 86.692(10)°
	b = 12.650(8) Å	β = 88.631(8)°
	c = 33.76(2) Å	γ = 79.903(9)°
Volume	4213(5) Å^3	
Z	2	
Density (calculated)	1.199 Mg/m^3	
Absorption coefficient	0.441 mm^{-1}	
F(000)	1544	
Crystal size	0.090 x 0.050 x 0.010 mm^3	
Theta range for data collection	0.665 to 25.499°	
Index ranges	$-10 \le h \le 11$, $-13 \le k \le 13$, $-36 \le l \le 37$	
Reflections collected	16821	
Independent reflections	11233 [R(int) = 0.2460]	
Completeness to theta = 25.500°	95.7%	
Absorption correction	Semi-empirical from equivalents	
Refinement method	Full-matrix least-squares on F^2	
Data / restraints / parameters	11233 / 1682 / 1001	
Goodness-of-fit on F^2	0.885	
Final R indices [$I > 2\sigma(I)$]	R_1 = 0.1990, wR_2 = 0.3410	
R indices (all data)	R_1 = 0.3872, wR_2 = 0.4152	
Largest diff. peak and hole	0.948 and −0.716 e.Å^{-3}	

The size and quality of the single crystals were not good enough to allow us to do an accurate bond length analysis. The contributions to the scattering arising from the presence of the disordered solvents in the crystals were removed by use of the utility SQUEEZE in the PLATON software package.[28]

Explanation for a "level A" alert: Since the crystals contained many severely disordered solvent molecules and a fullerene moiety, they gave only weak diffractions. However, these are not significant concern for the main skeletal structure.

3-7. Experimental Section

3-7-1. General

Materials

Anhydrous THF (Super Plus grade, stabilizer free) and CH_2Cl_2 (Super grade) were obtained from Kanto Chemical and used as received. All other solvents and chemicals were of reagent grade, were obtained commercially and were used without further purification. Tosylhydrazine ($TsNHNH_2$) was used after recrystallization from hot water. Tetrabutylammonium hexafluorophosphate ($TBAPF_6$) was used as an electrolyte for electrochemical measurements after recrystallization from EtOH. Semico cleane 53, a detergent of substrate, was purchased from Furuuchi Chemical. [6,6]-Phenyl-C_{61}-butyric acid methyl ester ($PC_{61}BM$, ≥ 99.5% by HPLC with respect to fullerene content) was purchased from SES Research, and was used without further purification. Spectral grade chloroform ($CHCl_3$) for sample deposition solvent was purchased from Nacalai tesque Inc. (3,4-ethylenedioxythiophene): poly(4-styrenesulfonate) (PEDOT:PSS, Clevios P VP AI4083) was purchased from Heraeus Deutschland GmbH & Co. and was used after filtration using MILLEX-HP Filter unit (0.45 μm, PES Membrane) purchased from Merck Millipore Ltd..

Bis(4,7-dihydro-4,7-ethano-*2H*-isoindol-1-yl)methane[15] (**4**), [6,6]-phenyl-C_{61}-butyric acid (PCBA)[8] (**3**), Bis(4,7-dihydro-8,8-dimethyl-4,7-ethano-*2H*-isoindol-1-yl)methane[20] (**8**), 4-(bromoethynyl)benzaldehyde[21] (**10**), and 4'-(2-trimethylsilylethynyl)acetophenone[22] (**12**) were prepared according to described literatures. Dimethyl-4,7-dihydro-*2H*-4,7-ethanoisoindol-1-yl)methanol[20] (**9**) was synthesized from ethyl 4,7-dihydro-8,8-dimethyl-4,7-ethano-*2H*-isoindole-1-carboxylate[20] as described in the literature. Because **9** is unstable compound under ambient condition, fresh **9** should be prepared every time for a reaction and directly used without further purification.

Purification and Characterization

Room temperature, or r.t., means 20–25 ºC. Thin-layer chromatography (TLC) was conducted on Art. 5554 (Merck KGaA) with visualization using UV light at 254 or

365 nm. Material purifications were performed by gravity column chromatography on Silica Gel 60N, 60 Å, 63–210 μm (Kanto Chemical Co.), Alumina Activated 200, Particle size: approx. 200mesh, Specially Prepared Reagent (NACALAI TESQUE, INC.), and gel permeation chromatography (GPC) using JAILC-9225NEXT equipped with JAIGEL 1H and 2H polystyrene gel columns (600 × 40 mm; bead size = 16 μm; pore size = 20–30 (1H) and 40–50 (2H) Å) at room temperature using $CHCl_3$ as an eluent. ^1H NMR and $^{13}C\{^1H\}$ NMR spectra were recorded on a JNM-ECX400 spectrometer using tetramethylsilane or solvent as an internal standard. The thermogravimetric analysis (TGA) was carried out on a Seiko Exstar 6000 TG/DTA 6200 instrument under a nitrogen gas flow with a heating rate of 5 ºC min^{-1}. Materials converted by heating (200 ºC, 10 min) were investigated by MALDI-TOF mass spectra. ESI and MALDI-TOF mass spectra were measured on a JEOL JMST100LC AccuTOF spectrometer and JEOL spiral TOF JMS-S3000 spectrometer, respectively. UV–vis spectra were obtained on a JASCO UV/VIS/NIR Spectrophotometer V-570. Steady-state fluorescence spectra were measured on a JASCO FP-6600 in the range of 300–800 nm. For spectral measurements in solution, spectral grade CH_2Cl_2 was purchased from Nacalai tesque Inc. Fluorescence quantum yields were measured on an Absolute PL Quantum Yield Measurement System C9920-02. Fluorescence lifetimes were measured on a C4780 picosecond fluorescence lifetime measurement device (Hamamatsu Photonics). A Mira Model 900-F & Pulse Switch femtosecond pulse laser was used, and the excitation light wavelength was 405 nm from a coherent Verdi V-5 Nd:YVO_4 laser. Cyclic voltammetry (CV) and differential pulse voltammograms (DPV) were measured on an ALS 612D electrochemical analyzer in a solution of 0.1 M $TBAPF_6$ in PhCN with a scan rate of 0.1 Vs^{-1} at room temperature in an argon-filled cell. A glassy carbon electrode and a Pt wire were used as a working and a counter electrode, respectively. An Ag/Ag^+ electrode was used as a reference electrode, which was normalized with the half-wave potential of ferrocene/ferrocenium$^+$ (Fc/Fc^+) redox couple.

Single Crystal X-Ray Crystallography

The single crystal of r-ZnBP–C_{60} was obtained by diffusion of acetonitrile into chlorobenzene solution. Single-crystal diffraction analysis data collection was carried out at a low temperature (90 K) on a Rigaku Saturn 724 diffractometer using Si (111)

monochromated synchrotron radiation (λ = 0.78203 Å) and a large cylindrical imaging plate camera at the SPring-8 beam line BL40XU (Hyogo, Japan), (proposal No. 2015A1388).

Substrates Cleaning for Sample Films

Slide glass, Indium-tin-oxide (ITO)/glass, and ITO-patterned glass substrate (20.0 × 25.0 mm, < 15 Ω per square) were washed with running water and were ultrasonically cleaned in detergent, pure-water and isopropanol for 10 min each. Then, the substrates were dried with N_2 gas blowing. In case of the ITO-patterned glass substrate used for device fabrications, ozone-treatment was performed for 30 min by UV-O_3 cleaner TC-003 (MEIWAFOSIS CO., LTD.) as a further cleaning.

SCLC Device Fabrication and Evaluation

Charge carrier mobilities in f-BP–C_{60}, r-BP–C_{60} and Bu-BP–C_{60} films were evaluated by the Space-charge-limited-current (SCLC) method. The SCLC device structures for hole-only and electron-only measurements were [ITO/MoO_3/active layer/MoO_3/Al] and [ITO/ZnO/active layer/LiF/Al], respectively. For hole only device, MoO_3 (15 nm) was vapor deposited on the cleaned ITO/glass substrate at high vacuum (< 5.0×10^{-4} Pa). For electron only device, ZnO film (28 nm) was prepared by sol-gel method using the ZnO precursor solution.[29] The ZnO precursor solution was spin coated (5000 rpm, 30 sec) on the cleaned ITO/glass substrate followed by heating (300 ºC, 1 h) under air condition to obtain the ZnO film. Then, substrates were transferred to a N_2-filled glove box (< 10.0 ppm O_2 and H_2O). Each active layer was prepared by spin coating of f-CP–C_{60}, r-CP–C_{60} and Bu-CP–C_{60} in chloroform (14 mg mL^{-1}) at 800 rpm for 30 seconds on ITO/MoO_3 (15 nm) or ITO/ZnO (28 nm), respectively. After spin coating, these films were heated in the same condition for the OPV device fabrication to convert to f-BP–C_{60}, r-BP–C_{60} and Bu-BP–C_{60} in the nitrogen-filled glove box. After preparation of the organic layers, MoO_3 (15 nm)/Al (50 nm) or LiF (1 nm)/Al (50 nm) were vapor deposited at high vacuum (< 5.0×10^{-4} Pa). Current–voltage (*J*–*V*) curves of fabricated SCLC devices were measured by Keithly 2400 source-measure unit in air. To estimate the charge mobility, curve fitting was performed according to the formula as follows,

$$J = \frac{8}{9} \cdot \frac{\varepsilon \varepsilon_0 \mu V^3}{L^3}$$

Where ε is the dielectric constant, ε_0 is the permittivity of space, μ is the charge mobility. V is the applied voltage, and L is the active layer thickness. The dielectric constant ε is assumed to be 3, which is atypical value for organic semiconductors.

OSC Device Dabrication and Evaluation

For fabrication of OSC devices, (3,4-ethylenedioxythiophene): poly(4-styrenesulfonate) (PEDOT:PSS, Clevios P VP AI4083) was spin coated (3000 rpm, 30 s) to the ITO-patterned glass substrates followed by a thermal annealing treatment at 130 ºC for 10 min in air. The thickness of the resulting PEDOT:PSS layer was about 30 nm. The resulting PEDOT:PSS/ITO/glass substrate was transferred to N_2-filled grove box (< 10.0 ppm O_2 and H_2O) for following deposition processes.

The active layers for the BHJ device were deposited by spin coating a chloroform solution (10 mg mL^{-1}, 1500 rpm, 30 seconds) of CP:$PC_{61}BM$ (1:1 mol/mol), Bu-CP–C_{60}, f-CP–C_{60}, r-CP–C_{60}, and followed by heating (160 ºC for CP:$PC_{61}BM$ and Bu-CP–C_{60}, 180 ºC for f-CP–C_{60} and r-CP–C_{60}, 20 min) for in situ conversion to BP:$PC_{61}BM$, Bu-BP–C_{60}, f-BP–C_{60}, and r-BP–C_{60}, respectively. To fabricate the p–i–n device, the p-layer was prepared by spin coating a chloroform solution (7 mg mL^{-1}, 2500 rpm, 30 seconds) of CP followed by heating (200 ºC, 20 min) to effect the in situ conversion of CP to BP. The film thickness was about 23 nm. Next, i-Layer was deposited on the p-layer by spin coating in same manner of BHJ devise deposition as mention above. The most effective i-layer of f-BP–C_{60} or r-BP–C_{60} can be deposited by spin coating (1500 rpm, 30 seconds) a $CHCl_3$ solution of f-CP–C_{60} (7 mg mL^{-1}), f-CP–C_{60} (10 mg mL^{-1}), and followed by heating (180 ºC, 20 min) to effect the in situ conversion to f-BP–C_{60} or r-BP–C_{60}. The n-layer was prepared by spin coating a $CHCl_3$ solution of $PC_{61}BM$ (7 mg mL^{-1}, 1500 rpm, 30 seconds), which was then annealed (195 ºC, 20 min). The film thickness was about 45 nm. After preparation of the organic layers, the buffer layer (Ca, 5 nm) and counter electrode (Al, 50 nm) were vapor deposited at a high vacuum (< 5.0×10^{-4} Pa) through a shadow mask with a defined active area of 4 mm^2. Note that OSC devices without Ca buffer were prepared and evaluated in the first effort (Direct comparison of a covalently-linked BP–C_{60} dyad and a 1:1 mixture of tetrabenzoporphyrin and fullerene as organic

photovoltaic materials). Current density–voltage (*J*–*V*) curves were measured using a Keithley 2611B SYSTEM Source Mater unit under AM1.5G illumination at an intensity of 100 mW cm^{-2} using a solar simulator (Bunko-keiki, CEP-2000RP). The external quantum efficiency (EQE) spectra were obtained under illumination of monochromatic light using the same system.

Film Preparation and Characterization for Thin Film Properties

The typical films of f-BP–C_{60}, r-BP–C_{60}, and Bu-BP–C_{60} for absorption measurements were prepared on clean glass substrates. The spin coating of a 10 mg mL^{-1} solution of f-CP–C_{60}, r-CP–C_{60}, and Bu-CP–C_{60} in chloroform at 1000 rpm for 30 s followed by heating at 200 ºC for 20 min gave f-BP–C_{60}, r-BP–C_{60}, and Bu-BP–C_{60} films. The spin coating and heating were done in a nitrogen-filled glovebox. The absorption spectra were measured by JASCO UV/VIS/NIR Spectrophotometer V-570. The sample films for evaluation of the bulk structure were prepared as described above on clean ITO glass with PEDOT:PSS. In this regard, thermal conversion temperature of CP–C_{60} films was same as OCS fabrications. The bulk structure of the thin films was evaluated by out-of-plane XRD θ–2θ measurements using a RINT-TTRIII/NM diffractometer equipped with a rotating anode (Cu *K*a radiation, λ = 1.5418 Å) operated at 15 kW and Rigaku D/teX Ultra 1D silicon strip detector. The films for measurement of ionization potential also fabricated with same condition described above. Ionization potential of BP, $PC_{61}BM$, and BP–C_{60} films were measured by a Riken photoelectron spectroscopy instrument, AC-3. The obtained ionization energies were used to approximate the HOMO levels of the materials in the thin-film state. Individual BHJ-, p-, p–i-, and p–i–n-films were prepared for measurements of film thickness and Atomic force microscope (AFM). Preparation condition of each film was same as OSCs fabrication as describe OSCs fabrication. Film thickness was measured by a Surface Profiler ET200 (Kosaka Laboratory Ltd) using the same films of AFM measurements. The value was obtained as an average of 10 measurement points. The surface morphology of organic films was observed by a SPA400, SPI3800N AFM (Seiko instruments Inc.) in tapping mode using silicon probes with a resonant frequency of ~138 kHz and a force constant of 16 N m^{-1}.

3-7-2. Synthetic Procedures

[5-butanol-15-butyl-tetrakis(BCOD)porphyrin]zinc (II) (2)

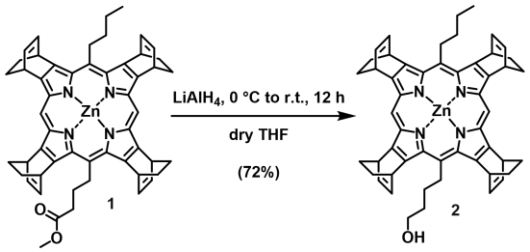

BCOD porphyrin **1** (400 mg, 0.48 mmol) and dry THF (12 mL) were added to a 50-mL two-necked round-bottom flask under nitrogen atmosphere. Lithium Aluminum Hydride ($LiAlH_4$, 36 mg, 0.96 mmol) was added to the solution slowly, and stirred at room temperature for 12 h. A saturated aqueous solution of potassium sodium tartrate was added to quench the reaction. The organic layer was extracted with ethyl acetate and washed with water and brine. Then the organic layer was dried over Na_2SO_4, and the solvent was removed under reduced pressure. The crude product was purified by silica gel column chromatography using ethyl acetate and hexanes (1:4 vol/vol) as an eluent and recrystallization from $CHCl_3$ and hexanes to afford the target compound **2** as pink powder in 72% (280 mg, 0.34 mmol).

^{1}H NMR ($CDCl_3$, 400 MHz): δ (ppm) = 10.14 (s, 2H), 7.04–7.22 (m, 8H), 5.69–5.82 (m, 8H), 5.17–5.47 (m, 4H), 3.79–4.04 (m, 2H), 2.64–3.06 (m, 4H), 1.80–2.51 (m, 20H), 1.22–1.46 (m, 4H); ^{13}C NMR ($CDCl_3$, 100 MHz): δ (ppm) = 151.34, 151.33, 148.01, 147.75, 143.90, 143.78, 140.58, 140.51, 137.21, 137.15, 137.06, 120.26, 119.51, 119.37, 96.62, 96.54, 63.11, 40.96, 36.04, 34.53, 33.48, 31.60, 28.30, 28.27, 28.22, 28.18, 27.69, 27.66, 27.61, 27.59, 27.55, 27.51, 27.47, 27.11, 23.85, 22.66, 14.86, 14.14; HR-MS (ESI): calcd for $C_{52}H_{53}N_4O_2Zn$, 813.3511 $[M + H]^+$; found, 813.3509.

Bu-ZnCP–C_{60}

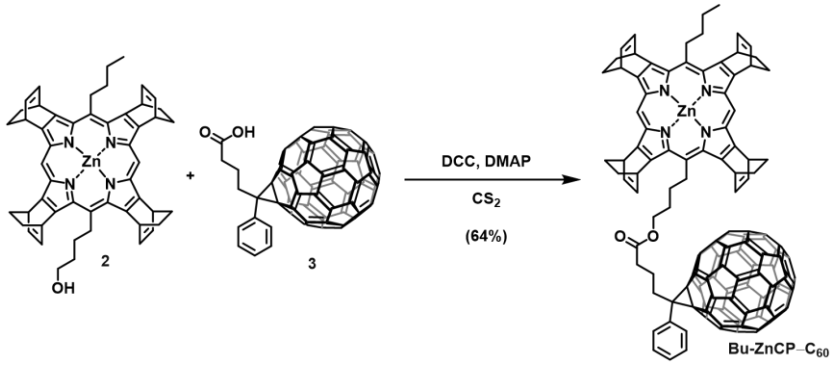

BCOD porphyrin **2** (250 mg, 0.31mmol), PCBA **3** (330 mg, 0.37 mmol), *N*,*N*′-dicyclohexylcarbodiimide (DCC, 95 mg, 0.47 mmol), *N*,*N*-dimethyl-4-aminopyridine (DMAP, 4 mg, 0.03 mmol), and CS_2 (5 mL) were added to a 20-mL round-bottom flask. The reaction mixture was stirred at room temperature for 48 h. Then, the solvent was removed under reduced pressure. The residue was purified by silica gel column chromatography using CH_2Cl_2 as an eluent, GPC using $CHCl_3$ as eluent, and recrystallization from $CHCl_3$ and MeOH to afford the target compound Bu-ZnCP–C_{60} as dark purple solid in 64% (338 mg, 0.20 mmol).

^{1}H NMR ($CDCl_3$, 400 MHz): δ (ppm) = 10.06–10.23 (m, 2H), 7.32–7.68 (m, 5H), 6.94–7.24 (m, 8H), 5.60–5.86 (m, 8H), 5.16–5.54 (m, 4H), 4.25–4.45 (m, 2H), 1.56–3.00 (m, 30H), 1.29–1.45 (m, 3H); ^{13}C NMR ($CDCl_3$, 100 MHz) δ (ppm) = 173.40, 173.26, 151.44–150.80,* 148.13–135.65,* 131.86, 131.75, 128.06, 127.93, 120.81, 120.61, 119.42, 119.37, 96.83, 96.70, 78.56, 78.35, 78.22, 78.18, 78.15, 65.67, 65.19, 65.07, 50.34, 41.13, 36.02, 35.97, 35.76, 34.16, 33.76, 32.84, 32.62, 32.41, 29.41, 28.78, 28.75, 28.53, 28.35, 27.73, 27.57, 27.41, 27.36, 23.78, 22.43, 14.96; HR-MS (ESI): calcd for $C_{123}H_{63}N_4O_2Zn$, 1691.4243 $[M + H]^+$; found, 1691.4253. *Overlapped broad peaks are observed presumably owing to intra or intermolecular interactions between the C_{60} core and the porphyrin unit, associated with the existence of multiple isomers depending on the orientation of bicyclo[2.2.2]octadieno-units.

Bu-CP–C_{60}

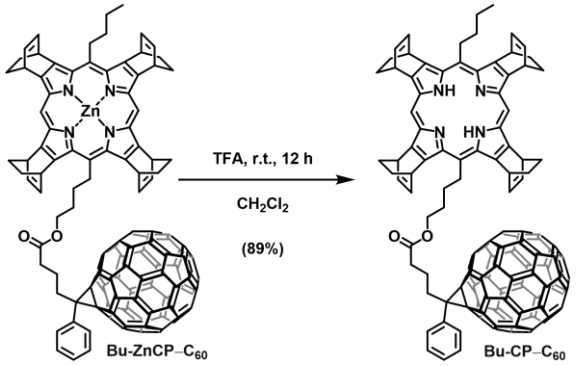

Bu-ZnCP-C_{60} (300 mg, 0.18 mmol) and CH_2Cl_2 (25 mL) was placed to a 50-mL round-bottom flask. TFA (67 μL, 0.88 mmol) was added to the solution, and stirred 12 h at room temperature. The solution was washed with $NaHCO_3$ aq., water, brine, and dried over Na_2SO_4. The solvent was removed by evaporation and the crude product was purified by recrystallization from $CHCl_3$ and MeOH to afford target compound **Bu-CP–C_{60}** as dark purple solid in 89% (260 mg, 0.16 mmol).

^{1}H NMR ($CDCl_3$, 400 MHz): δ (ppm) = 10.12–10.26 (m, 2H), 7.31–7.67 (m, 5H), 6.93–7.24 (m, 8H), 5.56–5.87 (m, 8H), 5.05–5.44 (m, 4H), 4.25–4.46 (m, 2H), 1.58–2.90 (m, 30H), 1.23–1.43 (m, 3H), −3.43–−3.11 (m, 2H); ^{13}C NMR ($CDCl_3$, 100 MHz): δ (ppm) = 173.43, 173.28, 151.46–150.83,* 146.20–135.68,* 131.89, 131.79, 128.07, 127.97, 127.90, 119.76, 119.68, 119.63, 118.24, 118.14, 96.41, 96.14, 78.60, 78.40, 78.27, 65.64, 65.26, 65.15, 64.43, 50.24, 40.68, 40.20, 40.12, 36.06, 35.55, 35.37, 34.32, 33.28, 33.13, 32.93, 32.73, 32.58, 29.62, 29.58, 28.57, 28.39, 27.65, 27.49, 25.34, 23.85, 22.42, 22.28, 14.82; HR-MS (ESI): calcd for $C_{123}H_{65}N_4O_2$, 1629.5108 $[M + H]^+$; found, 1629.5094. *Overlapped broad peaks are observed presumably owing to intra or intermolecular interactions between the C_{60} core and the porphyrin unit, associated with the existence of multiple isomers depending on the orientation of bicyclo[2.2.2]octadieno-units.

[5,15-butyl-tetrakis(BCOD)porphyrin]zinc (II) (DiBu-CP)

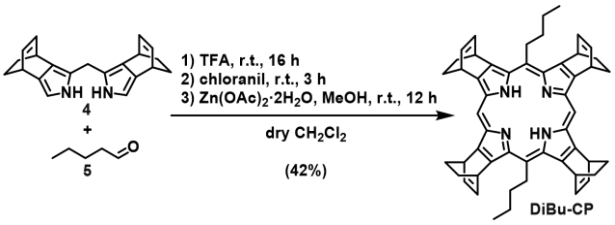

BCOD-dipyrrylmethane **4** (1.04 g, 3.46 mmol), valeraldehyde **5** (286 mg, 3.46 mmol) and dry CH_2Cl_2 (600 mL) were added to a 1-L three-neck round-bottom flask under Ar. TFA (19 µl) was added and the solution was stirred at room temperature for 16 h. After the addition of tetrachloro-p-benzoquinone (chloranil, 1.41 g, 5.75 mmol), the solution was stirred at room temperature for 3 h and neutralized with triethylamine (1 mL). The solvent was removed by evaporation and the crude product was purified by silica gel column chromatography with ethyl acetate and hexanes (1:6 vol/vol) as an eluent and recrystallization from $CHCl_3$ and MeOH to afford the target compound DiBu-CP in 42% as purple powder (534 mg, 0.73 mmol).

^{1}H NMR ($CDCl_3$, 400 MHz): δ (ppm) = 10.15–10.33 (m, 2H), 7.04–7.22 (m, 8H), 5.66–5.85 (m, 8H), 5.11–5.37 (m, 4H), 2.58–2.86 (m, 4H), 1.76–2.30 (m, 20H), 1.21–1.40 (m, 6H), −3.13 (s, 2H); ^{13}C NMR ($CDCl_3$, 100 MHz), δ: 151.17, 151.15, 151.11, 146.07, 146.05, 141.31, 141.22, 136.84, 135.72, 135.70, 134.48, 119.01, 95.71, 95.68, 40.69, 40.10, 36.10, 33.20, 28.01, 27.50, 27.15, 23.78, 14.73; HR-MS (ESI): calcd for $C_{52}H_{55}N_4$, 735.4427 $[M + H]^+$; found, 735.4418.

[5-bythyl-1-ol-tetrakis(BCOD)porphyrin]zinc (II) (7)

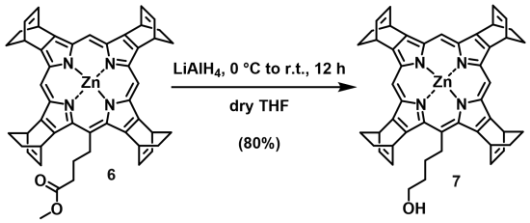

Under nitrogen atmosphere, $LiAlH_4$ (87 mg, 2.3 mmol) was added slowly to a solution of BCOD porphyrin **6** (360 mg, 0.46 mmol) in dry THF (15 mL) at 0 °C. The resulting mixture was stirred at room temperature for 12 h. The reaction mixture was quenched by water, filtrated on Celite, and the filtration was extracted with ethyl acetate. The organic layer was washed with water and brine, dried over Na_2SO_4, and concentrated under reduced pressure. The crude product was purified by silica gel column

chromatography using ethyl acetate and hexane (1:3 vol/vol) as an eluent and recrystallization from CH_2Cl_2 and hexane to afford the target compound **7** as purple powder in 80% (279 mg, 0.37 mmol).

^{1}H NMR ($CDCl_3$, 400 MHz): δ (ppm) = 10.34–10.20 (m, 3H), 7.18–6.90 (m, 8H), 5.83–5.50 (m, 8H), 5.40–5.15 (m, 2H), 3.61–3.20 (m, 2H), 2.90–2.50 (m, 2H), 2.30–0.75 (m, 19H); ^{13}C NMR ($CDCl_3$, 100 MHz): δ (ppm) = 151.32, 149.85, 149.80, 149.68, 147.85, 147.78, 143.29, 143.20, 142.89, 141.88, 140.88, 137.13, 136.92, 136.46, 129.52, 125.72, 120.94, 120.89, 120.73, 97.34, 97.30, 96.90, 62.81, 40.98, 40.92, 36.44, 36.05, 34.90, 34.62, 34.44, 33.10, 28.21, 27.97, 27.62, 27.48, 27.11, 19.72; HR-MS (ESI): calcd. for $C_{48}H_{44}NaN_4OZn$, 779.2704 $[M + Na]^+$; found, 779.2704.

f-ZnCP–C$_{60}$

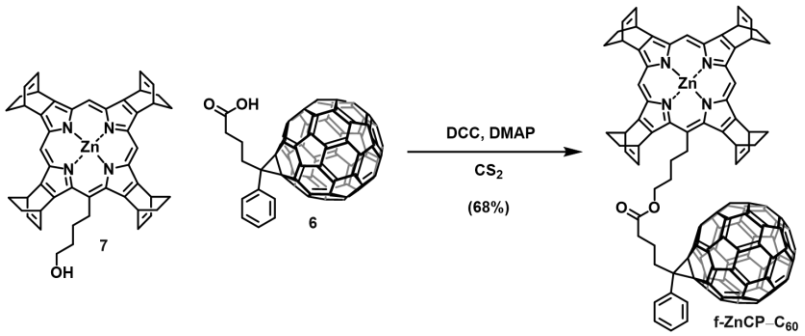

Under nitrogen atmosphere, BCOD porphyrin **7** (500 mg, 0.66 mmol), $PC_{61}BA$ **3** (710 mg, 0.79 mmol), *N*,*N'*-Dicyclohexylcarbodiimide (DCC, 160 mg, 0.79 mmol) and *N,N*-dimethyl-4-aminopyridine (DMAP) (8.5 mg, 0.07 mmol) were dissolved in CS_2 (20 mL). The reaction mixture was stirred at room temperature for 48 h. The solvent was removed by evaporation, and the crude product was purified by silica gel column chromatography using CH_2Cl_2 as an eluent and GPC using $CHCl_3$ as an eluent to afford the target compound **f-ZnCP–C$_{60}$** as dark purple solid in 68% (744 mg, 0.45 mmol).

^{1}H NMR ($CDCl_3$, 400 MHz): δ (ppm) = 10.26–10.10 (m, 3H), 7.60–7.30 (m, 5H), 7.24–6.98 (m, 8H), 5.85–5.58 (m, 8H), 5.50–5.28 (m, 2H), 4.47–4.26 (m, 2H), 2.85–1.37 (m, 28H); ^{13}C NMR ($CDCl_3$, 100 MHz): δ (ppm) = 173.47, 173.35, 173.30, 150.99–136.45*, 131.88, 131.79, 128.01, 128.00, 127.96, 127.92, 120.91, 120.89, 97.66, 97.58, 97.43, 97.38, 65.78, 65.34, 50.43, 50.40, 50.36, 50.30, 41.26, 41.18, 36.50, 36.45, 36.41, 36.09, 36.03, 34.29, 29.55, 28.40, 28.28, 28.04, 27.75, 27.59, 27.40, 27.36, 22.45; HR-MS (ESI): calcd. for $C_{119}H_{54}N_4NaO_2Zn$, 1657.3436 $[M + H]^+$; found, 1689.3613. *Overlapped broad

peaks are observed presumably owing to intra or intermolecular interactions between the C_{60} core and the porphyrin unit, associated with the existence of multiple isomers depending on the orientation of bicyclo[2.2.2]octadieno-units.

f-CP–C_{60}

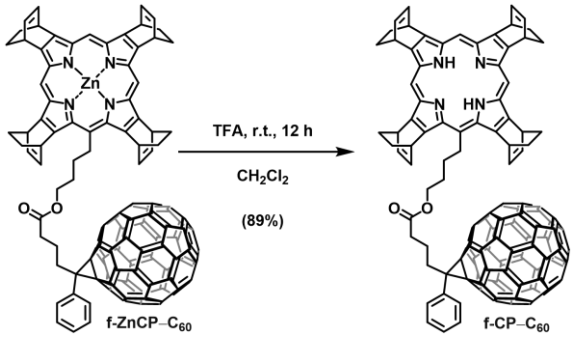

Excess TFA (0.1 mL, 0.59 mmol) was added to a solution of f-ZnCP–C_{60} (120 mg, 0.72 μmol) in CH_2Cl_2 (10 mL). After stirring for 12 h at the room temperature, the reaction mixture was washed with saturated $NaHCO_3$ aq, water, brine, and dried over Na_2SO_4. The solvent was removed by evaporation, and the crude product was purified by recrystallization from $CHCl_3$ and MeOH to afford the target compound f-CP–C_{60} as dark purple solid in 89% (92 mg, 0.64 μmol).

^{1}H NMR ($CDCl_3$, 400 MHz): δ (ppm) = 10.28–10.01 (m, 3H), 7.61–7.28 (m, 5H), 7.24–6.96 (m, 8H), 5.94–5.59 (m, 8H), 5.56–5.24 (m, 2H), 4.47–4.29 (m, 2H), 2.66–1.38 (m, 28H), −3.8–−4.5 (m, 2H); ^{13}C NMR ($CDCl_3$, 100 MHz): δ (ppm) = 173.49, 173.39, 150.91–136.06*, 131.91, 131.82, 128.10, 128.01, 127.94, 119.91, 119.89, 119.80, 96.95, 96.85, 96.36, 78.50, 78.45, 65.37, 50.29, 40.64, 40.52, 40.48, 36.42, 36.34, 36.05, 35.92, 34.12, 34.28, 29.61, 28.62, 28.29, 28.20, 27.92, 27.67, 27.54, 27.43, 22.38; HR-MS (ESI): calcd. for $C_{119}H_{57}N_4O_2$, 1573.4482 $[M + H]^+$; found, 1573.4477. *Overlapped broad peaks are observed presumably owing to intra or intermolecular interactions between the C_{60} core and the porphyrin unit, associated with the existence of multiple isomers depending on the orientation of bicyclo[2.2.2]octadieno-units.

[5-(bromoethynyl)benzyl-tetrakis(dimethylBCOD)porphyrin]zinc (II) (12)

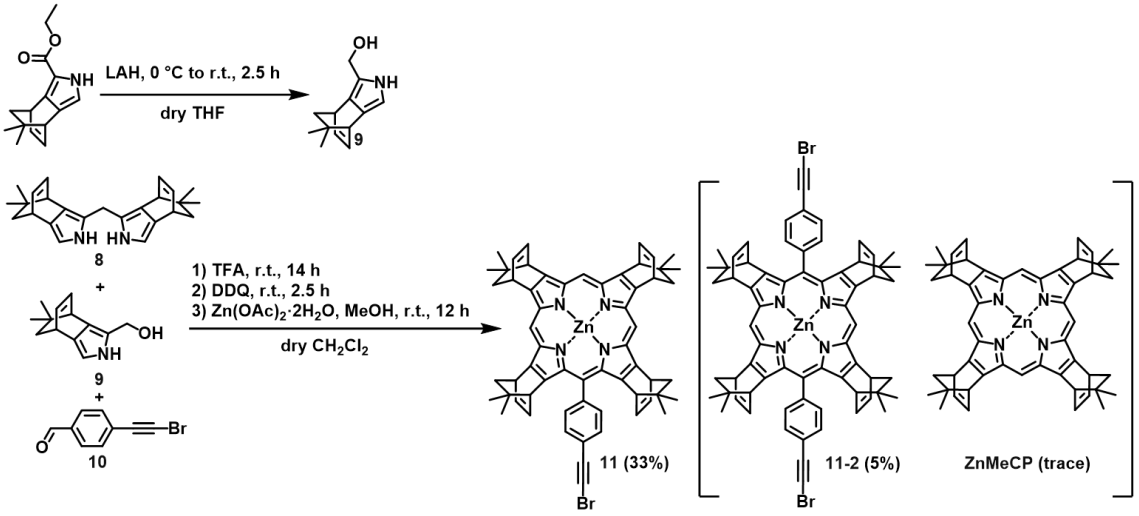

Ethyl 4,7-dihydro-8,8-dimethyl-4,7-ethano-*2H*-isoindole-1-carboxylate[2] (700 mg, 2.85 mmol) was dissolved in dry THF (20 mL), then lithyumaluminiumhydride (LAH, 530 mg, 13.95 mmol) was added to the solution slowly at 0 ºC. The mixture was stirred at room temperature with protection from light for 2.5 h. After quenching the reaction with water at 0 ºC, the reaction mixture was filtrated on Celite. The filtrate was extracted by AcOEt and washed with brine, dried over Na_2SO_4. Then solvent was removed to prepare compound **9**. The resulting compound **9**, dimethylBCOD-fused dipyrromethene **8** (500 mg, 1.39 mmol), 4-(bromoethynyl)benzaldehyde **10** (281 mg, 1.39 mmol), and dry CH_2Cl_2 (600 mL) were placed to a 1000-mL three-necked round-bottom flask under Ar atmosphere. After Ar gas bubbling for 25 min, trifluoroacetic acid (TFA, 50 μm) was added to the solution and the solution was stirred at room temperature under protection from light for 14 h. After the addition of 2,3-dichloro-5,6-dicyano-*p*-benzoquinone (DDQ, 790 mg, 3.48 mmol), the solution was stirred at room temperature for 2.5 h and was neutralized with triethylamine. After removing solvent, the residue was dissolved in CH_2Cl_2 (50 mL) and a solution of $Zn(OAc)_2{\cdot}2H_2O$ (310 mg, 1.39 mmol) in methanol (20 mL) was added. The solution was stirred at room temperature for 12 h. Then, the solvent was removed under reduced pressure. The crude product was purified by passing through a pad of aluminum and silica gel using CH_2Cl_2 as an eluent and GPC using $CHCl_3$ as an eluent to afford to afford the target products **12** in 33% (448 mg, 0.46 mmol) as red powder. At the same time, by-product of **12-2** in 5% (80 mg, 0.07 mmol) and trace of ZnMeCP also obtained, respectively.

12: ^{1}H NMR ($CDCl_3$, 400 MHz): δ (ppm) = 10.42–10.23 (m, 3H), 8.35–7.76 (m, 4H),

7.24– 6.58 (m, 8H), 5.70–5.50 (m, 3H), 5.20–5.04 (m, 3H), 3.64–3.15 (m, 2H), 2.17–0.18 (m, 32H); ^{13}C NMR ($CDCl_3$, 100 MHz): δ (ppm) = 152.16, 151.17, 151.12, 149.80, 148.58, 148.45, 148.36, 144.90, 144.35, 143.90, 143.53, 142.37, 142.17, 141.89, 138.03, 137.81, 136.30, 136.09, 134.06, 133.11, 130.09, 129.57, 129.42, 122.35, 117.46, 98.16, 97.50, 80.54, 51.09, 49.54, 49.08, 44.10, 43.43, 40.64, 40.62, 40.58, 40.55, 40.24, 40.07, 40.03, 39.97, 39.82, 37.82, 37.48, 31.34, 31.12, 30.93; HR-MS (ESI): calcd. for $C_{60}H_{56}BrN_4Zn$, 975.2980 $[M + H]^+$; found, 975.2979.

12-2: ^{1}H NMR ($CDCl_3$, 400 MHz): δ (ppm) = 10.41–10.20 (m, 2H), 8.47–7.79 (m, 8H), 7.22– 6.57 (m, 8H), 5.68–5.00 (m, 4H), 3.81–3.12 (m, 4H), 2.09–0.16 (m, 32H); ^{13}C NMR ($CDCl_3$, 100 MHz): δ (ppm) = 151.48, 151.40, 151.35, 150.26, 150.17, 150.14, 150.10, 149.95, 144.42, 144.27, 144.18, 144.16, 143.90, 142.57, 141.91, 141.84, 138.22, 137.99, 137.85, 135.96, 135.93, 134.74, 133.95, 130.15, 129.76, 129.02, 122.55, 122.42, 122.08, 117.25, 117.21, 177.17, 98.20, 80.51, 51.40, 51.32, 50.81, 50.59, 49.08, 43.89, 43.75, 40.36, 40.33, 40.23, 40.04, 39.99, 39.92, 39.80, 39.48, 37.40, 37.41, 31.59, 31.54, 31.49, 31.38, 31.20, 30.88, 30.76; HR-MS (ESI): calcd. for $C_{68}H_{58}Br_2N_4Zn$, 1152.2319 $[M + H]^+$; found, 1152.2316.

ZnMeCP: ^{1}H NMR ($CDCl_3$, 400 MHz): δ (ppm) = 10.43–10.27 (m, 4H), 7.28–7.09 (m, 8H), 5.71–5.60 (m, 4H), 5.23–5.11 (m, 4H), 2.17–1.32 (m, 20H), 0.93–0.55 (m, 12H); ^{13}C NMR ($CDCl_3$, 100 MHz): δ (ppm) = 151.08. 151.02, 150.81, 150.75, 148.53, 148.36, 148.28, 148.23, 148.09, 148.05, 144.32, 144.14, 144.08, 143.97, 144.23, 142.17, 142.11, 141.94, 141.91, 137.97, 137.90, 136.28, 136.198, 136.128, 98.17, 98.00, 97.93, 97.74, 49.63, 44.20, 40.72, 40.68, 40.65, 40.61, 40.58, 40.56, 31.79, 31.72, 31.68, 31.49, 31.44, 31.39, 31.24; HR-MS (ESI): calcd. for $C_{52}H_{53}N_4Zn$, 796.3562 $[M + H]^+$; found, 797.3563.

4-methyl-*N*'-(1-(4-((trimethylsilyl)ethynyl)phenyl)ethylidene)benzenesulfonohydrazide (13)

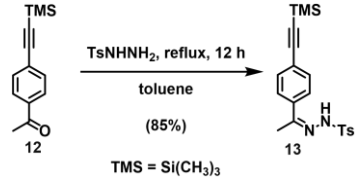

4'-(2-trimethylsilylethynyl)acetophenone **12** (7.39 g, 24.5 mmol) in toluene (60 mL) was refluxed with $TsHNNH_2$ (5.72 g, 30.7 mmol) for 12 hours. After removal of toluene, the residue was purified by silica gel column chromatography using CH_2Cl_2 as

an eluent to afford the target compound **13** in 85% (8.0 g, 20.8 mmol) as white powder. ^{1}H NMR ($CDCl_3$, 400 MHz): δ (ppm) = 7.91 (d, J = 8.2 Hz, 2H), 7.63 (br s, 1H), 7.59 (d, J = 8.7 Hz, 2H), 7.43 (d, J = 8.7 Hz, 2H), 7.32 (d, J = 8.2 Hz, 2H), 2.42 (s, 3H), 2.12 (3H, s), 0.25 (s, 9H); ^{13}C NMR ($CDCl_3$, 100 MHz): δ (ppm) = 151.42, 144.41, 136.99, 135.34, 132.00, 129.72, 128.23, 126.09, 124.41, 104.60, 96.29, 21.72, 13.15, 0.09; HR-MS (ESI): calcd. for $C_{20}H_{25}N_2O_2SSi$, 385.1412 $[M + H]^+$; found, 385.1401.

[6,6]-methyl-C_{61}-4-((trimethylsilyl)ethynyl)benzene (14)

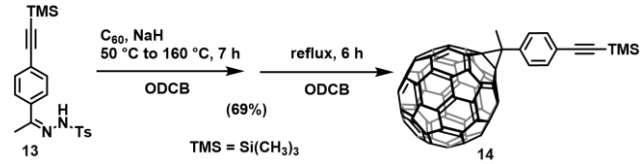

C_{60} (880 mg, 1.23 mmol) was dissolved in degassed *o*-dichlorobenzene (ODCB, 250 mL), and sodium hydride (60% in oil, 250 mg) and **13** (340 mg, 0.861 mmol) were introduced into the solution. The resulting mixture was heated stepwise (1 h at 50 ºC, 2 h at 80 ºC, 1 h at 100 ºC, 1 h at 120 ºC, 1 h at 140 ºC, and 1 h at 160 ºC) under argon gas atmosphere. After cooling, the reaction mixture was quenched with water (150 mL), stirred for 5 min, and filtered on Celite. The organic layer was decanted, washed with brine, and dried over Na_2SO_4. After removal of solvent, the residue was reprecipitated with $CHCl_3$ to defecate unreacted C_{60} by filtration. After evaporation, the isomeric mixture was dissolved in ODCB (50 mL) and refluxed for 6 h under argon gas atmosphere. Then, solvent was removed under reduced pressure. The crude product was purified by GPC using $CHCl_3$ as an eluent and recrystallization from $CHCl_3$ and MeOH to afford the target compound **14** in 69% (547 mg, 0.59 mmol) as brown powder.

^{1}H NMR ($CDCl_3$, 400 MHz): δ (ppm) = 7.91 (d, J = 8.2 Hz, 2H), 7.65 (d, J = 8.2 Hz, 2H), 2.53 (s, 3H), 0.28 (s, 9H); ^{13}C NMR ($CDCl_3$, 100 MHz): δ (ppm) = 148.61, 147.88, 145.84, 145.17, 145.08, 144.82, 144.72, 144.52, 144.41, 144.06, 143.78, 143.14, 143.07, 143.04, 143.00, 142.32, 142.17, 141.04, 140.84, 139.85, 138.10, 137.52, 132.34, 130.96, 122.84, 104.62, 80.58, 22.32, 0.05; HR-MS (ESI): calcd for $C_{73}H_{16}Si$, 920.1019 $[M]^{\bullet+}$; found, 920.1016.

[6,6]-methyl-C_{61}-4-(ethynyl)benzene (17)

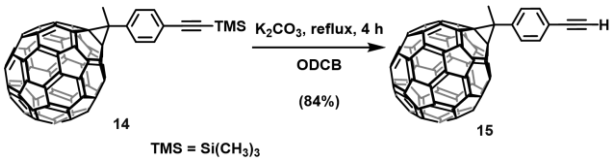

Potassium carbonate (K_2CO_3, 152 mg, 1.15 mmol) was added to a solution of **14** (230 mg, 0.25 mmol) in THF (200 mL) and MeOH (40 mL). The mixture was flushed with Ar gas for 15 min at room temperature with vigorous stirring and was heated at reflux for 4 h. The solvent was removed under pressure and filtrated through a pad of silica gel using CS_2 as an eluent. The solvent was removed under pressure and the crude product was purified by silica gel column chromatography using cyclohexane as an eluent to afford the target compound **15** in 84 % (178 mg, 0.21 mmol) as dark brown powder. ^{1}H NMR ($CDCl_3$, 400 MHz): δ (ppm) = 7.94 (d, J = 8.2 Hz, 2H), 7.68 (d, J = 8.2 Hz, 2H), 3.17 (s, 1H), 2.53 (s, 3H); ^{13}C NMR ($CDCl_3$, 100 MHz): δ (ppm) = 148.50, 147.81, 145.79, 145.20, 145.14, 145.05, 144.79, 144.69, 144.50, 144.38, 143.09, 142.97, 142.15, 141.01, 140.83, 140.19, 138.06, 132.50, 130.98, 121.86, 83.24, 80.49, 78.03, 62.91, 47.16, 22.35; HR-MS (ESI): calcd. for $C_{70}H_8$, 848.0623 $[M + H]^+$; found, 848.0621.

r-ZnCP–C_{60}

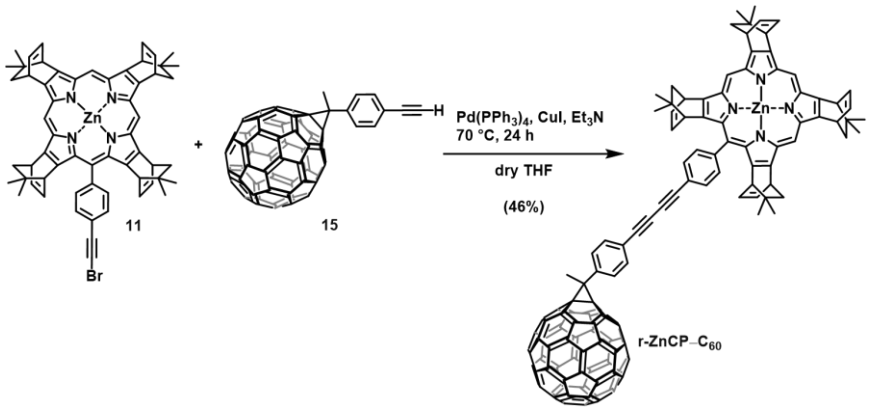

Under Ar atmosphere, a solution of **15** (85 mg, 0.098 mmol) in dry THF (45 mL) was added dropwise to a solution of **11** (110 mg, 0.13 mmol), $Pd(PPh_3)_4$ (16.0 mg, 1.4 μmol), CuI (10 mg, 5.3 μmol) in dry THF (15 mL) at 70 ºC. The resulting mixture was stirred at 70 ºC for 24 h, then the solvent was removed under reduced pressure. The crude product was purified by passing through a pad of silica gel using CH_2Cl_2 as an eluent and GPC using $CHCl_3$ as an eluent to afford the target compound **r-ZnCP–C_{60}** in 46% (104

mg, 0.045 mmol) as dark purple powder.

^{1}H NMR ($CDCl_3$, 400 MHz): δ (ppm) = 10.37–10.24 (m, 3H), 8.39–7.70 (m, 8H), 7.26–6.60 (m, 8H), 5.69–5.53 (m, 3H), 5.21–5.04 (m, 3H), 3.61–3.18 (m, 2H), 2.43–2.29 (m, 3H), 2.17– 1.10 (m, 21H), 0.94–0.20 (m, 11H); ^{13}C NMR ($CDCl_3$, 100 MHz): δ (ppm) = 151.20–135.97*, 132.87, 131.03, 130.61, 121.53, 121.51, 121.35, 98.36, 98.30, 82.50, 81.72, 80.02, 74.91, 74.82, 49.59, 49.11, 46.77, 46.73, 44.19, 43.95, 43.58, 40.67, 40.62, 40.60, 40.57, 40.27, 40.14, 40.06, 39.98, 39.93, 39.89, 37.84, 37.52, 37.44, 31.99, 31.84, 31.70, 31.57, 31.53, 31.43, 31.35, 31.20, 31.06, 22.08, 14.13; HR-MS (ESI): calcd for $C_{130}H_{63}N_4Zn$, 1743.4344 $[M + H]^+$; found, 1743.4354. *Overlapped broad peaks are observed presumably owing to intra or intermolecular interactions between the C_{60} core and the porphyrin unit, associated with the existence of multiple isomers depending on the orientation of dimethyl-bicyclo[2.2.2]octadieno-units.

r-CP–C$_{60}$

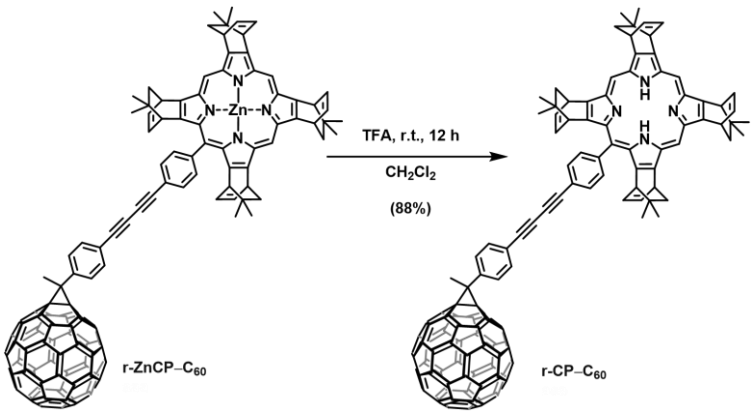

Excess TFA (0.1 mL, 0.59 mmol) was added to a solution of **r-ZnCP–C$_{60}$** (140 mg, 80.3 μmol) in CH_2Cl_2 (20 mL). After stirring at room temperature for 12 h, the solution was washed with saturated $NaHCO_3$ aq, water, brine, and dried over Na_2SO_4. The solvent was removed under reduced pressure and the crude product was purified by recrystallization from $CHCl_3$ and MeOH to afford the dark purple powder **r-CP–C$_{60}$** (119 mg, 88%).

^{1}H NMR ($CDCl_3$, 400 MHz): δ (ppm) = 10.66–10.10 (m, 3H), 8.50–7.60 (m, 8H), 7.26–6.52 (m, 8H), 5.80–5.37 (m, 3H), 5.35–4.95 (m, 3H), 3.82–3.08 (m, 2H), 2.66–0.12 (m, 35H), −3.6–−4.45 (m, 2H); ^{13}C NMR ($CDCl_3$, 100 MHz): δ (ppm) = 148.14–135.93*, 132.87, 131.01, 130.85, 127.22, 121.73, 121.56, 121.45, 120.94, 97.38, 82.35, 81.85, 80.15, 75.01, 74.82, 74.53, 49.47, 49.08, 46.89, 44.02, 43.68, 43.39, 40.56, 40.27, 40.03,

39.49, 37.68, 37.46, 31.76, 31.53, 31.29, 22.10; HR-MS (ESI): calcd. for $C_{130}H_{65}N_4$, 1681.5209 $[M + H]^+$; found, 1681.5248. *Overlapped broad peaks are observed presumably owing to intra or intermolecular interactions between the C_{60} core and the porphyrin unit, associated with the existence of multiple isomers depending on the orientation of dimethyl-bicyclo[2.2.2]octadieno-units.

Thermal conversion of Bu-CP–C_{60}, DiBu-CP, f-CP–C_{60}, r-CP–C_{60}, and r-ZnCP–C_{60} to Bu-BP–C_{60}, DiBu-BP, f-BP–C_{60}, r-BP–C_{60}, and r-ZnBP–C_{60} was carried out at 200 °C for 1 h in vacuum. Because of their terribly low solubility, Bu-BP–C_{60}, DiBu-BP, f-BP–C_{60}, r-BP–C_{60}, and r-ZnBP–C_{60} were identified by thermal gravimetric analysis (Figure. 3 and 18) and MALDI-TOF mass spectrum (Figure. S3-1 and S3-5).

3-7-3. NMR Charts

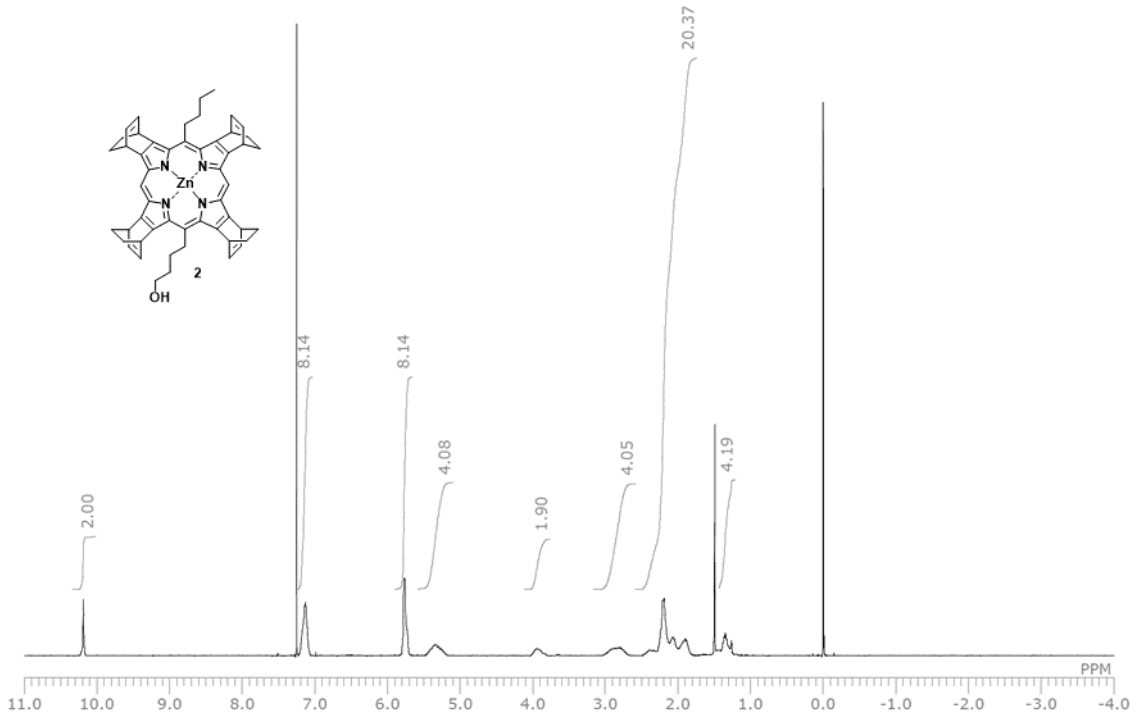

Figure S3-6-1. ^{1}H NMR spectrum of **2** in $CDCl_3$.

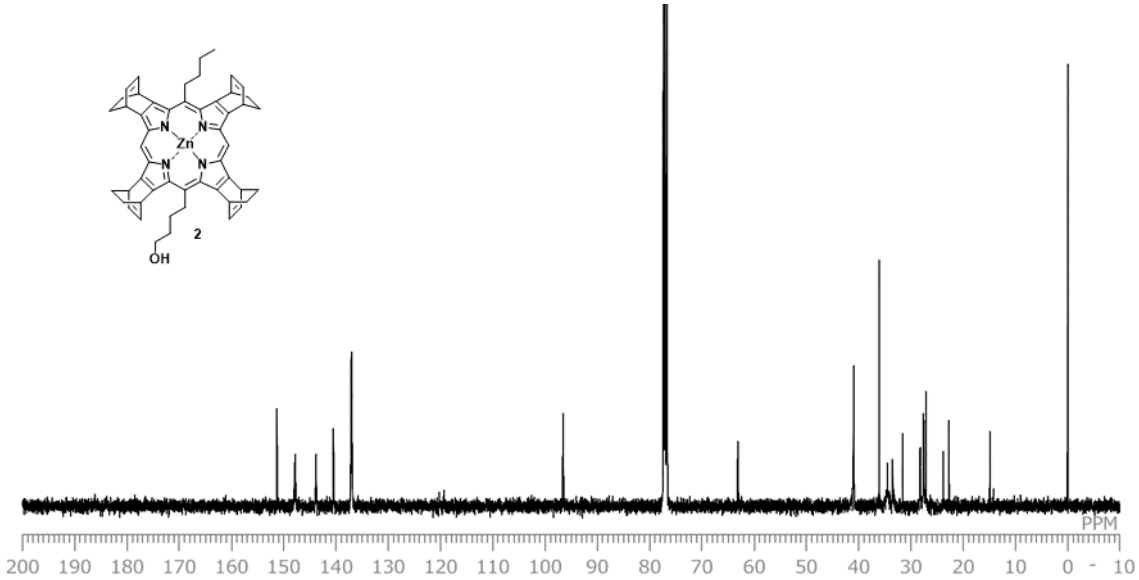

Figure S3-6-2. ^{13}C NMR spectrum of **2** in $CDCl_3$. (Minor peaks are occasionally observed alongside of the main peaks, which are presumably from the structural isomers differing in the orientation of bicycle[2.2.2]octadieno-units. The minor peaks are also listed in the spectroscopic characterization data above.)

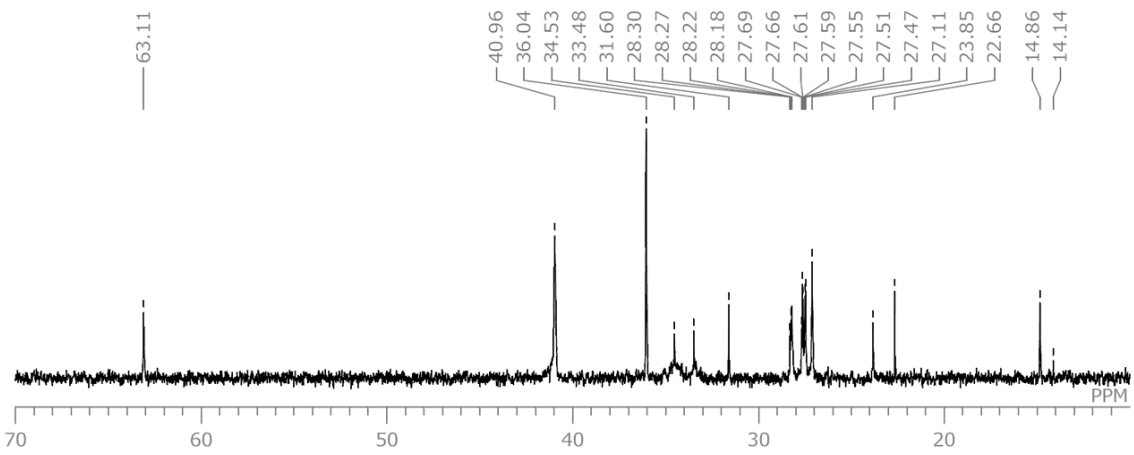

Figure S3-6-3. ^{13}C NMR spectrum of **2** in $CDCl_3$ (10–70 ppm).

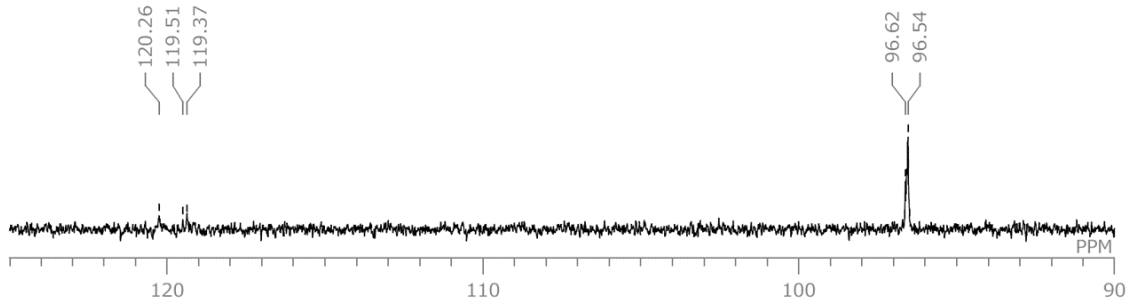

Figure S3-6-4. ^{13}C NMR spectrum of **2** in $CDCl_3$ (90–125 ppm).

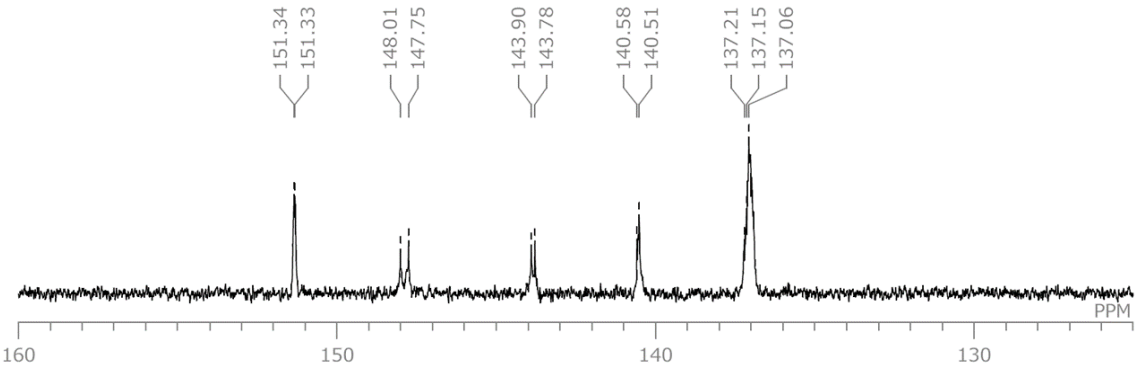

Figure S3-6-5. ^{13}C NMR spectrum of **2** in $CDCl_3$ (125–160 ppm).

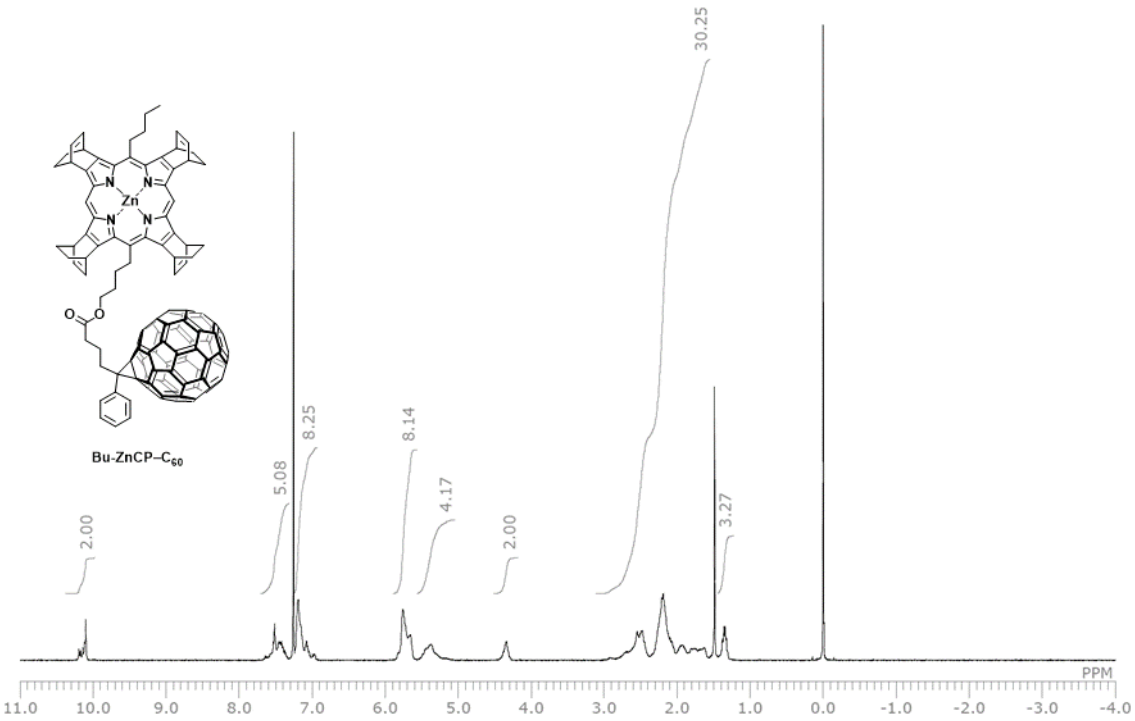

Figure S3-7-1. ^{1}H NMR spectrum of Bu-ZnCP–C_{60} in $CDCl_3$.

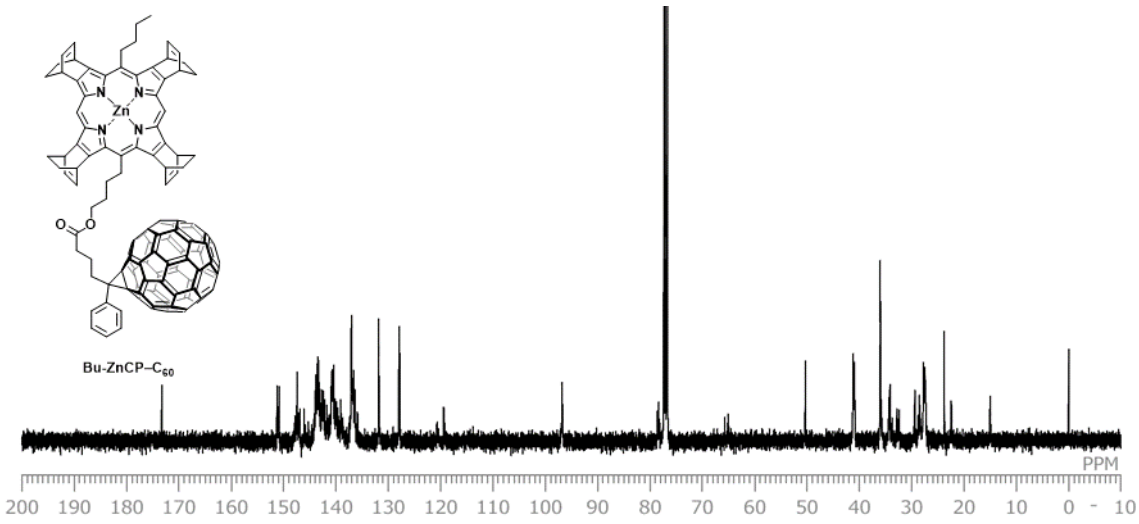

Figure S3-7-2. ^{13}C NMR spectrum of Bu-ZnCP–C_{60} in $CDCl_3$. (Minor peaks are occasionally observed alongside of the main peaks, which are presumably from the structural isomers differing in the orientation of bicycle[2.2.2]octadieno-units. The minor peaks are also listed in the spectroscopic characterization data above.)

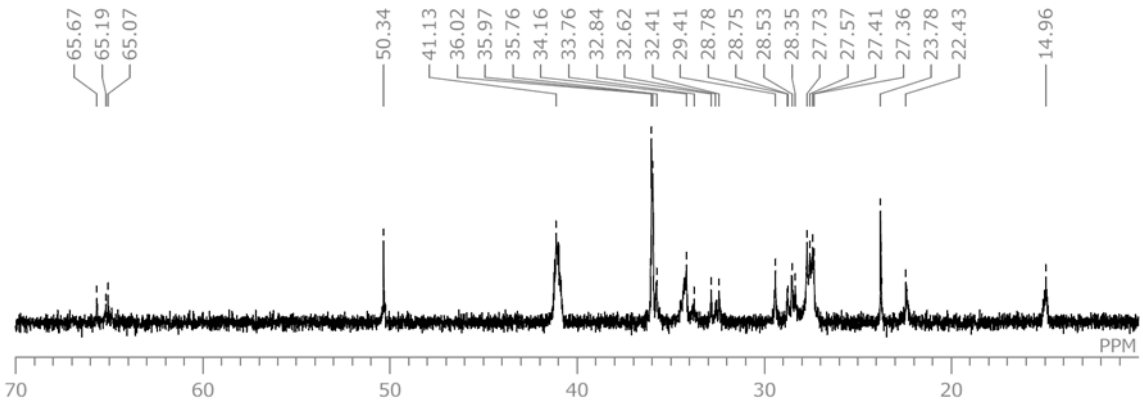

Figure S3-7-3. ^{13}C NMR spectrum of Bu-ZnCP–C_{60} in $CDCl_3$ (10–70 ppm).

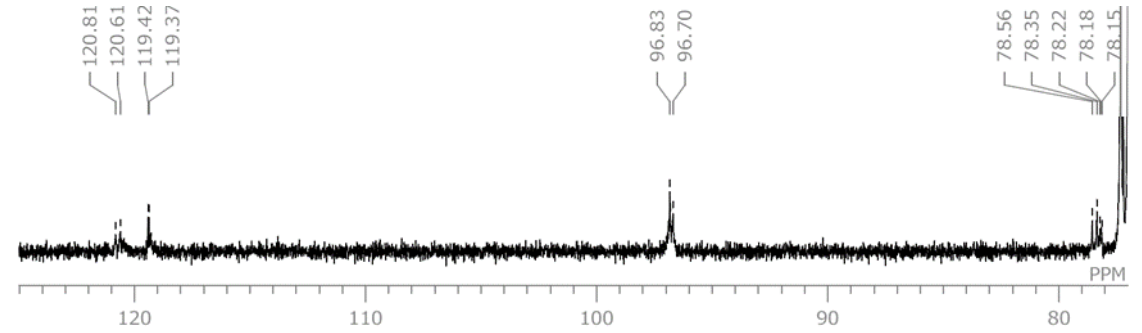

Figure S3-7-4. ^{13}C NMR spectrum of Bu-ZnCP–C_{60} in $CDCl_3$ (77–125 ppm).

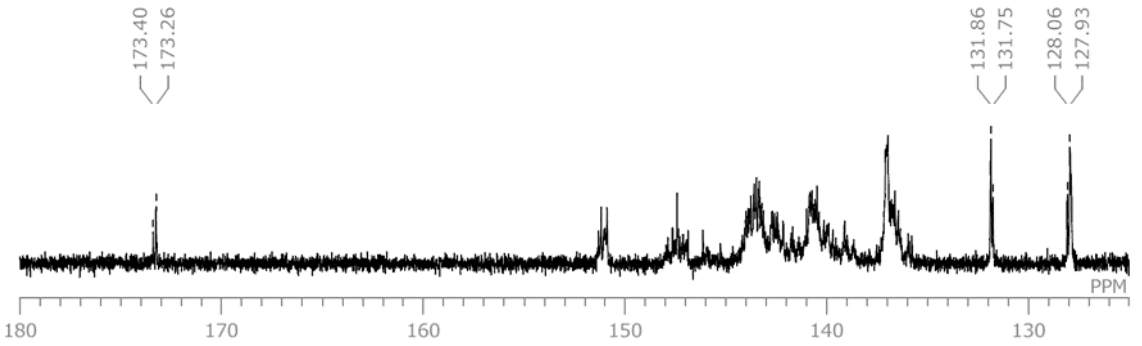

Figure S3-7-5. ^{13}C NMR spectrum of Bu-ZnCP–C_{60} in $CDCl_3$ (125–180 ppm).

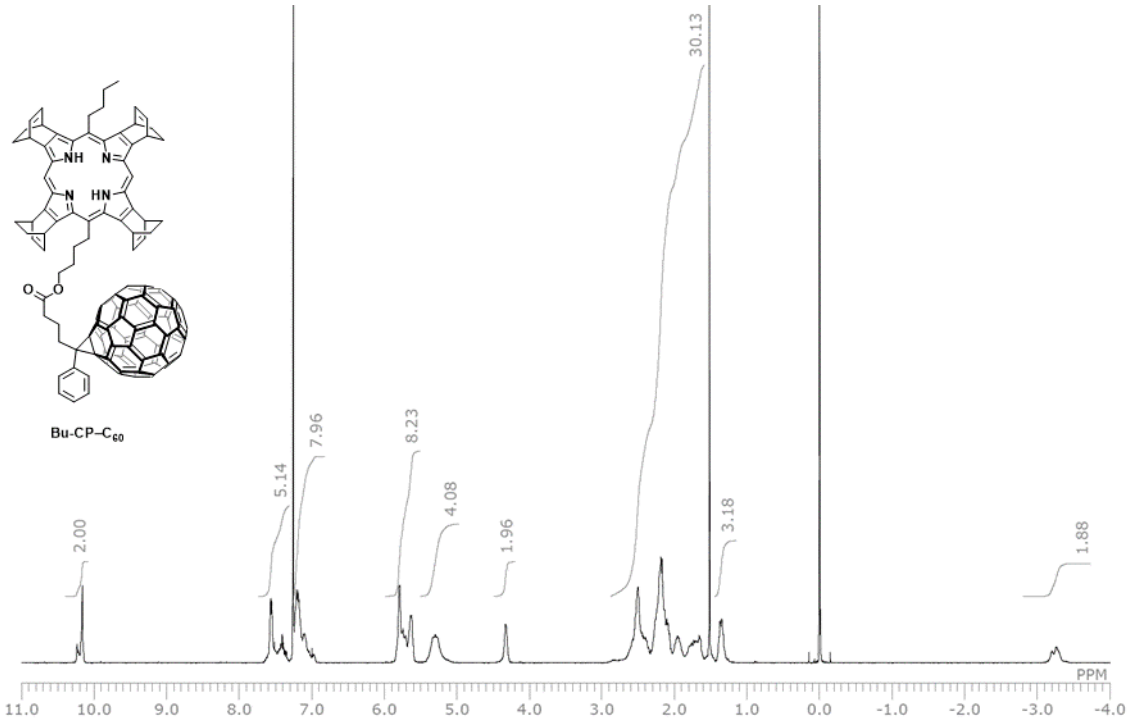

Figure S3-8-1. ^{1}H NMR spectrum of Bu-CP–C_{60} in $CDCl_3$.

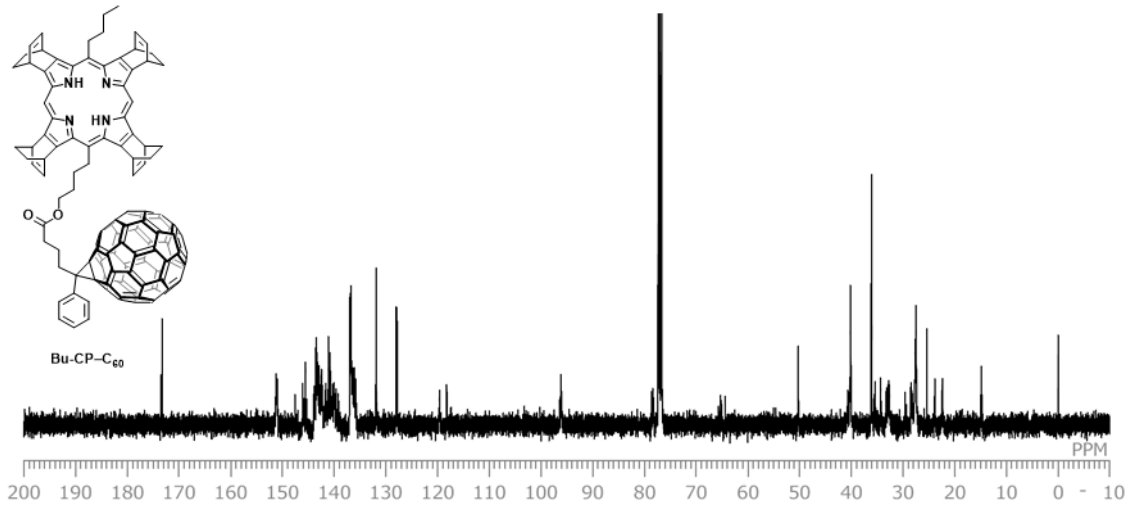

Figure S3-8-2. ^{13}C NMR spectrum of Bu-CP–C_{60} in $CDCl_3$. (Minor peaks are occasionally observed alongside of the main peaks, which are presumably from the structural isomers differing in the orientation of bicycle[2.2.2]octadieno-units. The minor peaks are also listed in the spectroscopic characterization data above.)

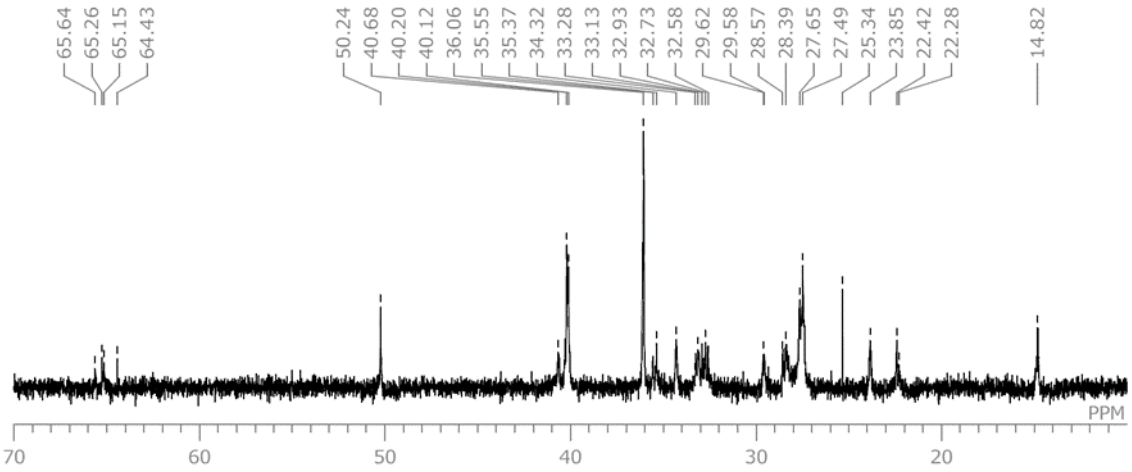

Figure S3-8-3. ^{13}C NMR spectrum of Bu-CP–C_{60} in $CDCl_3$ (10–70 ppm).

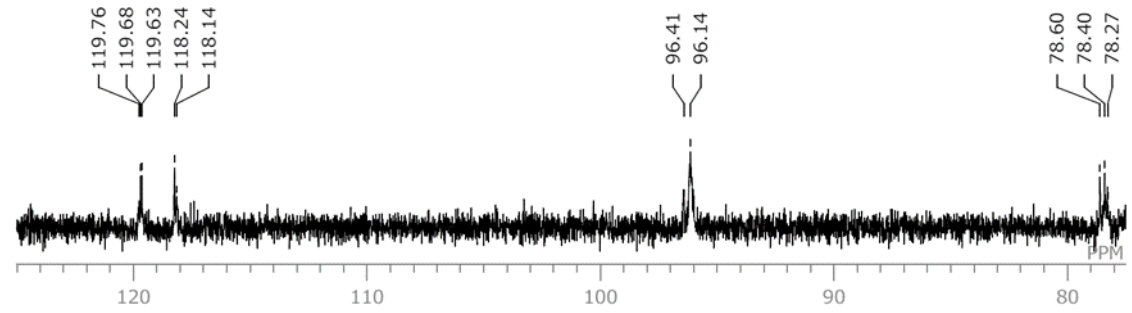

Figure S3-8-4. ^{13}C NMR spectrum of Bu-CP–C_{60} in $CDCl_3$ (78–125 ppm).

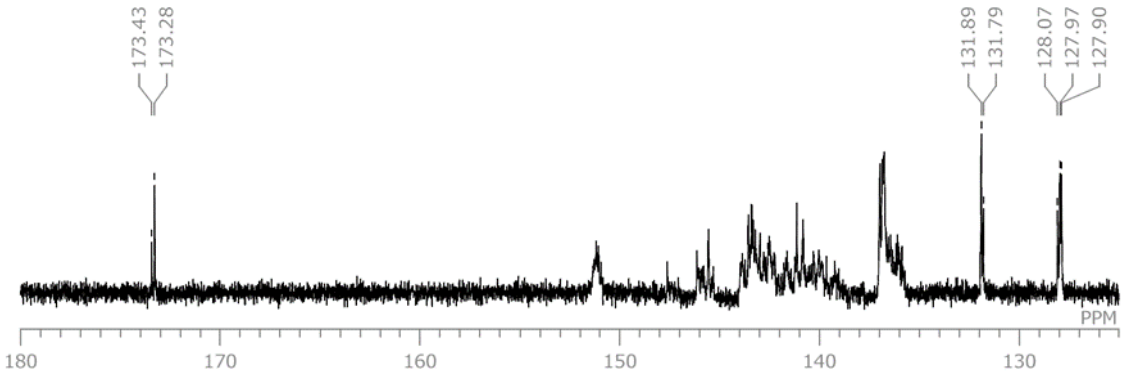

Figure S3-8-5. ^{13}C NMR spectrum of Bu-CP–C_{60} in $CDCl_3$ (125–180 ppm).

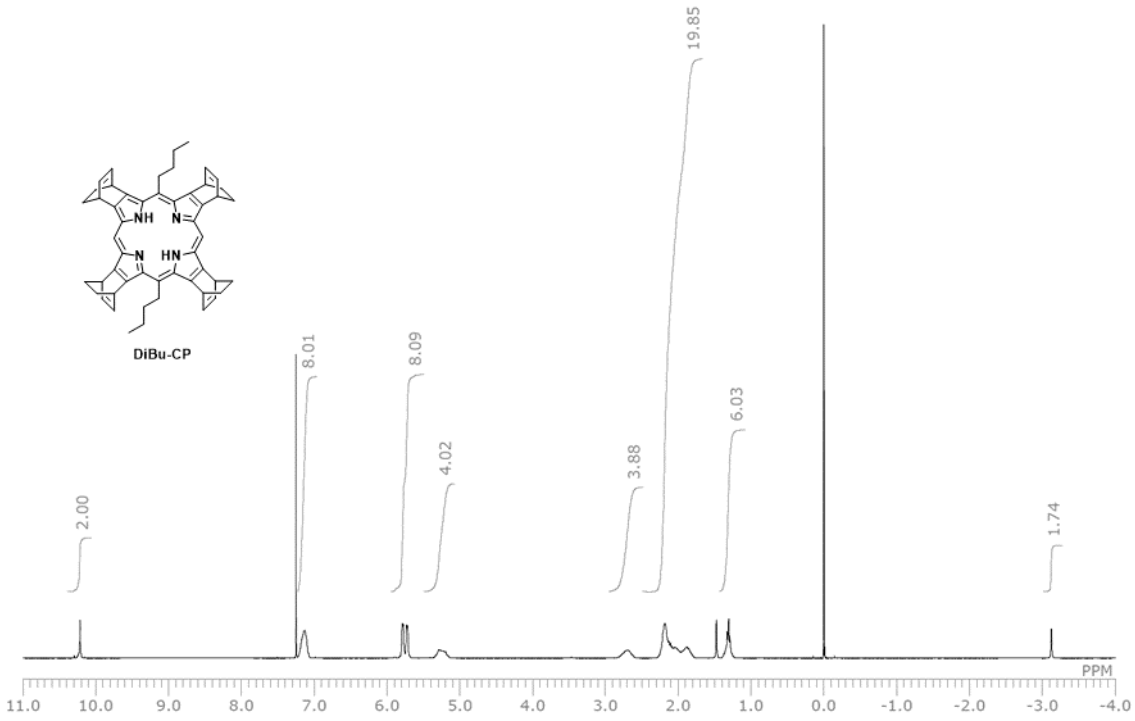

Figure S3-9-1. ^{1}H NMR spectrum of DiBu-CP in $CDCl_3$.

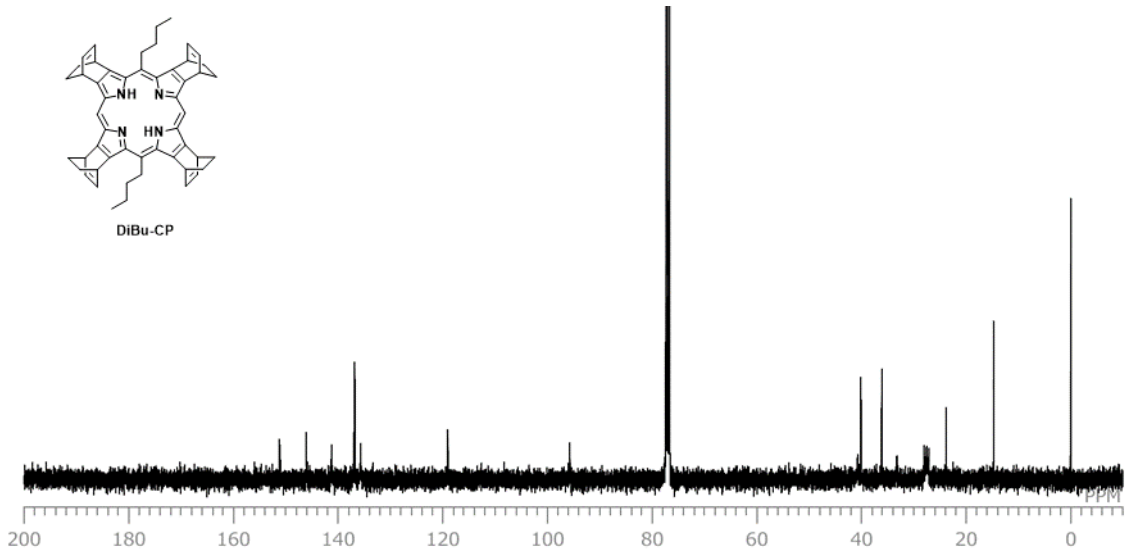

Figure S3-9-2. ^{13}C NMR spectrum of DiBu-CP in $CDCl_3$. (Minor peaks are occasionally observed alongside of the main peaks, which are presumably from the structural isomers differing in the orientation of bicycle[2.2.2]octadieno-units. The minor peaks are also listed in the spectroscopic characterization data above.)

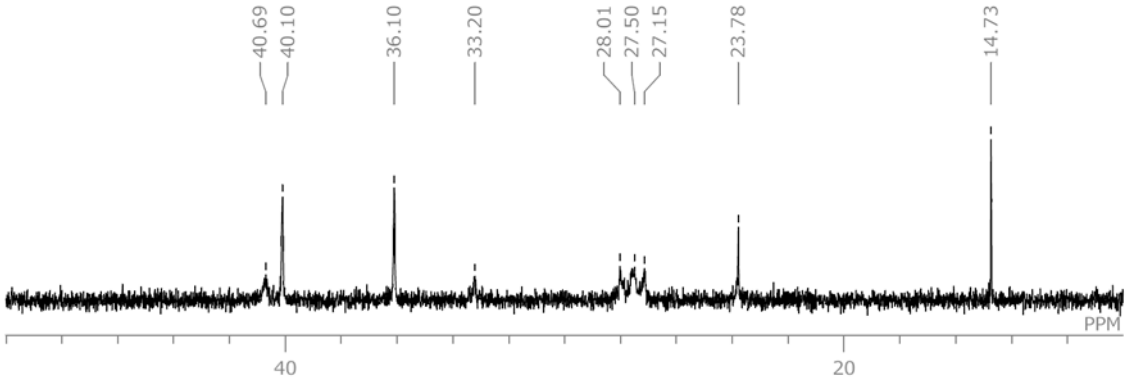

Figure S3-9-3. ^{13}C NMR spectrum of DiBu-CP in $CDCl_3$ (10–50 ppm).

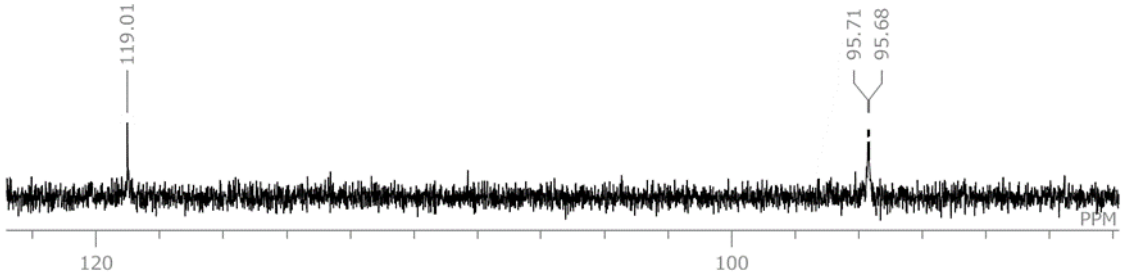

Figure S3-9-4. ^{13}C NMR spectrum of DiBu-CP in $CDCl_3$ (90–125 ppm).

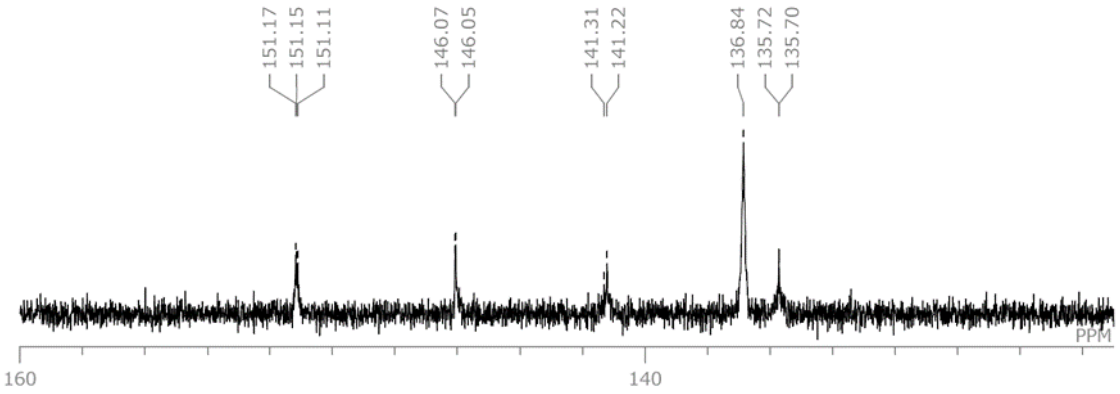

Figure S3-9-5. ^{13}C NMR spectrum of DiBu-CP in $CDCl_3$ (125–160 ppm).

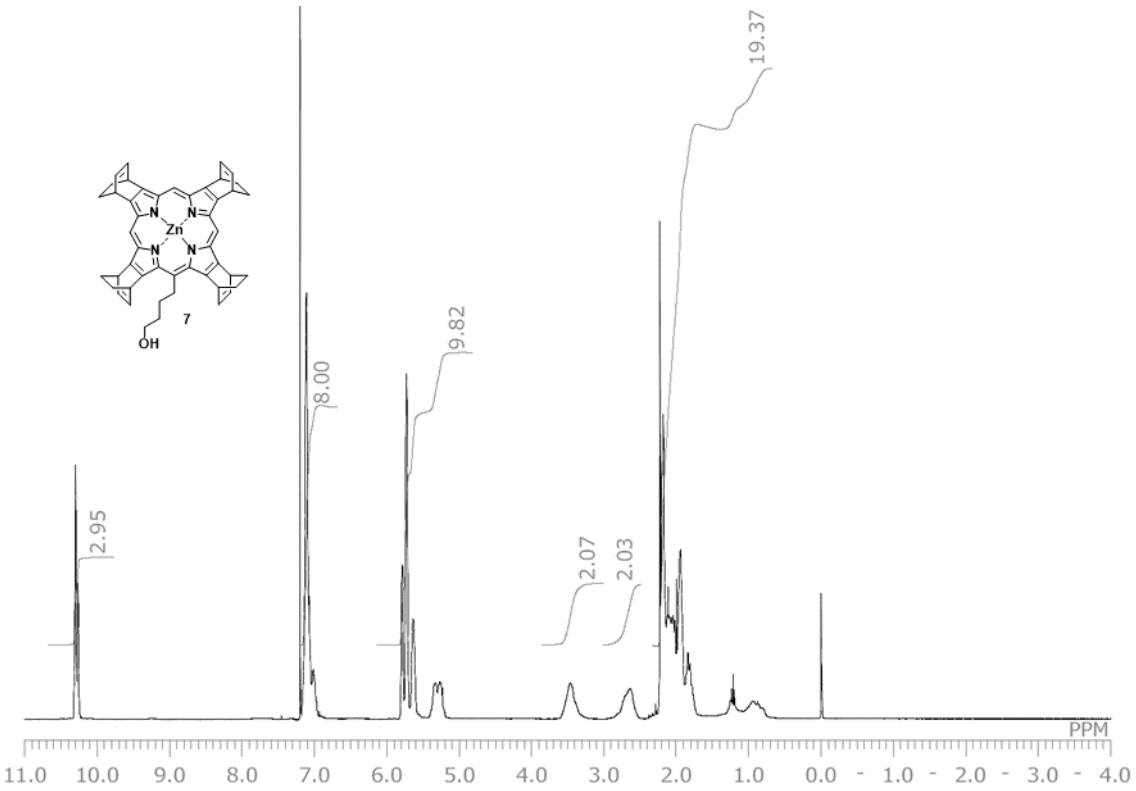

Figure S3-10-1. ^{1}H NMR spectrum of **7** in $CDCl_3$.

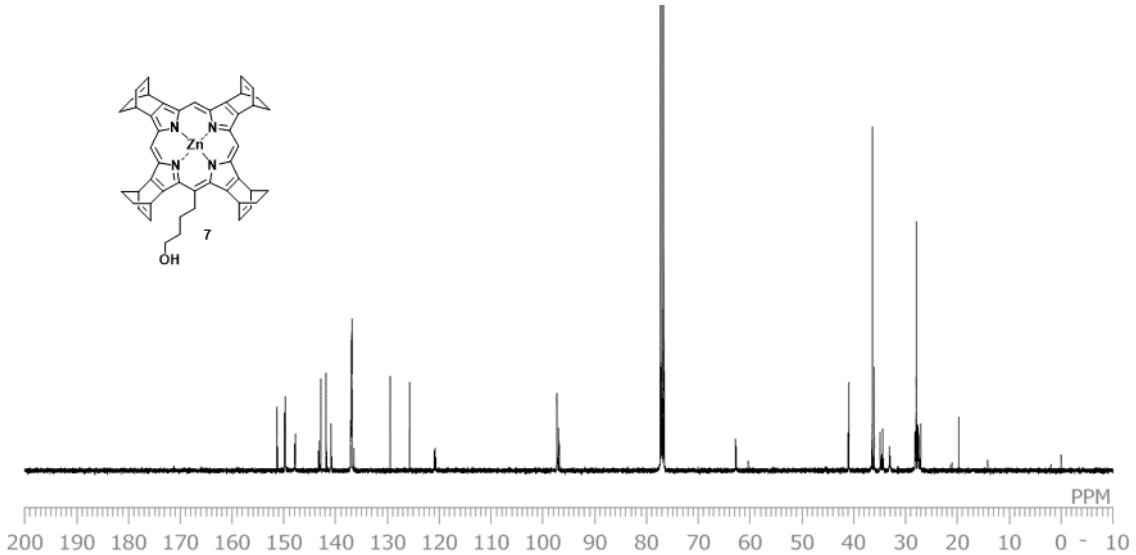

Figure S3-10-2. ^{13}C NMR spectrum of **7** in $CDCl_3$. (Minor peaks are occasionally observed alongside of the main peaks, which are presumably from the structural isomers differing in the orientation of bicycle[2.2.2]octadieno-units. The minor peaks are also listed in the spectroscopic characterization data above.)

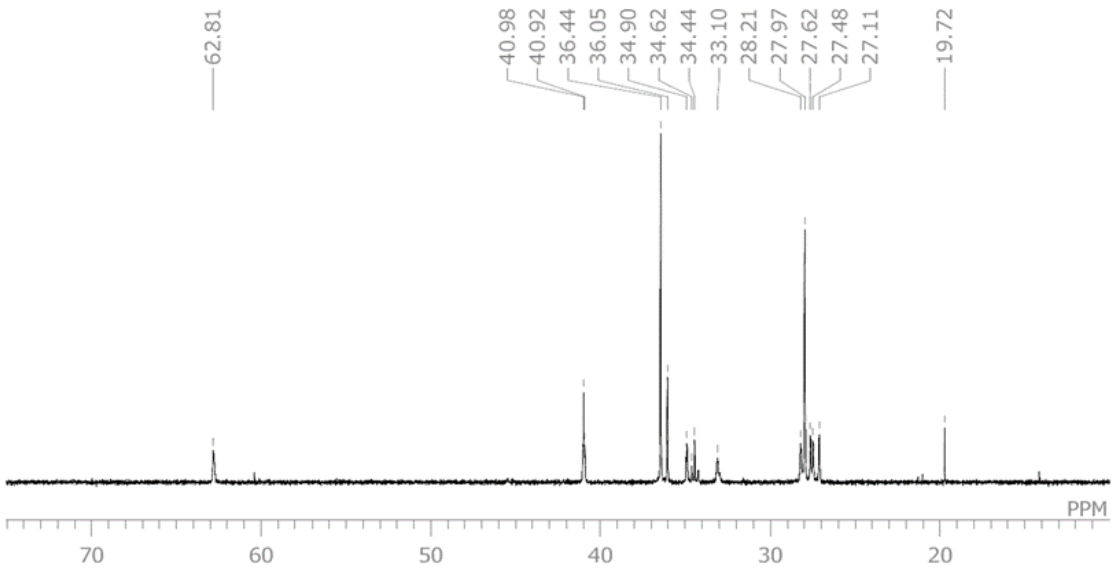

Figure S3-10-3. ^{13}C NMR spectrum of **7** in $CDCl_3$ (10–75 ppm).

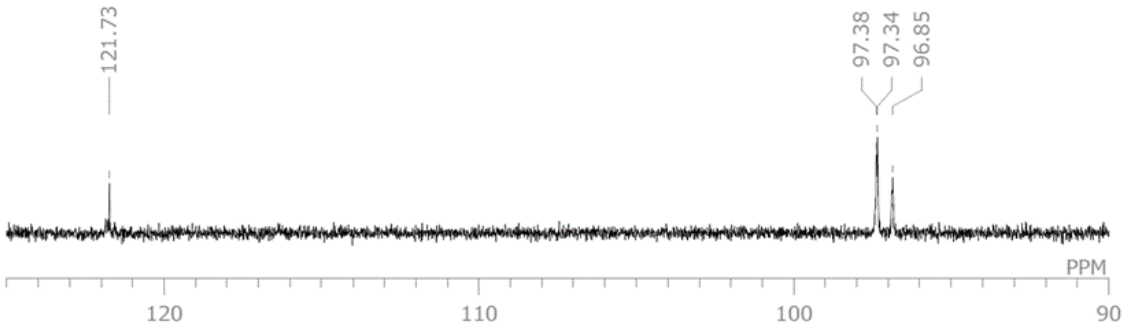

Figure S3-10-4. ^{13}C NMR spectrum of **7** in $CDCl_3$ (90–125 ppm).

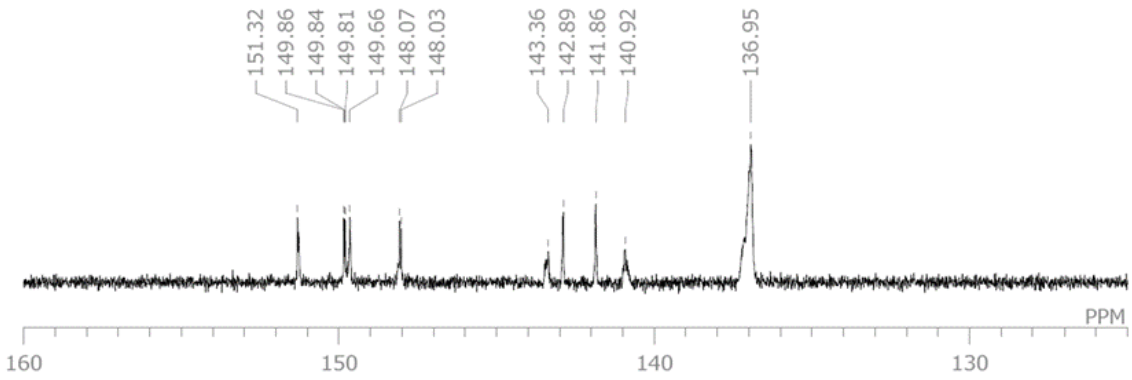

Figure S3-10-5. ^{13}C NMR spectrum of **7** in $CDCl_3$ (125–160 ppm).

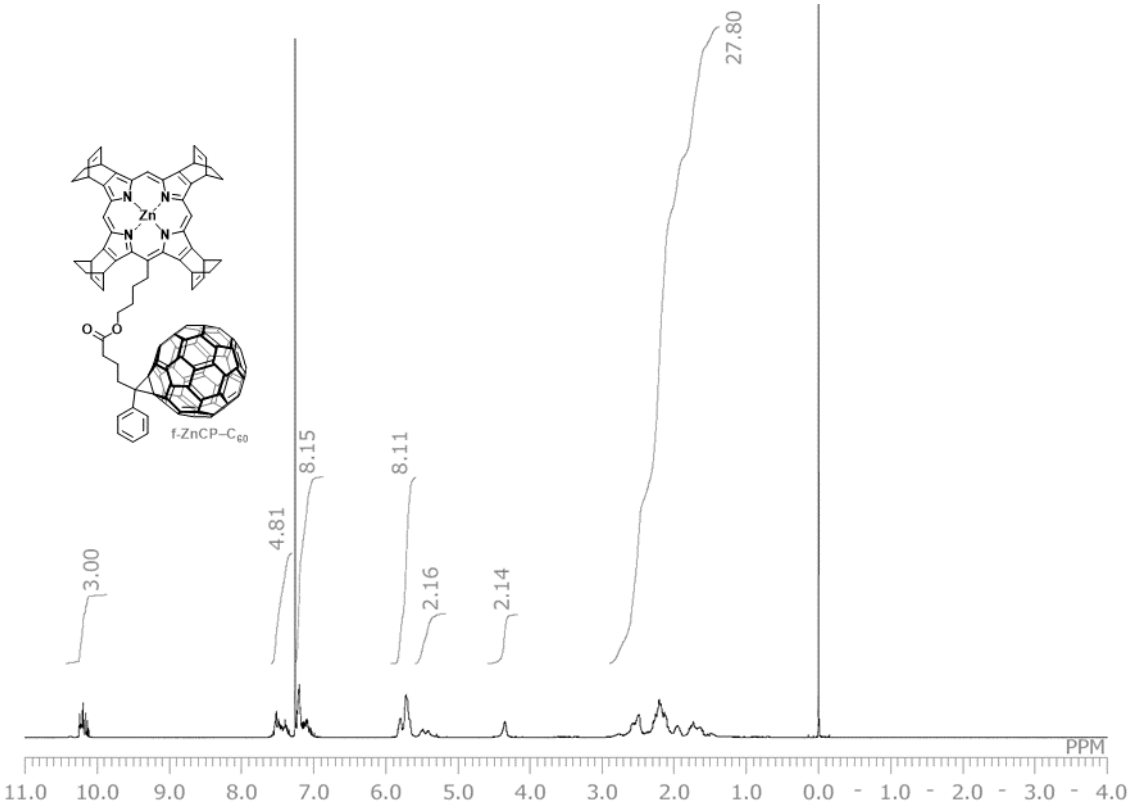

Figure S3-11-1. ^{1}H NMR spectrum of f-ZnCP–C_{60} in $CDCl_3$.

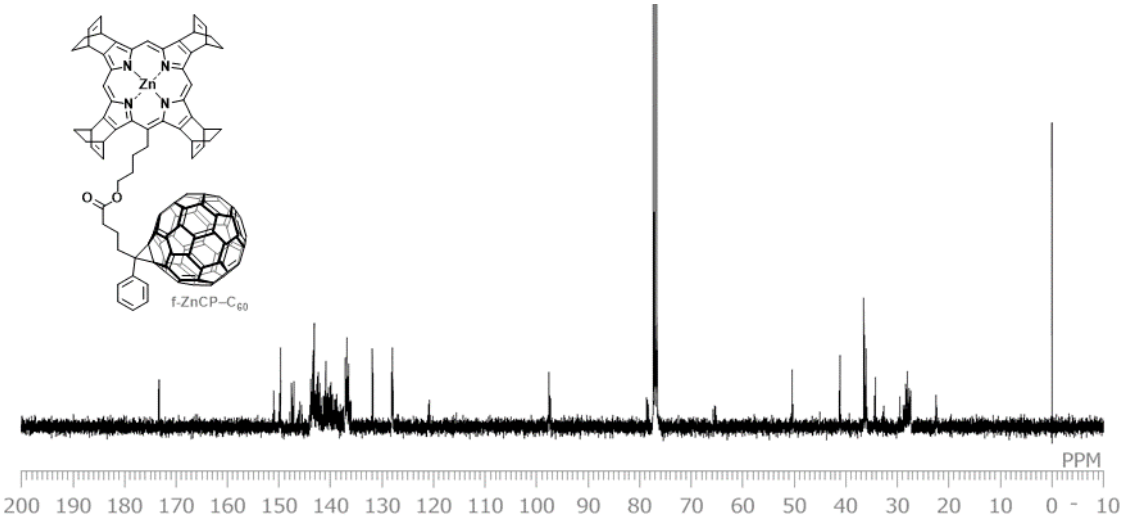

Figure S3-11-2. ^{13}C NMR spectrum of f-ZnCP–C_{60} in $CDCl_3$. (Minor peaks are occasionally observed alongside of the main peaks, which are presumably from the structural isomers differing in the orientation of bicycle[2.2.2]octadieno-units. The minor peaks are also listed in the spectroscopic characterization data above.)

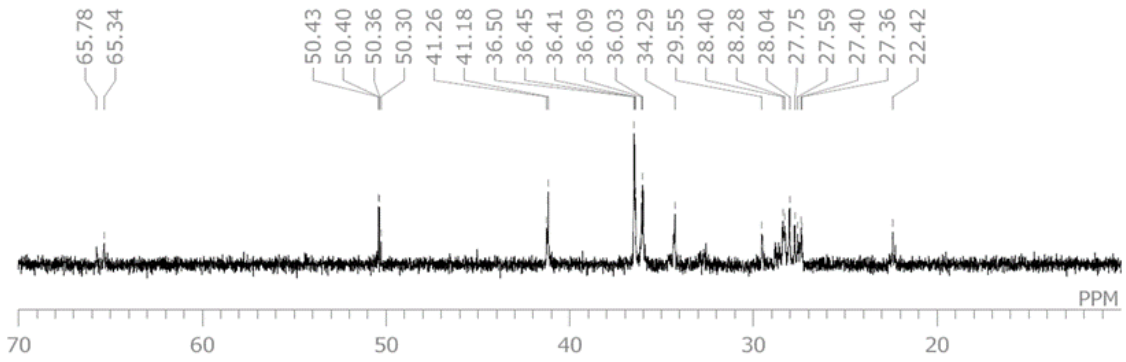

Figure S3-11-3. ^{13}C NMR spectrum of f-ZnCP–C_{60} in $CDCl_3$ (10–70 ppm).

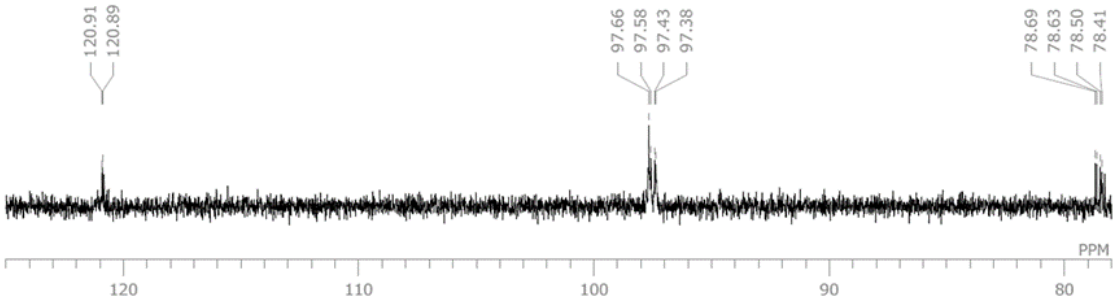

Figure S3-11-4. ^{13}C NMR spectrum of f-ZnCP–C_{60} in $CDCl_3$ (78–125 ppm).

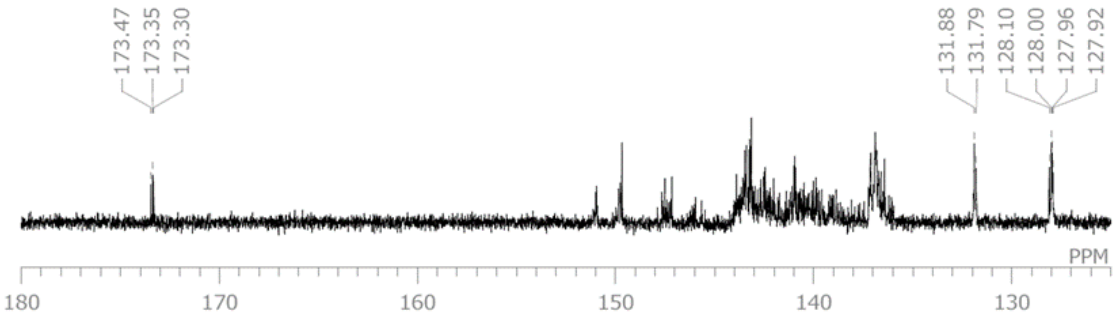

Figure S3-11-5. ^{13}C NMR spectrum of f-ZnCP–C_{60} in $CDCl_3$ (125–180 ppm).

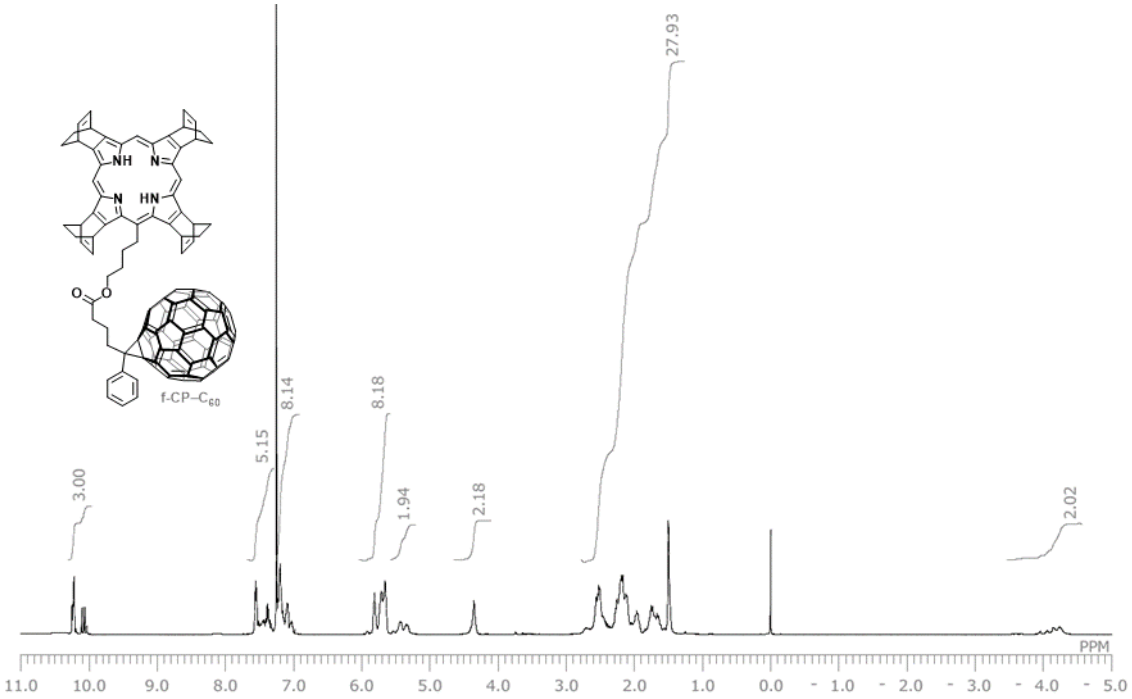

Figure S3-12-1. ^{1}H NMR spectrum of f-CP–C_{60} in $CDCl_3$.

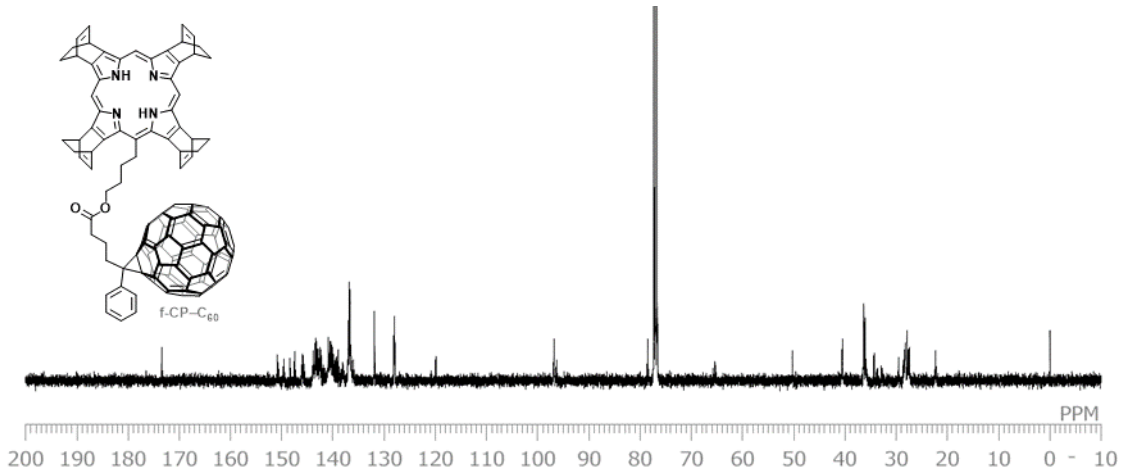

Figure S3-12-2. ^{13}C NMR spectrum of f-CP–C_{60} in $CDCl_3$. (Minor peaks are occasionally observed alongside of the main peaks, which are presumably from the structural isomers differing in the orientation of bicycle[2.2.2]octadieno-units. The minor peaks are also listed in the spectroscopic characterization data above.)

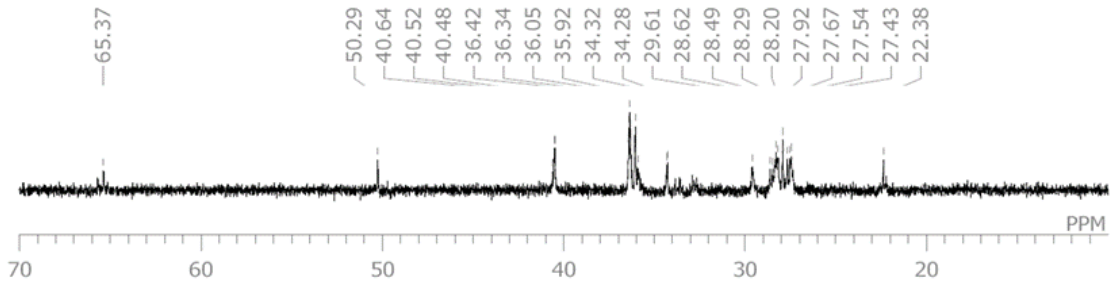

Figure S3-12-3. ^{13}C NMR spectrum of f-CP–C_{60} in $CDCl_3$ (10–70 ppm).

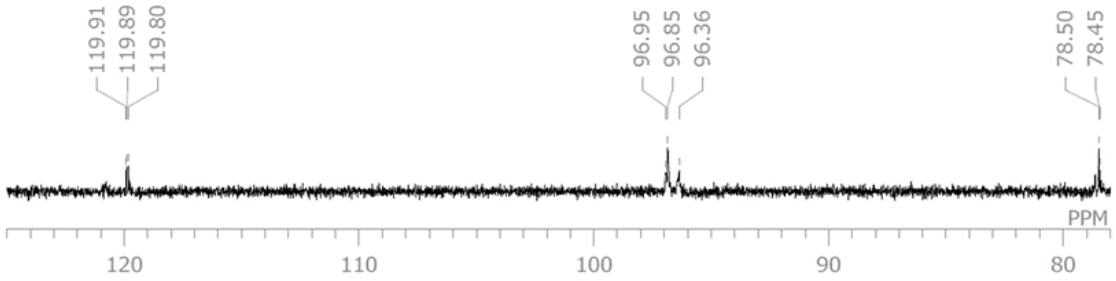

Figure S3-12-4. ^{13}C NMR spectrum of f-CP–C_{60} in $CDCl_3$ (75–125 ppm).

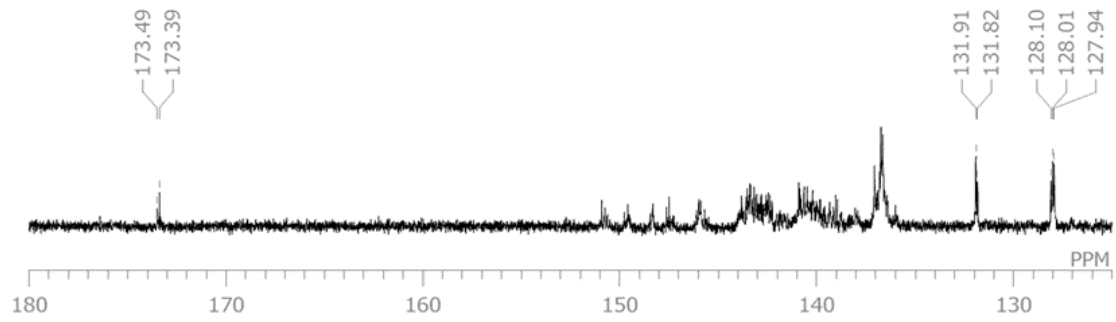

Figure S3-12-5. ^{13}C NMR spectrum of f-CP–C_{60} in $CDCl_3$ (125–180 ppm).

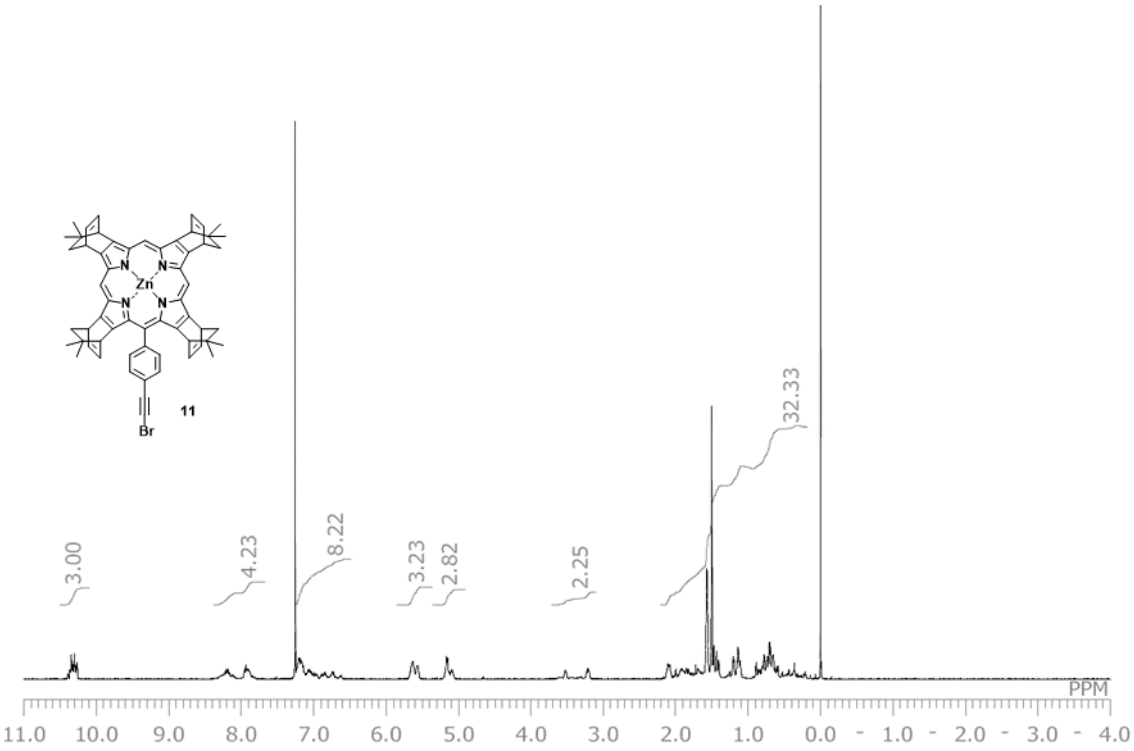

Figure S3-13-1. ^{1}H NMR spectrum of **11** in $CDCl_3$.

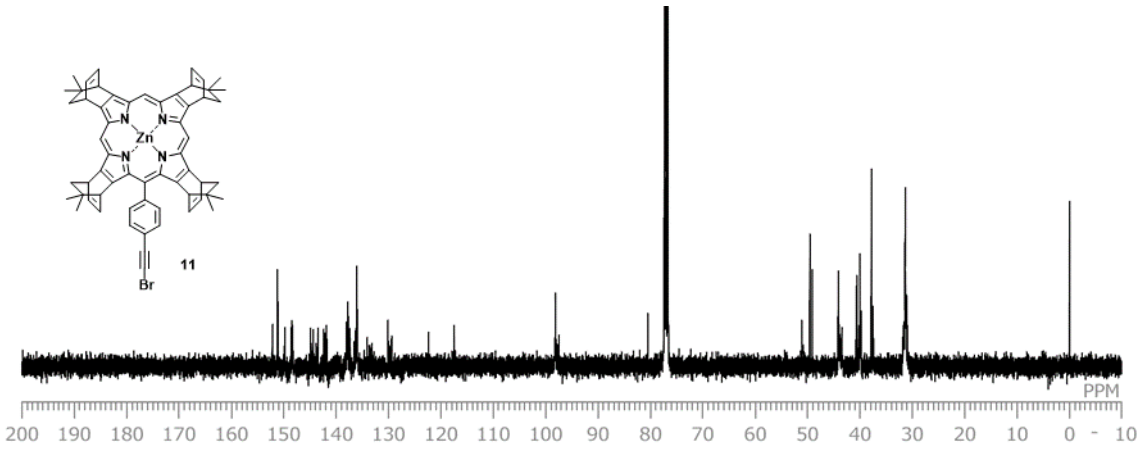

Figure S3-13-2. ^{13}C NMR spectrum of **11** in $CDCl_3$. (Minor peaks are occasionally observed alongside of the main peaks, which are presumably from the structural isomers differing in the orientation of dimethyl-bicycle[2.2.2]octadieno-units. The minor peaks are also listed in the spectroscopic characterization data above.)

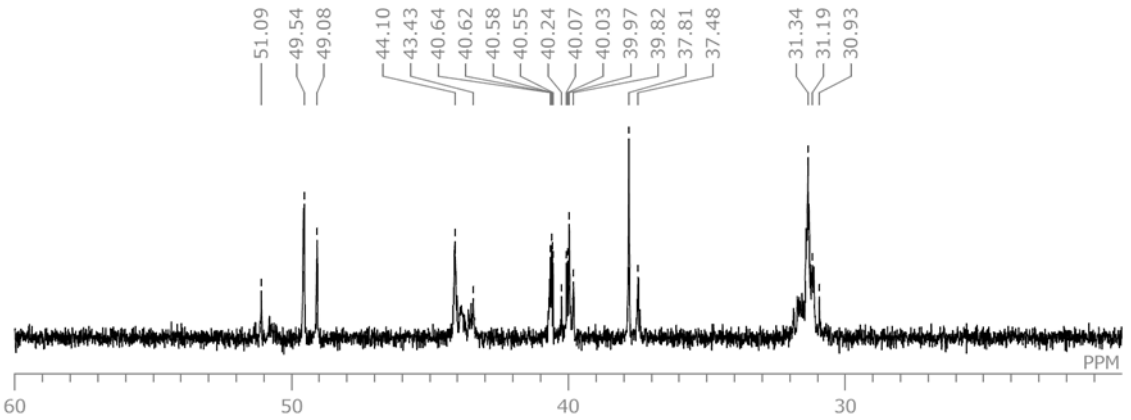

Figure S3-13-3. ^{13}C NMR spectrum of **11** in $CDCl_3$ (20–60 ppm).

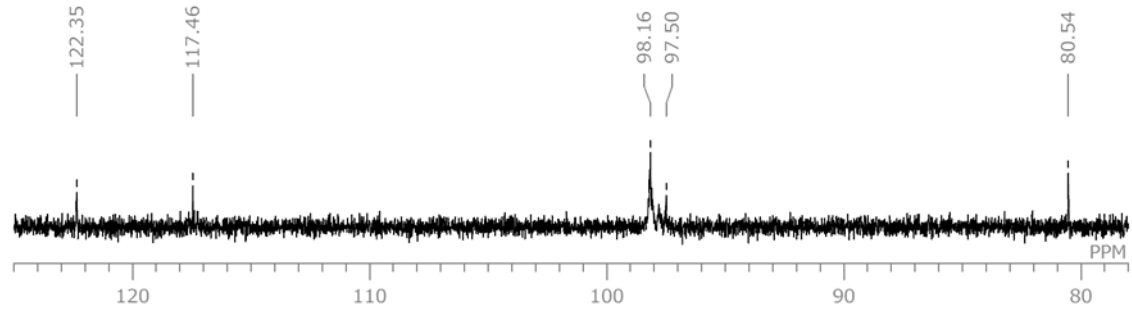

Figure S3-13-4. ^{13}C NMR spectrum of **11** in $CDCl_3$ (78–125 ppm).

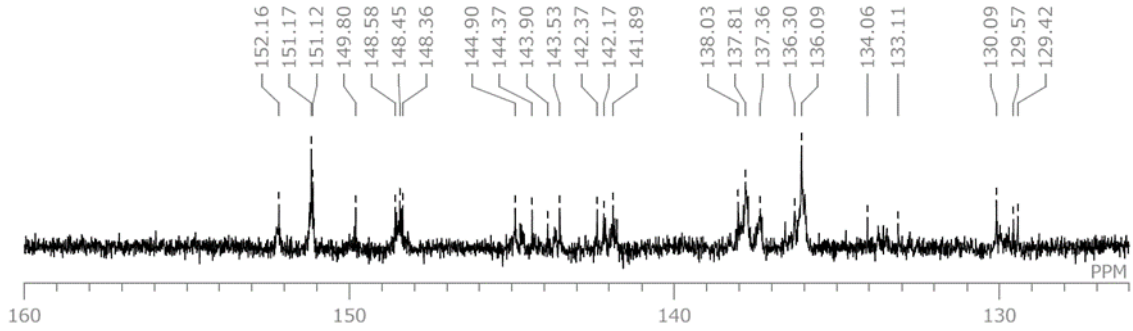

Figure S3-13-5. ^{13}C NMR spectrum of **11** in $CDCl_3$ (125–160 ppm).

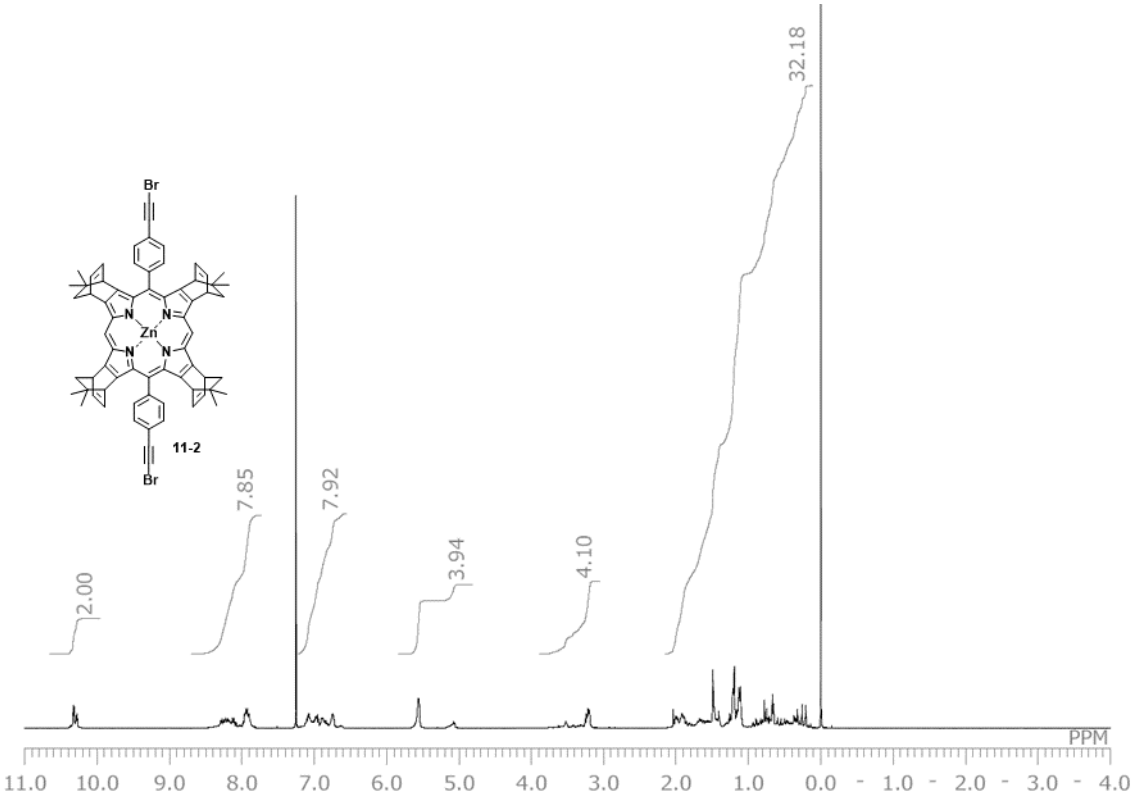

Figure S3-14-1. ^{1}H NMR spectrum of **11-2** in $CDCl_3$.

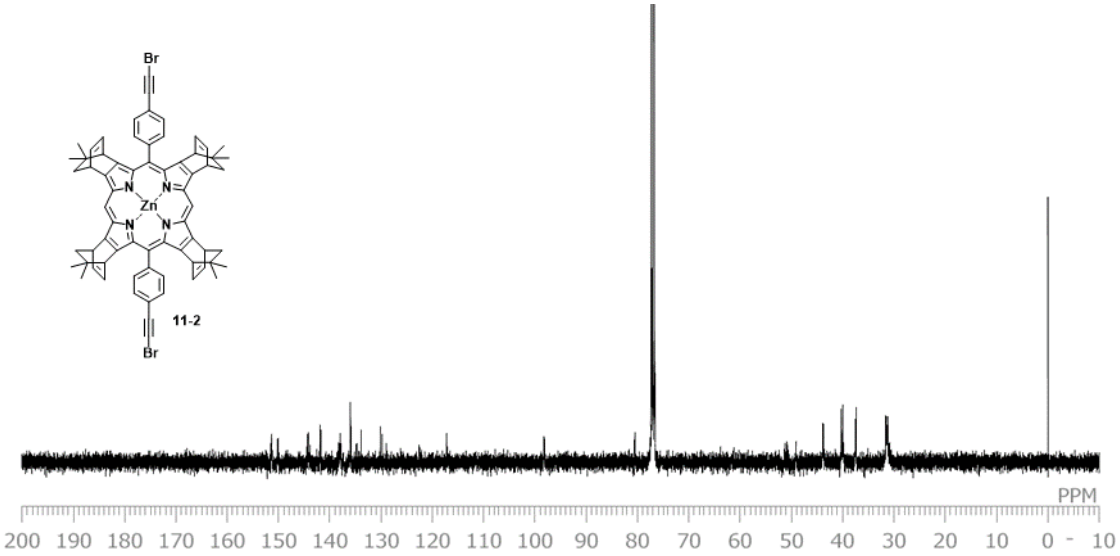

Figure S3-14-2. ^{13}C NMR spectrum of **11-2** in $CDCl_3$. (Minor peaks are occasionally observed alongside of the main peaks, which are presumably from the structural isomers differing in the orientation of dimethyl-bicycle[2.2.2]octadieno-units. The minor peaks are also listed in the spectroscopic characterization data above.)

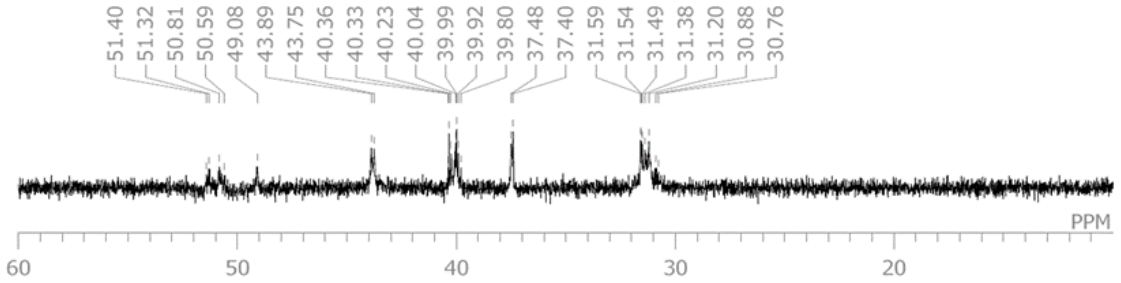

Figure S3-14-3. ^{13}C NMR spectrum of **11-2** in $CDCl_3$ (10–60 ppm).

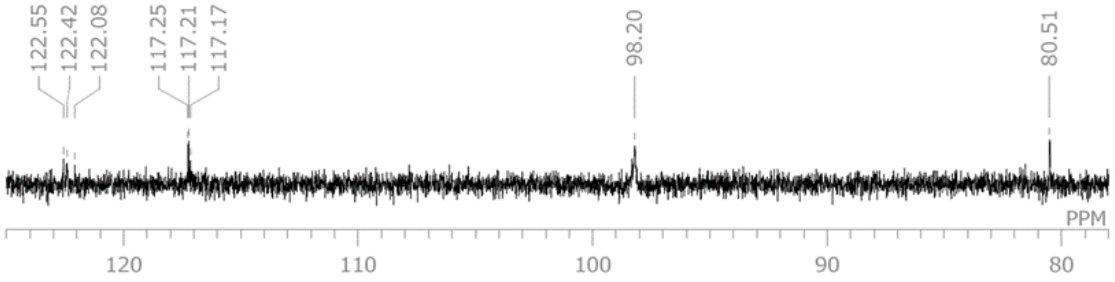

Figure S3-14-4. ^{13}C NMR spectrum of **11-2** in $CDCl_3$ (80–125 ppm).

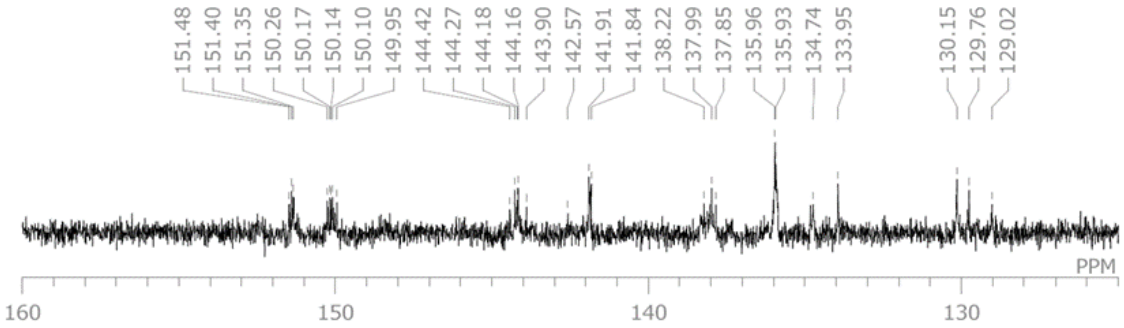

Figure S3-14-5. ^{13}C NMR spectrum of **11-2** in $CDCl_3$ (125–160 ppm).

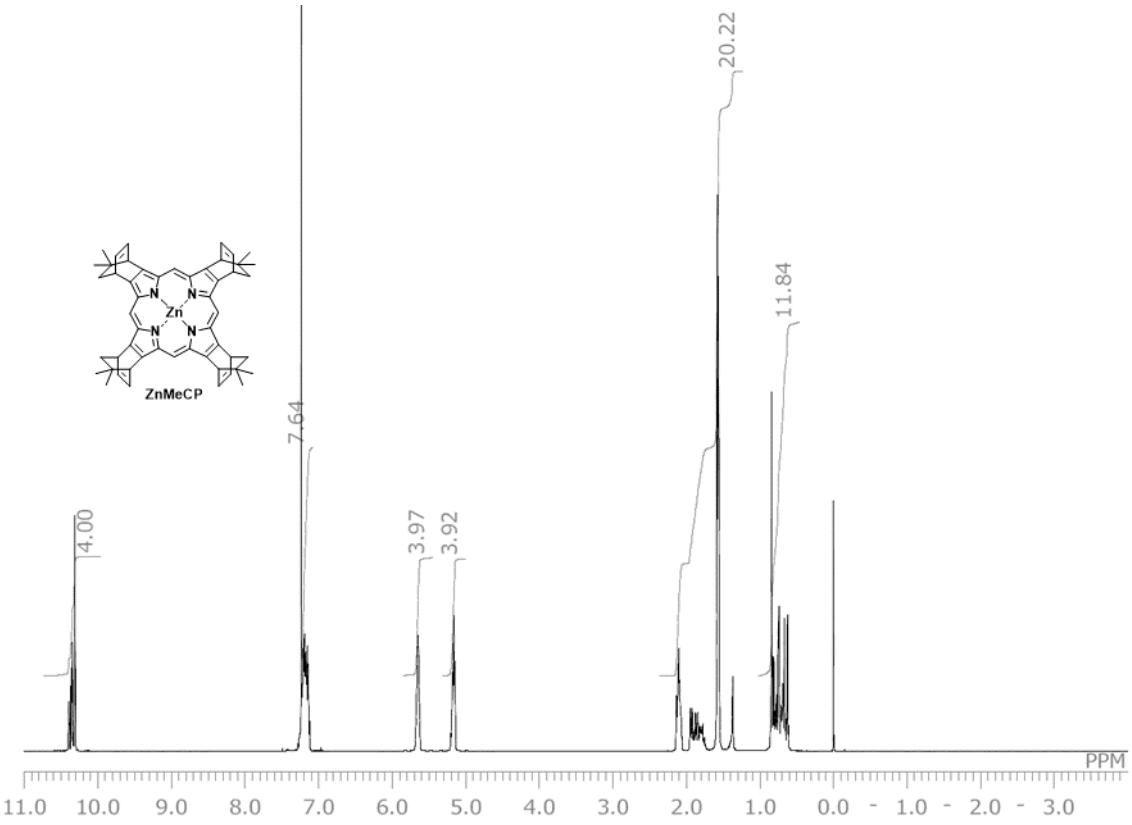

Figure S3-15-1. ^{1}H NMR spectrum of ZnMeCP in $CDCl_3$.

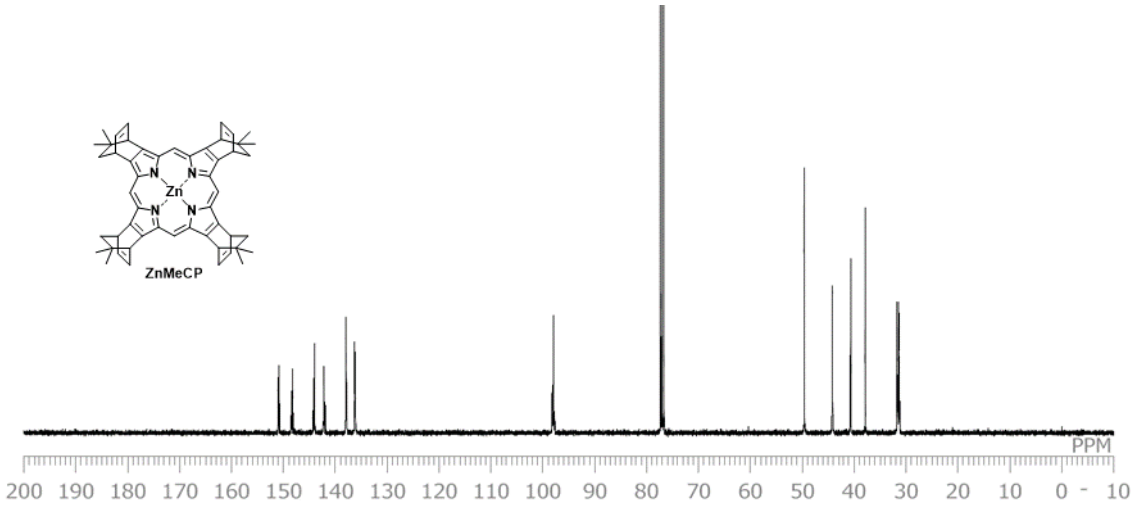

Figure S3-15-2. ^{13}C NMR spectrum of ZnMeCP in $CDCl_3$. (Minor peaks are occasionally observed alongside of the main peaks, which are presumably from the structural isomers differing in the orientation of dimethyl-bicycle[2.2.2]octadieno-units. The minor peaks are also listed in the spectroscopic characterization data above.)

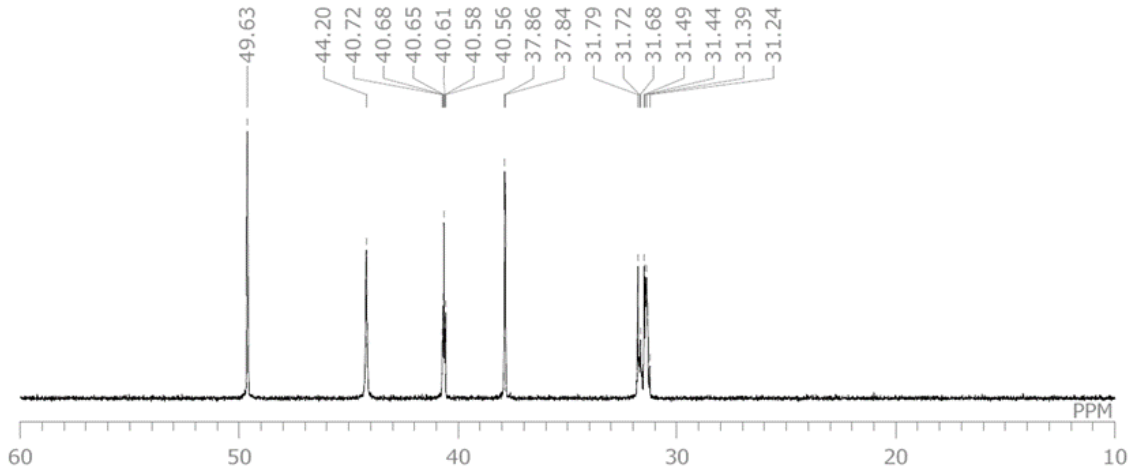

Figure S3-15-3. ^{13}C NMR spectrum of **ZnMeCP** in $CDCl_3$ (10–60 ppm).

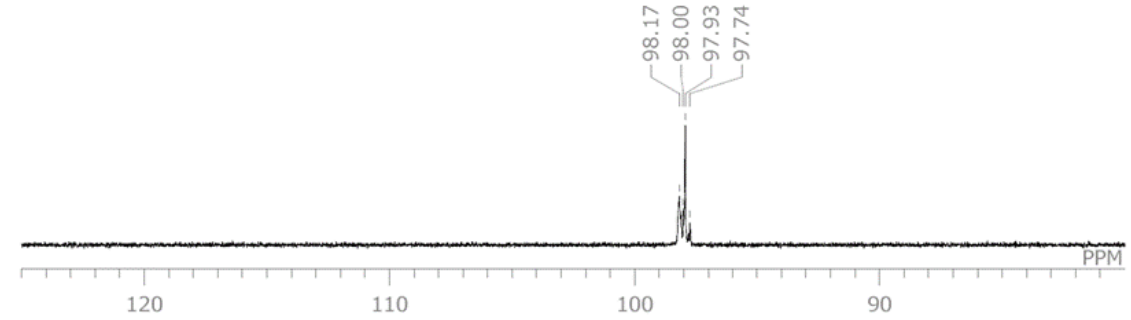

Figure S3-15-4. ^{13}C NMR spectrum of **ZnMeCP** in $CDCl_3$ (80–125 ppm).

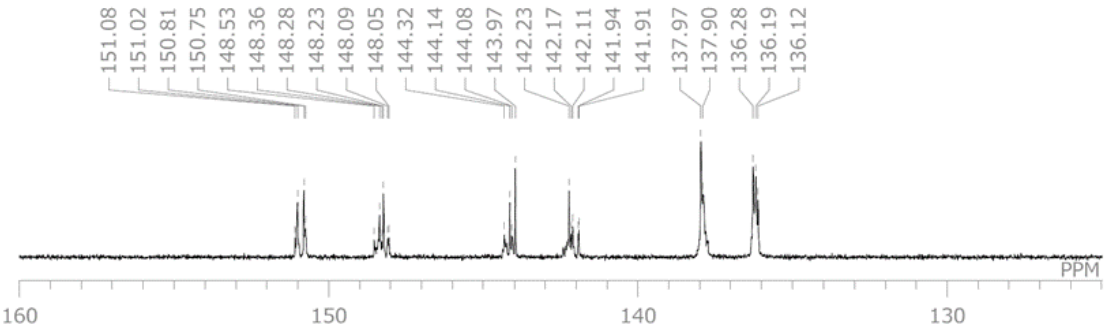

Figure S3-15-5. ^{13}C NMR spectrum of **ZnMeCP** in $CDCl_3$ (125–160 ppm).

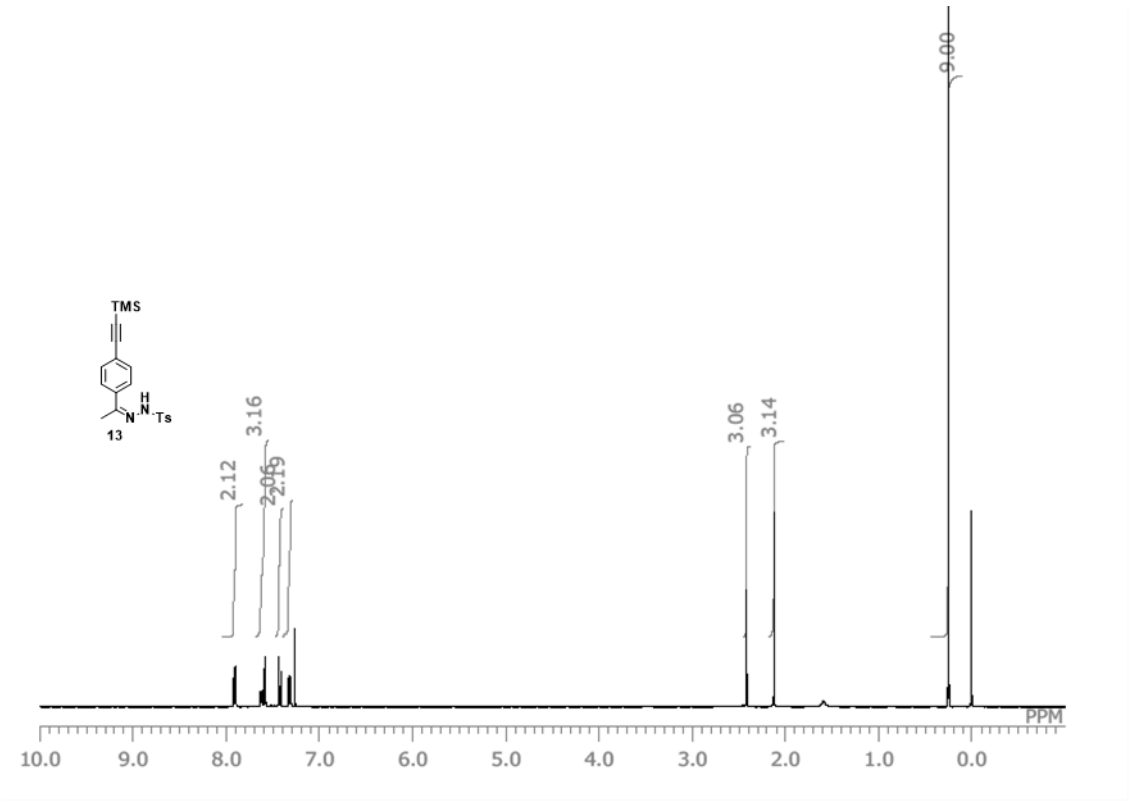

Figure S3-16-1. ^{1}H NMR spectrum of **13** in $CDCl_3$.

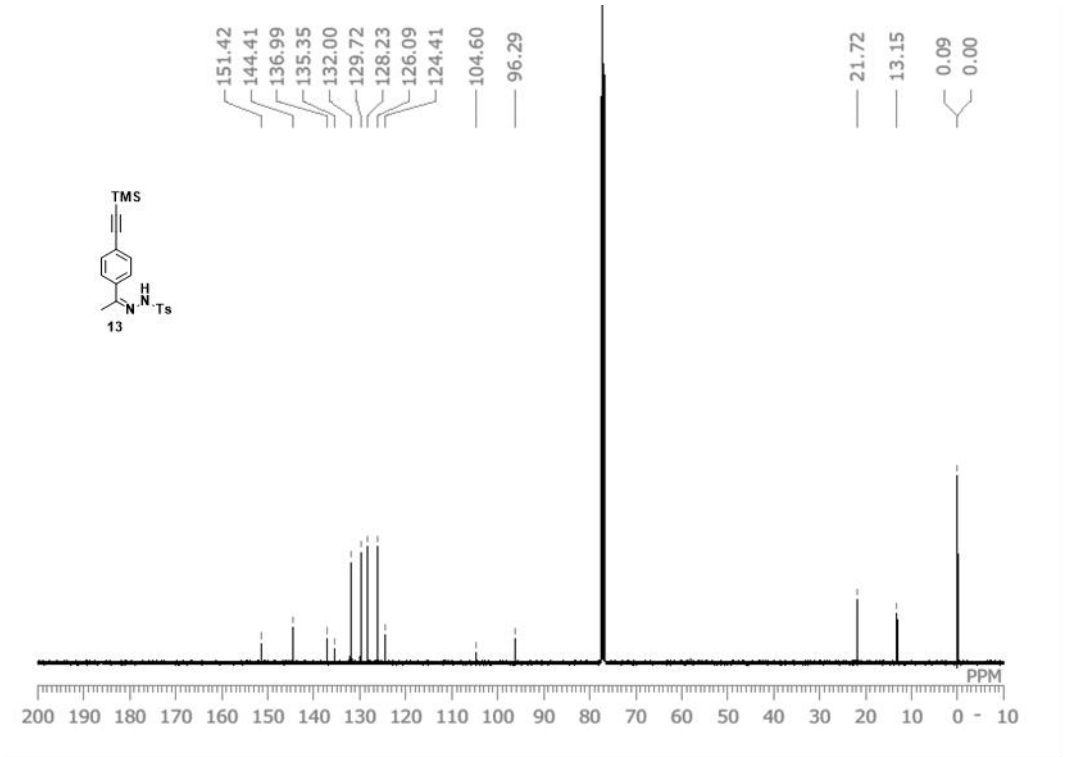

Figure S3-16-2. ^{13}C NMR spectrum of **13** in $CDCl_3$.

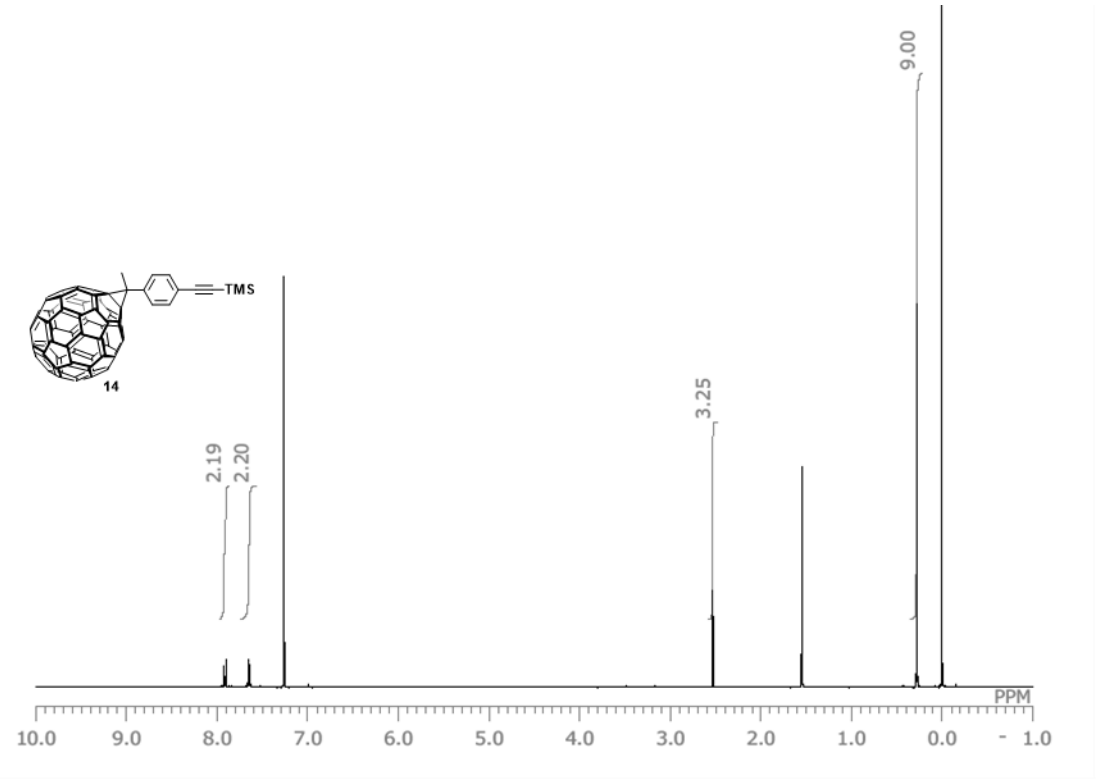

Figure S3-17-1. ^{1}H NMR spectrum of **14** in $CDCl_3$.

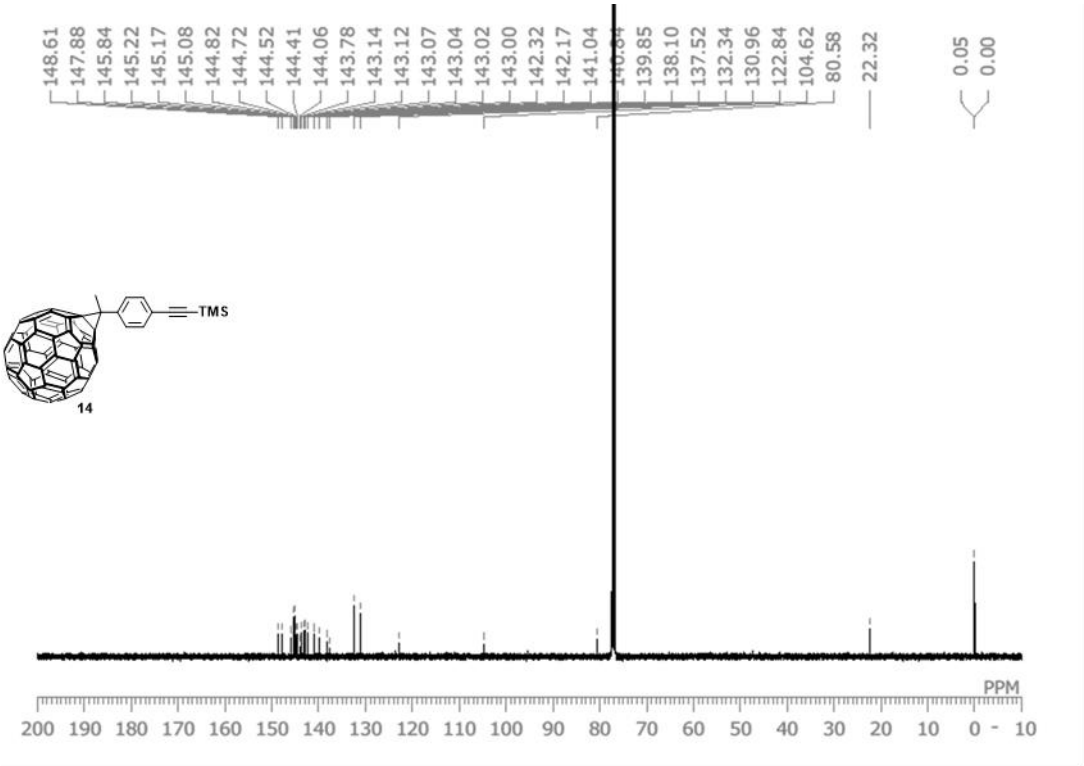

Figure S3-17-2. ^{13}C NMR spectrum of **14** in $CDCl_3$.

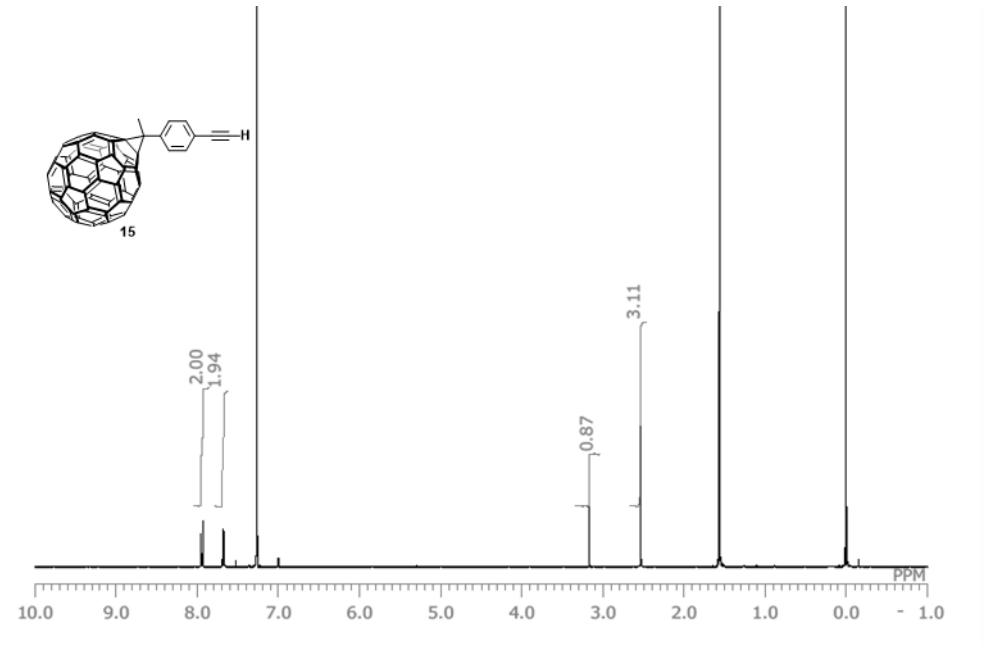

Figure S3-18-1. ^{1}H NMR spectrum of **15** in $CDCl_3$.

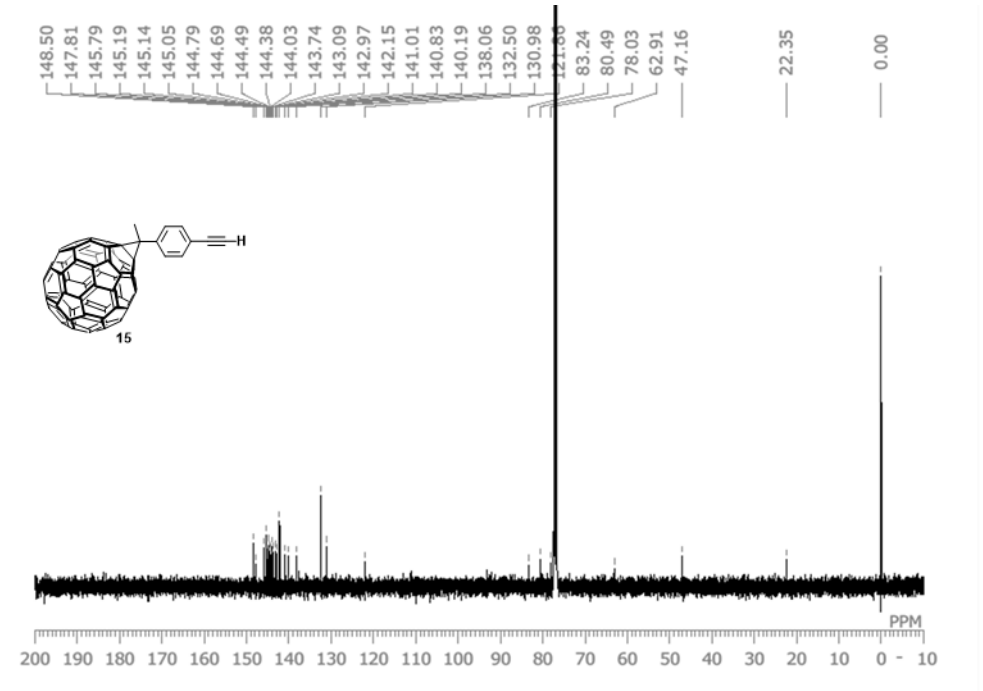

Figure S3-18-2. ^{13}C NMR spectrum of **15** in $CDCl_3$.

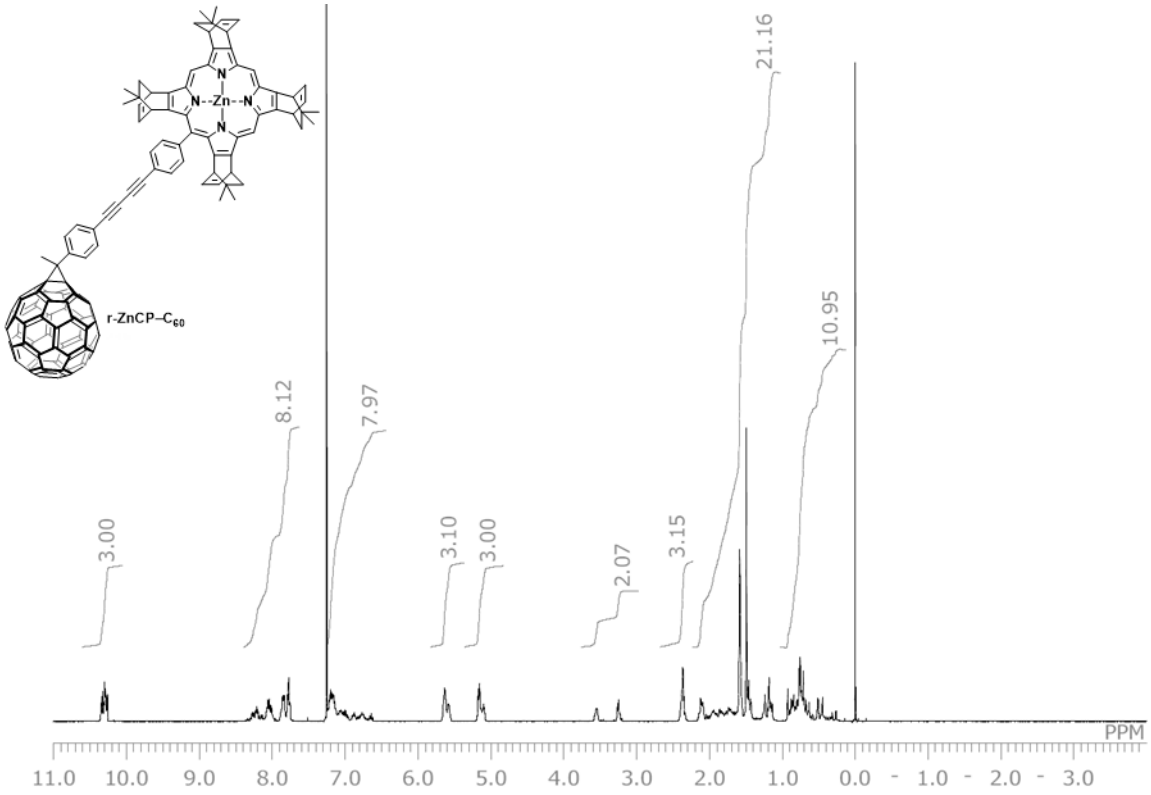

Figure S3-19-1. ^{1}H NMR spectrum of r-ZnCP–C_{60} in $CDCl_3$.

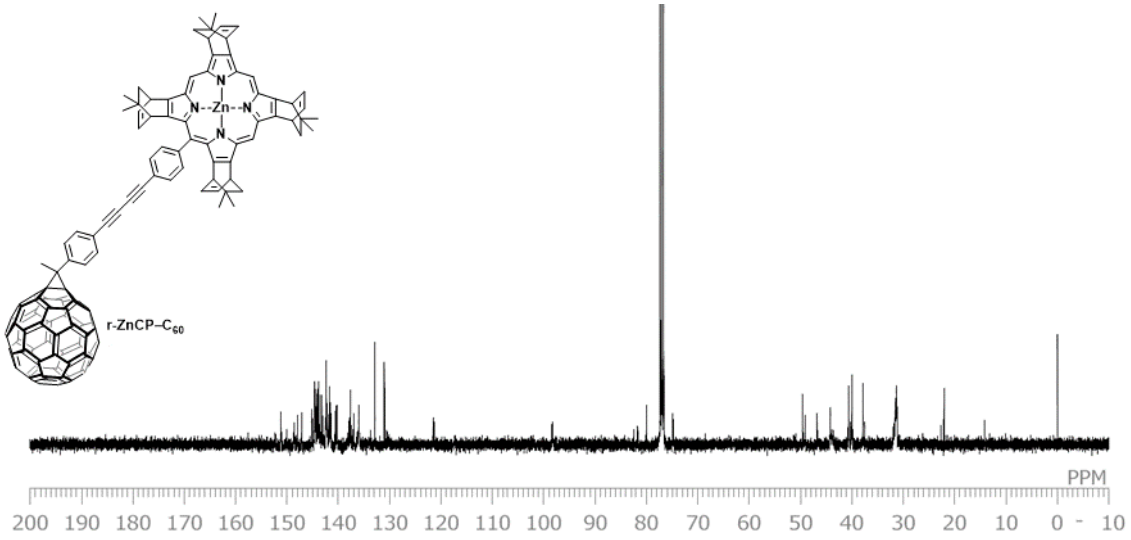

Figure S3-19-2. ^{13}C NMR spectrum of r-ZnCP–C_{60} in $CDCl_3$. (Minor peaks are occasionally observed alongside of the main peaks, which are presumably from the structural isomers differing in the orientation of dimethyl-bicycle[2.2.2]octadieno-units. The minor peaks are also listed in the spectroscopic characterization data above.)

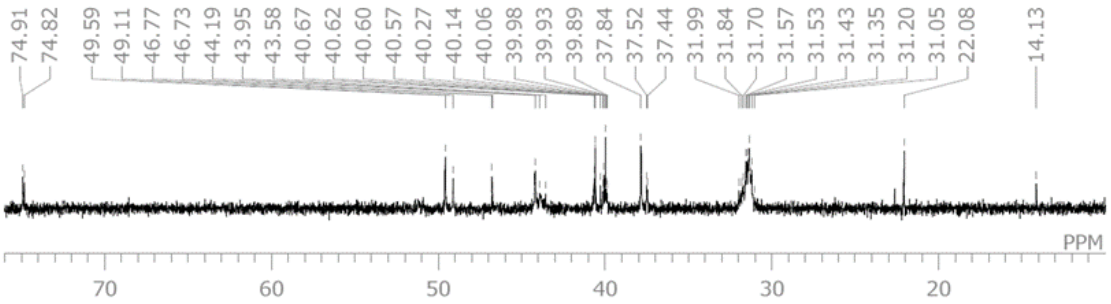

Figure S3-19-3. ^{13}C NMR spectrum of r-ZnCP–C_{60} in $CDCl_3$ (10–75 ppm).

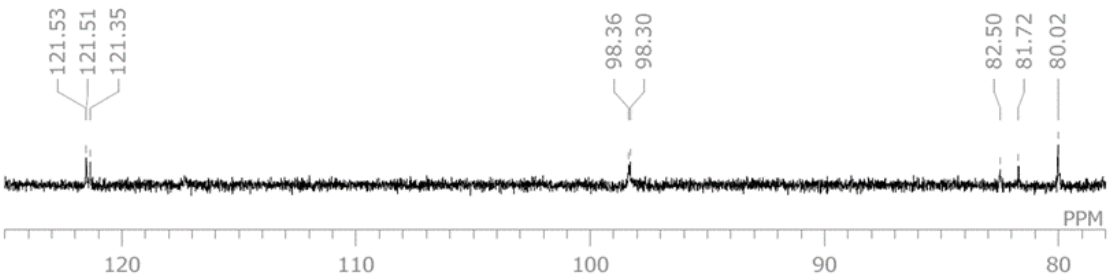

Figure S3-19-4. ^{13}C NMR spectrum of r-ZnCP–C_{60} in $CDCl_3$ (80–125 ppm).

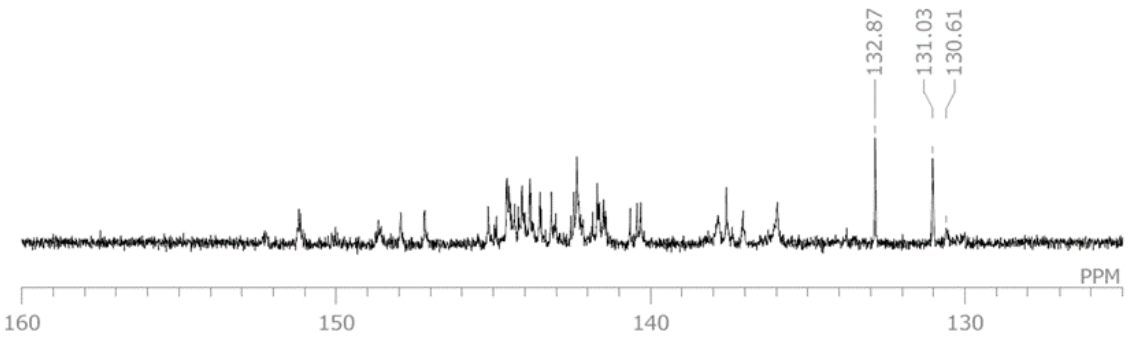

Figure S3-19-5. ^{13}C NMR spectrum of r-ZnCP–C_{60} in $CDCl_3$ (125–160 ppm).

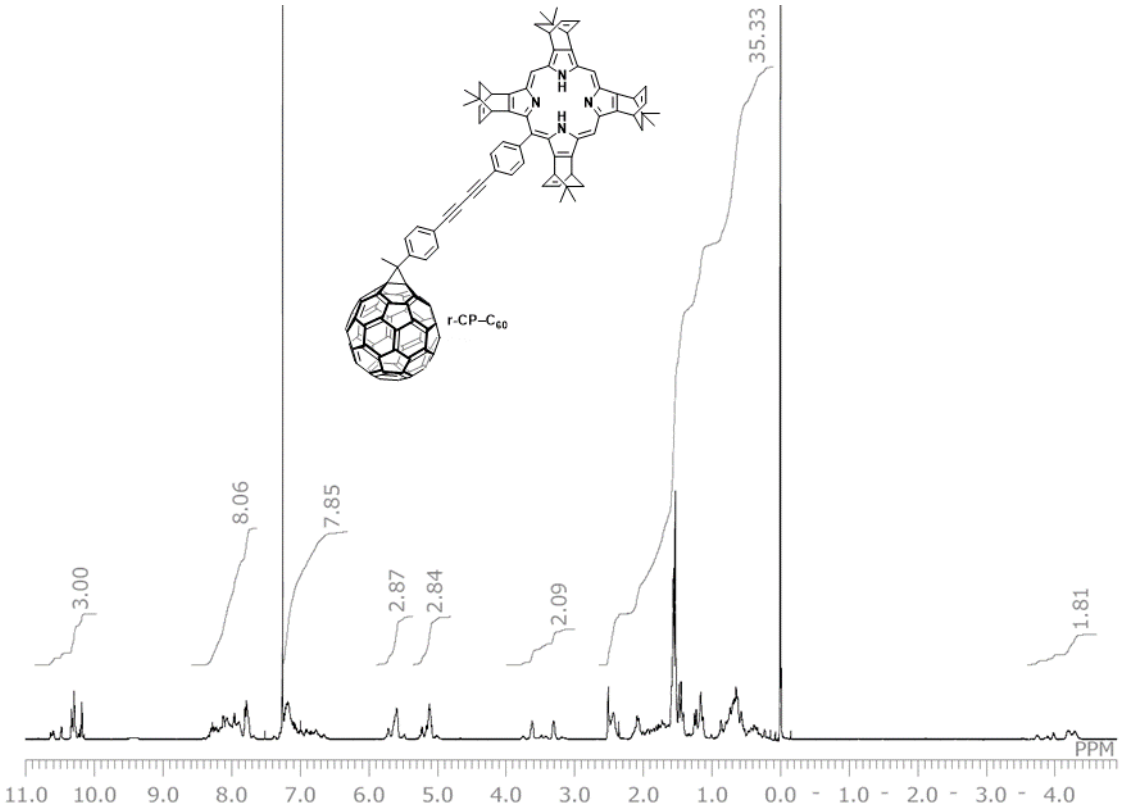

Figure S3-20-1. ^{1}H NMR spectrum of r-CP–C_{60} in $CDCl_3$.

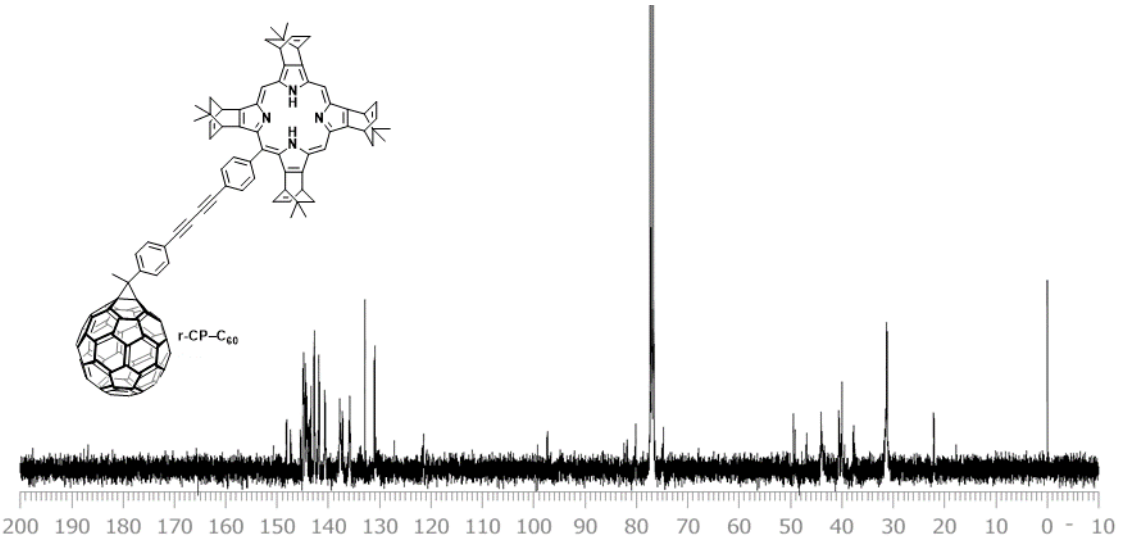

Figure S3-20-2. ^{13}C NMR spectrum of r-CP–C_{60} in $CDCl_3$. (Minor peaks are occasionally observed alongside of the main peaks, which are presumably from the structural isomers differing in the orientation of dimethyl-bicycle[2.2.2]octadieno-units. The minor peaks are also listed in the spectroscopic characterization data above.)

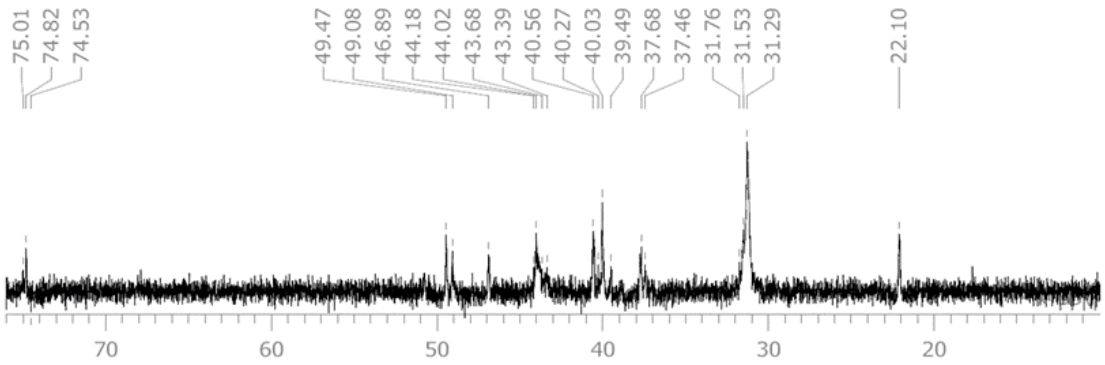

Figure S3-20-3. ^{13}C NMR spectrum of r-CP–C_{60} in $CDCl_3$ (10–75 ppm).

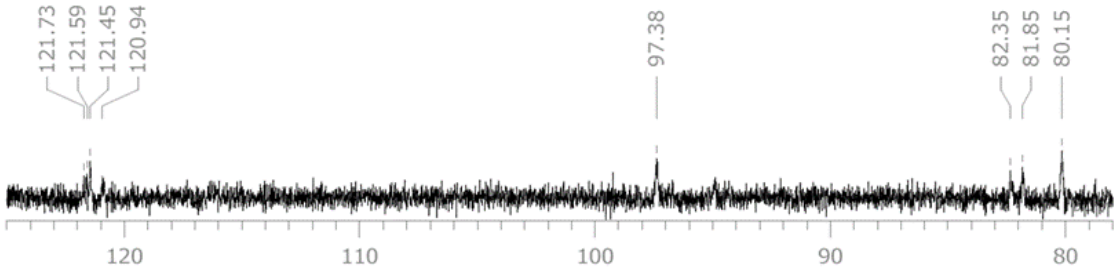

Figure S3-20-4. ^{13}C NMR spectrum of r-CP–C_{60} in $CDCl_3$ (80–125 ppm).

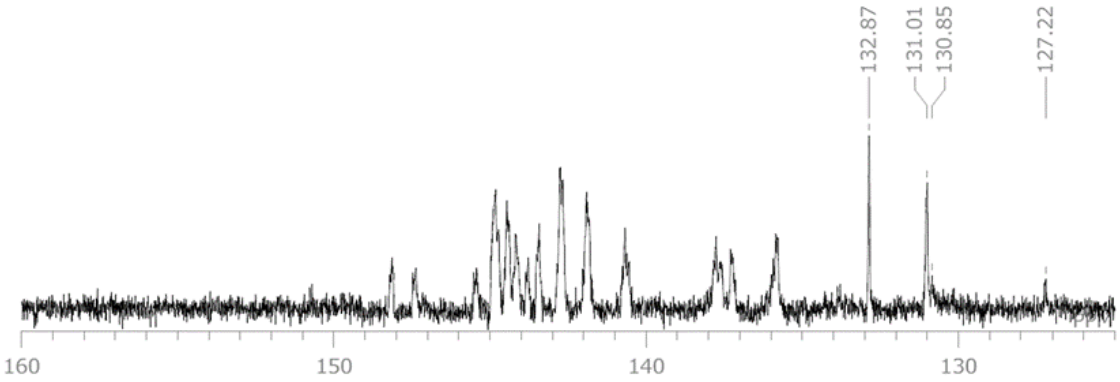

Figure S3-20-5. ^{13}C NMR spectrum of r-CP–C_{60} in $CDCl_3$ (125–160 ppm).

3-8. References

(1) Chen, T. L.; Zhang, Y.; Smith, P.; Tamayo, A.; Liu, Y.; Ma, B. Diketopyrrolopyrrole-Containing Oligothiophene-Fullerene Triads and Their Use in Organic Solar Cells. *ACS Appl. Mater. Interfaces* **2011**, *3*, 2275–2280.

(2) Izawa, S.; Nishizawa, T.; Hashimoto, K.; Koganezawa, T.; Tajima, K. Separated crystallization of donor and acceptor in oligo(*p*-phenylenevinylene)-naphthalenediimide dyad films. *Synthetic Metals* **2014**, *197*, 175–181.

(3) Bu, L.; Guo, X.; Yu, B.; Qu, Y.; Xie, Z.; Yan, D.; Geng, Y.; Wang, F. Monodisperse Co-Oligomer Approach toward Nanostructured Films with Alternating Donor-Acceptor Lamellae. *J. Am. Chem. Soc.* **2009**, *131*, 13242–13243.

(4) Miyanishi, S.; Zhang, Y.; Tajima, K.; Hashimoto, K. Fullerene attached sll-Semiconducting diblock copolymers for stable single-component polymer solar cells. *Chem. Commun.* **2010**, *46*, 6723−6725.

(5) Izawa, S.; Hashimoto, K.; Tajima, K. Morphological stability of organic solar cells based upon an pligo(*p*-phenylenevinylene)–C_{70} Dyad. *Phys. Chem. Chem. Phys.* **2012**, *14*, 16138−16142.

(6) Izawa, S., Hashimoto, K., Tajima, K. Efficient charge generation and collection in organic solar cells based on low band gap dyad molecules. *Chem. Commun.* **2011**, *47*, 6365–6367.

(7) Nishizawa, T.; Lim, H. K.; Tajima, K.; Hashimoto, K. Efficient dyad-based organic solar cells with a highly crystalline donor group. *Chem. Commun* **2009**, *1* , 2469–2471.

(8) Nishizawa, T.; Tajima, K.; Hashimoto, K. Supramolecular formation of fibrous nanostructure in donor−acceptor dyad film. *J. Mater. Chem.* **2007**, *17*, 2440−2445.

(9) Wong, W. W. H.; Vak, D.; Singh, T. B.; Ren, S.; Yan, C.; Jones, D. J.; Liaw, I. I.; Lamb, R. N.; Holmes, A. B. Ambipolar Hexa-*peri*-hexabenzocoronene- Fullerene Hybrid Materials. *Org. Lett.* **2010**, 12, 5000−5003.

(10) Narayanaswamy, K.; Venkateswararao, A.; Nagarjuna, P.; Bishnoi, S.; Gupta, V.; Chand, S.; Singh, S. P. An Organic Dyad Composed of Diathiafulvalene-Functionalized Diketopyrrolopyrrole–Fullerene for Single-Component High-Efficiency Organic Solar Cells. *Angew. Chem. Int. Ed.* **2016**, *55*, 12334–12337.

(11) Nguyen, T. L.; Lee, T. H.; Gautam, B.; Park, S. Y.; Gundogdu, K.; Kim, J. Y.; Woo, H. Y. Single Component Organic Solar Cells Based on Oligothiophene-Fullerene Conjugate. *Adv. Funct. Mater.* **2017**, *27*, 1702474.

(12) Yamaguchi, Y.; Suzuki, M.; Motoyama, T.; Sugii, S.; Katagiri, C.; Takahira, K.; Ikeda, S.; Yamada, H.; Nakayama, K. I. Photoprecursor approach as an effective means for preparing multilayer organic semiconducting thin films by solution processes. *Scientific Reports* **2014**, *4*, 7151.

(13) Matsuo, Y.; Sato, Y.; Niinomi, T.; Soga, I.; Tanaka, H.; Nakamura, E. Columnar Structure in Bulk Heterojunction in Solution-Processable Three-Layered p-i-n Organic Photovoltaic Devices Using Tetrabenzoporphyrin Precursor and silylmethyl[60]fullerene. *J. Am. Chem. Soc.* **2009**, *131*, 16048–16050.

(14) Guide, M.; Dang, X. D.; Nguyen, T. Q. Nanoscale Characterization of Tetrabenzoporphyrin and Fullerene-Based Solar Cells by Photoconductive Atomic Force Microscopy. *Adv. Mater.*

2011, *23*, 2313–2319.

(15) Ito, S.; Murashima, T.; Ono, N.; Uno, H. A new synthesis of benzoporphyrins using 4,7-dihydro-4,7-ethano-*2H*-isoindole as a synthon of isoindole. *Chem. Commun.* **1998**, 16, 1661–1662.

(16) Gust, D.; Moore, T. A.; Moore, A. L. Molecular Mimicry of Photosynthetic Energy and Electron Transfer. *Acc. Chem. Res.* **1993**, *26*, 198–205.

(17) Kashiwagi, Y.; Ohkubo, K.; McDonald, J. A.; Blake, I. M.; Crossley, M. J.; Araki, Y.; Ito, O.; Imahori, H.; Fukuzumi, S. Long-Lived Charge-Separated State Produced by Photoinduced Electron Transfer in a Zinc Imidazoporphyrin-C_{60} Dyad. *Org. Lett.* **2003**, *5*, 2719–2721.

(18) Wasielewski, M. R. Photoinduced Electron Transfer in Supramolecular Systems for Artificial Photosynthesis. *Chem. Rev.* **1992**, *92*, 435–461.

(19) Liman, C. D.; Choi, S.; Breiby, D. W.; Cochran, J. E.; Toney, M. F.; Kramer, E. J.; Chabinyc, M. L. Two-Dimensional GIWAXS Reveals a Transient Crystal Phase in Solution-Processed Thermally Converted Tetrabenzoporphyrin. *J. Phys. Chem. B* **2013**, *117*, 14557–14567.

(20) Okujima, T.; Hashimoto, Y.; Jin, G.; Yamada, H.; Uno, H.; Ono, N. Synthesis of extremely soluble precursors of tetrabenzoporphyrins. *Tetrahedron* **2008**, *64*, 2405–2411.

(21) Aakeröy, C. B.; Sinha, A. S.; Epa, K. N.; Spartz, C. L.; Desper, J. A versatile and green mechanochemical route for aldehyde–oxime conversions. *Chem. Commun.* **2012**, *48*, 11289–11291.

(22) Thorand, S.; Krause, N. Improved Procedures for the Palladium-Catalyzed Coupling of Terminal Alkynes with Aryl Bromides (Sonogashira Coupling). *J. Org. Chem.* **1998**, *63*, 8551–8553.

(23) Tkachenko, N. V; Guenther, C.; Imahori, H.; Tamaki, K.; Sakata, Y.; Fukuzumi, S.; Lemmetyinen, H. Near infra-red emission of charge-transfer complexes of porphyrin–fullerene films. *Chemical Physics Letters* **2000**, *326*, 344–350.

(24) Huang, J.; Carpenter, J. H.; Li, C. Z.; Yu, J. S.; Ade, H.; Jen, A. K. Y. Highly Efficient Organic Solar Cells with Improved Vertical Donor-Acceptor Compositional Gradient Via an Inverted Off-Center Spinning Method. *Adv. Mater.* **2016**, *28*, 967–974.

(25) Huang, J.; Wang, H.; Yan, K.; Zhang, X.; Chen, H.; Li, C. Z.; Yu, J. Highly Efficient Organic Solar Cells Consisting of Double Bulk Heterojunction Layers. *Adv. Mater.* **2017**, *29*, 1–9.

(26) Kumari, T.; Lee, S. M.; Kang, S.-H.; Chen, S.; Yang, C. Ternary solar cells with a mixed face-on and edge-on orientation enable an unprecedented efficiency of 12.1%. *Energy Environ. Sci.* **2017**, *10*, 258–265.

(27) Charvet, R.; Yamamoto, Y.; Sasaki, T.; Kim, J.; Kato, K.; Takata, M.; Saeki, A.; Seki, S.; Aida, T. Segregated and Alternately Stacked Donor/acceptor Nanodomains in Tubular Morphology Tailored with Zinc Porphyrin-C_{60} amphiphilic Dyads: Clear Geometrical Effects on Photoconduction. *J. Am. Chem. Soc.* **2012**, *134*, 2524–2527.

(28) Van Der Sluis, P.; Spek, A. L. BYPASS: An Effective Method for the Refinement of Crystal Structures Containing Disordered Solvent Regions. *Acta Cryst. A* **1990**, *46*, 194–201.

(29) Sun, Y.; Seo, J. H.; Takacs, C. J.; Seifter, J.; Heeger, A. J. Inverted Polymer Solar Cells Integrated with a Low-Temperature-Annealed Sol-Gel-Derived ZnO Film as an Electron Transport Layer. *Adv. Mater.* **2011**, *23*, 1679−1683.

Chapter 4.

Improvement of Interlayer Structure in p–i–n-Type Organic Solar Cells with Fullerene-Linked Tetrabenzoporphyrin Additive

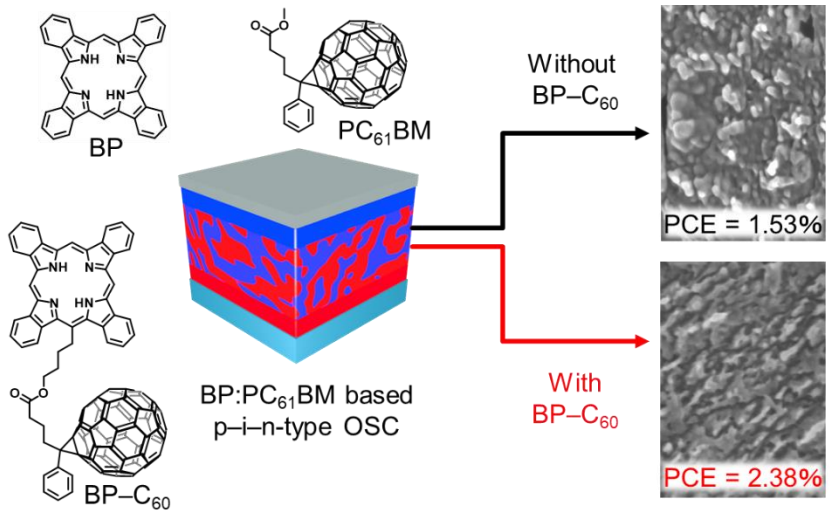

This chapter demonstrates that the addition of fullerene-linked tetrabenzoporphyrin (BP–C_{60}) as additive to the interlayer (i-layer) composed of BP and $PC_{61}BM$ improves the miscibility of BP and $PC_{61}BM$. The photoenergy conversion efficiency (PCE) of p–i–n type organic solar cells (OSCs), where the blend film of BP and $PC_{61}BM$ (i-layer) is sandwiched by BP (p-layer) and $PC_{61}BM$ (n-layer), was improved up to 150% of the control device by adding the BP–C_{60} to i-layer. The film morphology is carefully investigated by atomic force microscopy, fluorescence microspectroscopy, two-dimensional grazing-incident wide-angle X-ray diffraction, and scanning electron microscope to reveal that added BP–C_{60} can interact with both BP and $PC_{61}BM$ to arrange the grain size and to increase BP:$PC_{61}BM$ interface for effective charge separation in the p–i–n device.

4-1. Introduction

In the recent study of OSCs, the achievement of over 10% PCE has not been increasingly uncommon[1–8] because of the interactive evolution in photovoltaic materials (both p-type and n-type)[9–13] and device architectures (inverted or tandem structure).[14,15] Although these developments play the critical roles to improve the device performances, construction of optimized active layer structure is certainly required to obtain the best power conversion efficiencies (PCEs) in most every case. In the bulkhetero junction (BHJ) type active layers, p- and n-type organic semiconductor materials are blended to give large p–n heterojunction interfaces for effective exciton dissociation at the interface and bi-continuous phases for effective hole and electron carrier transport toward respective electrodes. Therefore, a lot of strategies have been proposed to modify the morphologies, e.g., choice of spin-coating solvents,[16] solvent additives,[17–19] and thermal-[20–24] or solvent-annealing conditions.[24–32] However, these efficiencies depend a great deal on the molecular properties such as solubility, crystallinity, miscibility, and molecular orientation. In addition, several studies show the difficulty in structural conservation of optimized BHJ layers with above strategies. Nanometer-scale morphologies of the active layer are metastable structure and therefore an initial optimized nano-structures are often lost with light exposure or elevated temperature.[33–37] In addition, significant damage in active layer due to the photo-induced degradation of the generally used solvent additive 1,8-diiodeoctane have been reported.[38–41] Therefore, the offer of the new morphological control method is still challenging work.

With above insight, two major approach using compatibilizer have been reported to control and stabilize the nano-scale morphology (Figure 1). The first approach is the use of polymer-type compatibilizer, e.g., graft–block type copolymer based on pendent Poly(3-hexylthiophene-2,5-diyl) (P3HT) repeat unit and pendent fullerene unit,[42] donor–acceptor block copolymer,[43–45] and fullerene-end capped P3HT.[46] These materials can suppress the aggregation of domains in the P3HT:[6,6]-phenyl-C_{61}-butyric acid methyl ester ($PC_{61}BM$)–based OSCs, resulting in the improved stability. Unfortunately, these syntheses are burdensome because of the multiple post-polymerization steps in spite of the low solubility due to the many pendent fullerenes. In addition, many parts of insulating moieties necessary to introduce fullerenes as second block could deteriorate

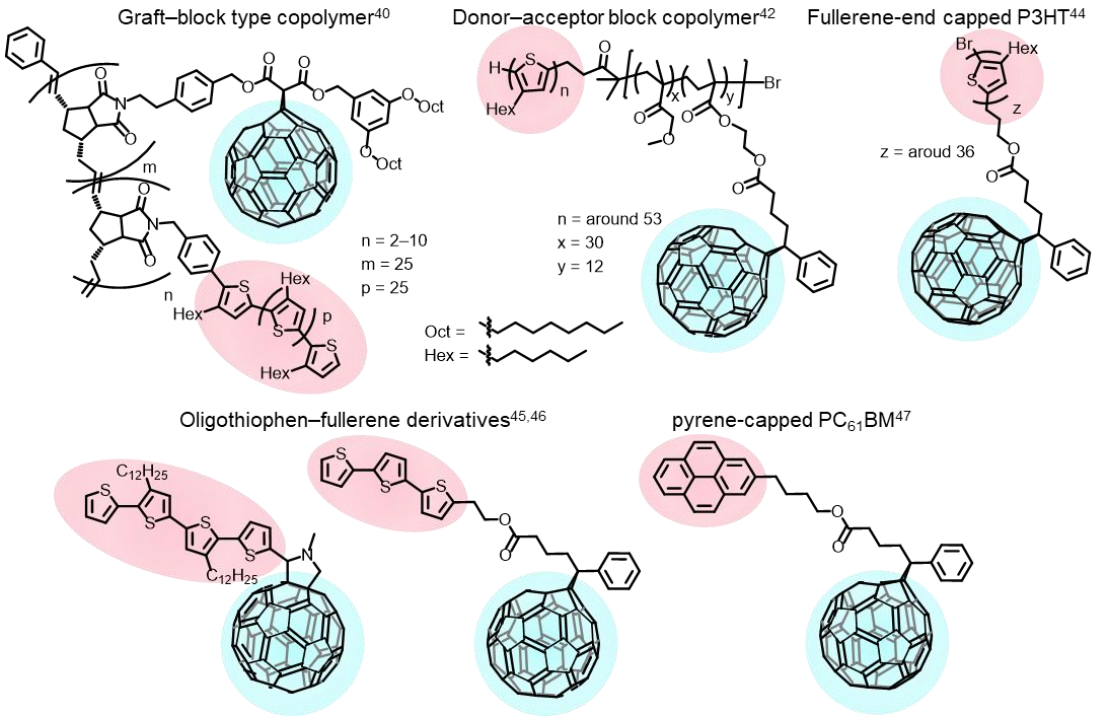

Figure 1. Examples of morphological compatibilizers for OSCs.

the charge carrier transport in the active layer. The second approach is the addition of small molecule compatibilizers, e.g. oligothiophen–fullerene derivatives[47,48] and pyrene-capped $PC_{61}BM$[49] with short synthetic steps with good solubility. They can also work for the constrained $PC_{61}BM$ dispersion in the P3HT phase due to the reducing surface energy between P3HT and $PC_{61}BM$ with long-term thermal stability. Moreover, significantly improved PCEs also were obtained because of their careful design and syntheses.[48,49]

As described above, examples of morphological compatibilizer have been well investigated in case of polymer based OSCs. However, the effects for small molecular based OSCs have been scarcely known to date. Moreover, morphological control of p–i–n-type device by an addition of compatibilizers has not been reported. As mentioned in chapter 3, the authors have reported fullerene-linked BP (BP–C_{60}) as OSCs material via the corresponding CP-type pre-cursor (CP–C_{60}) to systematically investigate the effect of covalent linkage between donor and acceptor units in solution processed OSCs. These compounds might be good compatibilizer of BP:$PC_{61}BM$ layer because BP–C_{60} compound includes both BP and C_{60} units as they are.

With these in mind, the study in this chapter demonstrates the morphological control using BP–C_{60} as the compatibilizer for the BP:$PC_{61}BM$ based p–i–n device.

4-2. Materials and Device Fabrications

As shown in Figure 2, the simplest flexible BP–C_{60} which showed the best PCE in the p–i–n device was used as compatibilizer of BP:$PC_{61}BM$ layer in this study. To date, no specific molecular design of compatibilizers for OSCs has been suggested with the exception of the affinity between the p- and n-type materials and the components of the compatibilizers. But, we realized that three features observed from the prior studies of BP–C_{60} are important points to construct the effective compatibilizer, giving the uniform modification of film structure result in the improved PCE: thermal non-crystallization property during the thermal conversion of CP–C_{60} to BP–C_{60} at 160–220 ºC (Figure S4-1 in the Support Information), a complete homogeneity as film, and a better photovoltaic performance compared with blended BP:$PC_{61}BM$ film.

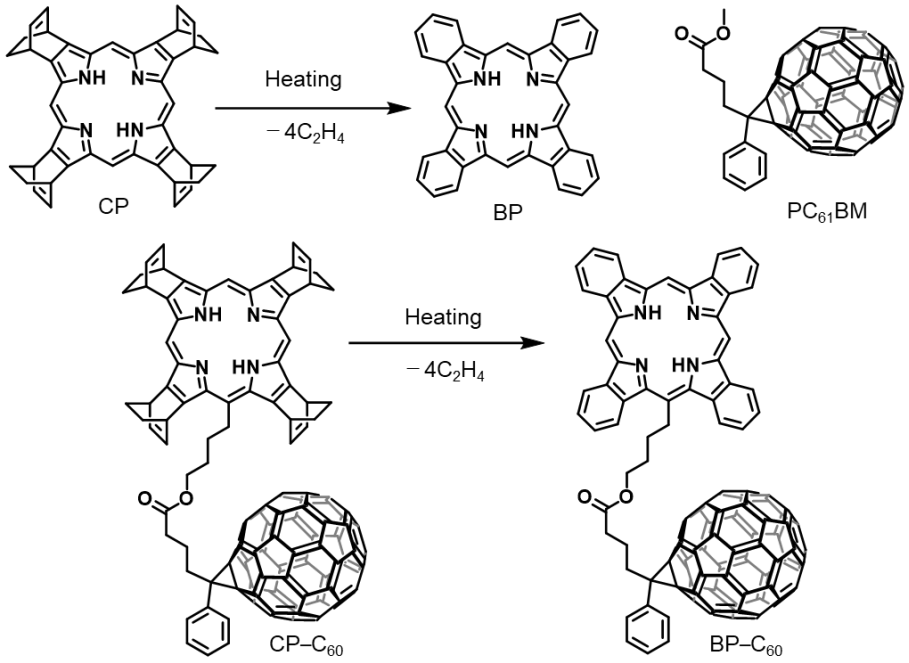

Figure 2. Chemical transformation of CP to BP and CP–C_{60} to BP–C_{60} with thermal annealing and Chemical structure of $PC_{61}BM$.

The p–i–n devices were prepared as shown in Figure 3 (see Experimental section for more details). The BP film for p-layer was prepared by thermal conversion of CP film on (3,4-ethylenedioxythiophene):poly(4-styrenesulfonate) (PEDOT:PSS)-coated Indium-tin-oxide (ITO)/glass substrate. In the same manner, i-layers containing

BP:$PC_{61}BM$ with and without BP–C_{60} were prepared on the BP film by spin coating of CP:$PC_{61}BM$ solution with and without CP–C_{60} followed by heating to fabricate the Structure I. n-Layer of $PC_{61}BM$ was deposited on the StructureI by spin coating of $PC_{61}BM$ solution followed by thermal annealing. Finally, buffer (Calcium: Ca) and metal electrode (Aluminum: Al) were deposited on n-layer to give p–i–n devices which compose different amounts of BP–C_{60}. For microscopic observations of the BP structure on the p-layer, the Structure I was rinsed by a drop of chloroform ($CHCl_3$) with spinning of the substrates to prepare the Structure II.

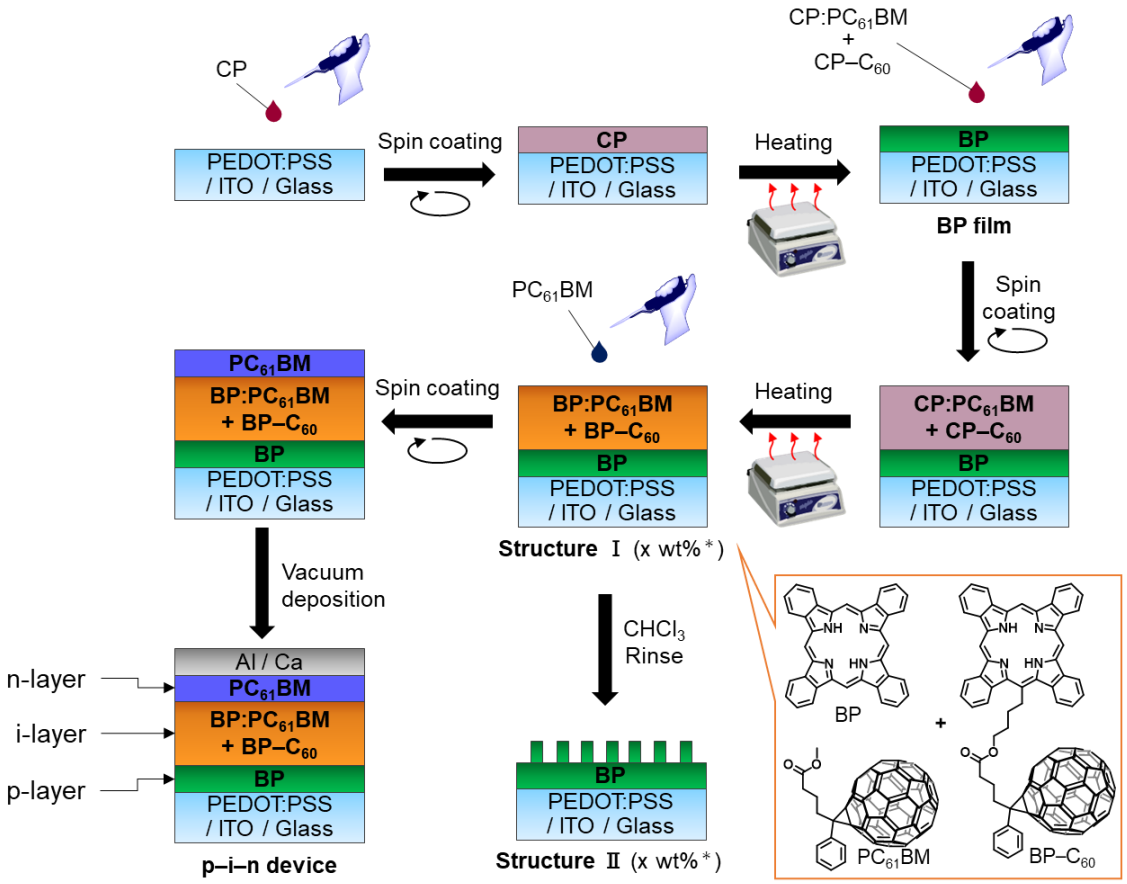

Figure 3. Device fabrication scheme and film preparations for morphological investigations. *Addition amounts of BP–C_{60} (0–10 wt%).

4-3. Device Performance

Photovoltaic performances of p–i–n devices are summarized in Figure 4 (a) and Table 1. The p–i–n (0 wt%) device, a control device, includes no BP–C_{60} in the i-layer. The p–i–n (3–10 wt%) devices include 3–10 wt% BP–C_{60} in the i-layer. When BP–C_{60} was added to the i-layer of BP:$PC_{61}BM$, significantly enhanced photovoltaic performances of p–i–n devices were observed. J_{SC}, V_{OC} and FF values were improved with increasing of BP–C_{60} addition from 0 to 3 and 5 wt%, leading to increase in PCE from 1.53 to 2.10 and 2.38%. On the other hand, when BP–C_{60} was added more than 7 wt%, PCE values were slightly decreased to 2.22 and 2.18% compared with the 5 wt% BP–C_{60} added condition. It should be noted that the thickness of i-layer is scarcely changed, suggesting that presence of BP–C_{60} in i-layer is conclusive for the observed change in the device performance. The p–i–n devices including larger amounts of BP–C_{60} (15–40 wt%) in i-layer were also fabricated and their photovoltaic performances were investigated (Table S4-1, Support Information). With larger amounts of additives, significant decrease of PCE was observed. Therefore, 0–10 wt% BP–C_{60} added condition has been focused for the detailed morphological investigation in this study.

To interpret the higher J_{SC} value in the BP–C_{60} composed p–i–n devices, the external quantum efficiency (EQE) spectra were measured and compared with that of p–i–n (0 wt%), as shown in Figure 4 (b). All of devices showed high EQE value in the 340 nm, 400–500 nm and 550–720 nm because of the absorption of $PC_{61}BM$ and BP. Although all of devices has same photoabsorption capability of the active layer (Figure 4 (c)), p–i–n (3–10 wt%) devices show the improved EQE values within a photoabsorption range of the BP:$PC_{61}BM$ blend, in comparison with the p–i–n (0 wt%) device. For example, the champion device, p–i–n (5 wt%), obtained 13%, 25% and 30% higher quantum efficiencies at 340 nm, 455 nm and 615 nm, respectively. This improvement can be attributed to morphological modifications of i-layer such as the increase of p–n interface for carrier generation or enhancement of charge carrier transport ability.

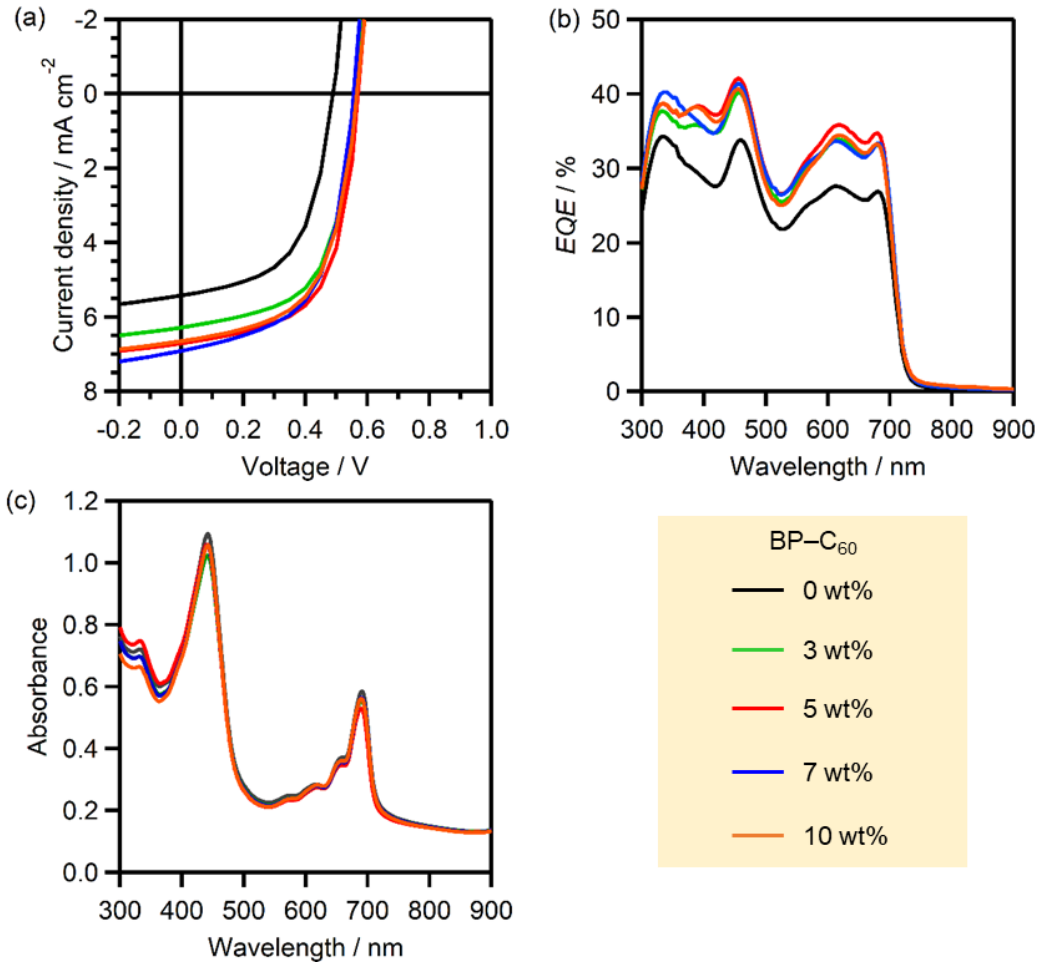

Figure 4. Photovoltaic performances of champion devices: (a) illuminated *J*–*V* characteristics; (b) EQE spectra; (c) absorption spectra of actual p–i–n devices.

Table 1. Device performances of p–i–n device*

BP–C_{60} / wt%	i-layer thickness / nm	PCE / %	J_{SC} / mA cm^{-2}	V_{OC} / V	FF	R_s / Ω cm^2	R_{sh} / Ω cm^2
0	65	1.58 (1.45 ± 0.13)	5.93	0.50	0.53	7	383
3	63	2.10 (2.02 ± 0.06)	6.29	0.56	0.60	10	795
5	67	2.38 (2.30 ± 0.08)	6.76	0.58	0.61	9	795
7	60	2.22 (2.12 ± 0.08)	6.91	0.56	0.58	9	600
10	64	2.18 (2.10 ± 0.06)	6.65	0.57	0.58	9	769

*Champion date of each device are shown with average values estimated from four devices in all.

4-4. Film Morphology

To investigate the microscopic surface morphology of the i-layer, the surface of Structure I was investigated by AFM as shown in Figure 5 (a–e). Several grains on film surface are observed in all of AFM images. These grains can be attributed to BP rich domains. Nguyen et al also reported the same types of grains in the surface of BP/BP:$PC_{61}BM$ film and they characterized the grains as BP rich domains by conductive- and photoconductive-AFM measurements.[50] In case of the Structure I (0 wt%) which has no BP–C_{60} in i-layer, around 1–2 μm sized spot- or needle-like domains and rough surface with root-mean square (RMS) roughness of 48.6 nm were observed. This inhomogeneous distribution of BP and $PC_{61}BM$ components is undesirable for the photovoltaic process and is probably the cause of the observed worst PCE of 1.58% with low FF value of 0.53. On the other hand, the smoother surface was observed in the Structure I with 3–10 wt% BP–C_{60}. RMS values were also decreased to 33.5 nm (3 wt%), 12.0 nm (5 wt%), 20.5 nm (7 wt%) and 6.4 nm (10 wt%). In the p–i–n device based on BP:fullerene derivatives, flat surface of the i-layer plays an important role to construct homogeneous morphology of

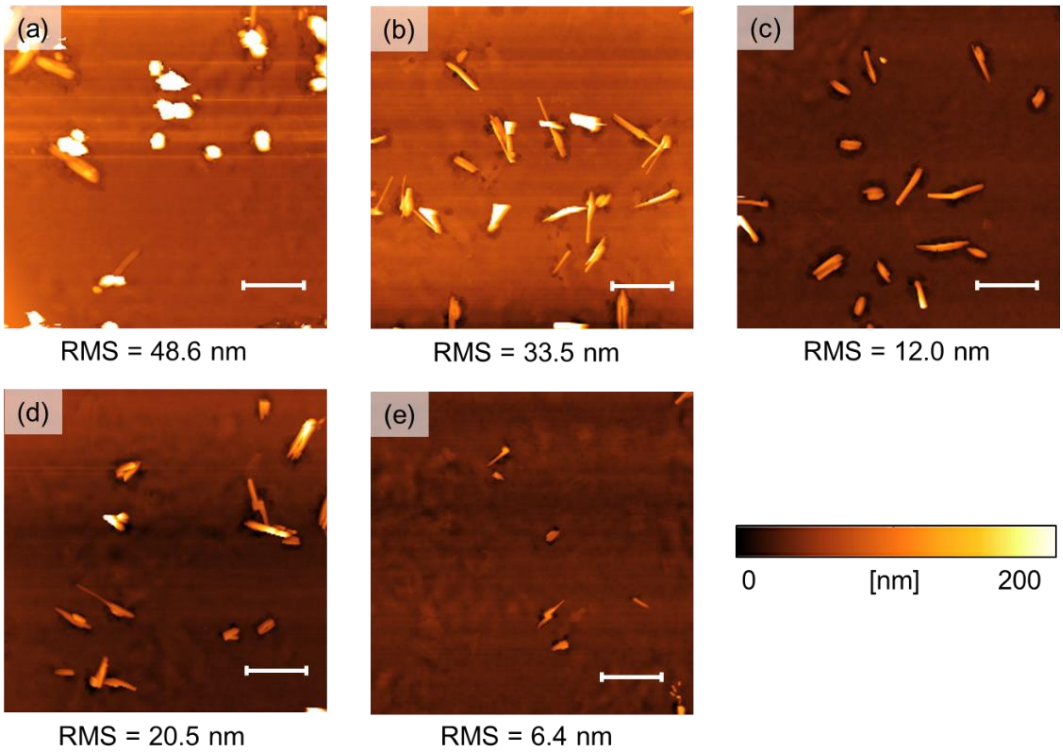

Figure 5. AFM height images of structure I with different amounts of BP–C_{60}: (a) 0 wt%; (b) 3 wt%;(c) 5 wt%; (d) 7 wt%: (e) 10 wt%. The scale bars correspond to 2 μm.

n-layer for higher performance.[50–52] Because, large BP grains in vertical direction often extends through the n-layer and $PC_{61}BM$-uncovered BP can come up on n-layer and reach to the electrode, leading to lower semiconducting properties. In fact, around two times higher shunt resistance values were observed in p–i–n (3–10 wt%) devices with flat n-layer compared with the p–i–n (0 wt%) device (Figure S4-2, Support Information). In general, the better V_{OC} value can be achieved in the device which shows higher shunt resistance values, thus the slight improvement of V_{OC} in the p–i–n (3–10 wt%) device can be attributable to these structural differences of i- and n-layers. Furthermore, needle–like grains which gradually become smaller with increase of BP–C_{60} were observed. The needle–like grains which have length of around 2 μm exist in the cases of 3 and 5 wt% BP–C_{60} added i-layer, whereas grains are around 1 μm or smaller in the cases of 7 and 10 wt% conditions. Considering that typical exciton diffusion lengths in molecular organic materials are within the range of only a few to tens of nanometers,[53] the grains in all films are probably too large for efficient charge separation. But smoother surface and smaller grains observed in the Structure I including BP–C_{60} might be better than the Structure I (0 wt%).

Further investigation of macrostructure in the Structure I was performed by fluorescence microspectroscopy. As shown in Figure 6 (a–e), the intensity of fluorescence radiated from BP was gradually decreased as the BP–C_{60} in the i-layer increase. This data clearly shows that addition of BP–C_{60} has led to more effective quenching of exciton in BP domains, supposedly increasing the beneficial BP:$PC_{61}BM$ interface for the generation of hole–electron pairs. In addition, several bright spots observed in the Structure I (0 wt%) were suppressed in the Structure I including BP–C_{60}. This suggests that more homogeneous BP:$PC_{61}BM$ films are formed by addition of BP–C_{60}, thus observed domains by AFM should contain an increased area of contact between BP and $PC_{61}BM$.

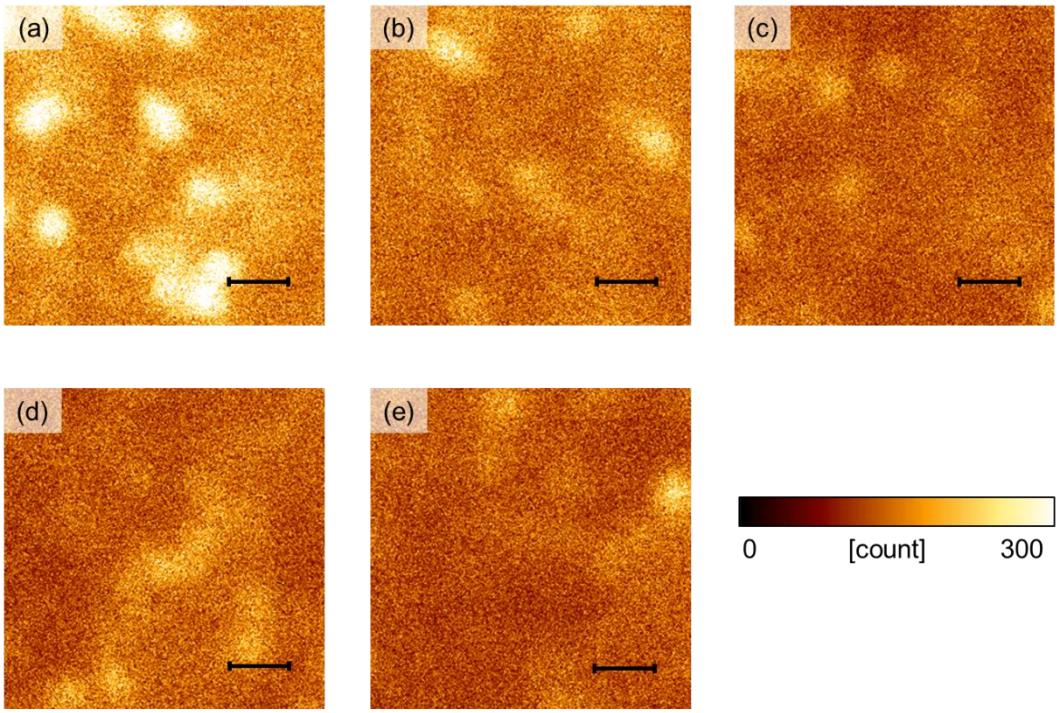

Figure 6. fluorescence microspectroscopy of structure I with different amounts of BP–C_{60}: (a) 0 wt%; (b) 3 wt%;(c) 5 wt%; (d) 7 wt%: (e) 10 wt%. The scale bars correspond to 2 μm. To detect the fluorescence of the BP, a 405 nm laser was used as an excitation source with 56 W cm^{-2} intensity.

4-5. Crystallinity and Molecular Orientation

The crystallinity and molecular orientation of the Structure I was investigated by 2D-GIWAXD and the obtained diffraction patterns are shown in Figure 7 (a–e). Through 2D-GIWAXD, it is definite that BP in the Structure I has a similar single crystal structure of a mono-clinic unite cell with the $P2_1/n$ space group reported by Aramaki et al[54], and the GIWAXD patterns of the BP film has been assigned by Chabinyc et al.[55] The GIWAXD patterns of BP in all of the Structure I (0–10 wt%) are almost same arcuate shape which suggests a random orientation of crystallites on the substrate. Note that arcs of (101) and (200) plane of BP which are most intense on in-plane direction (q_{xy} axis) were observed at q_{xy} = 0.71 and 0.82 $Å^{-1}$. Because of the (101) and (200) planes along the *b*-axis of the unit cell, their appearance on the q_{xy} axis suggests that herring bone columns of BP are standing on the substrate to achieve a hole transport in the device as shown in Figure 8. From this result, it assumes that presence of BP–C_{60} in the i-layer does not involve the orientation change of BP crystal. On the other hand, crystallinity of BP

tends to be decreased with the increasing amounts of BP–C_{60}, because the full width at half maximum values (FWHM) of (101) and (200) peaks estimated from 1D cut and fitting corresponding in-plane direction are increased with BP–C_{60} (Figure 9). Additionally, GIWAXD patterns identified to crystalline $PC_{61}BM$[56] were also found around q = 1.46, 1.39, and 1.37 $Å^{-1}$. Compared with the Structure I (0 and 3 wt%), these GIWAXD patterns of $PC_{61}BM$ were barely visible in the Structure I (5 wt%) and no longer appeared in the Structure I (7 and 10 wt%). These results clearly suggest that BP–C_{60} can interact with both BP and $PC_{61}BM$ to prevent the crystallization in the active layer.

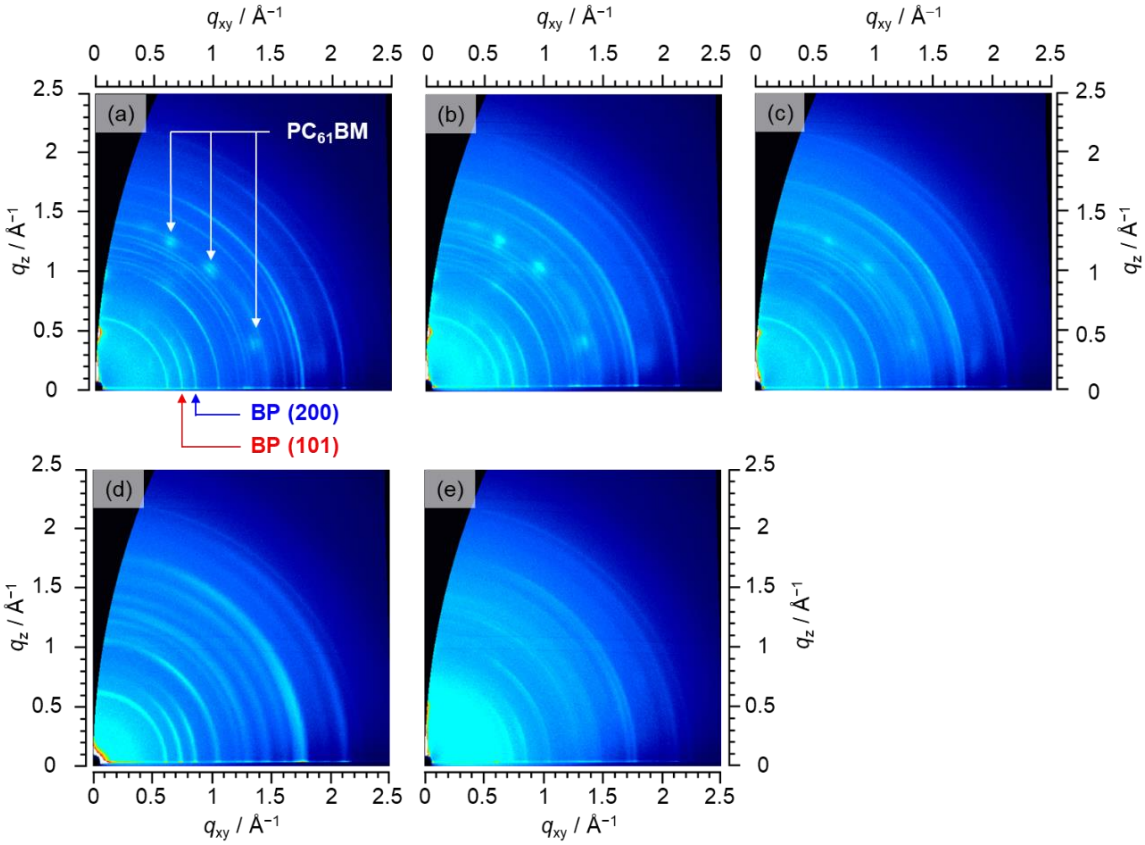

Figure 7. 2D-GIWAXD patterns of Structure I with different amounts of BP–C_{60}: (a) 0 wt%; (b) 3 wt%;(c) 5 wt%; (d) 7 wt%: (e) 10 wt%.

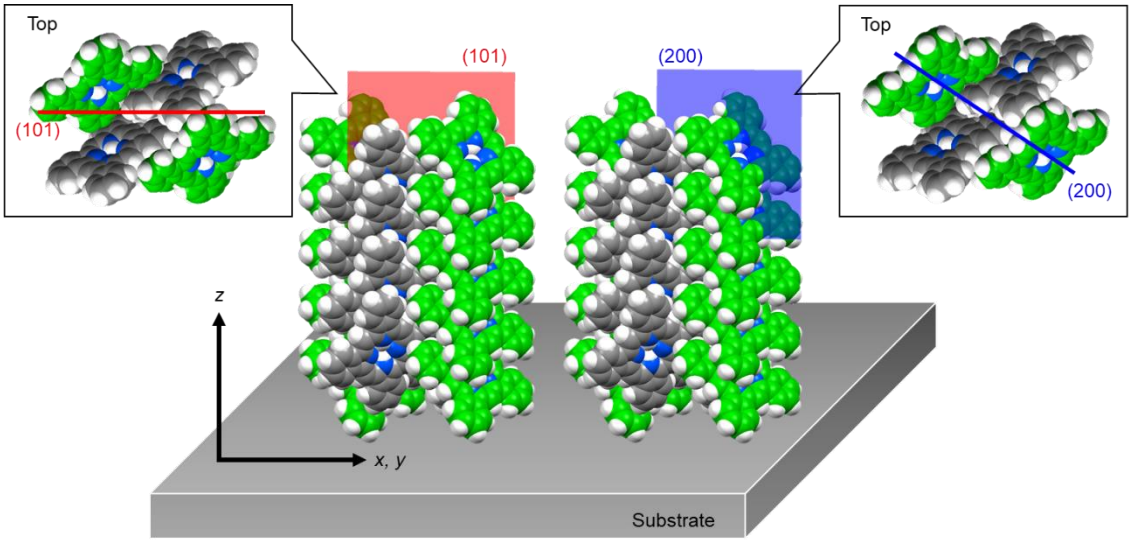

Figure 8. Crystal structure of BP with (101) and (200) plane. The single-crystal data can be obtained from the literature.[54]

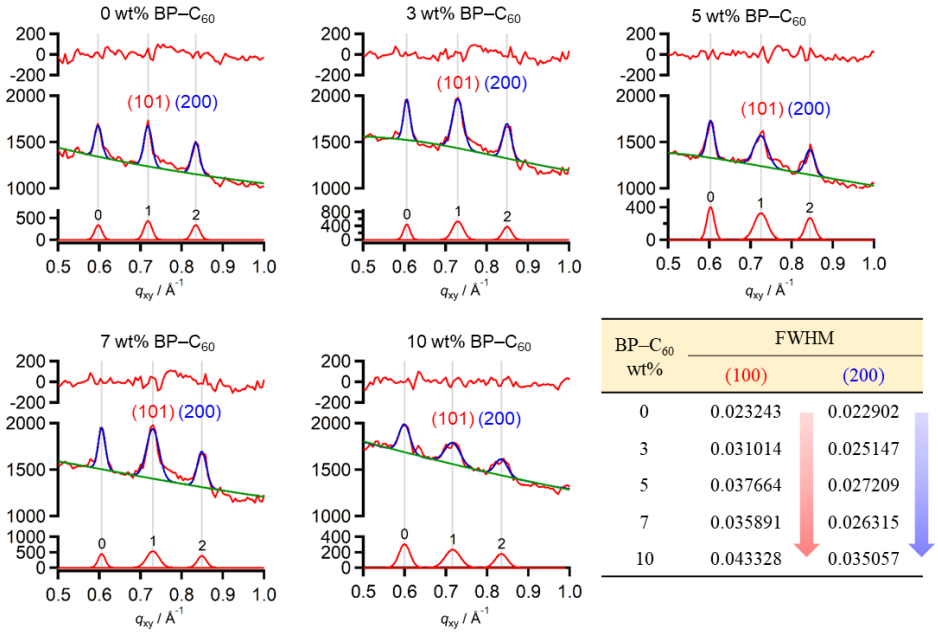

BP–C_{60} wt%	FWHM (100)	FWHM (200)
0	0.023243	0.022902
3	0.031014	0.025147
5	0.037664	0.027209
7	0.035891	0.026315
10	0.043328	0.035057

Figure 9. The fitting patterns of 1D line cuts in the out-of-plane direction of 2D-GIWAXD in the Structure I. Amounts of BP–C_{60} in the Structure I are (a) 0 wt%, (b) 3 wt%, (c) 5 wt%, (d) 7 wt%, and (e) 10 wt%, respectively. (101) and (200) planes of crystalline BP are observed at q_{xy} = 0.71 and 0.82 $Å^{-1}$ in all of films. The Gaussian function is used for these fitting to estimate FWHM values of (101) and (200) planes. Estimated FWHM values were summarized in the table.

4-6. Interfacial Architectures

The interfacial structure of BP between p- and i-layers was observed by SEM. For this investigation, the Structure II was prepared by surface rinsing of Structure I with a drop of $CHCl_3$. It can be achieved upon a selective washing $PC_{61}BM$ away from i-layer while hardly soluble BPs remained. The top-down view of SEM images of the Structure II and BP film are shown in Figure 10. Compared with the BP film, nanoscale textures of

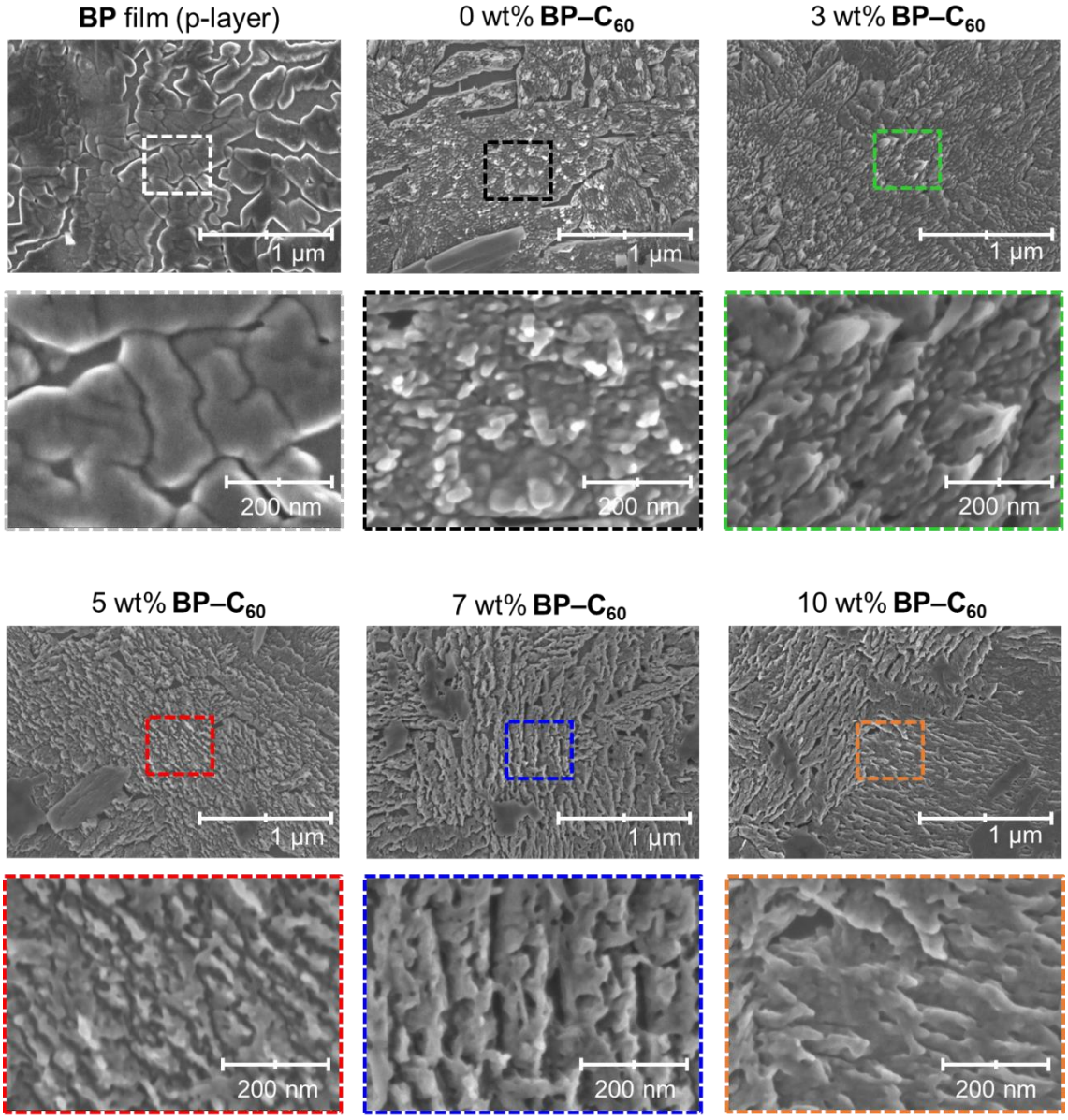

Figure 10. SEM images of the p-layer and Structure II surface with different amounts of BP–C_{60}.

BP were appeared. These textures are probably identified columnar BPs which grew on the p-layer, and they can work for charge separation and carrier transport.[57] In case of the Structure II (0 wt%), closely packed round column-like nanostructures of BP which have a diameter of around 20–60 nm. On the other hand, when BP–C_{60} was added in the i-layer, these textures are significantly changed. The Structure II (3 wt%) shows still column-like nanostructure but its top edge is slightly sharper than the Structure II (0 wt%). The finest textures are observed in the Structure II (5 wt%) with a gappy structure which have a random shape and diameter around10–40 nm. Since this is comparable to the exciton diffusion length of common organic semiconducting materials, Structure II (5 wt%) is more suitable for charge separation and carrier transport than Structure II (0 wt%). The Structure II (7 wt%) also shows a gappy structure, but BP textures are more aggregated than those of the Structure II (5 wt%). Finally, BP textures with an amorphous shape were observed in the Structure II (10 wt%). In order to investigate the height values of these texture, cross-sectional observation by scanning transmission electron microscope (STEM) was performed. The observed height values of textures caused by use of various amounts of BP–C_{60} are 27 nm (0 wt%), 26 nm (3 wt%), 28 nm (5 wt%), 24 nm (7 wt%) and 21 nm (10 wt%), respectively (Figure 11 a–f). In case of Structure II added BP–C_{60} of 5 wt% or less, same height values of the textures were observed, namely, increase of effective p–n interface for charge carrier generations would be achieved without loss of hole transport path in their p–i interfaces. On the other hand, Structure II added BP–C_{60} of over 7 wt% showed reduced height values of the textures result in the loss of hole transport path in their p–i-interfaces. Thus, the obtained device performances were probably related to the observed nanoscale textures. From these results, p–i–n (5 wt%) device which achieved the best performance with the improved J_{SC} (6.81 mA cm^{-2}) and the highest FF value (0.61) is assumed to have the best balance of p–n interface and charge transport pass in the i-layer. In contrast, decrease of FF value (0.58) in p–i–n (7 wt%) and (10 wt%) device can be explained by the loss of carrier pass by too much amount of BP–C_{60}.

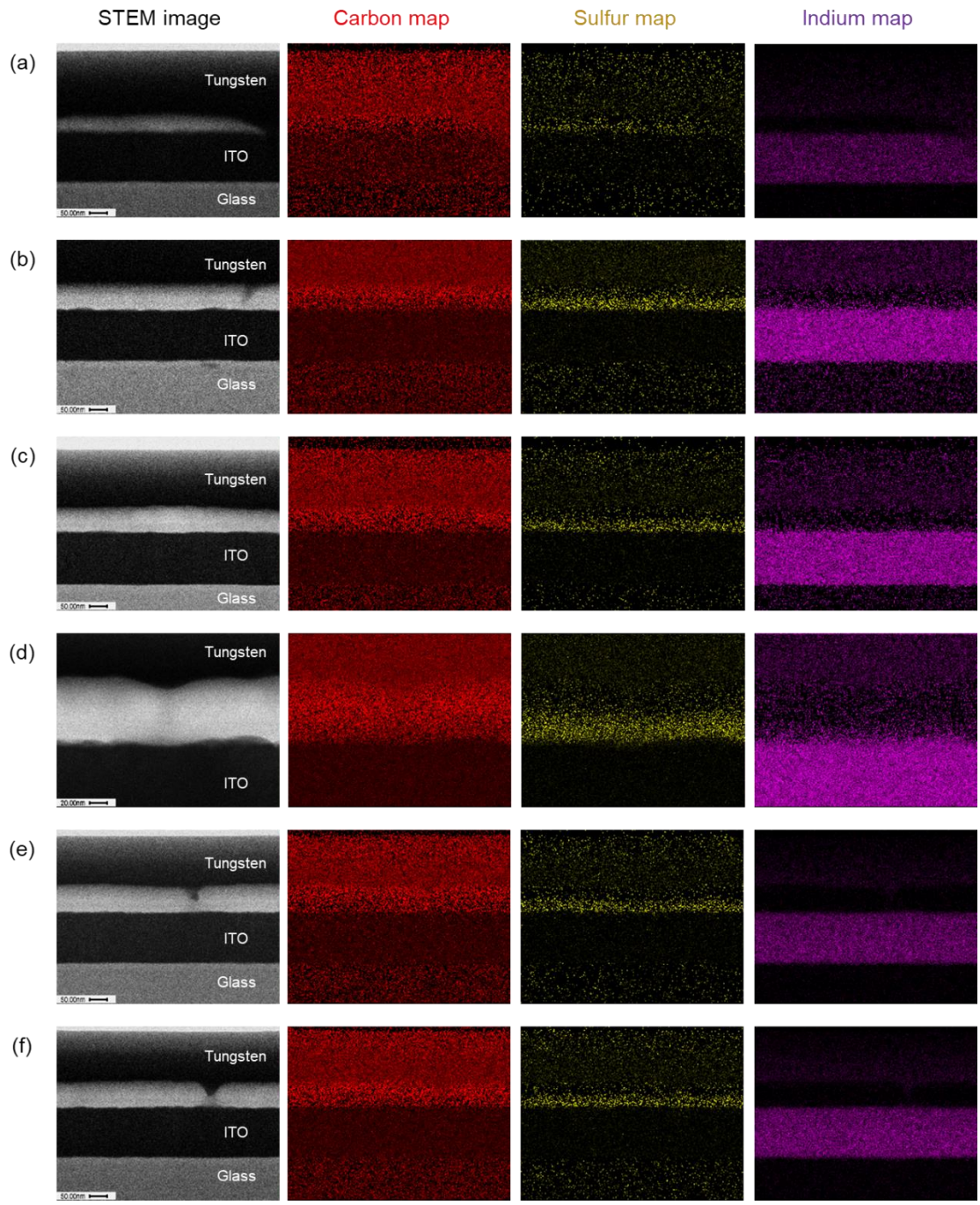

Figure 11. Cross-sectional STEM images of (a) BP film and (b–f) the Structure II with the elemental mapping. The Structure II was prepared from the Structure I which had been composed different amounts of BP–C_{60}: (b) 0 wt%; (c) 3 wt%; (d) 5 wt%; (e) 7 wt%; (f) 10 wt%. All of films were deposited tungsten layer on the top for preparations of the cross sectional samples suitable for STEM analysis using the micro sampling technique.[58]

4-7. Summary

This work has demonstrated the modification of internal layer structure of solution-processable p–i–n device based on BP:$PC_{61}BM$ by addition of small amount of BP–C_{60} to improve device performances. The p–i–n device including BP–C_{60} as the compatibilizer of i-layer showed the improved performance (PCE = 2.38%) compared with the device without BP–C_{60} (PCE = 1.58%). The value was even higher than the record performance of BP:$PC_{61}BM$ based p–i–n device (PCE = 2.00%) reported by Matsuo et al.[57] The presence of BP–C_{60} in the i-layer affected the vertical morphology, phase separation, and crystallinity. The AFM and fluorescence microspectroscopy measurement suggested that domain size became small to lead formation of larger p–n interface for charge-carrier generation and the smoother i- and n-layers for better semiconducting behavior by introducing BP–C_{60} into i-layer. In addition, SEM image suggested the interfacial BP network also can be modified by the presence of BP–C_{60} to be fine. However, more than 10 wt% of BP–C_{60} might work as the component which break the balance of p–n interface and carrier pass in the active layer. During these morphological changes by BP–C_{60} addition, crystalline orientation does not change but the crystallinity of both BP and $PC_{61}BM$ is gradually decline. The addition amount is an important key to work the BP–C_{60} as an efficient compatibilizer in this system.

4-8. Outlook

The capability of BP–C_{60} to control the morphology of the solution processed small molecules in a thin film shows a potential for becoming beneficial method to construct of suitable hetero-junctions for p–i–n-type OSCs. To further improve the performance, insulated alkyl linker is probably disturbing the potential of BP–C_{60} as compatibilizer. In this regard, rigid linked BP–C_{60} which showed better carrier mobilities as reported in Chapter 3 might be favorable for this morphological strategy. Note, however, that the distance of linker moiety between BP and C_{60} should be investigated carefully because compatibilizers can be preferential located at the interface between the hetero-phases of two-types material.[43,46,59]

As mentioned in the introduction part of this chapter, small molecular compatibilizers have not taken up the majority as OSC material. Nevertheless, their developments are promising to be new strong method to optimize a film morphology because of the minimized insulating component and variability from batch to batch compare with copolymer compatibilaizers.

To find the truly-important factors for high efficient small molecular compatibilizer, the author's BP–C_{60} system which can freely change the linkage structure will be powerful tool.

4-9. Support Information

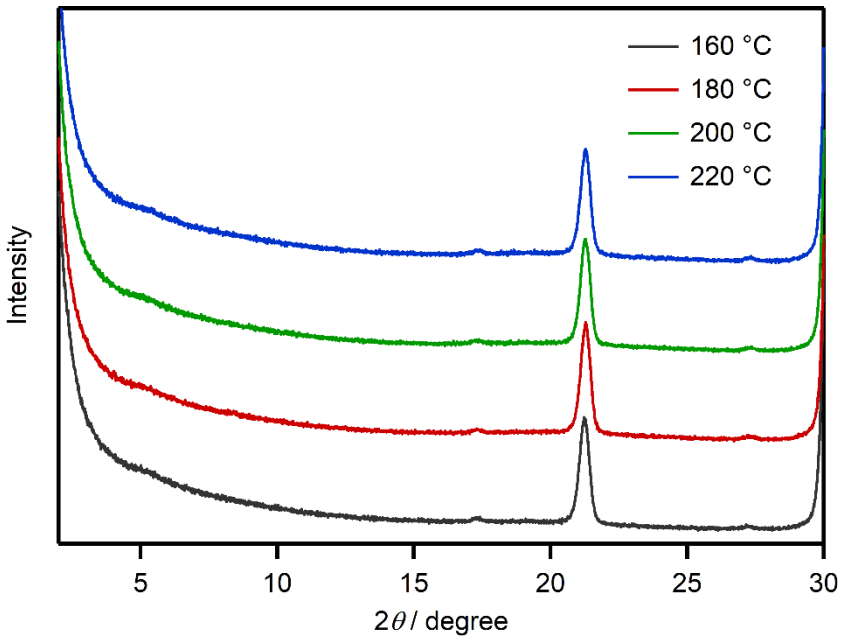

Figure S4-1. Out-of-plane XRD patterns of **BP–C60** prepared by heating of **CP–C60** films for 20 min on the ITO/glass substrate in nitrogen-filled glove box. The characteristic peaks around 21 º and 30 º are identified the ITO of substrate.

Table S4-1. Additional photovoltaic performance of p–i–n (15–40 wt%) devices.

BP–C_{60} / wt%	PCE / %	J_{SC} / mA cm^{-2}	V_{OC} / V	FF	R_s / Ω cm^{-2}	R_{sh} / Ω cm^{-2}
15	1.84 (1.82 ± 0.06)	6.03	0.55	0.55	9	628
20	1.79 (1.70 ± 0.07)	5.89	0.55	0.53	11	523
30	1.72 (1.60 ± 0.07)	5.51	0.54	0.57	10	656
40	1.72 1.53 ± 0.14	5.07	0.58	0.59	12	517

*Champion date of each device are shown with average values estimated from four devices in all.

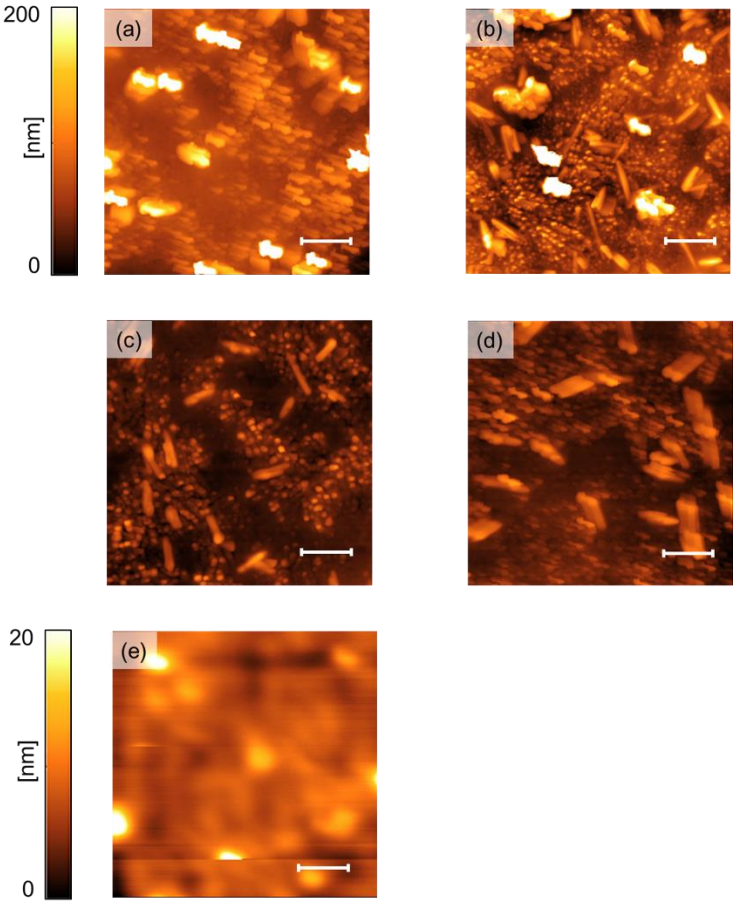

Figure S4-2. AFM height images of the surface of n-layer ($PC_{61}BM$) on the Layer I which composed different amounts of BP–C_{60}: (a) 0 wt%; (b) 3 wt%; (c) 5 wt%; (d) 7 wt%; (e) 10 wt%. RMS values of these films are (a) 44.7 nm, (b) 33.5 nm, (c) 19.0 nm, (d) 16.5 nm, and (e) 2.33 nm, respectively. The image (e) is attached different height scale bar because of the very smooth surface. The scale bars correspond to 2 μm.

4-10. Experimental Section

Materials

Semico cleane 53, a detergent of the ITO/glass substrate, was purchased from Furuuchi Chemical. [6,6]-Phenyl-C_{61}-butyric acid methyl ester ($PC_{61}BM \geq 99.5\%$ by HPLC with respect to fullerene content) was purchased from SES Research, and was used without further purification. Spectral grade chloroform ($CHCl_3$) for sample deposition solvent was purchased from Nacalai tesque Inc. (3,4-ethylenedioxythiophene):poly(4-styrenesulfonate) (PEDOT:PSS, Clevios P VP AI4083) was purchased from Heraeus Deutschland GmbH & Co. and was used after filtration using MILLEX-HP Filter unit (0.45 μm, PES Membrane) purchased from Merck Millipore Ltd..

CP[60] and CP–C_{60}[51] were prepared according to described literatures.

Device Fabrication

Indium-tin-oxide (ITO)-patterned glass substrates (20.0 × 25.0 mm, < 15 Ω per square) were washed with running water and were ultrasonically cleaned in detergent, pure-water and isopropanol for 10 min each. After drying the substrates, ozone-treatment was performed for 30 min by UV-O_3 cleaner TC-003 (MEIWAFOSIS CO., Ltd.) as a further cleaning. (3,4-ethylenedioxythiophene):poly(4-styrenesulfonate) (PEDOT:PSS, Clevios P VP AI4083) was spin coated (3000 rpm, 30 s) to the treated substrate followed by a thermal annealing treatment at 130 ºC for 10 min in air. The thickness of the resulting PEDOT:PSS layer was about 30 nm. The substrates were transferred to a N_2-filled glove box (< 10.0 ppm O_2 and H_2O) to fabricate p–i–n devices as follows.

The p-layer was prepared by spin coating a chloroform solution (7 mg mL^{-1}, 1500 rpm, 30 sec) of CP followed by heating (200 ºC, 10 min) to effect the in-situ conversion of CP to BP. The i-layers were deposited by spin coating (1500 rpm, 30 sec) a chloroform solution of CP:$PC_{61}BM$ (1:1.5 wt/wt) containing 0–10 wt% of CP–C_{60} (10 mg mL^{-1}) followed by heating (180 ºC, 20 min) to effect the insitu conversion to BP:$PC_{61}BM$ containing BP–C_{60}. The n-layer was prepared by spin coating a chloroform solution of $PC_{61}BM$ (7 mg mL^{-1}, 1500 rpm, 30 sec), which was then annealed (195 ºC, 10 min). After preparation of the organic layers, the buffer layer (Ca, 5 nm) and counter electrode (Al, 50 nm) were vapor deposited at a high vacuum (< 5.0×10^{-1} Pa) through a

shadow mask with a defined active area of 4 mm^2. Finally, the fabricated organic photovoltaic cell was encapsulated with backing glasses using a UV-curable resin under nitrogen atmosphere. OPV performances. Current–voltage (*J–V*) curves were measured using a Keithley 2611B SYSTEM Source Mater unit under AM1.5G illumination at an intensity of 100 mW cm^{-2} using a solar simulator (Bunko-keiki, CEP-2000RP). The external quantum efficiency (EQE) spectra were obtained under illumination of monochromatic light using the same system.

Film Thickness

Active layer thickness was measured by a Surface Profiler ET200 (Kosaka Laboratory Ltd.). The value was obtained as an average of 10 measurement points. The thin-film samples for these measurements were prepared on PEDOT:PSS-coated ITO/glass substrates in the same manner as in the device fabrication described above.

Atomic Force Microscope (AFM) Measurement

The surface morphology of organic films was observed by a SPA400, SPI3800N AFM (Seiko instruments Inc.) in tapping mode using silicon probes with a resonant frequency of ~138 kHz and a force constant of 16 N m^{-1}. The thin-film samples for these measurements were prepared on PEDOT:PSS-coated ITO/glass substrates in the same manner as in the device fabrication described above.

Scanning Electron Microscope (SEM) Measurement

The surface texture of organic films was observed by an Ultra High-Resolution Scanning Electron Microscope SU9000 (Hitachi, Ltd.) with accelerating voltage of 1.0 kV. The sample film surface was not deposited with conductive materials for prevention of static charge. The thin-film samples for these measurements were prepared on PEDOT:PSS-coated ITO/glass substrates in the same manner as in the device fabrication described above.

Scanning Transmission Electron Microscope (STEM) Measurement

The cross-section of the Structure I was observed by a HD-2700 (Hitachi, Ltd.) which combines an energy dispersive X-ray (EDX) spectroscopy Octane T Ultra W 100mm2SDD (AMETEK). For this measurement, Focused Ion Beam System FB2200 (Hitachi, Ltd.) has been used for site-specific preparation of cross sectional samples suitable for STEM analysis using the micro sampling technique.[58] The thin-film samples for these measurements were prepared on PEDOT:PSSITO-coated ITO/glass substrates in the same manner as in the device fabrication described above.

Fluorescence Microspectroscopy

The fluorescence from the Structure I was collected by an objective lens (60 ×, N.A.:0.7, LUCPlanFLN, Olympus) and passed through a confocal pinhole (100 μm) and suitable filters. To detect the fluorescence of the BP, a 405 nm laser was used as an excitation source, and a long-pass filter (LP02-442RU, Semrock) and a short-pass filter (FF01-650/SP, Semrock) were used to cut the excitation laser beam and fluorescence from $PC_{61}BM$, respectively. The detected fluorescence was split into two paths by a 50/50 beam splitter, and the two paths were detected using a spectrometer (SpectraPro2358, Acton Research Corporation) with a cooled CCD camera (PIXIS400B, Princeton Instruments) and an avalanche single-photon counting module (APD: SPCM-AQR-14, PerkinElmer). The signal from the APD was connected to a time-correlated single-photon counting board (SPC-630, Becker & Hickl) for the fluorescence images. The thin-film samples for these measurements were prepared on PEDOT:PSS-coated ITO/glass substrates in the same manner as in the device fabrication described above.

Two-Dimensional Grazing-Incident Wide-Angle X-Ray Diffraction (2D-GIWAXD)

2D-GIWAXD measurements were performed in a HUBER multiaxis diffractometer in-stalled in beamline BL-19B2 at SPring-8 (Hyogo, Japan). The X-ray beam was monochromatized by a double-crystal Si (111) monochromator, and the X-ray energy was 12.398 keV. Scattered X-rays from samples were detected by an X-ray pho-ton counting pixel detector (PILATUS 300 K). The X-ray-beam incidence angle was set

to 0.12°, and the sample-to-detector distance was 174 mm. The thin-film samples for the GIWAXD measurements were prepared on PEDOT:PSS-coated ITO/glass substrates in the same manner as in the device fabrication described above. All of sample substrates were kept a certain size (10 mm × 10 mm) to receive a similar effect of the footprint.

4-11. References

(1) He, Z.; Xiao, B.; Liu, F.; Wu, H.; Yang, Y.; Xiao, S.; Wang, C.; Russell, T. P.; Cao, Y. Single-junction polymer solar cells with high efficiency and photovoltage. *Nat. Photonics* **2015**, *9*, 174–179.

(2) Huang, J.; Carpenter, J. H.; Li, C. Z.; Yu, J. S.; Ade, H.; Jen, A. K. Y. Highly Efficient Organic Solar Cells with Improved Vertical Donor-Acceptor Compositional Gradient Via an Inverted Off-Center Spinning Method. *Adv. Mater.* **2016**, *28*, 967–974.

(3) Huang, J.; Wang, H.; Yan, K.; Zhang, X.; Chen, H.; Li, C. Z.; Yu, J. Highly Efficient Organic Solar Cells Consisting of Double Bulk Heterojunction Layers. *Adv. Mater.* **2017**, *29*, 1–9.

(4) Huang, J.; Zhang, X.; Zheng, D.; Yan, K.; Li, C.-Z.; Yu, J. Boosting Organic Photovoltaic Performance Over 11% Efficiency With Photoconductive Fullerene Interfacial Modifier. *Sol. RRL* **2017**, *1*, 1600008.

(5) Kumari, T.; Lee, S. M.; Kang, S.-H.; Chen, S.; Yang, C. Ternary solar cells with a mixed face-on and edge-on orientation enable an unprecedented efficiency of 12.1%. *Energy Environ. Sci.* **2017**, *10*, 258–265.

(6) Li, S.; Ye, L.; Zhao, W.; Zhang, S.; Mukherjee, S.; Ade, H.; Hou, J. Energy-Level Modulation of Small-Molecule Electron Acceptors to Achieve over 12% Efficiency in Polymer Solar Cells. *Adv. Mater.* **2016**, *28*, 9423–9429.

(7) Liu, Y.; Zhao, J.; Li, Z.; Mu, C.; Ma, W.; Hu, H.; Jiang, K.; Lin, H.; Ade, H.; Yan, H. Aggregation and morphology control enables multiple cases of high-efficiency polymer solar cells. *Nat. Commun.* **2014**, *5*, 1–8.

(8) Zhao, F.; Dai, S.; Wu, Y.; Zhang, Q.; Wang, J.; Jiang, L.; Ling, Q.; Wei, Z.; Ma, W.; You, W.; Wang, C.; Zhan, X. Single-Junction Binary-Blend Nonfullerene Polymer Solar Cells with 12.1% Efficiency. *Adv. Mater.* **2017**, *29*, 1700144.

(9) Benten, H.; Mori, D.; Ohkita, H.; Ito, S. Recent research progress of polymer donor/polymer acceptor blend solar cells. *J. Mater. Chem. A* **2016**, *4*, 5340–5365.

(10) Li, S.; Liu, W.; Li, C.-Z.; Shi, M.; Chen, H. Efficient Organic Solar Cells with Non-Fullerene Acceptors. *Small* **2017**, 1701120.

(11) Lin, Y.; Zhan, X. Non-fullerene acceptors for organic photovoltaics: An emerging horizon. *Materials Horizons* **2014**, *1*, 470.

(12) Lin, Y.; Zhan, X. Designing Efficient Non-Fullerene Acceptors by Tailoring Extended Fused-Rings with Electron-Deficient Groups. *Adv. Energy Mater.* **2015**, *5*, 1501063.

(13) Etxebarria, I.; Ajuria, J.; Pacios, R. Solution-processable polymeric solar cells: A review on materials, strategies and cell architectures to overcome 10%. *Organic Electronics* **2015**, *19*, 34–60.

(14) He, Z.; Zhong, C.; Su, S.; Xu, M.; Wu, H.; Cao, Y. Enhanced power-conversion efficiency in polymer solar cells using an inverted device structure. *Nat. Photonics* **2012**, *6*, 591–595.

(15) You, J.; Dou, L.; Yoshimura, K.; Kato, T.; Ohya, K.; Moriarty, T.; Emery, K.; Chen, C. C.; Gao, J.; Li, G.; Yang, Y. A polymer tandem solar cell with 10.6% power conversion efficiency. *Nat. Commun.* **2013**, *4*, 1410–1446.

(16) Ruderer, M. A.; Guo, S.; Meier, R.; Chiang, H. Y.; Körstgens, V.; Wiedersich, J.; Perlich, J.;

Roth, S. V.; Müller-Buschbaum, P. Solvent-Induced Morphology in Polymer-Based Systems for Organic Photovoltaics. *Adv. Funct. Mater.* **2011**, *21*, 3382–3391.

(17) Liao, H. C.; Ho, C. C.; Chang, C. Y.; Jao, M. H.; Darling, S. B.; Su, W. F. Additives for morphology control in high-efficiency organic solar cells. *Materials Today* **2013**, *16*, 326–336.

(18) Peet, J.; Kim, J. Y.; Coates, N. E.; Ma, W. L.; Moses, D.; Heeger, A. J.; Bazan, G. C. Efficiency Enhancement in Low-Bandgap Polymer Solar Cells by Processing with Alkane Dithiols. *Nat. Mater.* **2007**, *6*, 497–500.

(19) Suzuki, M.; Yamaguchi, Y.; Takahashi, K.; Takahira, K.; Koganezawa, T.; Masuo, S.; Nakayama, K. I.; Yamada, H. Photoprecursor Approach Enables Preparation of Well-Performing Bulk-Heterojunction Layers Comprising a Highly Aggregating Molecular Semiconductor. *ACS Appl. Mater. Interfaces* **2016**, *8*, 8644–8651.

(20) Zhao, G. J.; He, Y. J.; Li, Y. 6.5% Efficiency of Polymer Solar Cells Based on poly(3-Hexylthiophene) and Indene-C_{60} Bisadduct by Device Optimization. *Adv. Mater.* **2010**, *22*, 4355–4358.

(21) Yang, X.; Uddin, A. Effect of thermal annealing on P3HT:PCBM bulk-heterojunction organic solar cells: A critical review. *Renewable and Sustainable Energy Reviews* **2014**, *30*, 324–336.

(22) Kwon, O. K.; Uddin, M. A.; Park, J. H.; Park, S. K.; Nguyen, T. L.; Woo, H. Y.; Park, S. Y. A High Efficiency Nonfullerene Organic Solar Cell with Optimized Crystalline Organizations. *Adv. Mater.* **2016**, *28*, 910–916.

(23) Zhang, Q.; Kan, B.; Liu, F.; Long, G.; Wan, X.; Chen, X.; Zuo, Y.; Ni, W.; Zhang, H.; Li, M.; Hu, Z.; Huang, F.; Cao, Y.; Liang, Z.; Zhang, M.; Russell, T. P.; Chen, Y. Small-Molecule Solar Cells with Efficiency over 9%. *Nat. Photonics* **2014**, *9*, 35–41.

(24) Wang, J. L.; Liu, K. K.; Yan, J.; Wu, Z.; Liu, F.; Xiao, F.; Chang, Z. F.; Wu, H. Bin; Cao, Y.; Russell, T. P. Series of Multifluorine Substituted Oligomers for Organic Solar Cells with Efficiency over 9% and Fill Factor of 0.77 by Combination Thermal and Solvent Vapor Annealing. *J. Am. Chem. Soc.* **2016**, *138*, 7687–7697.

(25) Wei, G.; Wang, S.; Sun, K.; Thompson, M. E.; Forrest, S. R. Solvent-Annealed Crystalline Squaraine: $PC_{70}BM$ (1:6) Solar Cells. *Adv. Energy Mater.* **2011**, *1*, 184–187.

(26) Wang, K.; Azouz, M.; Babics, M.; Cruciani, F.; Marszalek, T.; Saleem, Q.; Pisula, W.; Beaujuge, P. M. Solvent Annealing Effects in Dithieno[3,2-*b*:2′,3′-*d*]pyrrole-5,6-Difluorobenzo[*c*][1,2,5]thiadiazole Small Molecule Donors for Bulk-Heterojunction Solar Cells. *Chem. Mater.* **2016**, *28*, 5415–5425.

(27) Wang, J.-L.; Xiao, F.; Yan, J.; Wu, Z.; Liu, K.-K.; Chang, Z.-F.; Zhang, R.-B.; Chen, H.; Wu, H.-B.; Cao, Y. Difluorobenzothiadiazole-Based Small-Molecule Organic Solar Cells with 8.7% Efficiency by Tuning of π-Conjugated Spacers and Solvent Vapor Annealing. *Adv. Funct. Mater.* **2016**, *26*, 1803–1812.

(28) Wang, J. L.; Wu, Z.; Miao, J. S.; Liu, K. K.; Chang, Z. F.; Zhang, R. B.; Wu, H. Bin; Cao, Y. Solution-Processed Diketopyrrolopyrrole-Containing Small-Molecule Organic Solar Cells with 7.0% Efficiency: In-Depth Investigation on the Effects of Structure Modification and Solvent Vapor Annealing. *Chem. Mater.* **2015**, *27*, 4338–4348.

(29) Miller, S.; Fanchini, G.; Lin, Y.-Y.; Li, C.; Chen, C.-W.; Su, W.-F.; Chhowalla, M. Investigation of nanoscale morphological changes in organic photovoltaics during solvent vapor annealing. *J. Mater. Chem.* **2008**, *18*, 306–312.

(30) Miao, J.; Chen, H.; Liu, F.; Zhao, B.; Hu, L.; He, Z.; Wu, H. Efficiency Enhancement in Solution-Processed Organic Small Molecule : Fullerene Solar Cells via Solvent Vapor Annealing. Appl. Phys. Lett. **2015**, *106*, 183302.

(31) Grob, S.; Bartynski, A. N.; Opitz, A.; Gruber, M.; Grassl, F.; Meister, E.; Linderl, T.; Hörmann, U.; Lorch, C.; Moons, E.; Schreiber, F.; Thompson, M. E.; Brütting, W. Solvent vapor annealing on perylene-based organic solar cells. *J. Mater. Chem. A* **2015**, *3*, 15700–15709.

(32) Gao, K.; Deng, W.; Xiao, L.; Hu, Q.; Kan, Y.; Chen, X.; Wang, C.; Huang, F.; Peng, J.; Wu, H.; Peng, X.; Cao, Y.; Russell, T. P.; Liu, F. New insight of molecular interaction, crystallization and phase separation in higher performance small molecular solar cells via solvent vapor annealing. *Nano Energy* **2016**, *30*, 639–648.

(33) Lee, J. U.; Jung, J. W.; Jo, J. W.; Jo, W. H. Degradation and stability of polymer-based solar cells. *J. Mater. Chem.* **2012**, *22*, 24265.

(34) Cardinaletti, I.; Kesters, J.; Bertho, S.; Conings, B.; Piersimoni, F.; D'Haen, J.; Lutsen, L.; Nesladek, M.; Van Mele, B.; Van Assche, G.; Vandewal, K.; Salleo, A.; Vanderzande, D.; Maes, W.; Manca, J. V. Toward bulk heterojunction polymer solar cells with thermally stable active layer morphology. *J. Photonics Energy* **2014**, *4*, 40997.

(35) Chang, L.; Jacobs, I. E.; Augustine, M. P.; Moulé, A. J. Correlating dilute solvent interactions to morphology and OPV device performance. *Organic Electronics* **2013**, *14*, 2431–2443.

(36) Treat, N. D.; Brady, M. A.; Smith, G.; Toney, M. F.; Kramer, E. J.; Hawker, C. J.; Chabinyc, M. L. Interdiffusion of PCBM and P3HT Reveals Miscibility in a Photovoltaically Active Blend. *Adv. Energy Mater.* **2011**, *1*, 82–89.

(37) Ciammaruchi, L.; Brunetti, F.; Visoly-Fisher, I. Solvent Effects on the Morphology and stability of PTB7:PCBM based solar cells. *Solar Energy* **2016**, *137*, 490–499.

(38) Kim, W.; Kim, J. K.; Kim, E.; Ahn, T. K.; Wang, D. H.; Park, J. H. Conflicted effects of a solvent additive on PTB7:$PC_{71}BM$ bulk heterojunction solar cells. *J. Phys. Chem. C* **2015**, *119*, 5954–5961.

(39) Tremolet De Villers, B. J.; O'Hara, K. A.; Ostrowski, D. P.; Biddle, P. H.; Shaheen, S. E.; Chabinyc, M. L.; Olson, D. C.; Kopidakis, N. Removal of Residual Diiodooctane Improves Photostability of High-Performance Organic Solar Cell Polymers. *Chem. Mater.* **2016**, *28*, 876–884.

(40) Zhao, X.; Zhao, J.; Wu, R.; Liu, D.; Wang, G.; Li, P.; Chen, L.; Zhu, L.; Ding, B.; Song, Q. Impact of additive residue on the photodegradation of high performance polymer solar cells. *Organic Electronics* **2017**, *49*, 226–233.

(41) Waters, H.; Bristow, N.; Moudam, O.; Chang, S. W.; Su, C. J.; Wu, W. R.; Jeng, U. S.; Horie, M.; Kettle, J. Effect of processing additive 1,8-octanedithiol on the lifetime of PCPDTBT based organic photovoltaics. *Organic Electronics* **2014**, *15*, 2433–2438.

(42) Sivula, K.; Ball, Z. T.; Watanabe, N.; Fréchet, J. M. J. Amphiphilic Diblock Copolymer Compatibilizers and Their Effect on the Morphology and Performance of Polythiophene:Fullerene Solar Cells. *Adv. Mater.* **2006**, *18*, 206–210.

(43) Lee, J. U.; Jung, J. W.; Emrick, T.; Russell, T. P.; Jo, W. H. Morphology control of a polythiophene-fullerene bulk heterojunction for enhancement of the high-temperature stability of solar cell performance by a new donor-acceptor diblock copolymer. *Nanotechnology* **2010**, *21*, 105201.

(44) Lee, J. U.; Cirpan, A.; Emrick, T.; Russell, T. P.; Jo, W. H. Synthesis and photophysical property of well-defined donor–acceptor diblock copolymer based on regioregular poly(3-hexylthiophene) and fullerene. *J. Mater. Chem.* **2009**, *19*, 1483–1489.

(45) Yang, C.; Lee, J. K.; Heeger, A. J.; Wudl, F. Well-defined donor–acceptor rod–coil diblock copolymers based on P3HT containing C_{60}: The morphology and role as a surfactant in bulk-heterojunction solar cells. *J. Mater. Chem.* **2009**, *19*, 5416.

(46) Lee, J. U.; Jung, J. W.; Emrick, T.; Russell, T. P.; Jo, W. H. Synthesis of C_{60}-end capped P3HT and its application for high performance of P3HT/PCBM bulk heterojunction solar cells. *J. Mater. Chem.* **2010**, *20*, 3287–3294.

(47) Kim, J. B.; Allen, K.; Oh, S. J.; Lee, S.; Toney, M. F.; Kim, Y. S.; Kagan, C. R.; Nuckolls, C.; Loo, Y. L. Small-Molecule Thiophene-C_{60} Dyads as Compatibilizers in Inverted Polymer Solar Cells. *Chem. Mater.* **2010**, *22*, 5762–5773.

(48) Lai, Y. C.; Higashihara, T.; Hsu, J. C.; Ueda, M.; Chen, W. C. Enhancement of power conversion efficiency and long-term stability of P3HT/PCBM solar cells using C_{60} derivatives with thiophene units as surfactants. *Solar Energy Materials and Solar Cells* **2012**, *97*, 164–170.

(49) Chen, L.; Yao, K.; Chen, Y. Can morphology tailoring based on functionalized fullerene nanostructures improve the performance of organic solar cells? *J. Mater. Chem.* **2012**, *22*, 18768–18771.

(50) Guide, M.; Dang, X. D.; Nguyen, T. Q. Nanoscale Characterization of Tetrabenzoporphyrin and Fullerene-Based Solar Cells by Photoconductive Atomic Force Microscopy. *Adv. Mater.* **2011**, *23*, 2313–2319.

(51) Tamura, Y.; Kuzuhara, D.; Suzuki, M.; Hayashi, H.; Aratani, N.; Yamada, H. Fullerene-linked tetrabenzoporphyrins for solution-processed organic photovoltaics: flexible vs. rigid linkers. *J. Mater. Chem. A* **2016**, *4*, 15333–15342.

(52) Yuto Tamura; Hiroyuki Saeki; Junpei Hashizume; Yukinori Okazaki; Daiki Kuzuhara; Mitsuharu Suzuki; Naoki Aratania; Yamada, H. Direct comparison of a covalently-linked dyad and a 1 :1 mixture of tetrabenzoporphyrin and fullerene as organic photovoltaic materials. *Chem. Commun.* **2014**, *50*, 10379–10381.

(53) Mikhnenko, O. V.; Blom, P. W. M.; Nguyen, T.-Q. Exciton Diffusion in Organic Semiconductors. *Energy Environ. Sci.* **2015**, *8*, 1867–1888.

(54) Aramaki, S.; Mizuguchi, J. 29*H*,31*H*-Tetrabenzo[*b*,*g*,*l*,*q*]Porphin. *Acta Cryst.* **2003**, *59*, o1556–o1558.

(55) Liman, C. D.; Choi, S.; Breiby, D. W.; Cochran, J. E.; Toney, M. F.; Kramer, E. J.; Chabinyc, M. L. Two-Dimensional GIWAXS Reveals a Transient Crystal Phase in Solution-Processed Thermally Converted Tetrabenzoporphyrin. *J. Phys. Chem. B* **2013**, *117*, 14557–14567.

(56) Gomez, E. D.; Barteau, K. P.; Wang, H.; Toney, M. F.; Loo, Y.-L. Correlating the scattered intensities of P3HT and PCBM to the current densities of polymer solar cells. *Chem. Commun.* **2011**, *47*, 436–438.

(57) Matsuo, Y.; Sato, Y.; Niinomi, T.; Soga, I.; Tanaka, H.; Nakamura, E. Columnar Structure in Bulk Heterojunction in Solution-Processable Three-Layered p-i-n Organic Photovoltaic Devices Using Tetrabenzoporphyrin Precursor and silylmethyl[60]fullerene. *J. Am. Chem. Soc.* **2009**, *131*, 16048–16050.

(58) Young, R. J.; Moore, M. V. *Dual-Beam (FIB-SEM) Systems Techniques and Automated Applications*; 2005.

(59) Koning, C. Strategies for Compatibilization of Polymer Blends. *Prog. Polym. Sci* **1998**, *23*, 707–757.

(60) Ito, S.; Murashima, T.; Ono, N.; Uno, H. A new synthesis of benzoporphyrins using 4,7-dihydro-4,7-ethano-*2H*-isoindole as a synthon of isoindole. *Chem. Commun.* **1998**, 16, 1661–1662.

Chapter 5.

General Conclusion and Future Prospect

This dissertation focused on advancements of covalently-linked D–A molecular contained BP as the key component toward optimum active-layer structure for OSCs. The effective syntheses of BP derivatives and BP–C_{60} were established. Two strategies toward optimum active layer structure, a construction of hetero-junction layer with BP–C_{60} to control phase separation (Strategy A) and domain size control of blended BP:$PC_{61}BM$ film upon an addition of BP–C_{60} as additive (Strategy B), were examined.

In Chapter 2, effective synthetic procedures which can obtain various asymmetric *meso*-substituted CPs were successfully developed. This synthetic research results not only made the foundation for studies in Chapter 3 and 4, it also contributed in a significant way to the synthesis of various BP derivatives.

In Chapter 3, Strategy A was performed. The first construction of p–i–n OPV devices using covalently-linked D–A molecules as the i-layer material was successful by in-situ thermal conversion from solution-deposited CP–C_{60} materials to hardly soluble BP–C_{60} materials. Covalently-linked BP–C_{60} system is a powerful methodology to improve the miscibility of BP and $PC_{61}BM$ components to lead better PCEs than blended BP:$PC_{61}BM$ system and morphological durability for thermal annealing. The linker and the side chain in the BP–C_{60} system are critically affected the charge transport property. In addition, the flexibility of linkage should be also considered to form effective p–i- or i–n-interfaces for better performance in the p–i–n-type OSC. Although this strategy gave the limited improvement of PCEs, it is no small accomplishment that the BP–C_{60} system prevents too large grain boundary of BP and provide the good homogeneity of both i- and n-layer to improve a vertical phase separation of the p–i–n-type OSC. Therefore, it can be concluded that Strategy A make a contribution enough to obtain a proper morphology and an improved performance. Constructing an ideal phase-separation for an effective bicontinuous structure remains a major challenge in this strategy. From morphological studies, the best active-layer structure has shown that a phase separation with an appropriate length scale for efficient charge generation and charge transport is necessary. Although several BP–C_{60} materials have been explored as active layers in this thesis, none

of them proved to be the perfect choice for providing the best active-layer structure. Therefore, the development of new BP–C_{60} materials and further understanding of their natures are required to reach the ultimate goal of achieving high performance OSCs. The search for better linkages which can induce crystallinity in the BP–C_{60} system and the influence on the length of linker structures should be conducted to improve the OSC performances.

In Chapter 4, Strategy B was examined. The architecture of covalent BP–C_{60} can work as an effective compatibilizer for the BP:$PC_{61}BM$ blend film to modify the morphology. The proper additive quantity boosts the device performance owing to the increase of effective hetero-junction interface for charge generations. The highest performance in BP:$PC_{61}BM$ based p–i–n-type OSCs (PCE = 2.38%) was achieved with this strategy because the added BP–C_{60} successfully arranged BP domains to favorable size for exciton diffusion length without losing a carrier transport path and absorption characteristics of the active layer. Therefore, it can be concluded that Strategy B accomplish a great deal to access the optimal morphology. In continuing to strive for optimum morphology which can deliver the full potential of BP, a lot of challenges remains. One of the most notable limitation of Strategy B is difficulty in homogeneous modification of a film morphology compared with Strategy A. Further understanding the fundamental correlation between the chemical structure of BP–C_{60} system as a compatibilizer and the morphology with multidisciplinary efforts of fabrication process (spin-coating solvent, heat-conversion temperature, film thickness etc.) will pave a pathway to forward.

In the last decade, OSC studies were allowed to access to critical issues (e.g. morphological stabilities and degradation processes) in the actual device because of the creations of inspirable OSC materials or device architectures which can achieve PCEs close to commercialization. Therefore, the author's work, creating a new material system with a novelty concept toward the simultaneous achievement of well-structured and stable morphologies in OSCs, will be also beneficial and may led further insights into proper molecular design, ideal film morphology, and device stability. Lastly, the author hopes that research findings in this dissertation with BP–C_{60} systems will be invaluable contributions toward an improved device performance and stability to acceptable and reliable levels for commercial OSCs in the future.

Research Achievement

First author papers

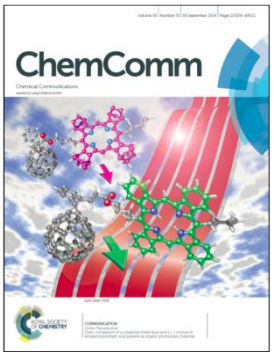

1. Direct comparison of a covalently-linked dyad and a 1:1 mixture of tetrabenzoporphyrin and fullerene as organic photovoltaic materials

   Yuto Tamura, Hiroyuki Saeki, Junpei Hashizume, Yukinori Okazaki, Daiki Kuzuhara, Mitsuharu Suzuki, Naoki Aratani and Hiroko Yamada

   Chemical Communications **2014**, *50*, 10379–10381. (Inside front cover)

2. Fullerene-linked tetrabenzoporphyrins for solution-processed organic photovoltaics: flexible vs. rigid linkers

   Yuto Tamura, Daiki Kuzuhara, Mitsuharu Suzuki, Hironobu Hayashi, Naoki Aratani and Hiroko Yamada

   Journal of Materials Chemistry A **2016**, *4*, 15333–15342. (Inside front cover)

3. Improvement of Interlayer Structure in p–i–n-Type Organic Solar Cells with Fullerene-Linked Tetrabenzoporphyrin Additive

   Yuto Tamura, Mitsuharu Suzuki, Takaki Nakagawa, Tomoyuki Koganezawa, Sadahiro Masuo, Hiroko Yamada

   Manuscript in preparation.

Other publications

1. Facile synthesis of indolizino[3,4,5-*ab*]isoindoles by an acid-induced cyclization of 1,2-di(1*H*-pyrrol-2-yl)benzenes

   Daiki Kuzuhara, Satoshi Miyake, Hirotake Moriyama, Yuto Tamura, Naoki Aratani, Hiroko Yamada

   Tetrahedron Letters, **2015**, *56*, 5564–5567.

2. Charge-Carrier Dynamics in Benzoporphyrin Films Investigated by Time-Resolved THz Spectroscopy

   Kaoru Ohta, Sho Hiraoka, Yuto Tamura, Hiroko Yamada, Keisuke Tominaga

   Applied Physics Letters, **2015**, *107*, 183302.

3. Probing Charge Carrier Dynamics in Porphyrin-Based Organic Semiconductor Thin Films by Time-Resolved THz Spectroscopy
   Kaoru Ohta, Shunrou Tokonami, Kotaro Takahashi, Yuto Tamura, Hiroko Yamada, Keisuke Tominaga
   The Journal of Physical Chemistry B, **2017**, *121*, 10157–10165.

International conferences

1. SYNTHESIS AND APPLICATION OF BENZOPORPHYRIN–FULLERENE LINKED MOLECULE FOR ORGANIC PHOTOVOLTAICS
   Yuto Tamura, Hiroyuki Saeki, Daiki Kuzuhara, Hiroko Yamada
   IUPAC Symposium on Photochemistry, Bordeaux, France, July 2014
2. Direct comparison of a covalently-linked dyad and a 1:1 mixture of tetrabenzoporphyrin and fullerene as organic photovoltaic materials
   Yuto Tamura, Hiroyuki Saeki, Daiki Kuzuhara, Hiroko Yamada
   KJF International Conference on Organic Materials for Electronics and Photonics, Tsukuba, Japan, September 2014
3. Fullerene Linked Benzoporphyrins for Solution-Processed Organic Photovoltaic Material
   Yuto Tamura, Daiki Kuzuhara, Mitsuharu Suzuki, Hiroko Yamada
   International Conference on Porphyrins and Phthalocyanines, Nanjing, China July 2016
4. Enhancement of photovoltaic performance of p-i-n type organic solar cells with fullerene-linked benzoporphyrin
   Yuto Tamura, Mitsuharu Suzuki, Hiroko Yamada
   9th International Conference on Materials for Advanced Technologies, Singapore, June 2017
5. Modification of Internal Layer Structure in p–i–n-Type Organic Solar Cells with Fullerene-Linked Tetrabenzoporphyrin
   Yuto Tamura, Mitsuharu Suzuki, Hiroko Yamada
   9th International Conference on Molecular Electronics and Bioelectronics, Ishikawa, Japan, June 2017

Domestic conferences

1. ポルフィリンーフラーレン連結分子の合成と物性
   田村悠人, 佐伯宏之, 葛原大軌, 鈴木充朗, 荒谷直樹, 山田容子
   第 7 回有機 π 電子系シンポジウム, 高崎ビューホテル (群馬県), 2013 年 12 月

2. ベンゾポルフィリン–フラーレン連結分子の合成と有機薄膜太陽電池への応用
   田村 悠人, 佐伯 宏之, 葛原 大軌, 山田 容子
   日本化学会第 94 春季年会, 名古屋大学 東山キャンパス, 2014 年 3 月
3. ベンゾポルフィリン–フラーレン連結分子の合成と有機薄膜太陽電池への応用
   田村 悠人, 佐伯 宏之, 葛原 大軌, 山田 容子
   第 75 回応用物理学会秋季学術講演会, 北海道大学 札幌キャンパス, 2014 年 9 月
4. ベンゾポルフィリン–フラーレントライアド分子の合成と有機薄膜太陽電池特性への応用
   第 76 回応用物理学会秋季学術講演会, 名古屋国際会議場, 2015 年 9 月
5. フラーレン連結ベンゾポルフィリンによる p–i–n 型有機薄膜太陽電池の性能改善
   田村 悠人, 鈴木 充朗, 山田 容子
   第 64 回応用物理学会春季学術講演会, パシフィコ横浜 (神奈川県), 2017 年 3 月

Award

1. 平成 28 年度奈良先端科学技術大学院大学優秀学生発表賞
2. Mid-Term Student Research Evaluation Symposium 2016, 奈良先端科学技術大学院大学, 2016 年 11 月

List of foundations

1. 平成 26 年度 競争的研究支援 (20 万円)
2. 平成 27 年度 競争的研究支援 (25 万円)
3. 平成 28 年度 科学研究費助成事業 (90 万円)
4. 平成 28 年度 科学研究費助成事業 (80 万円)

Others

平成 28–29 年度 日本学術振興会特別研究員(DC2)

Acknowledgement

This dissertation deals with the studies accomplished by the author under direction of Prof. Hiroko Yamada at Nara Institute of Science and Technology (NAIST).

First of all, I would like to appreciate to Prof. Hiroko Yamada in NAIST for excellent guidance and constant encouragement for my study during these past five years. I thanks to my supervisors Prof. Masakazu Nakamura and Prof. Takuya Nakashima for giving me important suggestions and useful advices for this study. I also appreciate very much from Prof. Naoki Aratani, Prof. Daiki Kuzuhara (Current professor in Iwate University), Prof. Mitsuharu Suzuki and Prof. Hironobu Hayashi at NAIST for useful advices and encouragements. I truly grateful to Prof. Qian Miao and his lab members in The Chinese University of Hong Kong for giving me an excellent opportunity to stay in his laboratory and study the ultimate level of organic field effect transistor fabrications and measurements. I would like to appreciate Prof. Sadahiro Masuo and Mr. Takaki Nakagawa in Kansai Gakuin University for obtaining of fluorescence microspectroscopy images and helpful discussions. I would like to express the appreciation to Dr. Hiroyuki Saeki for starting up research environment of organic devices and teachin how to fabricate OSCs and SCLC device with respect. I would like to thank Dr. Tomoyuki Koganezawa (Japan Synchrotron Radiation Research Institute (JASRI) for the technical support in 2D-GIWAXD measurement (proposal No. 2014B1655, 2015B1769, 2015A1683, 2017A1779). I would like to thank Ms. Yoshiko Nishikawa[1], Mr. Kazuhiro Miyake[2], and Mr. Yasuo Okajima[3] in NAIST for measuring and analyzing of high-resolution mass spectrometry[1], Atomic force microscope[2], scanning electron microscope[2], scanning transmission electron microscope[2], and fluorescence lifetime[3], respectively. The author also appreciates all technical staffs in NAIST for giving affable lectures and continuous maintenance of research facilities. I would also like to thank former members in Prof. Yamada group, especially, Dr. Tatsuya Aotake, Dr. Mitsuru Kojima, Dr. Kohtaro Takahashi, Dr. Masataka Yamashita, Mr. Kensuke Uchinaga, Ms. Mika Sakaguchi, and Mr. Shinpei Yamamoto, for giving me some valuable comments that inspired this work. Furthermore, I am greatly indebted to my colleagues in this

doctoral course, Mr. Takuya Okabe, Mr. Akira Tamoto, Dr. Akinobu Matsumoto, and Mr. Songlin Xue for sharing their vast knowledge during our daily discussions. I thank The Nippon Synthetic Chemical Industry Co., Ltd. (Osaka, Japan) for the supply of ethyl isocyanoacetate, a starting material for the synthesis of CP.

This work was partly supported by CREST, JST, Grants-in-Aid for Scientific Research (No. 26620167, JP26105004 and JP16H02286), Grant-in-Aid for JSPS Research Fellow, the Green Photonics Project in NAIST, and the program for promoting the enhancement of research universities in NAIST supported by MEXT.

Lastly, I would like to thank my family for all their love and encouragement.

Yuto Tamura
March 15, 2018